



Durham E-Theses

Production and performance of thin and thick film NTCR thermistors based on $NiMn_{(2)}O_{(4)+\delta}$

Schmidt, Rainer

How to cite:

Schmidt, Rainer (2003) *Production and performance of thin and thick film NTCR thermistors based on $NiMn_{(2)}O_{(4)+\delta}$* , Durham theses, Durham University. Available at Durham E-Theses Online:
<http://etheses.dur.ac.uk/3722/>

Use policy

The full-text may be used and/or reproduced, and given to third parties in any format or medium, without prior permission or charge, for personal research or study, educational, or not-for-profit purposes provided that:

- a full bibliographic reference is made to the original source
- a [link](#) is made to the metadata record in Durham E-Theses
- the full-text is not changed in any way

The full-text must not be sold in any format or medium without the formal permission of the copyright holders.

Please consult the [full Durham E-Theses policy](#) for further details.

Academic Support Office, Durham University, University Office, Old Elvet, Durham DH1 3HP
e-mail: e-theses.admin@dur.ac.uk Tel: +44 0191 334 6107
<http://etheses.dur.ac.uk>

Production and Performance of Thin and Thick Film NTCR Thermistors Based on $\text{NiMn}_2\text{O}_{4+\delta}$

A copyright of this thesis rests with the author. No quotation from it should be published without his prior written consent and information derived from it should be acknowledged.

By

Dipl. Phys. Rainer Schmidt



U O NEW 2003

*A Thesis submitted for the
Degree of Doctor of Philosophy
in the University of Durham*

August 2003

Abstract

In this study reliable film type NTCR thermistors based on $\text{NiMn}_2\text{O}_{4+\delta}$ were produced and their electrical properties were studied in detail.

Electron-beam evaporation procedures have been applied to produce thin film NTCR thermistors. Phase pure $\text{NiMn}_2\text{O}_{4+\delta}$ target material was produced via a traditional ceramic precursor oxide route and thin films were deposited in an optimised procedure. The thickness distribution of evaporated films showed good agreement with a theoretical model, derived from evaporation theory and the sticking coefficient of the vapour on the substrates was approximately $80\% \pm 1.5\%$.

The composition of electron-beam evaporated films was found to be not controllable in terms of the phase purity and the Ni : Mn ratio. In order to avoid these problems thick film $\text{NiMn}_2\text{O}_{4+\delta}$ NTCR thermistors were developed using direct screen-printing techniques. Detailed Rietveld refinement analysis was carried out for the source powder used for screen-printing.

The main focus of the work was the measurement of resistance-temperature (R - T) characteristics of thin and thick films and pellets. In the temperature range of concern (77 K – 550 K) conduction was found to be by variable-range hopping (VRH) and nearest-neighbour hopping (NNH); $R \sim \exp(T_0/T)^p$, where the index p depends on the mode of hopping. Detailed analysis of R - T data showed that screen-printed films and pellets exhibited a p -value of 0.5, which was identified with VRH with a parabolic density of states (DOS) with an exponential dependence of resistance: $R \sim \exp(T_0/T)^{0.5}$. For electron-beam evaporated films the mechanisms detected were NNH: $R \sim \exp(T_0/T)$; and VRH with a constant DOS ($p = 0.25$) following: $R \sim \exp(T_0/T)^{0.25}$.

For screen-printed films with incorporated glass phase the electrical conduction mechanism was analysed using a.c. impedance spectroscopy and at low frequencies the hopping conduction was in agreement with the d.c. behaviour. The time constant of this mechanism could be described by an equivalent circuit containing a RC element. For higher frequencies a second mechanism was found, best described by a CRL element.

Acknowledgements

In the first place I wish to thank my supervisor Dr. A.W. Brinkman for his commitment, patience, help and guidance provided throughout my PhD course and especially for the help in the preparation of this thesis.

I wish to thank Dr. T.P.A. Hase, Dr. K. Durose and Dr. I. Terry for valueable discussions and the help provided.

Thanks to Mr. P. Armstrong, Mr. J.F. Scott, Mr. N. Thompson and Mr. D. Pattinson for technical support.

The work of Gwyn Ashcroft and the good co-operation is acknowledged here explicitly.

I would like to thank the members of the Department of Material Science III, Glass and Ceramics, at the University of Erlangen-Nuremberg, in particular Prof.Dr. A. Roosen and Mr. A. Stiegelschmitt for their guidance and help provided with screen-printing films.

Thanks also to Dr. A. Goeta and Dr. J. Evans for allowing use of XRD facilities and all other members of the Crystallographic group in the Department of Chemistry, University of Durham, who provided help with the data analysis, especially Neil Withers.

A big thanks goes to Dr. A. Basu for the great cooperation, the very helpful discussions and the mutual exchange of knowledge. Thanks to Andrew Yates for conducting SEM and EDAX measurements and thanks for the great atmosphere in the research group to Ben Cantwell, Guillaume Zoppi, Keriya Mam, Nick Boyall, Dr. H. Sanghera, David Beet, Michael Beckham, Matt Hogan, Debbie Hales, Paul Edwards, Mike Cousins, Thomas Schmidt and everybody else I have forgotten.

Thanks also to all my friends I met in Durham, particularly in Graduate Society, making it the most special place in the world I know, Angel Galmiche-Tejeda, Maria-Jose Duaso, Ali Hajighasemi, Thomas Winiecki, Jane Arkell, Thomas Franchoo, Richard O'Brien, Maria Arantzamendi, Marco Palumbo, Fiona Tolan, Doug Lionais, Eva Cervera, Marco Cvitas, Jelena Trmcic, Hugo Horta, Kha-young Kim, Leandro Sepulveda-Ramirez, Matthias Hoffmann, Christine Lorenz, Martin Bickl, Oliver Vogt, Jens Lamping, Michael Meznar, Veronique Margerit, Alex Metcalfe, Alain Wolf, Ilona Bausch, Philipp Zuber, Rafael Meseguer, Alberto Fernandez, Amerigo Pagano and everybody else I have forgotten. A special thanks goes to Maria Sakkelli for her support.

Thanks also to all my friends in Germany who kept in touch with me, making me the distance to home feeling much more bearable, Veit Rössner, Matthias Kettl, Thomas Beyer, Stefan Petri, Martin Blaschke, Bernhard Klein and Kirsten Rosenbauer.

On a more personal note I wish to thank my parents for their great support and their financial effort enabling me to follow a PhD course.

DECLARATION

I declare that all the work in this thesis was carried out by the candidate unless stated otherwise. Parts of the work presented in chapter 4 were submitted for the degree of “Physik-Diplom” at the University of Erlangen-Nuremberg. This material is declared accordingly in chapter 4. The remaining parts of this work have not previously been submitted for any degree and are not being submitted for any other degree.



Dr A W Brinkman

Supervisor



Rainer Schmidt

Candidate

The copyright of this thesis rests with the author. No quotation from it should be published without prior written consent and information derived from it should be acknowledged.

Contents

Chapter 1 Introduction	1
1.1. Introduction	1
1.2. Historical development	4
1.3. Scope of the work presented	5
1.4. Other work	6
1.5. References	7
<hr/>	
Chapter 2 Theoretical background and literature review	8
2.1. Introduction	9
2.2. Crystal structure and cation distribution	10
2.3. Phase stability	14
2.4. Synthesis of $\text{NiMn}_2\text{O}_{4+\delta}$	16
2.5. Electrical conduction	18
2.5.1. Hopping transport in $\text{NiMn}_2\text{O}_{4+\delta}$	18
2.5.2. Electron hopping between localised electron states	20
2.5.3. Miller – Abrahams resistor network	21
2.5.4. Percolation theory	23
2.5.5. Nearest-Neighbour-Hopping (NNH)	25
2.5.6. Variable-Range-Hopping (VRH) with constant density of states (DOS)	26
2.5.7. VRH with a parameterised density of states	29
2.5.8. Small polaron hopping	32
2.5.9. Review of other hopping models	34
2.6. Doping in the system $\text{Ni}_{1-a}\text{Mn}_{2-b}\text{M}_a\text{N}_b\text{O}_4$ (M, N = In, Zn, Co, Cu, Li, Fe, Mg)	36
2.7. Conclusions	38
2.8. References	39

Chapter 3 Thin film production by Electron-beam evaporation	44
3.1. Introduction	45
3.2. Electron-beam evaporation processes	46
3.2.1. Basic principle of the growth process of films	46
3.2.2. Target powder production	47
3.2.3. Substrate preparation	49
3.2.4. The E-beam evaporation system	50
3.2.5. E-beam evaporation process parameters	53
3.3. Thickness distribution of E-beam films	55
3.3.1. Evaporation theory	55
3.3.2. Film profiles	59
3.3.3. Thickness distribution of films	60
3.4. Phase purity, Ni : Mn ratio and morphology of E-beam films	62
3.4.1. XRD patterns of the target material	63
3.4.2. XRD patterns of E-beam films	64
3.4.3. Energy Dispersive Analysis of X-rays (EDAX)	67
3.4.4. Scanning Electron Microscopy (SEM)	69
3.5. Conclusions	76
3.6. References	78

Chapter 4 Thick film production via screen-printing techniques	79
4.1. Introduction	80
4.2. Co-precipitated NiMn ₂ O _{4+δ} source powder	81
4.2.1. Powder production	81
4.2.2. XRD analysis of decomposed nickel manganese oxalates	84
4.2.3. The Rietveld refinement method	86
4.2.4. Rietveld refinement analysis	91
4.2.4.1. Refinement of atom positions	92
4.2.4.2. Goodness of fit S , R_{Bragg} , correction term z_{corr} and thermal factors B_{th}	95
4.2.4.3. Phase composition, unit cell parameter and average grain size	97

4.3. Screen-printing of thick film $\text{NiMn}_2\text{O}_{4+\delta}$ films	104
4.3.1. Principles of screen-printing	104
4.3.2. The screen-printing screen	106
4.3.3. The screen-printing process	107
4.3.4. XRD analysis of screen-printed films	109
4.3.5. Scanning Electron Microscopy (SEM) and surface profileometry	110
4.4. Conclusions	112
4.5. References	114
<hr/>	
Chapter 5 D.c. measurements of $\text{NiMn}_2\text{O}_{4+\delta}$ materials	116
5.1. Introduction	117
5.2. Theory	118
5.2.1. NNH model	118
5.2.2. VRH models	119
5.2.3. Analysis of Resistance vs. Temperature data	122
5.3. Experimental	125
5.3.1. Contacts	125
5.3.2. Low temperature regime measurements	126
5.3.3. Control software	128
5.3.4. High temperature regime measurements	132
5.4. Results	133
5.4.1. Electron-beam evaporated films	133
5.4.1.1. Thin films on Al_2O_3 substrates	134
5.4.1.2. Thin films on glass substrates	142
5.4.2. Screen-printed films	145
5.4.3. Pellets	148
5.4.4. Summary	150
5.5. Conclusions	152
5.6. References	155
<hr/>	
Chapter 6 A.c. impedance spectroscopy of screen-printed films with glass phase	157
6.1. Introduction	158

6.2. Theoretical Review	159
6.2.1. Basic principle of impedance spectroscopy	159
6.2.2. Data analysis and equivalent circuit modelling	161
6.2.3. A.c. impedance of hopping processes	165
6.3. Experimental techniques	169
6.4. Results/ Discussion	171
6.4.1. Impedance spectroscopy data presented as Z' - Z'' complex plane loci	171
6.4.2. Interpretation of Z' - Z'' complex plane loci	174
6.4.3. Data analysis by modulus M'' vs. frequency plots	177
6.4.4. Data analysis by Z' vs. f and Z'' vs. f plots	181
6.4.5. A.c. conductivity of the hopping mechanism	184
6.4.5.1. Extended Pair Approximation (EPA)	184
6.4.5.2. Impedance vs. temperature plots	186
6.4.6. Equivalent circuit modelling	191
6.4.6.1. Z' behaviour in respect to the equivalent circuit model	192
6.4.6.2. Z'' behaviour in respect to the equivalent circuit model	194
6.5. Conclusions	196
6.6. References	198
<hr/>	
Chapter 7 Conclusions	199
7.1. Conclusions	199
7.2. Scope for future work	206
7.3. References	209
<hr/>	
Appendix A List of Publications	
Appendix B XRD reference patterns from JCPDS data base	
Appendix C X-ray spectra of decomposed oxalates	
Appendix D I - V behaviour of Al contacts	
Appendix E Control Software for automated R - T data acquisition	
<hr/>	

List of Abbreviations

a.c.	Alternating current
CRL element	Capacitance – Resistance – Inductance element
d.c.	Direct current
DOS	Density Of States
E-beam	Electron-beam
EDAX	Energy Dispersive Analysis of X-Rays
e.s.d.	Estimated standard deviation
EPA	Extended Pair Approximation
HFR	High Frequency Regime
HTR	High Temperature Regime
IFR	Intermediate Frequency Regime
LFR	Low Frequency Regime
LTR	Low Temperature Regime
NNH	Nearest-Neighbour Hopping
NTCR	Negative Temperature Coefficient of Resistance
PTCR	Positive Temperature Coefficient of Resistance
PVD	Physical Vapour Deposition
RC element	Resistance – Capacitance element
rf	Radio frequency
R-T	Resistance- Temperature
RTD	Resistance Temperature Detectors
SEM	Scanning Electron Microscopy
STM	Scanning Tunnelling Microscopy

STS	Scanning Tunnelling Spectroscopy
UHFR	Ultra High Frequency Regime
VRH	Variable-Range Hopping
XPS	X-Ray Photoelectron Spectroscopy
XRD	X-Ray Diffractometry

Chapter 1

Introduction

1.1. Introduction

This work is about the production and performance of temperature sensing devices based on $\text{NiMn}_2\text{O}_{4+\delta}$. Temperature sensors in general have a wide range of applications in every part of our daily life. Besides the common domestic usage, for example in form of a thermometer, a huge variety of different types of temperature sensors are used for applications in technical, natural or medical sciences.

In these devices the temperature sensing mechanism is always based on a specific physical property of the sensor material, where the corresponding parameter depends on the temperature. Different mechanisms may be appropriate for different applications and the sensors may be classified accordingly:

1.) The most common temperature sensing mechanism is based on the thermal expansion of liquids or gases, such as the well known mercury thermometer used for common domestic applications or in medical environments for measuring body temperature.

2.) Thermocouples are based on the thermoelectric effect, where a voltage occurs as a result of a temperature gradient across a junction of two different materials [1] .

Thermocouples consist of two dissimilar metal wires welded together and the

difference in the heat capacitance leads to a temperature gradient across the junction, resulting in a voltage output. The most versatile thermocouples capable of measuring at higher temperature ranges ($90^{\circ}\text{C} - 1200^{\circ}\text{C}$) are chromel-alumel, chromel-constantan and constantan-iron and at lower temperature ranges ($-200^{\circ}\text{C} - 350^{\circ}\text{C}$) copper-constantan junctions [2]. Thermocouples are fast in response, relatively cheap to manufacture and may be used for a wide range of temperature, but are highly susceptible to noise due to a very small voltage output.

3.) Resistance thermometers or Resistance Temperature Detectors (RTD) are made of wires or thin films of one single metal such as copper, nickel or most commonly platinum. Sensors of this class exhibit a fairly linear resistance-temperature ($R-T$) characteristic, where the resistance increases due to increasing electron scattering with increasing temperature. RTDs are very accurate, but slow responding and costly to produce, thus unsuitable for high volume commercial applications.

4.) Nowadays most temperature sensing materials used in technical applications exhibit a temperature dependent electrical resistance and are called Thermistors (thermally sensitive resistors). Two main classes may be distinguished with either a Positive Temperature Coefficient of Resistance (PTCR) or a Negative Temperature Coefficient of Resistance (NTCR).

- a) PTCR thermistors are ideal for use as a circuit element on its own as a self-regulating heater, current overload protection or over-heat regulator in a whole spectrum of professional and domestic systems and applications ranging from simple ovens to telemetry [3].

- Semiconducting PTCRs are made of semiconducting films, slabs or pellets most commonly based on silicon [4]. These devices exhibit a better linearity of the R - T characteristic than RTDs or thermocouples ranging from -100°C – 200°C , the output voltage is comparatively high, they are cheap to manufacture, and thus quite widely used.

- Switching PTCR thermistors exhibit a very strong positive temperature dependence of the resistance over a restricted temperature region and show NTCR behaviour at all other temperatures. The materials for these devices are commonly based on semiconducting barium titanate. Lead or strontium titanate may be added to vary the temperature at which the PTCR effect occurs [3].

b) NTCR thermistors are probably the most widely used temperature sensors due to their low cost and high sensitivity. They exhibit an exponential dependence of resistance upon temperature, i.e. small changes in temperature result in large changes of resistance. NTCR thermistors are traditionally fabricated as pellets or slabs from sintered semiconducting oxide materials. The R - T characteristic is uniform over a wide range of temperature (-200°C – 350°C) enabling many different applications of temperature measurements [3].

NTCR thermistors are used where high accuracy is important, for example in the medical field for localised or general body temperature measurements, in meteorology for weather forecasting, in the chemical industry as process temperature controller and in the car industry as engine temperature controller [5]. NTCR thermistors are cheap to produce and suitable for mass

production in the industry. $\text{NiMn}_2\text{O}_{4+\delta}$ is one example of these materials and was investigated in this study.

1.2. Historical development

The history of NTCR thermistors commenced in 1833 with Faraday's discovery that the resistance of Ag_2S had a negative temperature coefficient, but little use could be made of this discovery, in part because the behaviour of semiconducting materials was not well understood before the development of quantum mechanics during the 1920/30s.

One of the main steps forward was the work carried out in the Philips laboratories in Holland and in the Bell telephone laboratories in the USA [6] during the World War II, which lead to an explanation for the mechanism dominating the resistivity in semiconducting oxide materials. During this time $\text{NiMn}_2\text{O}_{4+\delta}$ was first considered for use as a NTCR thermistor, along with other materials such as NiO , CoO and other compounds of the $\text{NiO-Co}_2\text{O}_3\text{-Mn}_2\text{O}_3$ system, and has been used since in industrial applications in bulk material form.

During the 1950/60s several studies were conducted on basic structural, electrical and magnetic properties of NTCR thermistors based on the $\text{NiO-Co}_2\text{O}_3\text{-Mn}_2\text{O}_3$ system to understand the interplay of structural properties such as cation distribution and type of spinel structure with the electrical or magnetic behaviour.

With the rapid development of film deposition techniques in recent decades the production of NTCR thermistor films became interesting, as reflected in a substantial increase in the number of publications in the late 1980s reporting different film production techniques and a variety of approaches to improve the sensor

performance by including different dopants into the system. This strong interest in NTCR thermistors based on the NiO-Mn₂O₃ system has continued up to now with the main focus being on the sensor performance of doped systems.

1.3. Scope of the work presented

As mentioned above, NiMn₂O_{4+δ} has been widely used in the industry as a temperature sensor in bulk material applications. Commercial bulk NTCR thermistors usually exhibit a temperature tolerance in the range of ± 0.2 °C, the resistance tolerance varies for different devices between ± 5% and ± 10% and the thermistor constants are normally in a range of 2750 - 4100 Kelvin.

However, despite optimisation of the production process of this type of devices severe problems of poor stability and reproducibility remain due to high porosity and incomplete inter-granular contact in the material. In addition, pores make the device sensitive to effects of the surrounding ambient such as changes in humidity which affect the resistivity or variations in oxygen partial pressure that can change the oxygen content of the sensor material [7].

In principle, these problems can be minimised in dense films and two different film production techniques were considered in this work, electron-beam (E-beam) evaporation and screen-printing. The films produced have been characterised and it was intended to clarify the electrical conduction mechanism(s), as several contradictory statements about electron hopping in NiMn₂O_{4+δ} can be found in the literature.

In chapter 2 the basic properties of $\text{NiMn}_2\text{O}_{4+\delta}$ in terms of the crystal structure, cation distribution and phase stability, and theoretical approaches to electron hopping are reviewed. In chapter 3 the deposition of thin films by electron-beam evaporation is discussed in detail, which is a Physical Vapour Deposition (PVD) method. The feasibility of screen-printing as an alternative deposition process is assessed in chapter 4. The target preparation for each process and the comprehensive structural characterisation of both types of film are presented in chapter 3 and 4. Chapter 5 presents the results of direct current (d.c.) R - T measurements of bulk, E-beam and screen-printed films. Chapter 6 reports on the temperature dependent impedance spectroscopy of the screen-printed films.

Chapter 7 provides a summary of all results and compares the performance of both types of films. The scope for future work is discussed in this chapter as well.

1.4. Other work

During the course of this study several papers describing the preparation and characterisation of $\text{NiMn}_2\text{O}_{4+\delta}$ films have been submitted and published ([7], [8], [9], [10]).

In an earlier study [11] the production of screen-printed thick $\text{NiMn}_2\text{O}_{4+\delta}$ films and their structural characterisation has been described, and this work was submitted for the degree of “Physik-Diplom” at the University of Erlangen-Nuremberg. Chapter 4 contains a review of this work.

1.5. References

1. McKelvey J.P., *Solid State and Semiconductor Physics*, 1966, New York, Harper&Row
2. <http://instserv.com/rmocoupl.htm>, *Thermocouple Data Base*,
3. Macklen E.D., *Thermistors*, 1979, Glasgow, Electrochemical Publications
4. <http://www.rtie.com/ptc/silicone.htm>, *PTC Silicon Thermistors*,
5. Basu A., *Deposition and Characterisation of Sputtered Nickel Manganate Thin Films*, PhD Thesis, Department of Physics, 2002, Durham, University of Durham
6. Sachse H.B., *Semiconducting temperature sensors and their applications*, 1975, New York, John Wiley & Sons
7. Schmidt R., Brinkman A.W., *Preparation and characterisation of NiMn₂O₄ films*, *International Journal of Inorganic Materials*, 2001, **3**, p. 1215
8. Schmidt R., Stiegelschmitt A., Roosen A., Brinkman A.W., *Preparation and Performance of Thick Film NTC Thermistors*, *Key Engineering Materials*, 2002, **206-213**, p. 1417
9. Schmidt R., Stiegelschmitt A., Roosen A., Brinkman A.W., *Screen Printing of Coprecipitated NiMn₂O₄ for Production of NTC Thermistors*, *Journal of the European Ceramic Society*, 2003, **23**(10), p. 1549
10. Schmidt R., Basu A., Brinkman A.W., *Production of NTCR thermistor devices based on NiMn₂O_{4+δ}*, *Journal of the European Ceramic society*, **In Press**
11. Schmidt R., *Screen Printing of Coprecipitated NiMn₂O₄ for Production of NTC Thermistors*, 2001, Diploma Dissertation, Department of Material Science III, University of Erlangen-Nuremberg, Erlangen

Chapter 2

Theoretical background and literature review

2.1. Introduction	9
2.2. Crystal structure and cation distribution	10
2.3. Phase stability	14
2.4. Synthesis of $\text{NiMn}_2\text{O}_{4+\delta}$	16
2.5. Electrical conduction	18
2.5.1. Hopping transport in $\text{NiMn}_2\text{O}_{4+\delta}$	18
2.5.2. Electron hopping between localised electron states	20
2.5.3. Miller – Abrahams resistor network	21
2.5.4. Percolation theory	23
2.5.5. Nearest-Neighbour-Hopping (NNH)	25
2.5.6. Variable-Range-Hopping (VRH) with constant DOS	26
2.5.7. VRH with a parameterised DOS	29
2.5.8. Small polaron hopping	32
2.5.9. Review of other hopping models	34
2.6. Doping in the system	
$\text{Ni}_{1-a}\text{Mn}_{2-b}\text{M}_a\text{N}_b\text{O}_4$ (M, N = In, Zn, Co, Cu, Li, Fe, Mg)	36
2.7. Conclusions	38
2.8. References	39

2.1. Introduction

In this chapter the basic properties of $\text{NiMn}_2\text{O}_{4+\delta}$ are presented and the close relation between crystal structure, cation distribution and the electrical conduction mechanism is highlighted. The analysis of the electrical conduction mechanism is the main focus of this work, so a detailed consideration of different models is presented. Electron transport in $\text{NiMn}_2\text{O}_{4+\delta}$ occurs by a thermal activated hopping process [1] and the fundamentals of hopping conduction are described, following the celebrated approaches from Miller and Abrahams [2], Ambegaokar [3] and Mott [4]. A general expression for hopping in $\text{NiMn}_2\text{O}_{4+\delta}$ will be derived and compared to models previously suggested in the literature.

Furthermore, the phase stability of $\text{NiMn}_2\text{O}_{4+\delta}$ is discussed and a review of several approaches to include dopants into the $\text{NiMn}_2\text{O}_{4+\delta}$ spinel system is given.

2.2. Crystal structure and cation distribution

NiMn_2O_4 crystallises in a typical cubic spinel structure. In general, spinels can be represented by the expression $\text{A}(\text{B}_2)\text{O}_4$ where usually A is a divalent and B a trivalent cation. The most well-known spinel is MgAl_2O_4 .

In a spinel structure the oxygen anions form a f.c.c. sub-lattice with the metal cations situated at two different types of interstices, tetrahedral and octahedral sites as can be seen from Fig. 2.1.

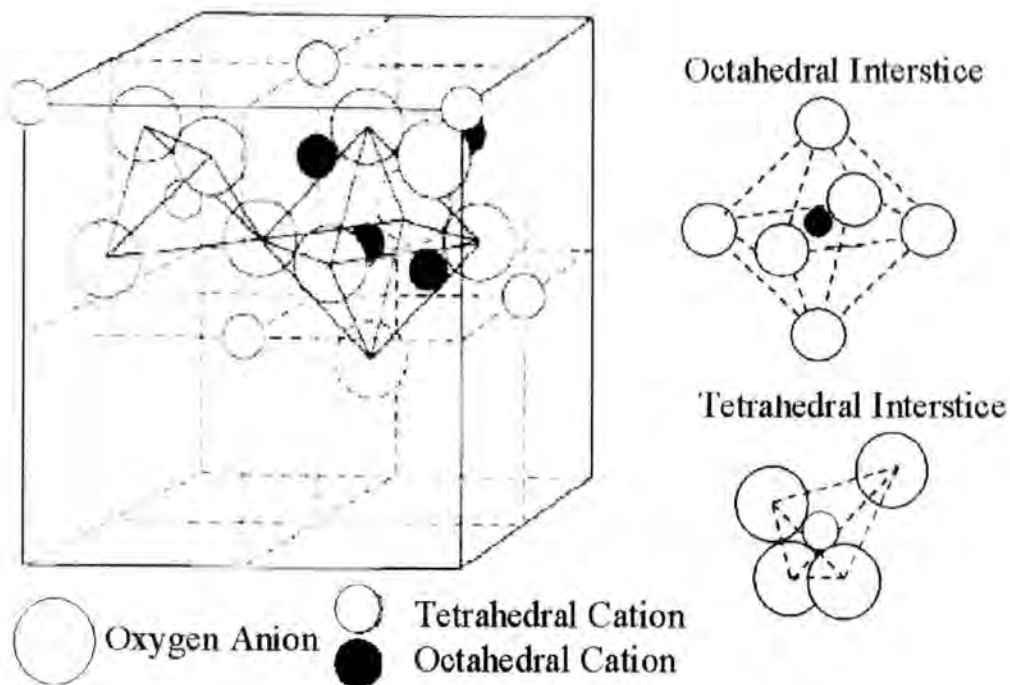


Fig. 2.1 Spinel structure showing the octahedral and tetrahedral interstices, [5]

A complete cubic unit cell of NiMn_2O_4 contains 64 tetrahedral and 32 octahedral interstices of which 8 tetrahedral and 16 octahedral sites are occupied, thus the

occupancy is 12.5% for tetrahedral and 50% for octahedral interstices. Including 32 oxygen anions, 16 manganese and 8 nickel cations, the unit cell comprises 56 ions. As can be seen from Fig. 2.2, the unit cell can be represented by 8 different layers perpendicular to the (111) plane of the oxygen sub-lattice [5].

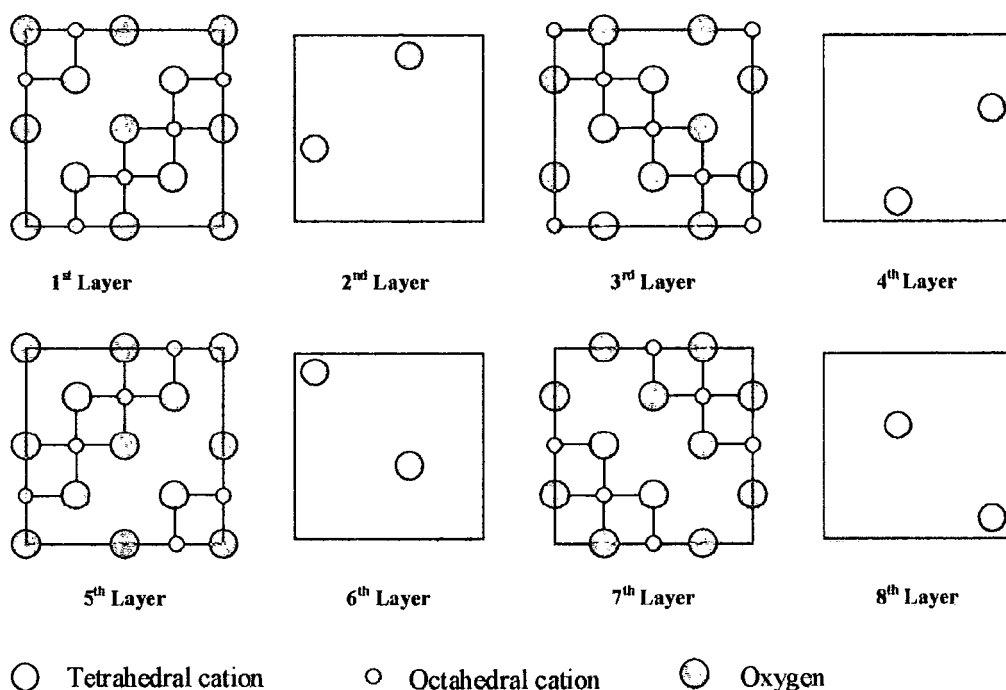
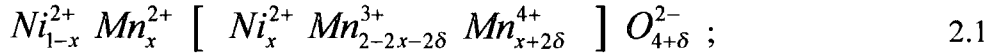


Fig. 2.2 Eight layers of the unit cell, [5]

In a regular spinel, divalent and trivalent cations are situated on tetrahedral and octahedral sites respectively. In contrast, in a complete inverse spinel structure all divalent cations move to octahedral sites and half the trivalent cations move from octa- to tetra-hedral sites. NiMn_2O_4 is an intermediate type of spinel where only a fraction of the Ni^{2+} cations transfer to octahedral sites, the Mn^{3+} cations on octahedral sites disproportionate to Mn^{2+} and Mn^{4+} , and Mn^{2+} cations move to tetrahedral sites to compensate all Ni^{2+} vacancies.

Depending on the ambient conditions and the temperature during the production process of $\text{NiMn}_2\text{O}_{4+\delta}$ materials, the oxygen content varies and is compensated by a corresponding change in the $\text{Mn}^{3+}/\text{Mn}^{4+}$ ratio. The cation distribution can then be described by [6]:



The brackets [] indicate the cation concentration on octahedral sites. x is the fraction of nickel cations on octahedral sites and is referred to as the inversion parameter. δ is the stoichiometric excess ($\delta > 0$) or loss ($\delta < 0$) of oxygen. Larson et al. [7] suggested that $x = 1$ and both, Mn^{2+} and Mn^{3+} are present on tetrahedral sites, which would be inconsistent with 2.1. However, Boucher et al. [8] have shown conclusively by neutron diffraction studies that x decreased from 0.76 to 0.74 as the temperature was increased from 750°C to 950°C.

Several other suggestions for cation distributions have been made by Sinha et al. [9], Baltzer and White [10] or Bhandage and Keer [11], but their models are all in contradiction with the findings from Brabers et al. [12], Hashemi and Brinkman [13], and Töpfer et al. [14], who all identified 3 different valencies of manganese (i.e. $\text{Mn}^{2+}/\text{Mn}^{3+}/\text{Mn}^{4+}$) using XPS, consistent with the distribution given in 2.1.

The x - values obtained by Boucher et al. [8] at particular temperatures differ from the results obtained by Macklen [15], who gave the following relation :

$$x = 1 - 0.0005 (T - 200^\circ\text{C}) ; \quad 2.2$$

According to this relation x drops from 0.73 to 0.63 with increasing temperatures between 750°C – 950°C. Macklen obtained his results by relating conductivity data to the inversion parameter, which was supposed to vary by sintering at different temperatures. The samples were quench cooled to retain the high temperature configuration. The discrepancy with the findings of Boucher et al. may indicate that Macklen's assumptions made about the dependency of conductivity upon the inversion parameter and the cation distribution may have been incomplete, as discussed later.

However, a change of x with temperature would involve a migration of cations, which was described by Brabers and Terhell [6], who proposed the following equation:



The subscripts A and B indicate the occupancy of either tetrahedral (A) or octahedral (B) sites and E_{Tr} is the energy which is released when the spinel transfers to an energetically favourable configuration by disproportionation of Mn^{3+} cations. The equilibrium constant K for this reaction was found by applying the law of mass action to eq. 2.3 with the concentrations of the cations being denoted by the subscripts in 2.1. δ was set to 0 here.

$$K = \frac{x^3}{4(1-x)^3} = \exp\left(\frac{E_{Tr}}{k_B T}\right); \quad 2.4$$

The energy E_{Tr} was found to be about 0.66 eV [6].

Using neutron-diffraction data, Boucher et al. [8] reported the following relationship between the lattice parameter a and the inversion parameter x :

$$a = 8.441 - 0.057 x ; \quad 2.5$$

As x is temperature dependent, this relation would modify the regular thermal expansion behaviour. According to Brabers, the thermal expansion is regular below 450°C and deviates from linearity above. This would suggest that cation migration starts to take place only above 450°C. However, it is believed that in fact eq. 2.5 can only be applied for temperatures between ~ 750°C - 900°C as the regular $\text{NiMn}_2\text{O}_{4+\delta}$ spinel is only stable within this small temperature window. This is described in more detail in the next section.

2.3. Phase stability

For the analysis of electrical conduction in $\text{NiMn}_2\text{O}_{4+\delta}$ it is of vital importance to ensure phase purity. A change in electrical conduction behaviour at temperatures between 200°C and 750°C has been related to a change in cation distribution or other physical parameters by many authors, although the $\text{NiMn}_2\text{O}_{4+\delta}$ spinel is not stable in this temperature region and conductivity may well be affected by a second phase.

A comprehensive phase diagram for the Ni-Mn-O system for temperatures between 500°C and 1200°C and for different ratios of manganese and nickel was given by Wickham (see Fig. 2.3) [16]. In this study a variation of the oxygen content in

$\text{NiMn}_2\text{O}_{4+\delta}$ or in other compounds occurring was not taken into account, therefore $\delta = 0$.

According to this phase diagram the cubic NiMn_2O_4 spinel is stable in air between $\sim 750^\circ\text{C}$ and 900°C and dissociates at intermediate temperatures ($T < 750^\circ\text{C}$) to NiMnO_3 and Mn_2O_3 . At higher temperatures ($T > 900^\circ\text{C}$) a release of NiO and O_2 was reported to occur.

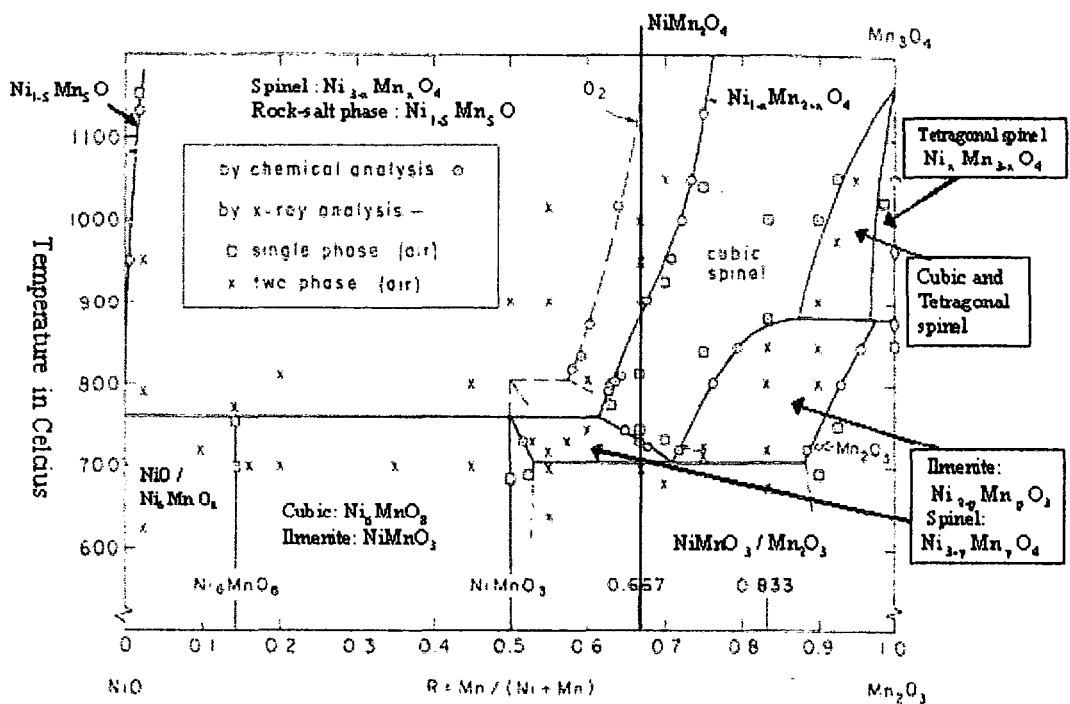


Fig. 2.3 Phase diagram for the system $\text{NiO-Mn}_2\text{O}_3\text{-O}_2$ [16], solid lines are for an oxygen partial pressure of 0.21 atm (air), dashed lines for 1 atm. R is the Ni/Mn ratio defined as: $R = [\text{Mn}] / \{ [\text{Ni}] + [\text{Mn}] \}$

Recently, the phase diagram has been extended for lower temperatures by Tang et al. [17]. They found that for about $0.6 < R < 0.7$ a cubic spinel phase exists at temperatures below 400°C . In the same temperature range for $R > 0.7$ a cubic spinel phase and Mn_5O_8 were reported to be present while for $R < 0.6$ a cubic spinel and a

rock salt phase forms. For stoichiometric $\text{NiMn}_2\text{O}_{4+\delta}$ ($R = 0.67$), the cubic spinel phase present at low temperatures was reported to exhibit cation vacancies or in other terms an excess of oxygen [18].

In the stability region of $\text{NiMn}_2\text{O}_{4+\delta}$ between 750°C - 900°C slightly different oxygen contents may occur as well. Jung [19] claimed that both, an excess and loss of oxygen is possible, depending on the sintering-ambient, -time and -temperature, but no equation could be formulated to describe this effect. Therefore, throughout this work the notation $\text{NiMn}_2\text{O}_{4+\delta}$ is used.

2.4. Synthesis of $\text{NiMn}_2\text{O}_{4+\delta}$

For any technological approach to produce NTCR thermistor materials, a source powder is the basis for any further processing. In this study $\text{NiMn}_2\text{O}_{4+\delta}$ powder was synthesised in a laboratory process, as it is not available on the free market, following two different production routes:

1.) NiO and Mn_2O_3 are mixed thoroughly (1:1 molar ratio) and sintered at 1150°C . NiO is released at temperatures over $\sim 900^\circ\text{C}$ (see Fig. 2.3) and an extended annealing process at 800°C for up to 60 hours is necessary to re-incorporate NiO [9], [20], [21]. This is a traditional ceramic powder processing route.

2.) Wet chemical processes based on pre-cursor oxalates were first introduced by Wickham [16]. More recently this technique of precipitation and thermal decomposition of oxalates has been further developed and small average grain size powders on micro- or even nanometer scales can be achieved [18], [19], [22].

Nickel manganese oxalate ($\text{NiMn}_2(\text{C}_2\text{O}_4)_3 \cdot 6 \text{H}_2\text{O}$) may be precipitated by adding $\text{C}_2\text{O}_4^{2-}$ anions to a Ni^{2+} and Mn^{2+} containing aqueous solution. In the Ni^{2+} , Mn^{2+} and $\text{C}_2\text{O}_4^{2-}$ stock solutions the concentrations have to be determined precisely to control the stoichiometry. Thermal decomposition of the precipitate at temperatures up to 400°C results in the defect spinel phase, or in the regular $\text{NiMn}_2\text{O}_{4+\delta}$ spinel phase by sintering at 850°C for 30 minutes [23].

The first route has been used for producing target material for electron-beam evaporation processes, the second for screen-printing. The experimental procedures are described more explicitly in the respective chapters later.

Other common synthesis routes for $\text{NiMn}_2\text{O}_{4+\delta}$ can be found in the literature:

3.) By adding NaOH or NH_4Cl to an aqueous solution of $\text{Ni}^{2+}(\text{aq})$ and $\text{Mn}^{2+}(\text{aq})$, both, $\text{Ni}(\text{OH})_2$ and $\text{Mn}(\text{OH})_2$ can be co-precipitated at a pH value of 10. The hydroxides are then thermally decomposed at 950°C and annealed at 800°C yielding phase pure $\text{NiMn}_2\text{O}_{4+\delta}$ [24], [25].

A problem with this method is that Na or Cl both cause serious impurities in the hydroxides, which have to be removed in a tedious washing process.

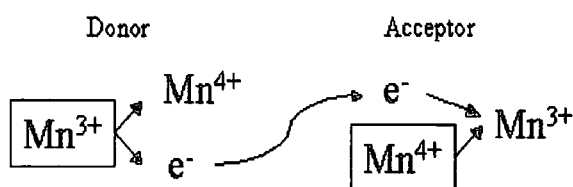
4.) Kamiyama and Nara [26] reported that a reduced sintering time of 3 hours can be achieved by firing a mixture of NiO and MnO_2 in the appropriate molar ratio at 1300°C . The material is annealed at 800°C for 24 hours.

5.) According to Gorgeu [27], $\text{NiMn}_2\text{O}_{4+\delta}$ can also be obtained by sintering the sulphates NiSO_4 and MnSO_4 , mixed in the appropriate ratio.

2.5. Electrical conduction

2.5.1. Hopping transport in $\text{NiMn}_2\text{O}_{4+\delta}$

In $\text{NiMn}_2\text{O}_{4+\delta}$ the electrical conduction is based on a thermally activated hopping mechanism where electrons transfer between manganese cations of different valence states according to the mechanism [1]:



2.6

In this type of thermally activated hopping the transfer rate and thus the conductivity show an exponential dependence on temperature and the resistance decreases with increasing temperature (NTCR). Although often referred to as semiconducting behaviour, the contributing manganese cations should be regarded as localised electron states and conduction is quite different to conventional band semiconductors.

As mentioned in section 2.2., Macklen [15] investigated the hopping conductivity in $\text{NiMn}_2\text{O}_{4+\delta}$, in relation to the cation distribution. Previously, Macklen [1] had stated that in principal electron hopping only takes place between atoms of the same sort, differing in their valencies by not more than one unit. In the case of $\text{NiMn}_2\text{O}_{4+\delta}$ only Mn^{3+} and Mn^{4+} cations on octahedral sites would contribute. Manganese cations of

different valencies on tetrahedral sites would exhibit a large distance to each other due to the low occupancy (12.5%), compared to octahedral sites (50%).

Electrical conductivity would thus be dependent on the $\text{Mn}^{3+}/\text{Mn}^{4+}$ ratio on octahedral sites and maximum conductivity would occur if the ratio is 1:1 [15], [28], [29], which corresponds to an inversion parameter of $x = 2/3$ in the case of stoichiometric NiMn_2O_4 .

However, none of the authors took into account that jumps between Mn^{2+} and Mn^{3+} on tetrahedral and octahedral interstices respectively could possibly take place. As can be seen from Fig. 2.2, Mn^{2+} and Mn^{3+} cations on tetrahedral and octahedral sites are only slightly further distanced from each other than octahedral cations, which could result in a perceptible hopping probability, especially as electrons in Mn^{2+} might show a weaker bonding than in Mn^{3+} . On the other hand, the occupancy of tetrahedral sites is low and the number of transitions occurring would be correspondingly low compared to hopping between octahedral sites.

Macklen [15] related the conductivity data to the inversion parameter x to obtain eq. 2.2, which assumes only pure $\text{Mn}^{3+}/\text{Mn}^{4+}$ hopping. It was shown that with decreasing oxygen content and thus with decreasing Mn^{4+} concentration the conductivity decreases. However, a maximum in conductivity for an even ratio of Mn^{3+} and Mn^{4+} did not occur, suggesting that conduction may not rely just on simple hopping between Mn^{3+} and Mn^{4+} cations and might explain the fact that eq. 2.2 did not correspond to the neutron diffraction data from Boucher et al. [8].

It is clear that the cation distribution, and thus conductivity, varies with oxygen content, but it may be the case that it is not only the resulting change in cation distribution which is important. A loss of oxygen would also increase the occupancy

of possibly both tetrahedral and octahedral sites, leading in turn to a higher conductivity, in contrast to Macklen.

Given these uncertainties it will be extremely difficult to directly relate conductivity quantitatively to the oxygen content and cation distribution. No conclusive relation between sintering temperature and oxygen content is given in the literature.

Furthermore, in $\text{NiMn}_2\text{O}_{4+\delta}$ the electron transport might be directly supported by oxygen anions, which was reported to be the case between Mn^{3+} and Mn^{4+} cations in layered manganate perovskite structures [30], [31]. In these types of compound electron hopping takes place from a Mn^{4+} cation to a O^{2-} anion and coincidentally from the same O^{2-} anion to Mn^{3+} . This double exchange effect has not been considered yet for $\text{NiMn}_2\text{O}_{4+\delta}$ in any study so far, and possible effects on the conductivity are not known.

However, a qualitative analysis of most parameters affecting the conductivity may well be possible and a model can be deduced as presented in the next section.

2.5.2. Electron hopping between localised electron states

Electron hopping conduction theories were first developed in order to describe electron transport in crystalline semiconductors at very low temperature regimes ($T < 5\text{K}$). At these temperatures electron hopping between localised impurity states can occur and can dominate any other electrical transport, for example by ionisation of donor and acceptor levels or by excitation of electrons from valence to conduction band. Impurity states can be described by a so-called Hubbard impurity band [32]. If electron bands of delocalised states exist, impurity states are always located in the

gap between the regular bands of delocalised states, because localised and delocalised states cannot coexist at the same energy [33].

Electron hopping also occurs in amorphous and highly disordered materials such as amorphous semiconductors, which normally exhibit quite a large energy range of localised electron states. Despite their localisation, these electron states can be described by the same concept of a density of states $g(\epsilon)$ in energy and space.

It is believed that this is a valid concept in $\text{NiMn}_2\text{O}_{4+\delta}$ materials as well, where the manganese cations participating in the electron hopping can be regarded as localised electron states.

The most basic work describing hopping conduction was carried out by Miller and Abrahams [2]. All subsequent research has been based on their fundamental considerations of hopping conductivity.

2.5.3. Miller - Abrahams resistor network

Miller and Abrahams proposed a random resistor network to describe electron transfer between localised states. Randomly distributed vertices, for example i and j , represent two electron states, which are connected by a resistor R_{ij} . Fig. 2.4 shows such a network. For small applied electric fields, the resistance R_{ij} connecting site i and j is of the form:

$$R_{ij} = R_{ij}^0 \exp(\xi_{ij}); \quad 2.7$$

R_{ij}^0 is the limiting value at $T \rightarrow \infty$, and ξ_{ij} is called the percolation value given by the fundamental expression :

$$\xi_{ij} = \frac{2r_{ij}}{a} + \frac{\varepsilon_{ij}}{k_B T} ; \quad 2.8$$

where r_{ij} and ε_{ij} are the separation of electron states in real and energy space respectively.

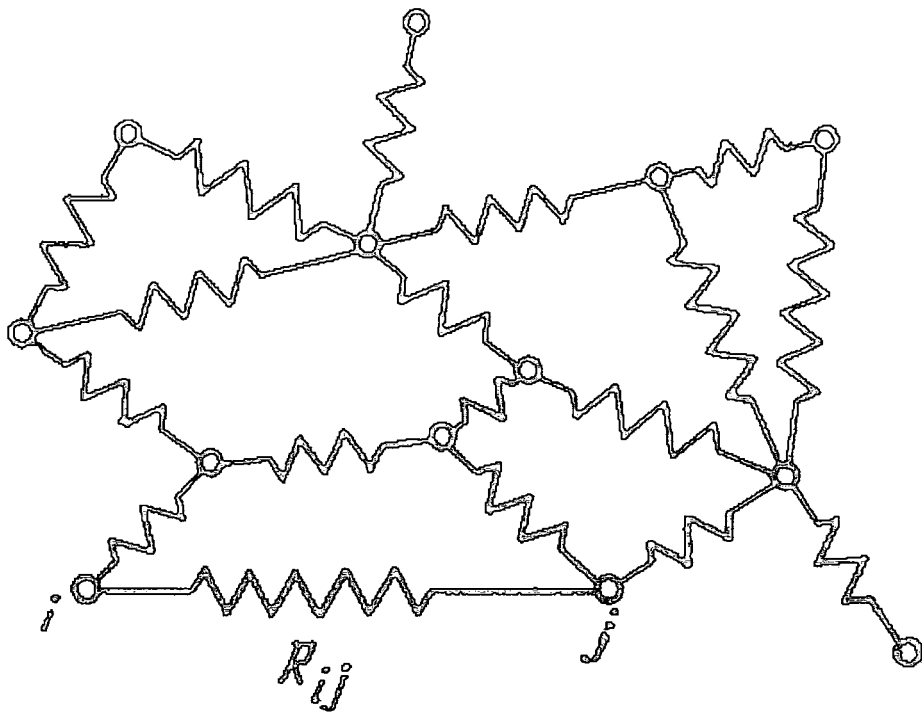


Fig. 2.4 Random resistor network proposed by Miller and Abrahams, [34]

In equation 2.8 the first term on the right hand side describes the exponential dependence of the resistance upon the overlap of the wave functions, which for hydrogen like wave functions decrease with distance r according to $\sim \exp(-r/a)$,

where $1/a$ is an atom specific parameter in m^{-1} . The second term describes the dependency of R_{ij} on the separation of states in energy space. Strictly speaking, the transfer of an electron is achieved by the absorption or emission of a phonon and the second term in 2.8 is proportional to the number of phonons available at the required energy. Multi-phonon processes may be neglected as mentioned in more detail later.

In the following discussion it will be assumed that the hopping sites are randomly distributed, that the number of random sites is large and the distance between sites is small compared to the size of the system.

The more fundamental parameter Γ_{ij} may be defined as the hopping rate or the number of electrons transferring per unit time.

$$\Gamma_{ij} = \gamma_{ij}^0 \exp\left(\frac{-2r_{ij}}{a}\right) \exp\left(\frac{-\epsilon_{ij}}{k_B T}\right); \quad 2.9$$

where γ_{ij}^0 describes all parameters which depend on Γ_{ij} in a non-exponential way. R_{ij} would be inversely proportional to Γ_{ij} .

2.5.4. Percolation theory

In hopping conduction electrons propagate through a sample preferentially along the most conducting paths. These would be randomly distributed sequences of sites with a low average distance between them and hence a low mean value of R_{ij} . The problem of describing electrons “finding” the most conducting path through a sample is a percolation problem, which is illustrated in Fig. 2.5:

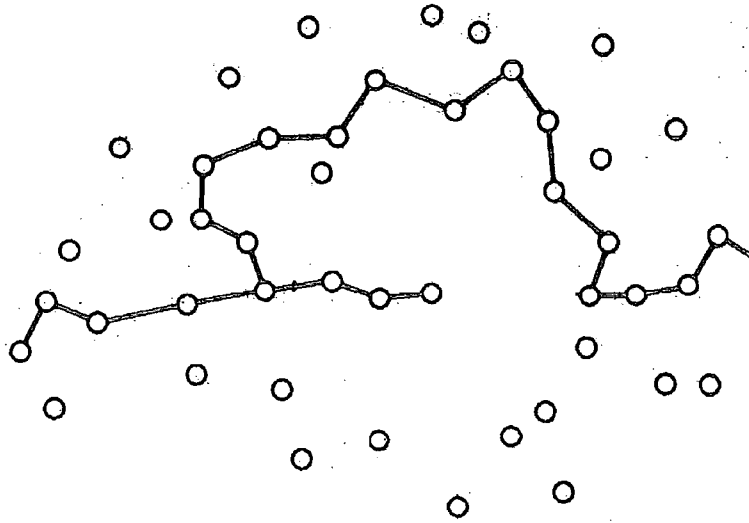


Fig. 2.5 Percolation through an array of randomly distributed electron states, [34]

From Fig. 2.5 it can be readily understood that on each of the more conducting paths there will be a certain critical radius r_C , which is the largest distance between 2 sites. Miller and Abrahams argued that any hopping conduction in a sample would be dominated by electrons propagating via several of these most conductive paths, and hopping along those paths again would be dominated by the critical radius r_C , which can be determined as an average by simulation methods dependent on the site concentration N . Instead of calculating r_C it is more convenient to introduce the dimensionless percolation constant B_C .

$$B_C = \frac{4}{3} \pi N r_C^3 ; \quad 2.10$$

Several methods have been used by different researchers to calculate B_C . The most established method is Monte Carlo simulation and there is agreement that $B_C = 2.7$ [34], [35] and therefore $r_C = (0.865) N^{-1/3}$.

However, the connectivity between sites does not only depend on their spatial distribution, but also on their separation in energy space. Therefore, strictly speaking the following percolation threshold ξ_C applies :

$$\xi_C \geq \xi_{ij} \quad \text{or} \quad \xi_C \geq \frac{2r_{ij}}{a} + \frac{\varepsilon_{ij}}{k_B T} ; \quad 2.11$$

The resistivity is dominated by hopping processes exhibiting a ξ_{ij} value close to the threshold value and for the macroscopic resistivity it follows that [34]:

$$\rho = \rho_0 \exp(\xi_C) ; \quad 2.12$$

Equation 2.12 is a fundamental expression and is the starting point of all theoretical considerations of hopping conduction. The form and temperature dependence of ρ_0 depends on γ_{ij}^0 (eq. 2.9), which in turn depends on the physical assumptions made concerning the hopping mechanism.

2.5.5. Nearest-Neighbour-Hopping (NNH)

Nearest-Neighbour-Hopping (NNH) occurs if the first term on the right hand side in eq. 2.8 is large compared to the second term. This is the case at higher temperatures, at low values of a , i.e. a small overlap of the wave functions, or at high values of r_{ij} , i.e. a low concentration of localised electron states. If the second term is significantly smaller it will contribute to the overall resistance only marginally, even for a high

energy separation between the two states ε_{ij} . Conversely, the overall resistance is reduced significantly if electrons only transfer to the nearest neighbour, resulting in a small value for r_{ij} , because generally hopping processes having a low value of ξ_{ij} are favourable. For NNH the first term in eq. 2.8 is independent of temperature, as r_{ij} is the dominating distance r_C to the nearest neighbour, and the resistivity becomes:

$$\rho = \rho_0 \exp\left(\frac{\varepsilon_3}{k_B T}\right); \quad 2.13$$

ε_3 is the average activation energy between nearest-neighbour donors and acceptors and is constant for all temperatures.

The form and possible temperature dependence of ρ_0 is again determined by physical assumptions.

2.5.6. Variable-range-hopping (VRH) with constant density of states (DOS)

Electrons may also hop to a more remote site if the separation in energy is favourable and a lower value of ξ_{ij} can be obtained than for a relevant nearest-neighbour hop. In this situation, the two terms in eq. 2.8 are competing with each other, although the percolation threshold of eq. 2.11 remains valid.

The highest spatial separation r_{\max} for a hop permitted by the threshold value ξ_C is achieved if the separation in energy tends to zero and the opposite holds for the highest energy separation ε_{\max} permitted. From eq. 2.11 it follows:

$$\varepsilon_{\max} = k_B T \xi_C; \quad \text{and} \quad r_{\max} = \frac{a \xi_C}{2}; \quad 2.14$$

Obviously, the maximum separation in energy varies with temperature, and so does r_{\max} as shown below. This conduction mechanism is referred to as variable-range hopping (VRH), because the maximum hopping distance r_{\max} between electron states participating in the hopping process is changing with temperature.

On a macroscopic scale, the resistivity is dominated by hops with high percolation values ξ_{ij} and the activation energy ε_{ij} may be replaced by ε_{\max} , and r_{ij} by r_{\max} [36], [37].

In the first instance, the DOS will be assumed to be uniform, i.e. $g(\varepsilon) = g(\varepsilon_F)$ at all energies. In Fig. 2.6 ε_{\max} is illustrated at $T = 0$ as a band of contributing localised states distributed symmetrically around the Fermi level with the temperature dependent width of $2\varepsilon_{\delta}$.

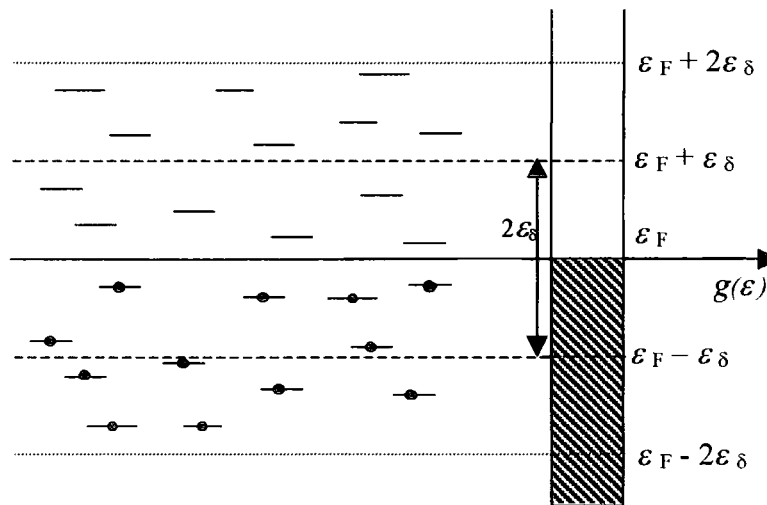


Fig. 2.6 Contributing states around the Fermi level forming a conductive band

It is clear that the position of the ε_{\max} band is variable between $\varepsilon_F + 2\varepsilon_\delta$ and $\varepsilon_F - 2\varepsilon_\delta$ as hops from Fermi level ε_F to $\varepsilon_F + 2\varepsilon_\delta$ are also possible and strictly speaking the conduction band of contributing states has the width of $4\varepsilon_\delta$ or $2\varepsilon_{\max}$ as indicated in Fig. 2.6.

By analogy with the dimensionless percolation constant in eq. 2.10, $n(\xi_C)$ can be defined as a dimensionless critical concentration of states in 4-dimensional ε - r space. $n(\xi_C)$ is determined by the DOS $g(\varepsilon_F)$ in energy and real space of the material, the width of the conduction band $2\varepsilon_{\max}$ of contributing states and the limiting distance of states r_{\max} :

$$n(\xi_C) = g(\varepsilon_F) 2\varepsilon_{\max} r_{\max}^3 ; \quad 2.15$$

From 2.14 follows :

$$n(\xi_C) = \frac{1}{4} g(\varepsilon_F) k_B T a^3 \xi_C^4 ; \quad \text{and} \quad \xi_C = \left[\frac{4n(\xi_C)}{g(\varepsilon_F) k_B T a^3} \right]^{\frac{1}{4}} ; \quad 2.16$$

Again, Monte Carlo simulation was carried out to determine $n(\xi_C)$. Skal and Shklovskii [38] found $n(\xi_C) = 5.7$, whereas Shklovskii and Efros [34] gave $n(\xi_C) = 5.3$ in a later study, and for further consideration the latter value will be taken.

Substituting ξ_C (eq. 2.16) into eq. 2.12 one arrives at the well-known equation for variable-range hopping, first introduced by Mott [4]:

$$\rho = \rho_0 \exp\left(\frac{T_0}{T}\right)^{\frac{1}{4}}; \quad \text{with} \quad T_0 = \frac{21.2}{\left[g(\varepsilon_F) k_B a^3\right]}; \quad 2.17$$

Substituting ξ_C into eq. 2.14, ε_{\max} and r_{\max} are given by

$$\varepsilon_{\max} = \frac{2.146 (k_B T)^{\frac{3}{4}}}{\left[g(\varepsilon_F) a^3\right]^{\frac{1}{4}}}; \quad 2.18$$

$$r_{\max} = 1.073 \left(\frac{a}{g(\varepsilon_F) k_B T}\right)^{\frac{1}{4}}; \quad 2.19$$

2.5.7. Variable-range hopping with a parameterised density of states

So far, the DOS $g(\varepsilon_F)$ was assumed to be constant with energy. A more general expression can be derived if the following parameterisation of $g(\varepsilon)$ is taken instead :

$$g(\varepsilon) = g' \left(\frac{|\varepsilon - \varepsilon_F|}{\varepsilon'}\right)^z; \quad 2.20$$

g' , ε' and z are scaling factors to parameterise the DOS under examination. In this formulation it is implicitly assumed that $g(\varepsilon)$ is symmetrical about ε_F .

The critical concentration $n(\xi_C)$ is then given by :

$$n(\xi_C) = r_{\max}^3 \int_{\varepsilon_F - \varepsilon_{\max}}^{\varepsilon_F + \varepsilon_{\max}} g(\varepsilon) d\varepsilon = 2r_{\max}^3 \int_{\varepsilon_F}^{\varepsilon_F + \varepsilon_{\max}} g(\varepsilon) d\varepsilon ; \quad 2.21$$

Integration is carried out from the Fermi level ε_F to $\varepsilon_F + \varepsilon_{\max}$ and assumes a symmetric distribution of the DOS around the Fermi level. Integrating and substituting for $g(\varepsilon)$ by eq. 2.20 and for ε_{\max} and r_{\max} by the expressions in eq. 2.14 leads to :

$$n(\xi_C) = \frac{a^3 g'}{4(\varepsilon')^z} \frac{1}{z+1} (k_B T)^{z+1} \xi_C^{z+4}; \quad \text{and}$$

$$\xi_C = \left[\frac{4n(\xi_C)}{a^3 g'} \frac{(\varepsilon')^z (z+1)}{(k_B T)^{z+1}} \right]^{\frac{1}{z+4}} ; \quad 2.22$$

As for eq. 2.18, the following expression for ρ can be found:

$$\rho = \rho_0 \exp\left(\frac{T_0}{T}\right)^{\frac{z+1}{z+4}} ; \quad \text{with} \quad T_0 = \frac{1}{k_B} \left(\frac{21.2}{a^3 g'} (\varepsilon')^z (z+1) \right)^{\frac{1}{z+1}} ; \quad 2.23$$

ε_{\max} and r_{\max} are given by :

$$\varepsilon_{\max} = \left[\frac{21.2}{a^3 g'} (\varepsilon')^z (z+1) (k_B T)^3 \right]^{\frac{1}{z+4}} ; \quad 2.24$$

$$r_{\max} = \frac{a}{2} \left[\frac{21.2}{a^3 g'} (\varepsilon')^z (z+1) \frac{1}{(k_B T)^{z+1}} \right]^{\frac{1}{z+4}} \quad 2.25$$

Eq. 2.24 and 2.25 are general expressions and by choosing the correct set of parameters z , g' , ε' and a , an expression describing hopping conduction in $\text{NiMn}_2\text{O}_{4+\delta}$, may be obtained. From eq. 2.23 and 2.24 it can be seen that the following relation between T_0 and ε_{\max} holds :

$$\varepsilon_{\max} = (k_B T_0)^{\frac{z+1}{z+4}} (k_B T)^{\frac{3}{z+4}} ; \quad 2.26$$

It is interesting to note that the exponents of both terms on the right hand side of eq. 2.26 are equal for $z = 2$. In this case the band width ε_{\max} may be significantly broader than $k_B T$, as T_0 is typically several orders of magnitude higher than T . In semiconductors at temperatures above 0 K, electrons occupy electron states above the Fermi level for an energy range in the order of $2k_B T$ [39]. It is believed that this is the case in $\text{NiMn}_2\text{O}_{4+\delta}$ as well and for $z = 2$, the energy range of occupied states above the Fermi level would be low compared to the full band width ε_{\max} . On the other hand, as z approaches 0, as for a uniform DOS, the T_0 dependent term in eq. 2.26 becomes much less pronounced and the energy band ε_{\max} may contain a considerable fraction of occupied states over the full range.

The pre-exponential factor ρ_0 in eq. 2.23 has to be described for the specific mechanism present in the material and may be dependent on ε_{\max} and r_{\max} , depending on the physical assumptions made. This is attempted in the next section in order to obtain a general expression for the pre-exponential factor ρ_0 .

2.5.8. Small polaron hopping

It is generally accepted that in $\text{NiMn}_2\text{O}_{4+\delta}$ a small polaron is associated with the electron hop [29]. A polaron is a lattice distortion, which occurs as a result of the reconfiguration of the electron distributions that takes place when an electron is transferred from a donor ion (e.g. Mn^{3+}) to an acceptor (e.g. Mn^{4+}). The rearrangement in the local charge distributions leads to a slight displacement of the participating ions, i.e. a local distortion of the lattice. If the orbital of the electron causing the distortion is small, then the polaron transfer is referred to as “small polaron hopping”, [40].

It is assumed that the hopping distance r_{ij} is large compared to the displacement of the donor cation and that the polaron transfer takes place via the absorption or emission of a single phonon. Multi-phonon processes are neglected according to common practice [36], [29], [37]. The resistivity is given in the usual way by :

$$\rho = \frac{1}{\sigma} = \frac{1}{ne\mu} ; \quad 2.27$$

where n is the concentration of donor electron states in real space, i.e. the charge carrier density. e is the elementary charge and μ the mobility, which is connected to the hopping rate Γ via the Einstein equation [41] :

$$\mu = \frac{eD}{k_B T} ; \quad 2.28$$

D is the diffusion constant given by

$$D = r_{ij}^2 \Gamma ; \quad 2.29$$

where Γ is the macroscopic hopping rate:

$$\Gamma = \frac{E_1^2 e^4}{36 \pi^3 \rho_v s^5 \hbar^4 \epsilon_r^2 \epsilon_0^2 a^4} \epsilon_{ij} r_{ij}^2 \exp(-\xi_C) ; \quad 2.30$$

E_1 is the deformation energy of the donor, ρ_v the density of the material, s the velocity of sound, $\epsilon_r \cdot \epsilon_0$ the permittivity of the material and \hbar the reduced Planck's constant. Corresponding to the resistivity, the macroscopic hopping rate is determined by hops exhibiting percolation values close to ξ_C , and ϵ_{ij} and r_{ij} may be regarded as the dominating separation in energy and real space, exhibiting values close to the maximum values permitted.

Eq. 2.30 is essentially in agreement with the approaches of Shklovskii and Efros and Allen and Adkins. The expressions proposed in these two studies differ by a small correction term, but following common practice in the application of small polaron theory to real systems [41], [29], [37], the correction term has been neglected.

Furthermore, it was assumed that the electron and polaron transfers are accomplished simultaneously. Strictly speaking, the hopping rate Γ has to be multiplied by the probability P , that the electron transfer follows the polaron instantly; only in the adiabatic case is P approximately 1. Arguably it is only at very low temperatures that

electron transfer might be prevented, as there would be few phonons available in the required energy state to be absorbed and enable the electron transfer.

Using the equations 2.27 –2.30 a general expression for ρ can be obtained, which is valid for all types of polaron hopping conduction.

$$\rho = \frac{36 k_B T \pi^3 \rho_V s^5 \hbar^4 \epsilon_r^2 \epsilon_0^2 a^4 \exp(\xi_C)}{e^6 n E_1^2 r_{ij}^4 \epsilon_{ij}} ; \quad 2.31$$

Eq. 2.31 contains several material specific constants, which have to be determined to describe hopping conduction quantitatively. For $\text{NiMn}_2\text{O}_{4+\delta}$ these constants are not all known, and consequently quantitative analysis of the resistivity is not possible.

2.5.9. Review of other hopping models

In order to describe experimental data for the resistance vs. temperature characteristics of $\text{NiMn}_2\text{O}_{4+\delta}$ several attempts have been made by different authors to find the appropriate expressions. Fritsch et al. [29] suggested that the resistivity can be described by small polaron hopping theory assuming NNH.

$$\rho = \frac{k_B T r_C^2}{N_{\text{Oct}} e^2 v_0} \frac{1}{NC} \exp\left(\frac{\epsilon_3}{k_B T}\right) ; \quad 2.32$$

where N_{Oct} is the concentration of octahedral sites, NC the total number of participating charge carriers, r_C the critical jump distance and v_0 the lattice

vibrational frequency. Expression 2.32 is in agreement with eq. 2.31 in respect of the temperature dependence of the exponential and the pre-exponential factor, but the constant parameters in the pre-exponential factor in eq. 2.31 differ significantly.

In earlier studies, several other empirical relations assuming NNH have been developed by fitting experimental data to arbitrary functions or by introducing empirical correction parameters :

$$\text{Becker et al. [42] : } \rho = C T^{-4.83} \exp\left(\frac{\varepsilon_3}{k_B T}\right); \varepsilon_3 = 0.178 \text{ eV}; \quad 2.33$$

$$\text{Bossom et al. [43] : } \rho = \rho_0 \exp\left(\frac{\varepsilon_3}{k_B (T + \theta)}\right); \varepsilon_3 = 0.193 \text{ eV}; \theta = 47.79 \text{ K}; \quad 2.34$$

$$\text{Feltz et al.: [44] } \rho = C \left(\frac{T_1}{T}\right)^{2.91} \exp\left[\frac{\varepsilon_3}{k_B} \left(\frac{1}{T} - \frac{1}{T_1}\right)\right]; \quad 2.35$$

T_1 is a fixed temperature dependent on the measurement

However, these empirical models are lacking fundamental theoretical justification and are not considered in this work.

Baliga and Jain [45] were the first authors who suggested that the conduction mechanism relies on variable-range hopping for all ranges of temperature. They claim that the DOS is constant and that eq. 2.17 is valid with an exponential factor of $\frac{1}{4}$. This is in contrast to the findings of Basu et al. [46], [47] who found that the DOS is parabolic in which case the exponential factor in eq. 2.23 would be $\frac{1}{2}$ with z being 2. This is discussed in more detail in chapter 6.

2.6. Doping in the system $\text{Ni}_{1-a}\text{Mn}_{2-b}\text{M}_a\text{N}_b\text{O}_4$ (M, N=In, Zn, Co, Cu, Li, Fe, Mg)

Much research has been conducted on the improvement of the temperature sensing performance of $\text{NiMn}_2\text{O}_{4+\delta}$ materials by substitution of Ni^{2+} or Mn^{3+} with various dopants. Different authors have focused on different aspects, such as improvement of the phase stability, adjustment of conductivity or minimisation of ageing effects.

Feltz and Neidnicht [48] have shown that the MgNiMnO_4 spinel is more stable and, unlike $\text{NiMn}_2\text{O}_{4+\delta}$, does not decompose between 400°C and 750°C , which enables thermistor application at these temperatures. The same effect was observed by Feltz and Seidel [49] for $\text{Zn}_b\text{NiMn}_{2-b}\text{O}_4$ compounds.

For low temperature sensing applications the low conductivity at low temperatures gives rise to problems with the feasibility of thermistor devices. This is especially the case for thin and also thick films. It has been reported by many authors [50],[51], [11], [52],[53] that doping with Cu can increase the conductivity significantly.

The replacement of both, Ni^{2+} in $\text{Ni}_{1-a}\text{Mn}_2\text{Cu}_a\text{O}_4$ and Mn^{3+} in $\text{NiMn}_{2-b}\text{Cu}_b\text{O}_4$ would increase the amount of charge carriers. In these compounds Cu is present at tetrahedral (Cu^{1+} and Cu^{2+}) and octahedral (Cu^{2+}) sites.

Alternatively, Metzmacher et al. [54] have shown that the resistance and activation energy can be increased by doping with In: $\text{NiMn}_{2-b}\text{In}_b\text{O}_4$. Carnet [55] has achieved the same effect by doping with Ti instead. An increase of resistance and particularly activation energy is advantageous if the sensitivity of the sensor is to be improved by increasing the temperature dependence of the material.

By In doping the ageing effects could be minimised as well and it is believed that In on octahedral sites can prevent or minimise the migration of Ni cations from tetrahedral to octahedral sites.

In $\text{NiMn}_2\text{O}_{4+\delta}$ this migration takes place over a comparatively long period of time accompanied by a slow change of resistance, until the resistance finally levels off after up to 500 hours [56]. This ageing behaviour could also be minimised by Co doping [57], [58], [59]. Again Ni^{2+} and Mn^{3+} replacement is possible, where Co occurs as Co^{2+} on tetrahedral and as Co^{3+} on octahedral sites. Vakiv et al. [60] suggested co-doping with Co and Cu to exploit the advantages of both dopants for NTCR thermistor applications. $\text{Cu}_{0.4}\text{Ni}_{0.4}\text{Co}_{0.4}\text{Mn}_{1.8}\text{O}_4$ and $\text{Cu}_{0.1}\text{Ni}_{0.8}\text{Co}_{0.2}\text{Mn}_{1.9}\text{O}_4$ compounds were proposed to be most favourable [61].

Doping with Fe [62] and Li [63] has been mentioned in the literature, but may be of less technological significance for NTCR thermistor applications. The “main stream” research nowadays focuses on Co and Cu doping.

2.7. Conclusions

The general properties of $\text{NiMn}_2\text{O}_{4+\delta}$ materials presented in this chapter reflect the current state of knowledge. A detailed description of the phase stability of the system was given, which is essential for the next chapter where the production process of $\text{NiMn}_2\text{O}_{4+\delta}$ powder will be described and is based on the phase diagram given in 2.3.

The importance of the cation distribution for the conduction mechanism has been noted and a general expression for a hopping resistivity was derived from basic theoretical considerations.

An explicit expression is deduced in chapter 6, where the parameterisation of the DOS $g(\varepsilon)$ is specified for different hopping models considered for describing electrical conduction in $\text{NiMn}_2\text{O}_{4+\delta}$.

Finally, it was observed that the doping of $\text{NiMn}_2\text{O}_{4+\delta}$ materials can improve the sensor performance and Co and Ni are presently the most widely used dopants.

2.8. References

1. Macklen E.D., *Thermistors*, 1979, Glasgow, Electrochemical Publications
2. Miller A., Abrahams E., *Impurity conduction at low concentrations*, Physical Review, 1960, **120**(3), p. 745
3. Ambegaokar V., Halperin B.I., Langer J.S., *Hopping conductivity in disordered systems*, Physical Review B, 1971, **4**(8), p. 2612
4. Mott N.F., *Conduction in glasses containing transition metal ions*, J. Non-Crystal.Solids, 1968, **1**, p. 1
5. Kingery W.D., Bowen H.K., Uhlmann D.R., *Introduction to ceramics*, 1960, New York, John Wiley & Sons
6. Brabers V.A.M., Terhell J.C.J.M., *Electrical conductivity and cation valencies in nickel manganite*, Physica Status Solidi (A), 1982, **69**, p. 325
7. Larson E.G., Arnott R.J., Wickham D.G., *Preparation, semiconduction and low-temperature magnetization of the system $Ni_{1-x}Mn_{2+x}O_4$* , Journal of Physics and Chemistry of Solids, 1962, **23**, p. 1771
8. Boucher B.P., Buhl R., Perrin M., *Etude cristallographique du manganite spinelle cubique $NiMn_2O_4$ par diffraction de neutron*, Acta Cryst, 1969, **B25**, p. 2326
9. Sinha A.P.B., Sanjana N.R., Biswas A.B., *On the structure of some manganites*, Acta Cryst., 1957, **10**, p. 439
10. Baltzer P.K., White J.G., *Crystallographic and Magnetic Studies of the System $(NiFe_2O_4)_{(1-x)} + (NiMn_2O_4)_x$* , J. App. Phys., 1958, **29**, p. 445
11. Bhandage G.T., Keer H.V., *A correlation of the physical properties of the $Ni_xCu_{1-x}Mn_2O_4$ system*, Journal of Physics C: Solid State Physics, 1976, **9**, p. 1325
12. Brabers V.A.M., Van Setten F.M., Knapen P.S.A., *X-ray photoelectron spectroscopy study of the cation valencies in nickel manganite*, Journal of Solid State Chemistry, 1983, **49**, p. 93
13. Hashemi T., Brinkman A.W., *X-ray photoelectron spectroscopy of nickel manganese oxide thermistors*, Journal of the Materials Research Society, 1992, **7**(5), p. 1278
14. Töpfer J., Feltz A., Gräf D., Hackl B., Raupach L., Weissbrodt P., *Cation Valencies and Distribution in the Spinels $NiMn_2O_4$ and $M_2NiMn_{(2-z)}O_4$ ($M = Li, Cu$) Studied by XPS*, Phys. Stat. Sol. A, 1992, **134**, p. 405

15. Macklen E.D., *Electrical conductivity and cation distribution in nickel manganite*, Journal of Physics and Chemistry of Solids, 1986, **47**(11), p. 1073
16. Wickham D.G., *Solid-phase equilibria in the system NiO-Mn₂O₃-O₂*, Journal of Inorganic Nuclear Chemistry, 1964, **26**, p. 1369
17. Tang X.-X., Manthiram A., Goodenough J.B., *NiMn₂O₄ revisited*, Journal of Less-Common Metals, 1989, **156**, p. 357
18. Feltz A., Töpfer J., *Bildung von Defektspinellen und Phasenbeziehungen im System Ni_xMn_{3-x}O₄*, Zeitschrift fuer anorganische und allgemeine Chemie, 1989, **576**, p. 71
19. Jung J., Töpfer J., Mürbe J., Feltz A., *Microstructure and phase development in NiMn₂O₄ spinel ceramics during isothermal sintering*, Journal of the European Ceramic Society, 1990, **6**, p. 351
20. Parlak M., Hashemi T., Hogan M.J., Brinkman A.W., *Electron beam evaporation of nickel manganite thin-film negative temperature coefficient thermistors*, Journal of Material Science Letters, 1998, **17**, p. 1995
21. Csete de Gyoergyfalva G.D.C., Nolte A.N., Reaney I.M., *Correlation between microstructure and conductance in NTC thermistors produced from oxide powders*, Journal of the European Ceramic society, 1999, **19**, p. 857
22. Drouet C., Alphonse P., Rousset A., *New spinel materials for catalytic NO-CO reaction: nonstoichiometric nickel-copper manganites*, Applied Catalysis B: Environmental, 2001, **33**, p. 35
23. Schmidt R., *Screen Printing of Coprecipitated NiMn₂O₄ for Production of NTC Thermistors*, 2001, Diploma Dissertation, Department of Material Science III, University of Erlangen-Nuremberg, Erlangen
24. Gallagher P.K., Schrey F., *Preparation and thermal analysis of mixed magnesium-manganese-iron oxalates and hydrated oxides*, Journal of The American Ceramic Society, 1964, **47**(9), p. 434
25. Torry Y., Tsuzuki H., Journal of Material Science, 1996, **31**, p. 2603
26. Kamiyama M., Nara Z., Oyo Butsuri, 1952, **21**, p. 400
27. Gorgeu A., Bull.Soc.Chim. France, 1903, **29**(3), p. 1111
28. Brabers V.A.M., *Cation migration cation valencies and the cubic - tetragonal transition in Mn_xFe_{3-x}O₄*, Journal of Physics and Chemistry of Solids, 1971, **32**, p. 2181
29. Fritsch S., Sarrias J., Brieu M., Couderc J.J., Baudour J.L., Snoeck E., Rousset A., *Correlation between the structure, the microstructure and the electrical properties of nickel manganite negative temperature coefficient (NTC) thermistors*, Solid State Ionics, 1998, **109**, p. 229

30. Zener C., *Interaction between d-Shells in the Transition Metals. II. Ferromagnetic Compounds of Manganese with Perovskite Structure*, Physical Review, 1951, **82**(3), p. 403
31. Gennes P.-G.d., *Effects of Double Exchange in Magnetic Crystals*, Physical Review, 1960, **118**(1), p. 141
32. Mott N.F., Davis E.A., *Electronic Processes in Non-crystalline Materials*, 1979, Oxford, Clarendon Press
33. Mott N.F., *Metal-insulator transitions*, 1974, London, Taylor&Francis
34. Shklovskii B.I., Efros A.L., *Electronic properties of doped semiconductors*, Solid State Sciences 45, 1984, Berlin, Springer - Verlag
35. Skal A.S., Shklovskii B.I., *Influence of impurity concentration on the hopping conduction in semiconductors*, Sov.Phys.Semicond., 1973, **7**, p. 1058
36. Allen F.R., Adkins C.J., *Electrical conduction in heavily doped Germanium*, Philosophical Magazine, 1972, **26**, p. 1027
37. Mansfield R., *Hopping conduction in III-V compounds*, in *Hopping transport in Solids*, Shklovskii B., Editor, 1991, Elsevier Science, Amsterdam, p. 349
38. Skal A.S., Shklovskii B.I., *Mott equation for low temperature edge conductivity*, Sov.Phys.Solid State, 1971, **16**, p. 1190
39. Ibach H., Lüth H., *Festkörperphysik*, p.113, 1995, Berlin, Springer Verlag
40. Mott N.F., *Conduction in Non-Crystalline Materials*, 1993, Oxford, Clarendon Press, Oxford Science Publications
41. Tuller H.L., Nowick A.S., *Small polaron electron transport in reduced CeO₂ single crystals*, Journal of Physics and Chemistry of Solids, 1977, **38**, p. 859
42. Becker J.A., Green C.B., Pearson G.L., Bell Syst. Tech. J., 1947, **26**, p. 170
43. Bossom G., Gutmann F., Simmons L.M., J. Appl. Phys., 1950, **21**, p. 1267
44. Feltz A., Töpfer J., Schirrmeister F., *Conductivity data and preparation routes for NiMn₂O₄ thermistor ceramics*, Journal of the European Ceramic Society, 1992, **9**, p. 187
45. Baliga S., Jain A.L., *Hopping conduction in sputtered Ni-Co-Mn-O spinel films*, Materials Letters, 1991, **11**(5,6,7), p. 226
46. Basu A., Brinkman A.W., Hase T.P.A., Klusek Z., Datta P.K., Pierzgalski S., *In situ study of the effect of temperature on electronic structure of Ni_xMn_{3-x}O_{4+δ} thin films using scanning tunnelling spectroscopy*, Journal of Applied Physics, 2002, **92**, p. 4123

47. Basu A., Brinkman A.W., Schmidt R., Klusek Z., Kowalczyk P., Datta P.K., *A study of electronic states of $Ni_xMn_{3-x}O_{4+\delta}$ thin films using scanning tunneling microscopy and current imaging tunneling spectroscopy*, Journal of the European Ceramic society, **in Press**
48. Feltz A., Neidnicht B., *Investigations on electronically conducting oxide systems XX. $MgNiMnO_4$ and properties of $Mg_zNiMn_{2-z}O_4$* , Journal of Alloys and Compounds, 1991, **177**, p. 149
49. Feltz A., Seidel A., *Stabile Spinelle $Zn_zNiMn_{2-z}O_4$ und Vergleich mit Spinellen $Mg_zNiMn_{2-z}O_4$* , Zeitschrift fuer anorganische und allgemeine Chemie, 1992, **608**, p. 166
50. Singh K., Pandit N.D., Mande C., *Effect of CuO as an impurity on the electrical properties of NiO- Mn_2O_3 NTC thermistor material*, Journal of Material Science Letters, 1982, **1**, p. 99
51. Baliga S., Jain A.L., *Electrical conduction and ordering in $Cu_xNi_{1-x}Mn_2O_4$ spinels*, Materials Letters, 1990, **9(5,6)**, p. 180
52. Castelan P., Ai B., Loubiere A., Rousset A., Legros R., *Ageing study of nickel-copper-manganite negative temperature coefficient thermistors by thermopower measurements*, Journal of Applied Physics, 1992, **72(10)**, p. 4705
53. Kshirsagar S.T., *Electrical and crystallographic studies of the system $Cu_xNi_{1-x}Mn_2O_4$* , Journal of the Physical Society of Japan, 1969, **27(5)**, p. 1164
54. Metzmacher C., Mikkenie R., Groen W.A., *Indium containing ceramics with negative temperature coefficient characteristics*, Journal of the European Ceramic Society, 2000, **20**, p. 997
55. Carnet R., 1986, Toulouse, PhD Thesis, University Paul Sabatier
56. Castelan P., Bui A., Loubiere A., Rousset A., Legros R., *Ageing study of NTC thermistors by thermopower measurements*, Sensors and Actuators A, 1992, **33**, p. 119
57. de Vidales J.L.M., Garcia-Chain P., Rojas R.M., Vila E., Garcia-Martinez O., *Preparation and characterization of spinel-type Mn-Ni-Co-O negative temperature coefficient ceramic thermistors*, Journal of Materials Science, 1998, **33**, p. 1491
58. Hosseini M., Yasaei B., *Effect of grain size and microstructures on resistivity of Mn-Co-Ni thermistor*, Ceramics International, 1998, **24**, p. 543
59. Meguro T., Yokoyama T., Komeya K., *Preparation of Mn-Co-Ni mono-phase spinel oxide by oxidation of rock salt-type oxide*, Journal of Materials Science, 1992, **27**, p. 5529

60. Vakiv M., Shpotyuk O., Mrooz O., Hadzaman I., *Controlled thermistor effect in the system $Cu_xNi_{1-x-y}Co_{2y}Mn_{2-y}O_4$* , Journal of the European Ceramic Society, 2001, **21**, p. 1783
61. Shpotyuk O., Vakiv M., Mrooz O., Hadzaman I., Plewa J., Uphoff H., Altenburg H., *Aging phenomena in $Cu_{0.1}Ni_{0.8}Co_{0.2}Mn_{1.9}O_4$ NTC ceramics*, Key Engineering Materials, 2002, **206-213**, p. 1317
62. Battault T., Legros R., Rousset A., *Electroceramics made of iron-nickel manganite spinels: synthesis and microstructural and electrical properties*, Journal of Materials Synthesis and Processing, 1996, **4(6)**, p. 361
63. Töpfer J., Feltz A., Dordor P., Doumerc J.P., *Thermopower analysis of substituted nickel manganite spinels*, Materials Research Bulletin, 1994, **29(3)**, p. 225

Chapter 3

Thin film production by electron-beam evaporation

3.1. Introduction	45
3.2. Electron-beam evaporation processes	46
3.2.1. Basic principle of the growth process of films	46
3.2.2. Target powder production	47
3.2.3. Substrate preparation	49
3.2.4. The E-beam evaporation system	50
3.2.5. E-beam evaporation process parameters	53
3.3. Thickness distribution of E-beam films	55
3.3.1. Evaporation theory	55
3.3.2. Film profiles	59
3.3.3. Thickness distribution of films	60
3.4. Phase purity, Ni : Mn ratio and morphology of e-beam films	62
3.4.1. XRD patterns of the target material	63
3.4.2. . XRD patterns of E-beam films	64
3.4.3. Energy Dispersive Analysis of X-rays (EDAX)	67
3.4.4. Scanning Electron Microscopy (SEM)	69
3.5. Conclusions	76
3.6. References	78

3.1. Introduction

The rapid developments that have taken place in film deposition techniques over recent decades have made possible the production of thin and thick films of NTCR $\text{NiMn}_2\text{O}_{4+\delta}$ thermistors. In principle, the problems experienced with bulk material applications can be minimised in dense polycrystalline films and several attempts have been made by different authors to produce thin films of NTCR thermistor material based on the Ni-Mn spinel system. Rf magnetron sputtering has been successfully carried out by Basu [1], Baliga [2] and Fau et al. [3]. Lindner and Feltz [4] have described film production by electrophoretic deposition.

In this chapter the novel production of thin $\text{NiMn}_2\text{O}_{4+\delta}$ films by electron-beam evaporation is presented. The experimental steps are discussed in detail, such as the production of phase pure $\text{NiMn}_2\text{O}_{4+\delta}$ powder target material, the E-beam evaporation process itself and post-deposition annealing treatments. The cleaning procedures employed for the glass and alumina substrates are described as is the careful adjustment of the parameters involved in setting up an E-beam evaporation experiment for the production of dense polycrystalline films.

The target powder and the deposited films were both examined in terms of phase purity and stoichiometry (i.e. Ni : Mn ratio), and the films were studied in terms of the morphology and the film profile. The thickness distribution of evaporated films was analysed and compared to a theoretical model, derived from evaporation theory.

3.2. Electron-beam evaporation processes

3.2.1. Basic principle of the growth process of films

In E-beam evaporation experiments an electron beam is emitted from a filament and focused on the target material by means of a high potential, heating the target sufficiently to cause sublimation.

In basic evaporation processes a small region with a high density of evaporated particles occurs directly above the target surface and diffusion processes contribute to the normal advective or molecular flow [5], [6]. Away from the target surface the beam density is much lower and the mean free path of the particles is significantly increased such that diffusion no longer occurs. The evaporation rates of the system used for this study were low ($\sim 0.8 \text{ nm sec}^{-1}$) and therefore the region of high particle density was presumed to be small and diffusion effects were neglected for theoretical considerations [7].

Accounting for molecular flow only, the number of particles dN_e which evaporate from the source surface area A_e per time dt are given by the well known Hertz-Knudsen equation [8]:

$$\frac{dN_e}{A_e dt} = (2\pi m k_B T)^{-\frac{1}{2}} (p^* - p); \quad 3.1$$

where m is the mass of the evaporated particles, p^* the vapour pressure of the target material, p the hydrostatic pressure and T the target temperature. E-beam evaporation is usually carried out in high vacuum and assuming a comparatively high vapour

pressure of the target the hydrostatic pressure p can be neglected to a good approximation [8].

Evaporated particles incident on the substrate will either be adsorbed or reflected with a certain probability, described by the sticking coefficient κ ($0 < \kappa < 1$). Nucleation takes place if adsorbed particles are forming pairs acting as nucleation centres for further incident particles. Nucleation initiates if the incident beam exceeds a critical density D_c which was given by Langmuir and Frenkel [9]:

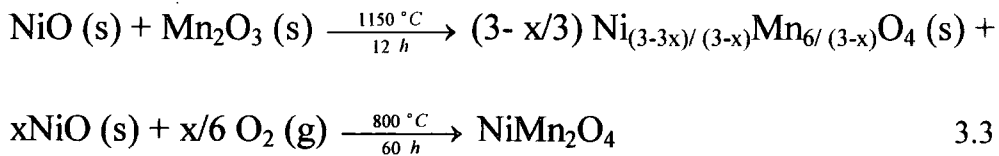
$$D_c = \frac{\nu}{4A} \exp\left(-\frac{E_{Ad}}{k_B T}\right); \quad 3.2$$

A is the cross section for capture of a particle, E_{Ad} the sum of adsorption energy of a single particle and dissociation energy of a pair, and ν is a vibrational frequency characteristic for the adsorbed particle. With all types of E-beam evaporation systems currently used, the critical beam density can be reached easily, such that continuation of the nucleation process leads to the film formation.

3.2.2. Target powder production

For the evaporation of the target material the average grain size and the grain size distribution of the target powder are believed to have no significant influence on the process. Therefore, $\text{NiMn}_2\text{O}_{4+\delta}$ target powder was synthesized by a production route based on firing pre-cursor oxides at 1150°C because of the ease of this procedure as described in chapter 2.4. The melting point of the pre-cursor oxides is 1984°C for NiO and 1585°C for Mn_2O_3 and the chemical reaction of both oxides leading to

$\text{NiMn}_2\text{O}_{4+\delta}$ can therefore be regarded as a solid state reaction. To ensure an appropriate efficiency of solid state reactions a thorough mix of the reactants is essential since inter-diffusion will be slow in solids. To achieve this, equimolar NiO and Mn_2O_3 were mixed with a pestle and mortar for up to 30 minutes. The mix was then fired for 12 hours at 1150°C in a furnace (Lenton Thermal Design) controlled by a manual temperature controller (Eurotherm). An annealing process at 800°C for 60 hours was carried out to re-incorporate released NiO into the spinel crystal. According to the phase diagram presented in chapter 2.3 the following reactions occurred:



The oxygen gain/loss parameter δ in $\text{NiMn}_2\text{O}_{4+\delta}$ has been neglected in eq. 3.3. The resulting solid $\text{NiMn}_2\text{O}_{4+\delta}$ was crushed by using a pestle and mortar and the phase purity was assessed by using X-Ray diffractometry (XRD) (Philips PW2273). With this device only small amounts of powder could be examined, as the powder had to be placed on an IPA (Iso-2-Propanol) covered glass slide enabling adhesion to the glass after the IPA had dried. The XRD patterns collected were smoothed, the α_2 intensity stripped out and the background subtracted using PowderX software [10].

3.2.3. Substrate preparation

NiMn₂O_{4+δ} films were grown on blank 1 mm thick soda-lime glass substrates of 25 x 75 mm size and heat resistive quartz glass substrates of 6 x 6 mm size and 0.5 mm thickness.

Layers were also deposited on Al₂O₃ substrates, which had been previously patterned with an inter-digitated Al electrode structure as shown in Fig. 3.1. They were supplied in sheets on which several 8 x 15 mm electrode patterns had been printed. The single patterns had been scribed, so that the sheet could be broken into individual samples.

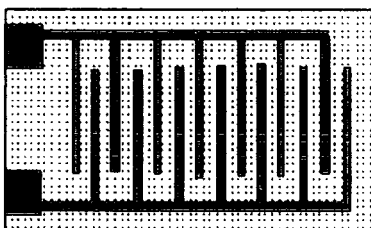


Fig. 3.1 Al₂O₃ substrate with pre-digitated Al contacts

After deposition the two square Al contact pads were used to connect the sample to two copper wires with solder using a solder iron. For the E-beam film deposition the Al₂O₃ substrates were placed on a purpose-built mask to prevent coverage of the two contact pads by the film. Contact deposition for all types of NiMn₂O_{4+δ} materials is described in more detail in chapter 5.3.1.

Before film deposition, all types of substrates were cleaned thoroughly in a multi-step procedure to remove all types of impurities. First, manual cleaning with a common detergent and scrub in hot water was carried out, followed by an ultrasonic

water bath with the substrates placed in a solution containing decontamination agent (Decon 90). Finally a refluxing procedure in hot IPA (Iso-2-Propanol) for up to 4 hours was applied. IPA contained in a glass flask was boiled and the vapour allowed to rise by-passing the substrates through a vapour collector pipe. The IPA vapour was then condensed and allowed to drop in order to rinse the substrates in the main refluxing chamber, ideally removing any organic or inorganic impurities. Once the IPA level had reached a siphon level, all IPA was siphoned out and returned to the bottom flask in order for the cycle to be repeated. For refluxing, the substrates were loaded in a PTFE purpose-built sample holder, which had been cleaned manually with hot water and detergent beforehand.

3.2.4. The E-beam evaporation system

The E-beam evaporation system used for film depositions is shown in the schematic diagram in Fig. 3.2. Electrons emitted from a tungsten filament were accelerated through a variable high potential (high voltage) and focussed onto the source, in this case $\text{NiMn}_2\text{O}_{4+\delta}$ powder contained in a graphite crucible. The rising $\text{NiMn}_2\text{O}_{4+\delta}$ vapour condensed on the substrate forming an even and dense film as described in section 3.2.1.

The high voltage and the beam current had to be adjusted carefully to allow sufficient heating of the target, but to avoid spontaneous discharge, which short-circuited the system. Unfortunately, this tended to occur regularly every few minutes and the target heating process then had to be re-started. It is believed that the target temperature varied significantly during the course of one full deposition process depending on the number and frequency of interruptions.

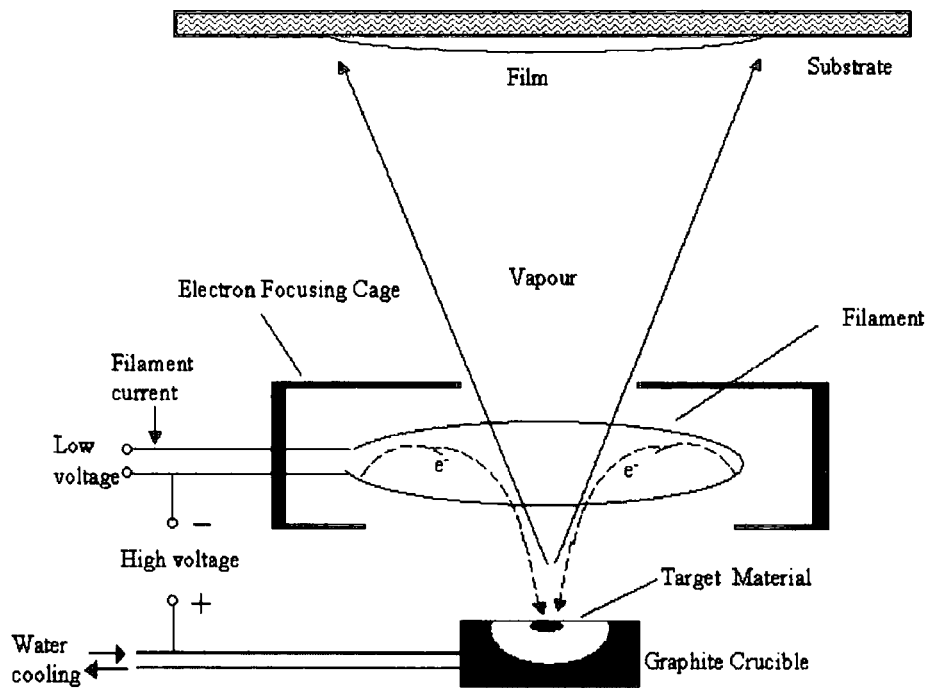


Fig. 3.2 Basic principle of E-beam evaporation

Furthermore, the beam current and the electron beam focus (spot size s) varied significantly with the shape and size of the filament and the reproducibility of the target temperature might well have been affected again, as the filament had to be changed regularly every few evaporation processes.

The full evaporation process was carried out in an evacuated chamber under a glass dome (10^{-2} Pa – 10^{-3} Pa) using a combined rotary and oil diffusion pump system (Fig. 3.3). The substrates could be heated with a quartz-halogen lamp controlled by a chromel-alumel thermocouple linked with a temperature controller (Eurotherm Cal 9900). The electron beam source assembly is shown in Fig. 3.4. Three crucibles could be fixed on a moveable water cooled pedestal, enabling the deposition of 3 crucible loads within one experiment.

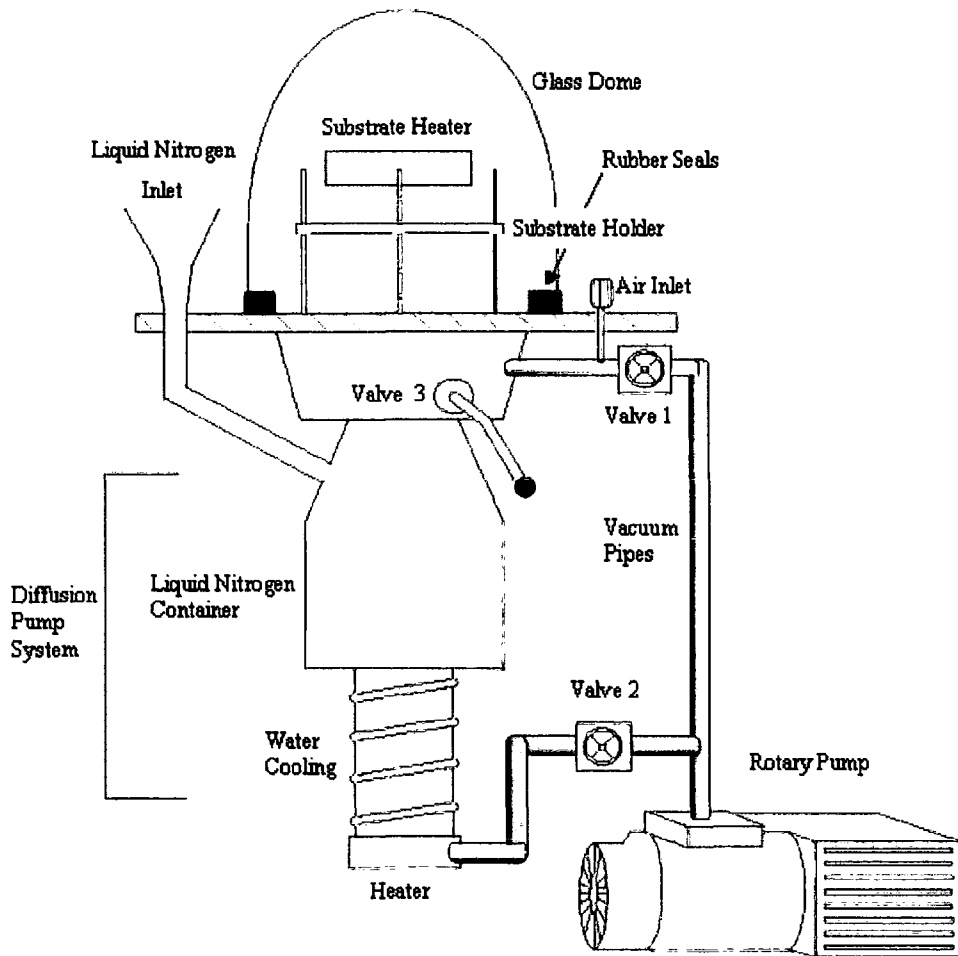


Fig. 3.3 Schematic diagram of the E-beam evaporation system

The clean substrates were placed on the metal substrate holder above this arrangement (see Fig. 3.3) and it was ensured that the substrates were insulated. The substrate holder was earth-grounded and it was found that unless steps were taken to prevent it, once the substrate was fully covered with hot conducting $\text{NiMn}_2\text{O}_{4+\delta}$, the beam would be diverted away from the source onto the film and discharge over the substrate holder. This resulted in excessive heating of the substrate, shattering it in the case of glass slides and the efficiency of the target heating would be reduced as well.



Fig. 3.4 Electron-beam source assembly

3.2.5. E-beam evaporation process parameters

For the electron-beam evaporation procedure the following process parameters proved to be appropriate:

Substrate temperature :	100°C
Distance source-substrate (h) :	85 mm
Distance source-filament:	25 mm
Filament diameter :	~ 15 mm
Deposition time :	20 – 90 minutes
Beam current :	~ 20 mA
High voltage :	~ 5 kV
Deposition rate :	~ 0.8 nm sec ⁻¹
Target (crucible) diameter :	11 mm

Radius of the electron spot

on the target surface (s) : $1.5 \text{ mm} \pm 0.3 \text{ mm}$

The parameter s describes the radius of the E-beam spot on the target surface, which determines the active region releasing the vapour.

Films were grown on the pre-printed Al_2O_3 substrate units containing 4 electrode patterns, which were subsequently broken into individual samples and annealed at different temperatures. Annealing was carried out in an air tube furnace (Lenton Thermal Design) in order to improve crystallinity and microstructure. The complicated phase diagram for $\text{NiMn}_2\text{O}_{4+\delta}$ would suggest that ideally annealing should be carried out at a temperature of 800°C . However, for Al_2O_3 substrates annealing had to be restricted to temperatures below 500°C to avoid oxidation of the pre-printed Al contacts, with the annealing time shortened to 30 minutes in order to minimise possible segregation of additional phases (see phase diagram in chapter 2.3.).

Two samples were produced on Al_2O_3 substrates, sample 1 was annealed at 200°C , 300°C and 500°C and one section kept in the as-deposited state, sample 2 was annealed at 300°C and 400°C and again one as-deposited section kept. Films deposited on soda-lime glass slides were cut into smaller pieces and annealed at temperatures up to 300°C as the slides tended to melt at higher temperatures. As a consequence, films were also deposited on temperature resistive quartz glass, but the films tended to re-evaporate during annealing at 800°C for 30 minutes.

Sample 3 was grown on soda-lime glass, one section was annealed at 300°C and one kept as-deposited. During optimisation of the E-beam evaporation procedure samples 4 – 7 were grown on soda-lime glass without post-deposition annealing.

3.3. Thickness distribution of E-beam films

3.3.1. Evaporation theory

On deposited films, the spatial distribution $g(\varphi)$ of evaporated particles for deposition rates lower than 5 nm sec^{-1} is described by the classical cosine law of emission [11].

$$g(\varphi) = \frac{1}{\pi} \cos(\varphi) ; \quad 3.4$$

where φ is the evaporation angle (Fig. 3.5). Following the approach described by Maissel and Glang [8], the mass sublimation rate Γ per unit evaporating area A_e can be written by using eq. 3.1 as:

$$\Gamma = m \frac{dN_e}{A_e dt} = \left(\frac{m}{2\pi k_B T} \right)^{\frac{1}{2}} p^* ; \quad 3.5$$

and after time t the total amount of evaporated material M_e is

$$M_e = \int_t \int_{A_e} \Gamma dA_e dt ; \quad 3.6$$

Based on the cosine law of emission (eq. 3.4), the mass evaporated from a point source dA_e into the elemental solid angle $d\omega$ is given by

$$dM_e(\varphi) = M_e \cos \varphi \frac{d\omega}{\pi} ; \quad 3.7$$

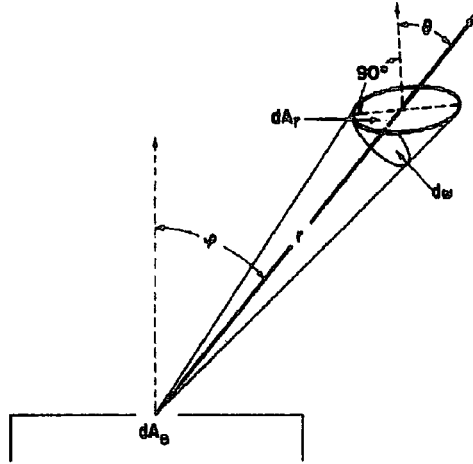


Fig. 3.5 Elemental solid angle $d\omega$, evaporating area dA_e and substrate area dA_r , [8]

For a substrate element dA_r as shown in Fig. 3.5 the deposited mass is

$$dM_r(\varphi, \theta) = \frac{\kappa M_e}{\pi r^2} \cos \varphi \cos \theta dA_r ; \quad 3.8$$

using $dA_r = r^2 d\omega / \cos \theta$, and κ is the sticking coefficient ($\kappa < 1$) The film thickness in dA_r is

$$d = \frac{1}{\rho_v} \frac{dM_r}{dA_r} ; \quad 3.9$$

where ρ_v is the density of the material. For a substrate parallel to the source it is clear that $\theta = \varphi$ ($\cos \theta = \cos \varphi = h/r$ (Fig. 3.6)) and one obtains from eq. 3.8 and 3.9:

$$d = \frac{1}{\rho_v} \frac{\kappa M_e h^2}{\pi r^4} ; \quad 3.10$$

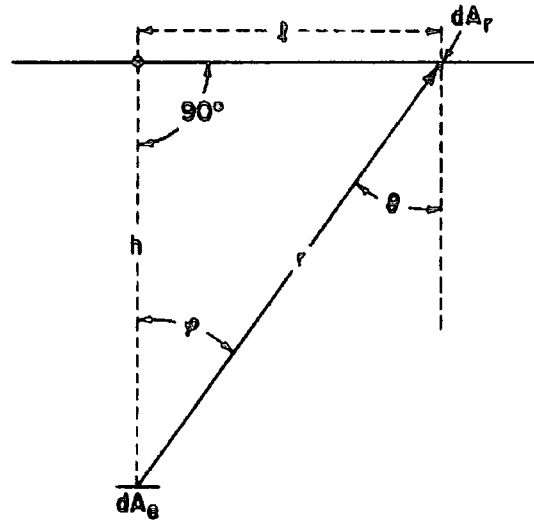


Fig. 3.6 Relations between θ , φ , l , h and r for parallel source and substrate, [8]

Substituting eq. 3.6 into 3.10 leads to:

$$d = \iint_{A_e} \frac{\kappa h^2}{\rho_V \pi r^4} \Gamma dA_e dt ; \quad 3.11$$

Eq. 3.11 strictly applies to a point source, so for disc sources of radius s it is necessary to integrate over the source area:

$$d = \iiint_{t \ s \ \alpha} \frac{s \Gamma d\alpha}{\rho_V \pi} \frac{\kappa h^2}{r^4} ds dt ; \quad 3.12$$

where the source area is $dA_e = s d\alpha ds$ (Fig. 3.7).

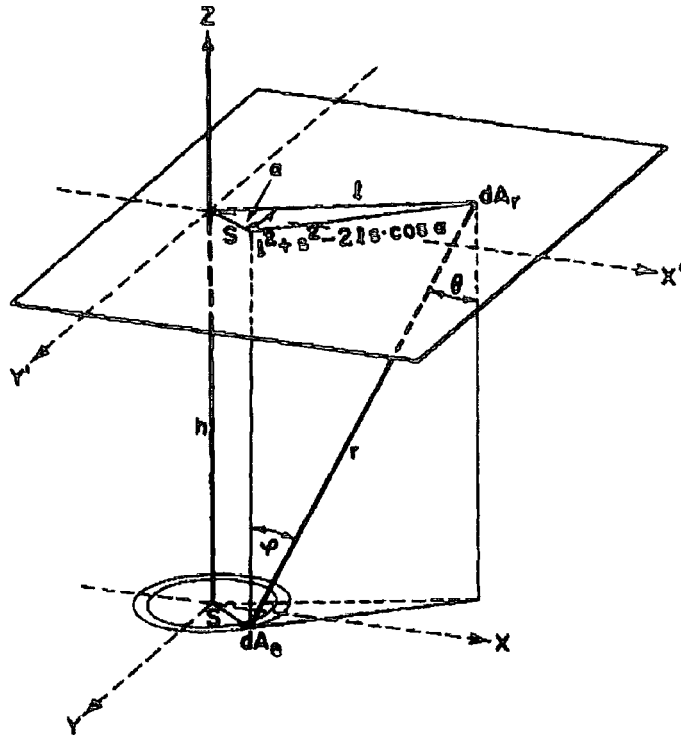


Fig. 3.7 Geometry of a circular disc source, [8]

Integration over $d\alpha$ and ds may be carried out by using the relation

$r^2 = h^2 + l^2 + s^2 - 2ls \cos \alpha$, to give :

$$d = \frac{\kappa M_e}{2\pi \rho_v s^2} \left(1 - \frac{1}{\sqrt{1 + \frac{4h^2 s^2}{(h^2 - s^2 + l^2)^2}}} \right); \quad 3.13$$

Eq. 3.13 describes the film thickness d dependent upon the distance l of the film element to the source- substrate axis, the total mass of the evaporated material M_e and the density of the films ρ_v .

3.3.2. Film profiles

The film profiles for all types of E-beam evaporated films were examined using alpha-step stylus profileometry (Tencor Systems Alphastep 200). A line was scratched through an appropriate part of the film using a razor blade and a scan over the resulting substrate-film step gave the film thickness.

In order to compare eq. 3.13 to the thickness distribution of grown films, a regular array of holes was marked into a film in the as-deposited state grown on 3 soda-lime glass slides revealing the substrate as depicted in Fig. 3.8.

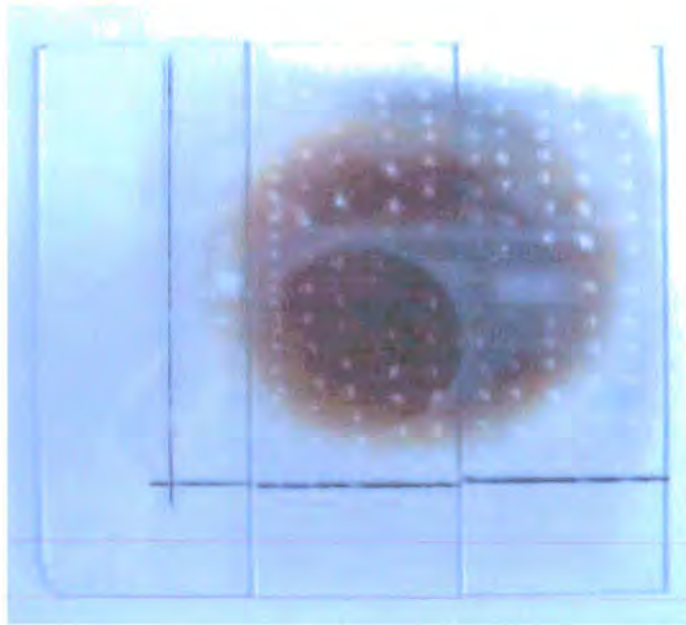


Fig. 3.8 E-beam evaporated film on glass slides with arrays of holes

The film thickness at each of the holes was measured with the Alphastep profileometer.

Examination of eq. 3.13 indicates that the film thickness is critically dependent on the beam spot radius s and should be determined as precisely as possible in order to

minimise uncertainty in the predicted distribution. As mentioned above the uncertainty in s is about $\pm 20\%$, which is rather high leading to high inaccuracy in determining the thickness distribution.

3.3.3. Thickness distribution of films

The profile of the E-beam evaporated film shown in Fig. 3.8 was obtained by plotting the film thickness at each hole scratched in the sample versus the position on the film (X/Y Data).

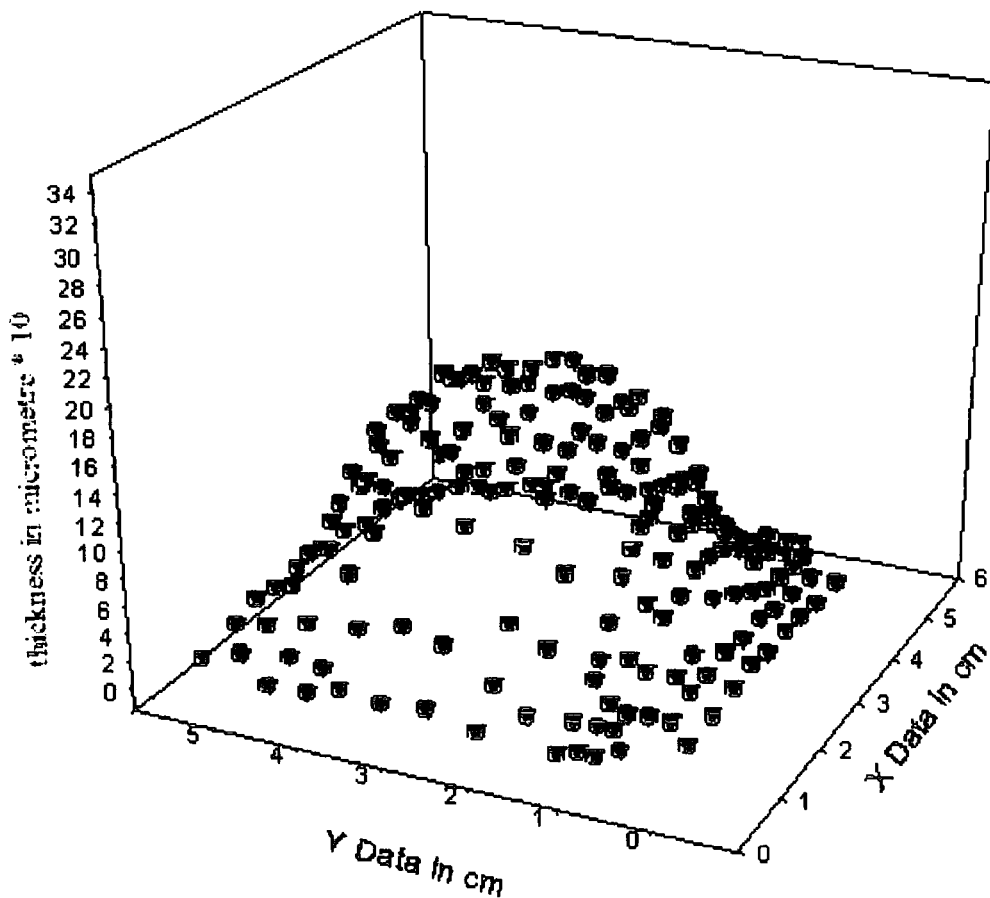


Fig. 3.9 Film profile of E-beam evaporated film

From the thickness distribution in Fig. 3.9 a cross section through the middle of the film was taken and plotted in Fig. 3.10 together with a theoretical curve calculated from eq. 3.13. For clarity the theoretical curve has been shifted towards higher values.

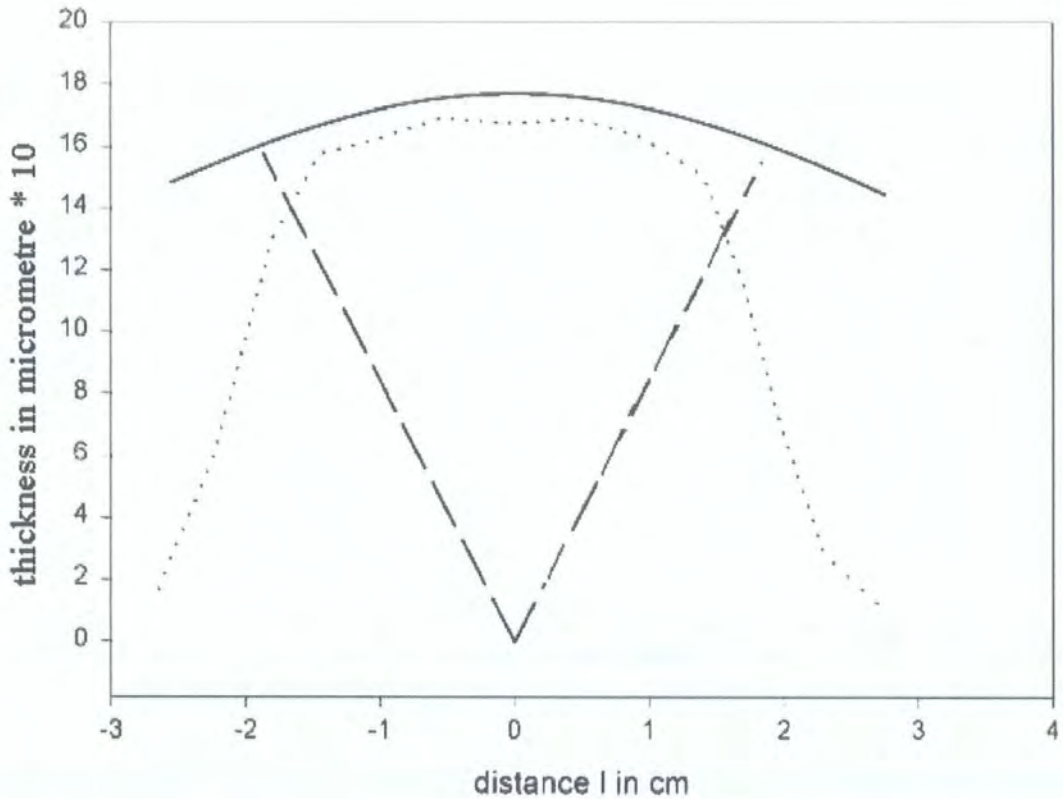


Fig. 3.10 Film profile, _____ theoretical curve, experimental distribution, --- target – filament – substrate trajectories

The theoretical and experimental curves may be aligned by assuming that a sticking coefficient κ of $80 \pm 1.5\%$ occurred, which is a reasonable value for an E-beam evaporation process.

The total evaporated mass M_e was measured from the weight loss of the target to be 0.24 ± 0.01 g and the density ρ_v of the films was taken to be $5.25 \text{ g}\cdot\text{cm}^{-3}$, calculated

from the unit cell. For thin evaporated films it is reasonable to assume that the film density is very close to the theoretical value especially as there were no pores or other irregularities observable in the films (see next section).

From Fig. 3.10 it can be seen that at the film periphery the thickness drops dramatically. This is due to the shadowing effect of the focussing cage as demonstrated by the target - filament - substrate trajectories in Fig. 3.2 and in Fig. 3.10. The opening angle of the trajectories was determined by the aperture in the focusing cage, which was 12 mm in diameter.

3.4. Phase purity, Ni : Mn ratio and morphology of E-beam films

The phase purity and orientation of the various layers was assessed by XRD (Philips PW2273). The data obtained was smoothed, the α_2 intensity stripped out and the background subtracted using PowderX software [10] as was done for the source material.

The morphology of the films and the residues of the evaporation process left in the crucibles were examined by SEM (Scanning Electron Microscopy) using either a Cambridge Instruments S600, or a Jeol JSMIC848.

The Ni : Mn ratio in the source powder and films was assessed using EDAX (Energy Dispersive Analysis of X-rays), Link Systems Analytical AN1000, which was linked with the SEM systems. The relative concentrations of Ni and Mn were determined taking into account ZAF correction terms. For the manganese $K\alpha_1$ line the Z, A and F correction terms were 1.016, 1.005 and 0.912 respectively leading to a total correction parameter of 0.9310. For the nickel $K\alpha_1$ line 0.982 (Z), 1.037 (A) and 1.000 (F) gave a total correction of 1.0184.

3.4.1. XRD patterns of the target material

The X-ray diffraction patterns for the source powders obtained from the precursor oxide route are shown in Fig. 3.11, indicating the phase purity of the powder when annealed at 800°C for 60 hours. The scan for the non-annealed powder shows the expected NiO impurities. All peaks apparent could be assigned to $\text{NiMn}_2\text{O}_{4+\delta}$ reference peaks obtained from a data base (JCPDS [12] no. 71-852) or NiO impurities (JCPDS no. 44-1159).

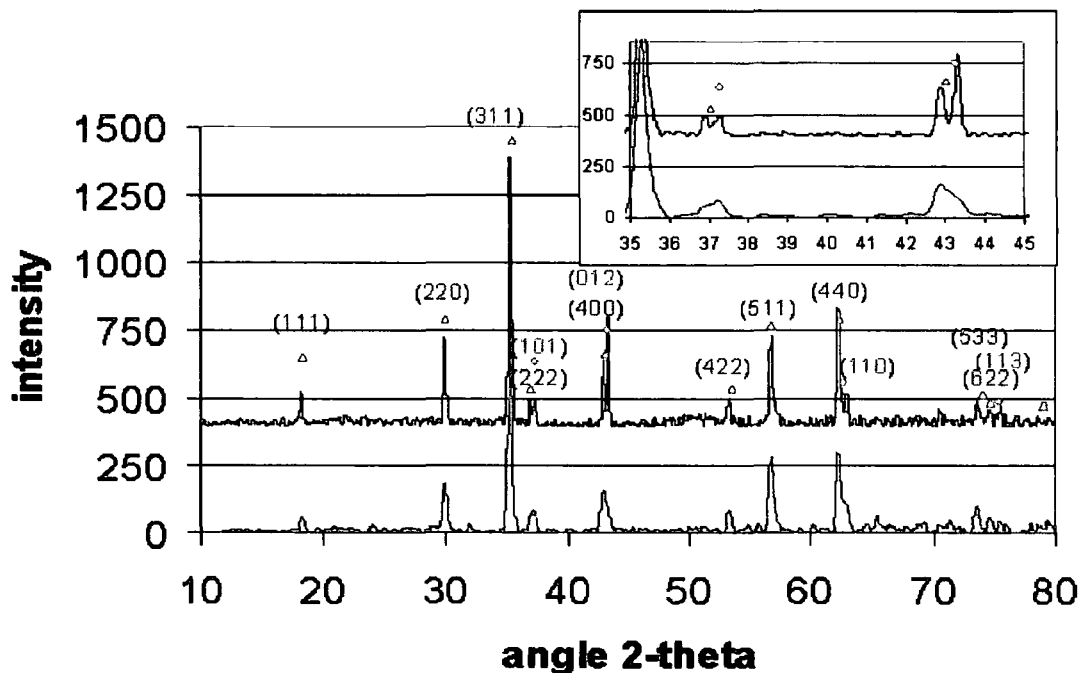


Fig. 3.11 X-ray diffraction pattern of $\text{NiMn}_2\text{O}_{4+\delta}$ powder fired at 1150°C for 12 h and annealed at 800°C for 60 hours

The resolution of NiO and $\text{NiMn}_2\text{O}_{4+\delta}$ peaks is difficult as they occur at similar angles. Two critical $\text{NiMn}_2\text{O}_{4+\delta}$ peaks are shown in detail in the inset of Fig. 3.11 and could be resolved as double-peaks for the non-annealed powder indicating the occurrence of NiO impurities. The scan for the annealed powder may exhibit hints of

NiO at the shoulders of the peaks at 43° and 62.3° towards higher angles, but this trend is not clear and the concentration of NiO impurities, if present at all, would be well below the resolution threshold of 5% wt. The reference spectra for all compounds containing Ni, Mn and O are given in Appendix B.

3.4.2. XRD patterns of E-beam films

In Fig. 3.12 the XRD scans of the thin film sample 1 are shown, E-beam evaporated on Al_2O_3 substrate sections, which were annealed at different temperatures after deposition. The phase pure XRD pattern from Fig. 3.11 is shown as a reference.

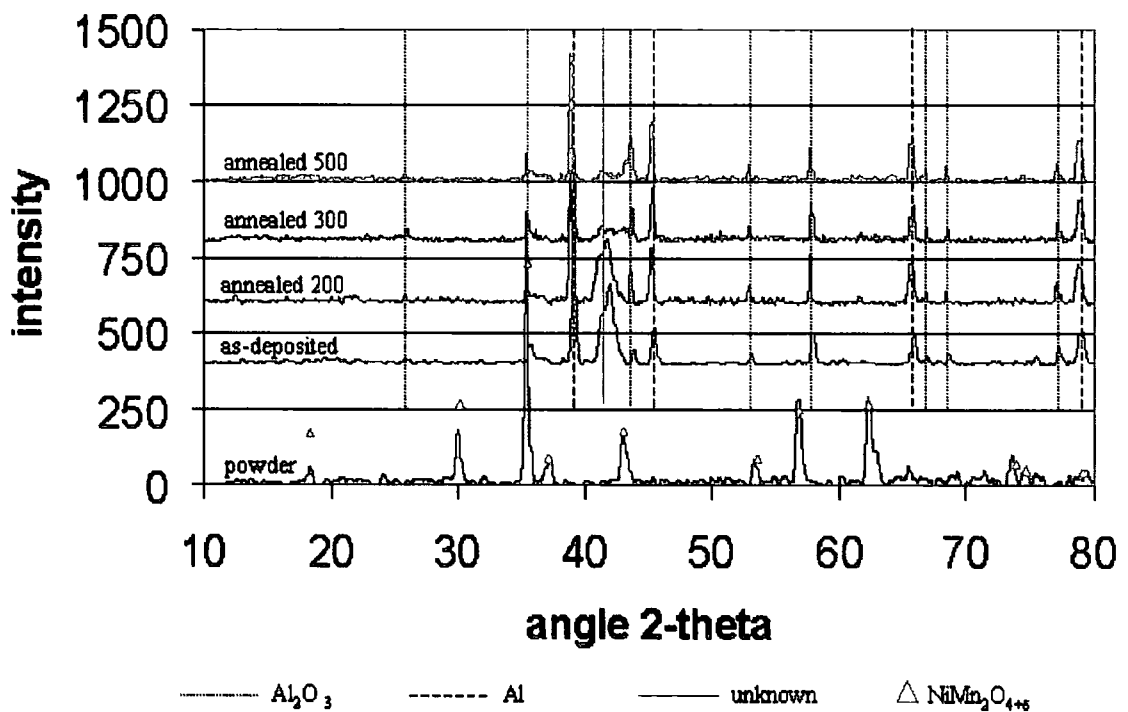


Fig. 3.12 XRD pattern of E-beam film sample 1, grown on Al_2O_3 substrate, annealed at different temperatures

It can be seen that the XRD-patterns of the films changed significantly compared to the target material. The pre-digitated Al contacts and the Al₂O₃ substrates showed XRD patterns in agreement with reference spectra obtained from the JCPDS data base (Al₂O₃ no. 46-1212 / Al no. 4-787), which allowed an unambiguous identification. The films showed only one clear broad peak at ~ 41.8° , but the main NiMn₂O_{4+δ} line at 35.5° could be overlaid by one from Al₂O₃ at 35.2°. However, the peak at ~ 41.8° is not associated with any compound which could be present in the films, such as MnO (JCPDS no. 7-230), Mn₂O₃ (24-508), MnO₂ (30-820), Mn₃O₄ (24-734), NiMnO₃ (48-1330), Ni₆MnO₈ (42-479), NiO (44-1159) and NiMn₂O_{4+δ}. According to the JCPDS data base several peaks with lower intensities for some of these compounds can be found near 41.8° , but their intensities are all lower than 35% of the main peak which makes it very unlikely that one of these occurred. With higher annealing temperatures the 41.8° peak in the spectra gets weaker while the crystallinity of the film improves significantly as will be shown later. Therefore, it is suggested that an amorphous-like phase existed with unknown composition and no references available.

Fig. 3.13 shows the XRD traces from 5 non-annealed films of different thickness, deposited onto soda-lime glass slides. Variations in the XRD-patterns of films with different thickness can be seen, but no clear trend is apparent. It may therefore be concluded that the differences displayed in the spectra may not be related to film thickness, but arise from other origins, such as fluctuations in the target temperature during evaporation. In section 3.2.4. it was mentioned that temperature variations were very likely to occur.

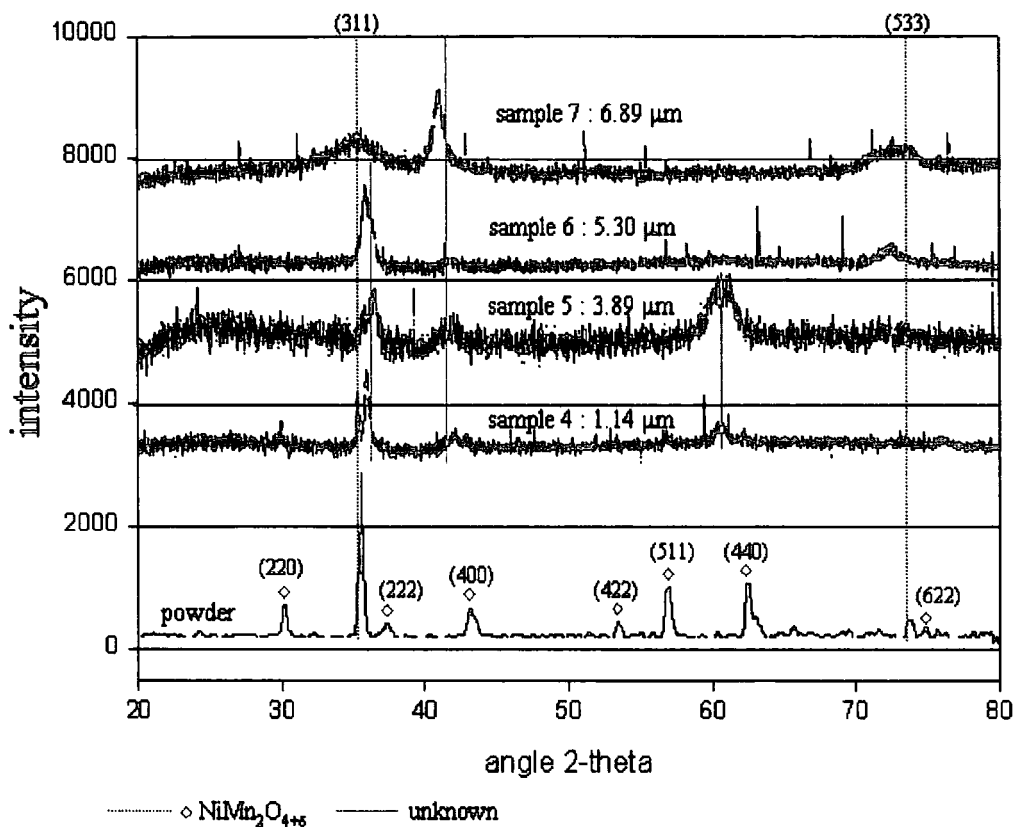


Fig. 3.13 X-ray diffraction patterns for thin film samples 4 - 7,
non-annealed on soda lime glass

Samples 4 and 7 seem to exhibit the main $\text{NiMn}_2\text{O}_{4+\delta}$ peak at 35.5° , but all spectra in Fig. 3.13 show unassigned peaks as well, one corresponding to the 41.8° peak previously mentioned and additionally at $\sim 36.0^\circ$ and $\sim 61.0^\circ$.

It is suggested that different types of amorphous-like phases may possibly occur dependent on the deposition procedure, i.e. the target temperature. The degree of disorder in the amorphous-like phases might vary and a short range ordering of unknown type might be responsible for the unassigned peaks.

The presence of an amorphous-like phase raises the question about the cation distribution, if no typical spinel crystal structure is present and the effect on the electron transport between localised electron states. It may well be possible that the

valencies of Mn cations may be different in amorphous-like $\text{NiMn}_2\text{O}_{4+\delta}$ and the type of hopping transport may vary compared to (poly-) crystalline materials.

In general it may be concluded that the composition of E-beam evaporated films in form of an amorphous phase varied significantly in a rather unpredictable way, which prevented the establishment of a reproducible production process of thin $\text{NiMn}_2\text{O}_{4+\delta}$ films for the use in temperature sensing applications.

Annealing at higher temperatures of 800°C could possibly lead to a crystalline $\text{NiMn}_2\text{O}_{4+\delta}$ phase, but the Al contacts on the Al_2O_3 would evaporate and soda-lime glass substrates would melt. Therefore, films were grown on heat resistive quartz glass and annealing at 800°C was attempted, but most of the deposited material evaporated during annealing and the residues were too small for XRD analysis.

3.4.3. Energy Dispersive Analysis of X-rays (EDAX)

The target material, the deposited films and the residues of the evaporation process were examined by EDAX and the ratio of Ni : Mn determined for the target and films. Table 3.1 shows the percentage of Ni and Mn detected for a representative experiment, together with the ideal value in $\text{NiMn}_2\text{O}_{4+\delta}$.

Table 3.1 Ni and Mn concentrations of the powder and deposited films

	Ni % wt.	Mn % wt.	Ni% at.	Mn% at.	Ni : Mn at.
powder	34.5	65.5	33.1	66.9	1 : 2.03
films	44.6	55.4	43.0	57.0	1 : 1.33
$\text{NiMn}_2\text{O}_{4+\delta}$	34.8	65.2	33.3	66.7.0	1 : 2

From table 3.1 it is evident that the E-beam evaporated films were Ni-rich as is also evident from the representative EDAX scans shown in Fig. 3.14 and 3.15, where the ratios of Ni to Mn peaks for the target and film were clearly different.

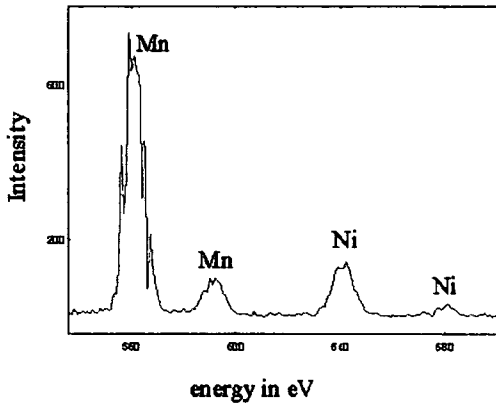
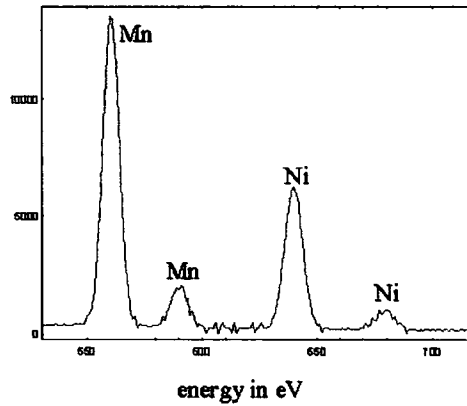
Fig. 3.14 EDAX for $\text{NiMn}_2\text{O}_{4+\delta}$ powder

Fig. 3.15 EDAX for E-beam film

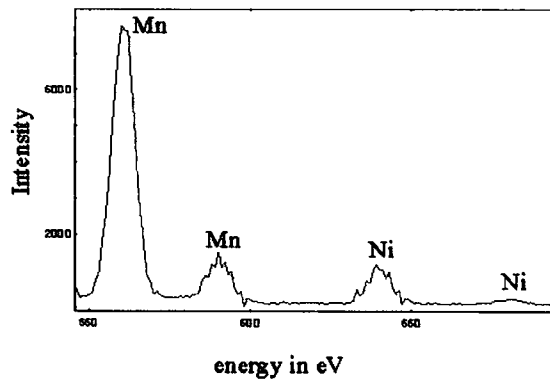


Fig. 3.16 EDAX scan for evaporation residues

An EDAX scan for the residues of the evaporation process is shown in Fig. 3.16, which seemed to be Mn rich compared to the target, but quantitative analysis was not carried out.

Interpretation of these results is difficult as the evaporation process of $\text{NiMn}_2\text{O}_{4+\delta}$ powder is not known. $\text{NiMn}_2\text{O}_{4+\delta}$ may well dissociate during sublimation and Ni and

Mn atoms or oxides may form the vapour and could recombine on the substrate in an unknown way. In steady state, quasi thermal equilibrium may become established in the heated part of the source, in which case it is possible that the constituent elements of dissociated $\text{NiMn}_2\text{O}_{4+\delta}$ will tend to establish their respective equilibrium partial pressures. This in turn would result in preferential evaporation and may explain why the films were Ni- rich and the source residues Mn- rich.

It is interesting to note that the sublimation temperature for pure elements is higher for Ni than for Mn [13], and it might be concluded that Ni and Mn oxides had been formed and evaporated. Unfortunately, the evaporation residues extracted did not provide enough material to allow XRD analysis.

All the films investigated were found to be Ni rich, but quantitative values for the Ni : Mn ratios varied from sample to sample, probably reflecting differences in the deposition conditions.

Generally, the problems faced with retaining or controlling the composition of E-beam evaporated films were found to be severe and a production process leading to a reproducible film composition could not be established.

3.4.4. Scanning Electron Microscopy (SEM)

SEM (S600 Cambridge Instruments) examinations were carried out for sample 1, grown on Al_2O_3 substrate sections, which had been annealed at different temperatures. Figs. 3.17 – 3.21 show the morphology of the films.

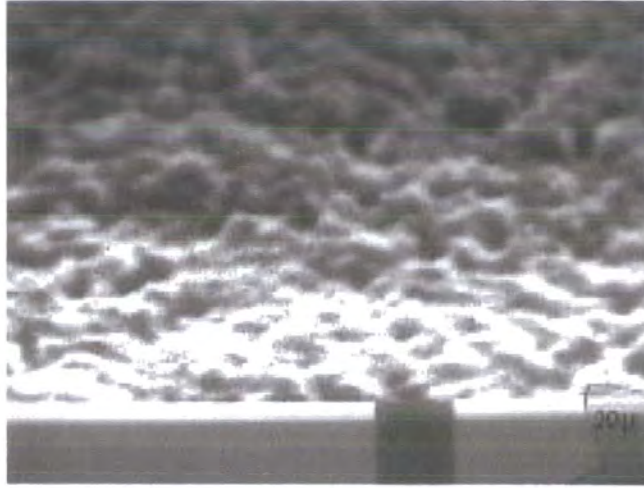


Fig. 3.17 E-beam evaporated film on Al₂O₃, as-deposited

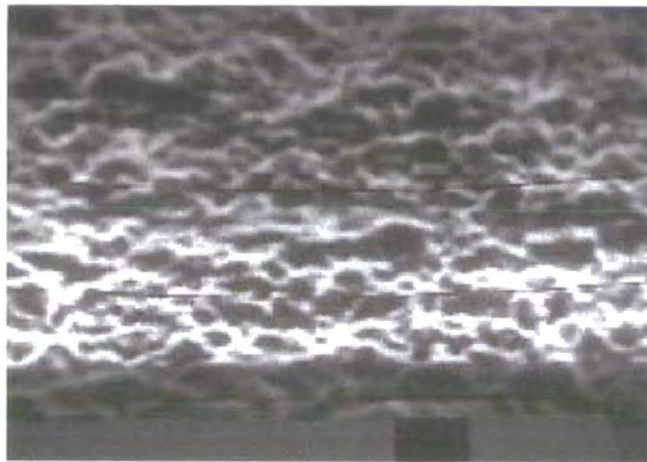


Fig. 3.18 E-beam evaporated film on Al₂O₃, annealed at 200°C

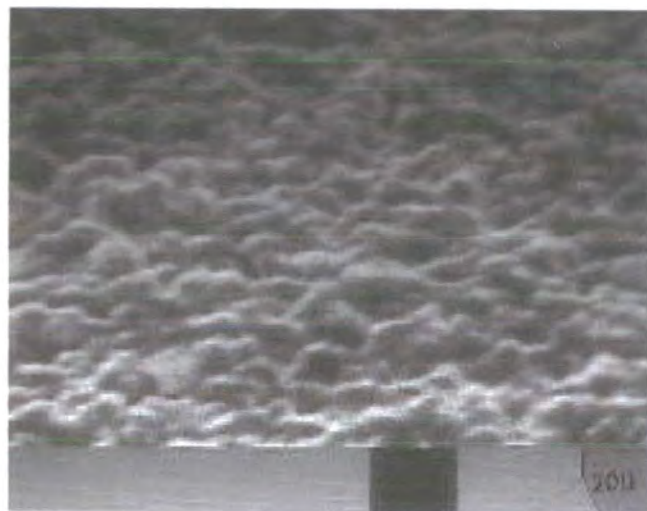


Fig. 3.19 E-beam evaporated film on Al₂O₃, annealed at 300°C

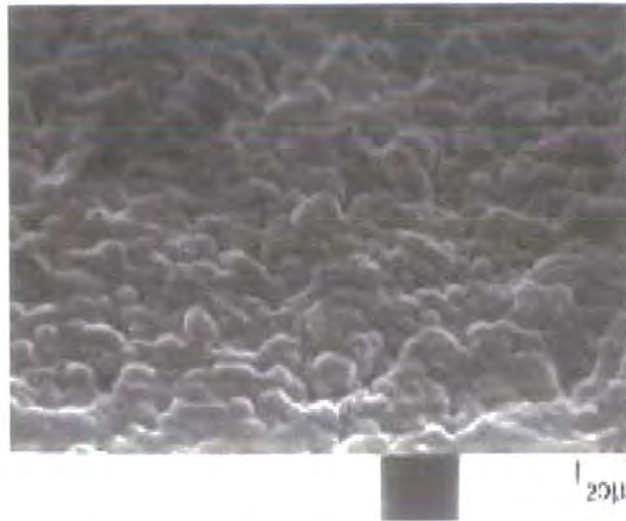


Fig. 3.20 E-beam evaporated film on Al₂O₃, annealed at 400°C



Fig. 3.21 E-beam evaporated film on Al₂O₃, annealed at 500°C

The black square at the bottom line of each image corresponds to 20 μm and the annealing time was 30 minutes at each temperature.

The films in Fig. 3.17 and 3.18 seem to exhibit no pronounced grain structure, although the resolution is quite poor. Image resolution in Figs. 3.19 - 21 is better and indicates the formation of a more distinct grain structure in films annealed at temperatures above 300°C. At 500°C the grains are more strongly differentiated, but

the surface roughness had increased. This might be due to increased phase separation, which may well occur at intermediate temperatures $T \geq 400^\circ\text{C}$ according to the phase diagram described in chapter 2.3.

The Jeol JSMIC848 SEM system was used to examine thin films grown on heat resistive quartz glass. Confirming the trend from the previous SEM images, Figs. 3.22 and 3.23 show that the film crystallinity improved significantly if post-deposition annealing was carried out at 800°C . Fig. 3.22 seems to confirm the presence of an amorphous-like phase, as previously suggested, whereas the film annealed at 800°C showed clear crystallographic grains.

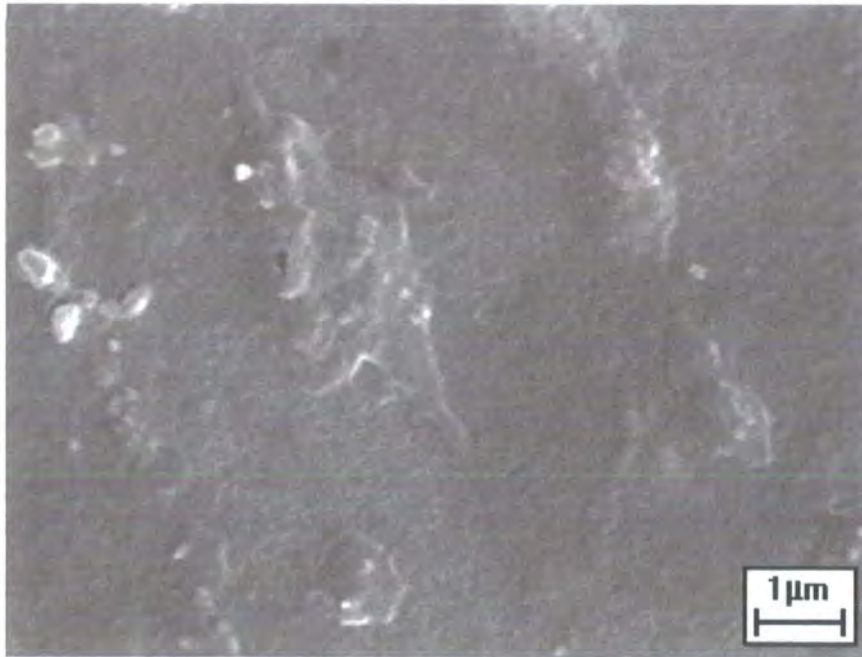


Fig. 3.22 E-beam evaporated film on quartz glass, as-deposited

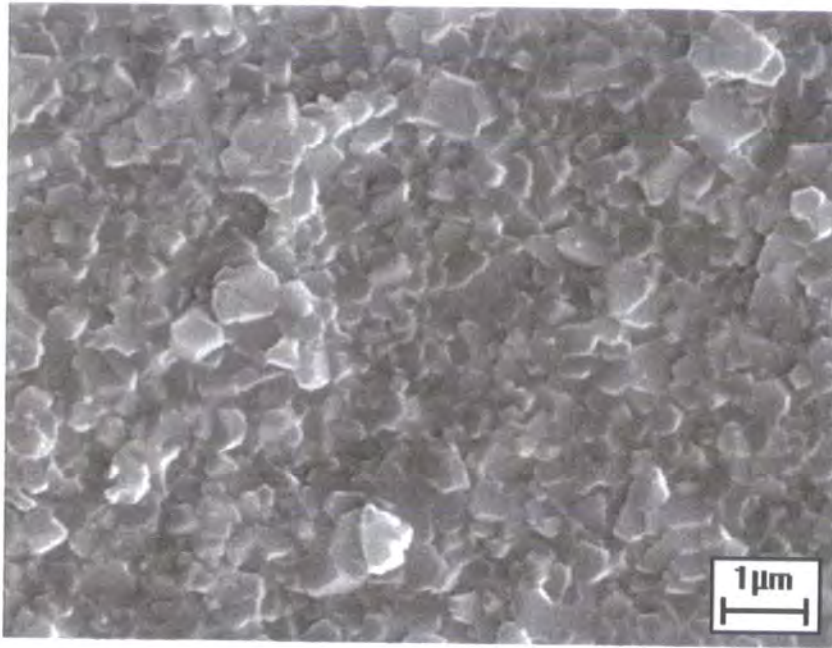


Fig. 3.23 E-beam evaporated film on quartz glass, annealed at 800°C

An SEM image of source residues left in the crucibles is shown in Fig. 3.24 and it can be seen clearly that two different phases were present.

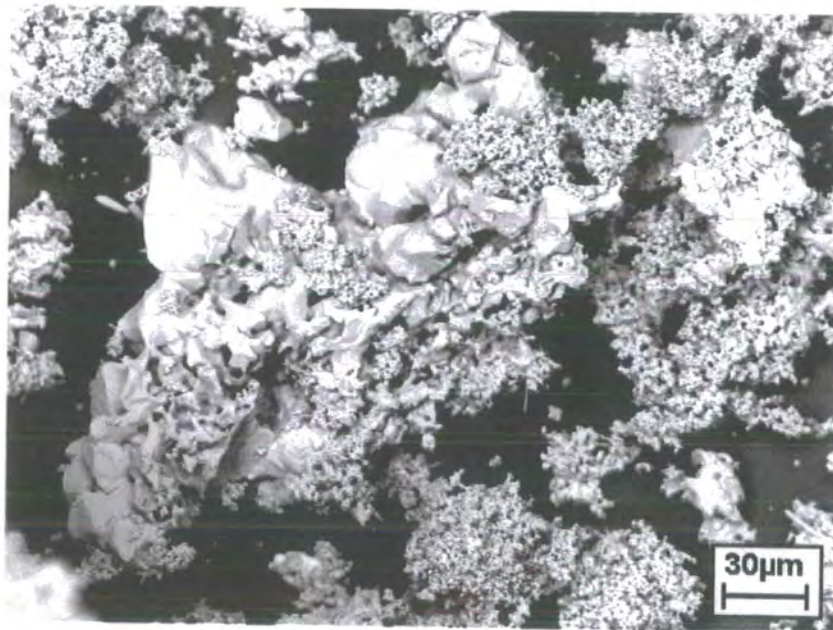


Fig. 3.24 Evaporation residues, magnification: x 300

In the sequence of images Figs. 3.25 - 27 the magnification of the SEM was increased step-wise, revealing the structure of the different phases.

These images suggest that the target temperature during evaporation was high enough to initiate crystal growth of separated phases. It appears that at least two different structures are present.

EDAX was carried out focussing the electron beam on the two different phases separately. No quantitative analysis was carried out, but the fine structured phase was found to be nickel and the coarse phase to be manganese rich, which supports the notion that the $\text{NiMn}_2\text{O}_{4+\delta}$ target dissociated when heated by the electron beam.

Reference to the phase diagram shown in chapter 2.3 (Fig. 2.3) implies that $\text{NiMn}_2\text{O}_{4+\delta}$ would dissociate into NiO and a tetragonal spinel Mn_3O_4 type structured phase at temperatures above $\sim 900^\circ\text{C}$.

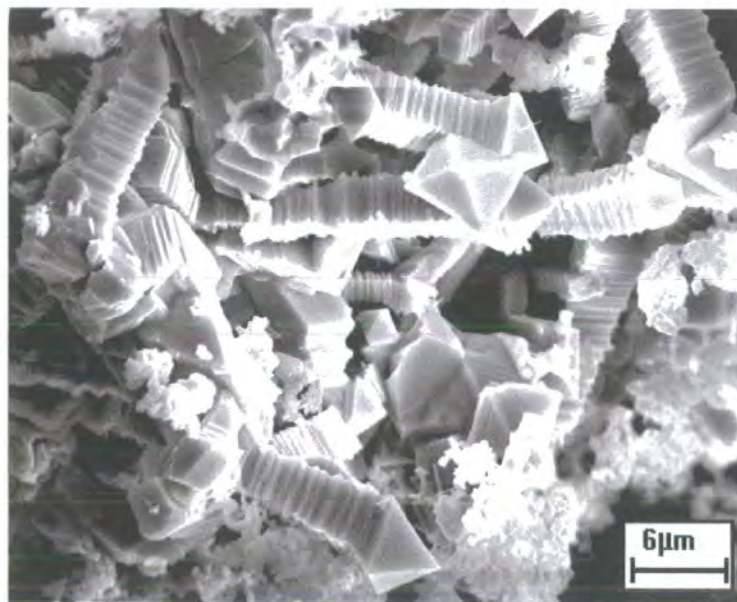


Fig. 3.25 Evaporation residues, focus on fine structured phase

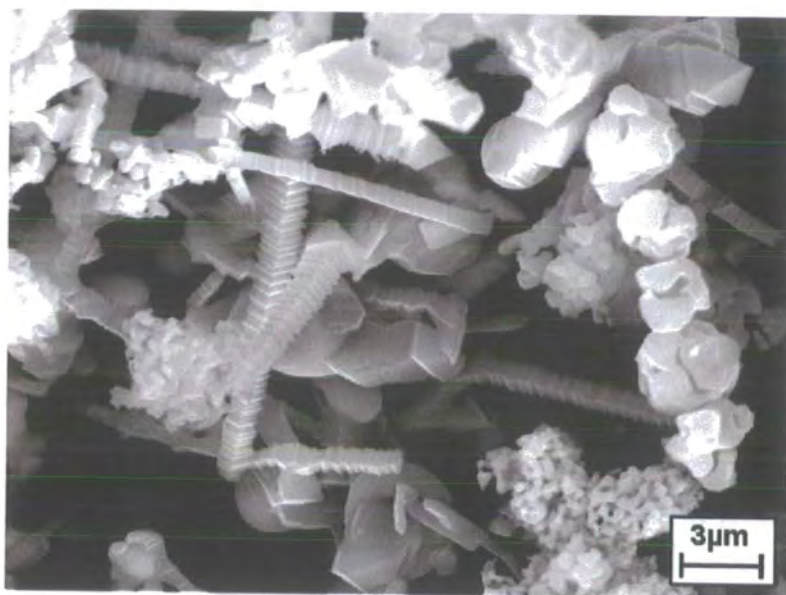


Fig. 3.26 Evaporation residues

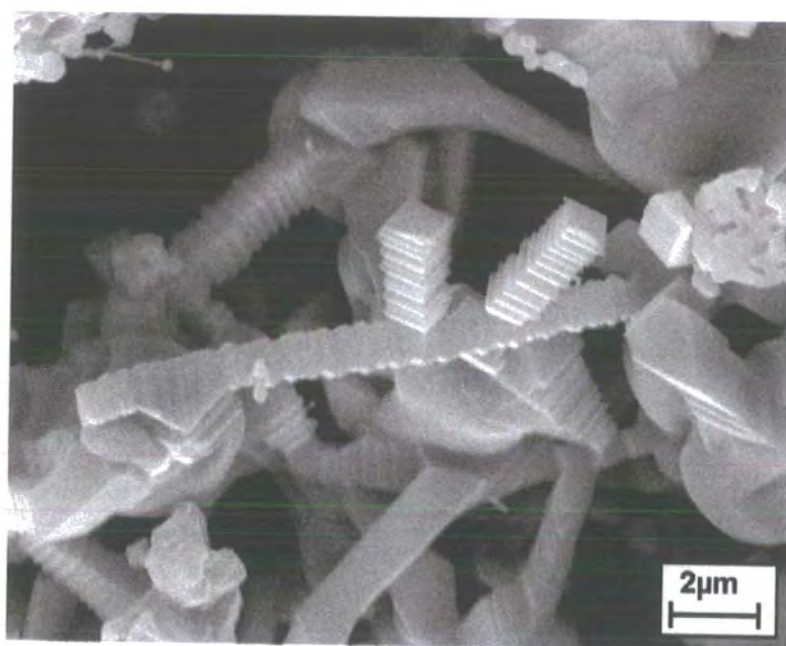


Fig. 3.27 Evaporation residues

3.5. Conclusion

Thin films were produced from a $\text{NiMn}_2\text{O}_{4+\delta}$ target material by electron-beam evaporation techniques, but the composition of the films varied significantly from the target and were not reproducible as could be seen from XRD and EDAX experiments. It is suggested that this was due to variations in the target temperature during deposition, which could not be controlled, leading to differences in the mechanism of the evaporation process.

Annealing procedures were not successful, because the annealing process was limited to 500°C for 30 minutes for films grown on Al_2O_3 substrates as the pre-digitated Al contacts would oxidise. Soda-lime glass substrates would melt and films deposited on heat resistive quartz glass substrates evaporated during annealing at higher temperatures. It was shown by XRD and SEM that E-beam evaporated films may exhibit an amorphous-like structure in the as-deposited state, but the film crystallinity can be improved by annealing processes, particularly if annealed at 800°C .

It is suggested that substrates without pre-digitated contacts should be used and the substrate material should be chosen more carefully to match the crystalline structure of $\text{NiMn}_2\text{O}_{4+\delta}$ as far as possible. This would enable better adhesion between substrate and film and annealing at 850°C for up to 30 minutes could lead to a pure $\text{NiMn}_2\text{O}_{4+\delta}$ spinel phase making the process independent of differences in the film composition in the as-deposited state.

Additionally, variations of the Ni : Mn ratio in the films and the target material were detected using EDAX, and turned out to be not reproducible in the films.

The electrical conductivity might vary significantly with different cation distribution, which in turn varies with the Ni : Mn ratio, and could be different in a disordered amorphous-like phase. (Conduction in the E-beam evaporated films is discussed later in chapter 5.4.1.).

Variations in the target temperature may be responsible for these inconsistencies. However, for laboratory processes the reproducibility of the production process is essential for further investigations and it is believed that the E-beam evaporation system used in this study was not appropriate to produce thin films based on $\text{NiMn}_2\text{O}_{4+\delta}$. However, the problems encountered with retaining stoichiometry are common using PVD methods, especially for depositing complex ternary compounds like $\text{NiMn}_2\text{O}_{4+\delta}$.

Other methods may be more useful, such as thick film techniques where the source powder is mixed with a carrier material forming a paste, which can be screen-printed directly onto the substrates. Such screen-printing procedures were established to produce thick $\text{NiMn}_2\text{O}_{4+\delta}$ films and are described in detail in the next chapter.

In the present chapter it was also shown that the thickness and shape of E-beam evaporated films was highly controlled and in good agreement with predictions obtained from a theoretical evaporation model.

3.6. References

1. Basu A., *Deposition and Characterisation of Sputtered Nickel Manganate Thin Films*, PhD Thesis, Department of Physics, 2002, Durham, University of Durham
2. Baliga S., Jain A.L., Zachofsky W., *Sputter deposition and characterisation of Ni-Mn-O and Ni-Co-Mn-O spinels on polyamide and glass substrates*, Applied Physics A : Solids and Surfaces, 1990, **50**, p. 472
3. Fau P., Bonino J.P., Demai J.J., Rousset A., *Thin films of nickel manganese oxide for NTC thermistor applications*, Applied Surface Science, 1993, **65/66**, p. 319
4. Lindner F., Feltz A., *Thin layer NTC semiconductor ceramics based on NiMn₂O₄ and Zn_zNiMn_{2-2z} (z = 1/3, 2/3)*, Journal of the European Ceramic Society, 1993, **11**, p. 269
5. Chaleix D., Choquet P., Bessaudou A., Frugier L., Machet J., *A spatial distribution study of a beam vapour emitted by electron-beam-heated evaporation sources*, Journal of Physics D: Applied Physics, 1996, **29**, p. 218
6. Holland L., *Vacuum deposition of thin films*, 1963, London, Chapman & Hall Ltd.
7. Schiller S., Jäsch G., Neumann M., *High rate electron beam evaporation*, Thin Solid Films, 1983, **110**, p. 149
8. Maissel L.I., Glang R., *Handbook of thin film technology*, 1970, New York, McGraw-Hill
9. Chopra K.L., *Thin film phenomena*, 1969, New York, McGraw-Hill Book Company
10. Dong C., *Powder-X software*, Chinese Academy of Sciences, Institute of Physics, Beijing
11. Piot O., Malaurie A., Machet J., *Experimental and theoretical studies of coating thickness distributions obtained from high rate electron beam evaporation sources*, Thin Solid Films, 1997, **293**, p. 124
12. http://www.ncnr.nist.gov/programs/crystallography/software/icdd_search.html, JCPDS-ICDD crystallographic database,
13. Weast R.C., ed. *CRC Handbook of Chemistry and Physics*. 1977/1978, CRC Press, Cleveland

Chapter 4

Thick film production via screen-printing techniques

4.1. Introduction	80
4.2. Co-precipitated $\text{NiMn}_2\text{O}_{4+\delta}$ source powder	81
4.2.1. Powder production	81
4.2.2. XRD analysis of decomposed nickel manganese oxalates	84
4.2.3. The Rietveld refinement method	86
4.2.4. Rietveld refinement analysis	91
4.2.4.1. Refinement of atom positions	92
4.2.4.2. Goodness of fit R_{Bragg} , correction term z_{corr} , scaling factor S and thermal factors B_{th}	95
4.2.4.3. Phase composition, unit cell parameter and average grain size	97
4.3. Screen-printing of thick film $\text{NiMn}_2\text{O}_{4+\delta}$ films	104
4.3.1. Principles of screen-printing	104
4.3.2. The screen-printing screen	106
4.3.3. The screen-printing process	107
4.3.4. XRD analysis of screen-printed films	109
4.3.5. Scanning Electron Microscopy (SEM) and surface profileometry	110
4.4. Conclusions	112
4.5. References	114

4.1. Introduction

In this chapter the sample production of a reliable thick film temperature-sensing device based on $\text{NiMn}_2\text{O}_{4+\delta}$ NTCR thermistor material is described. In the previous chapter it was suggested that thin or thick films of $\text{NiMn}_2\text{O}_{4+\delta}$ may be a way of circumventing problems with bulk material and attempts to prepare thin films via electron-beam evaporation were described. However, $\text{NiMn}_2\text{O}_{4+\delta}$ is a complex ternary compound and the vapour deposition of thin layers without loss of stoichiometry and changes in composition proved to be difficult. Consequently screen-printing procedures were developed as an alternative and direct film production technique. The aim of this chapter is to review the full thick film sample production process, which was largely developed at the University of Erlangen - Nuremberg. The thick film $\text{NiMn}_2\text{O}_{4+\delta}$ samples produced in Erlangen were examined in detail in this study in terms of their electrical characteristics, as described in later chapters, 5 and 6. During the previous work in Erlangen [1], the production process of $\text{NiMn}_2\text{O}_{4+\delta}$ source powder by the thermal decomposition of co-precipitated nickel manganese oxalate was optimised and the powder was mixed with dispersing agent, glass binder and a “vehicle” to produce a suitable and printable paste. The optimised paste was printed onto Al_2O_3 thick film substrates and the layers were sintered for densification and to control phase purity, and the morphology and profile assessed. The production of $\text{NiMn}_2\text{O}_{4+\delta}$ thick films has been further investigated in this study by the detailed examination of different source powders and screen-printed films using XRD. The powder XRD data was further analysed using the Rietveld refinement method [2].

4.2. Co-precipitated $\text{NiMn}_2\text{O}_{4+\delta}$ source powder

4.2.1. Powder production

The production of $\text{NiMn}_2\text{O}_{4+\delta}$ source powder from the co-precipitation of oxalates was investigated in an earlier study [1] and is published in detail elsewhere [3]. This method was also used in this work, where the powder production was achieved by the thermal decomposition of co-precipitated $\text{NiMn}_2(\text{C}_2\text{O}_4)_3 \cdot 6 \text{H}_2\text{O}$ as first described by Feltz et al. [4]. This compound has the required 1:2 nickel-manganese ratio appropriate for forming homogeneous $\text{NiMn}_2\text{O}_{4+\delta}$ powder and guaranteed an intimate mix of nickel and manganese atoms. $\text{NiMn}_2(\text{C}_2\text{O}_4)_3 \cdot 6 \text{H}_2\text{O}$ may be thermally decomposed at temperatures of $\sim 800^\circ\text{C}$ resulting in a $\text{NiMn}_2\text{O}_{4+\delta}$ powder with a small average grain size distribution. The more conventional procedure of firing precursor oxides of the NiO- Mn_2O_3 system would require higher temperatures and an annealing process at 800°C to retain phase purity (see the phase diagram given in chapter 2.3.). This extensive heat exposure results in to strong grain growth and a high average grain size, unsuitable for screen-printing procedures.

Fig. 4.1 shows the co-precipitation production route, which involves three different stock solutions containing nickel, manganese and oxalate ions as a starting point. The nickel stock solution was prepared by the dissolution of nickel carbonate tetra-hydrate ($\text{NiCO}_3 \cdot 4 \text{H}_2\text{O}$, 99.996% purity) in diluted acetic acid (10%). Aqueous solutions of manganese (II) acetate tetra-hydrate ($\text{Mn}(\text{CH}_3\text{COO})_2 \cdot 4 \text{H}_2\text{O}$, 99.99% purity) and oxalic acid di-hydrate ($\text{H}_2\text{C}_2\text{O}_4 \cdot 2 \text{H}_2\text{O}$, 99.5% purity) were used for the manganese and oxalate stock solutions. The concentrations of the nickel and the oxalate stock solutions were determined precisely by titration methods.

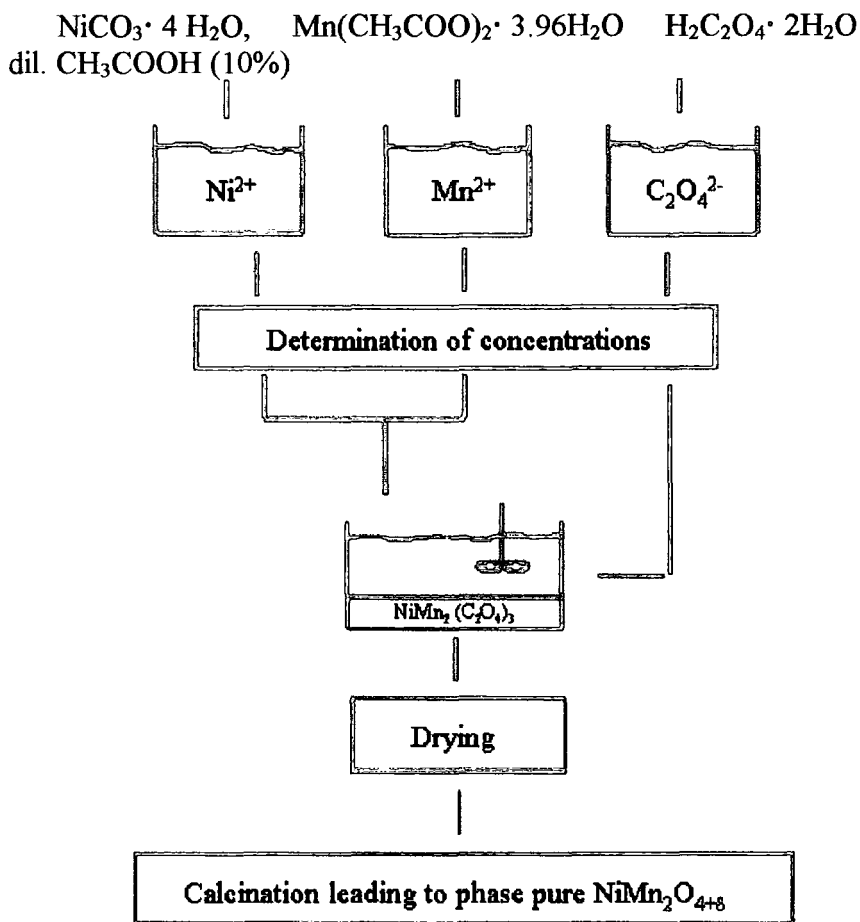


Fig. 4.1 Principle of the mixed oxalate route, [3]

For the nickel titration a nickel-amine complex $[\text{Ni}(\text{NH}_3)_6]^{2+}$ solution was produced by adding ammonium hydroxide (NH_4OH) solution to a few millilitres of precisely measured nickel solution. The titration was carried out with Titriplex III ($\text{Na}_2\text{-EDTA}$) titration solution using murexide as an indicator, where the concentration of the Titriplex III solution had been checked by titrating a nickel standard solution of well-known concentration.

The oxalate titration was carried out in a sulphuric acid environment at 80°C using potassium permanganate titration solution (KMnO_4) without an additional indicator. The concentration of the titration solution had been checked previously using a

sodium oxalate $\text{Na}_2(\text{C}_2\text{O}_4)$ standard solution, as $\text{Na}_2(\text{C}_2\text{O}_4)$ has no water of hydration and a reference solution of precise concentration can be produced.

The manganese titrations turned out to be not reproducible. Therefore, the amount of water of hydration of the manganese acetate $(\text{Mn}(\text{CH}_3\text{COO})_2 \cdot 4 \text{H}_2\text{O})$ was determined more precisely by thermal decomposition at 1200°C and weighing the original and the resulting powder, the latter being Mn_3O_4 . Five thermal decompositions gave a mean value of 3.96 H_2O water of hydration $(\text{Mn}(\text{CH}_3\text{COO})_2 \cdot 3.96 \text{H}_2\text{O})$, which is in the range of the original value given by the manufacturer. The required quantity of manganese acetate $\text{Mn}(\text{CH}_3\text{COO})_2 \cdot 3.96 \text{H}_2\text{O}$ was then weighed accurately and dissolved in water.

The nickel, manganese and oxalate stock solutions of well-known concentrations were mixed together in the appropriate ratio and $\text{NiMn}_2(\text{C}_2\text{O}_4)_3 \cdot 6 \text{H}_2\text{O}$ precipitated, which was expected to be complete after ~ 24 h. The remaining solution was evaporated using an evacuated rotating evaporator at 60°C and 60 mbar, which is appropriate for the evaporation of H_2O as well as organic impurities.

In order to further investigate the formation of $\text{NiMn}_2\text{O}_{4+8}$, co-precipitated $\text{NiMn}_2(\text{C}_2\text{O}_4)_3 \cdot 6 \text{H}_2\text{O}$ was decomposed for 6 hours at different decomposition temperatures T_d of 300°C , 330°C , 350°C , 375°C , 400°C , 500°C , 600°C 700°C and 800°C .

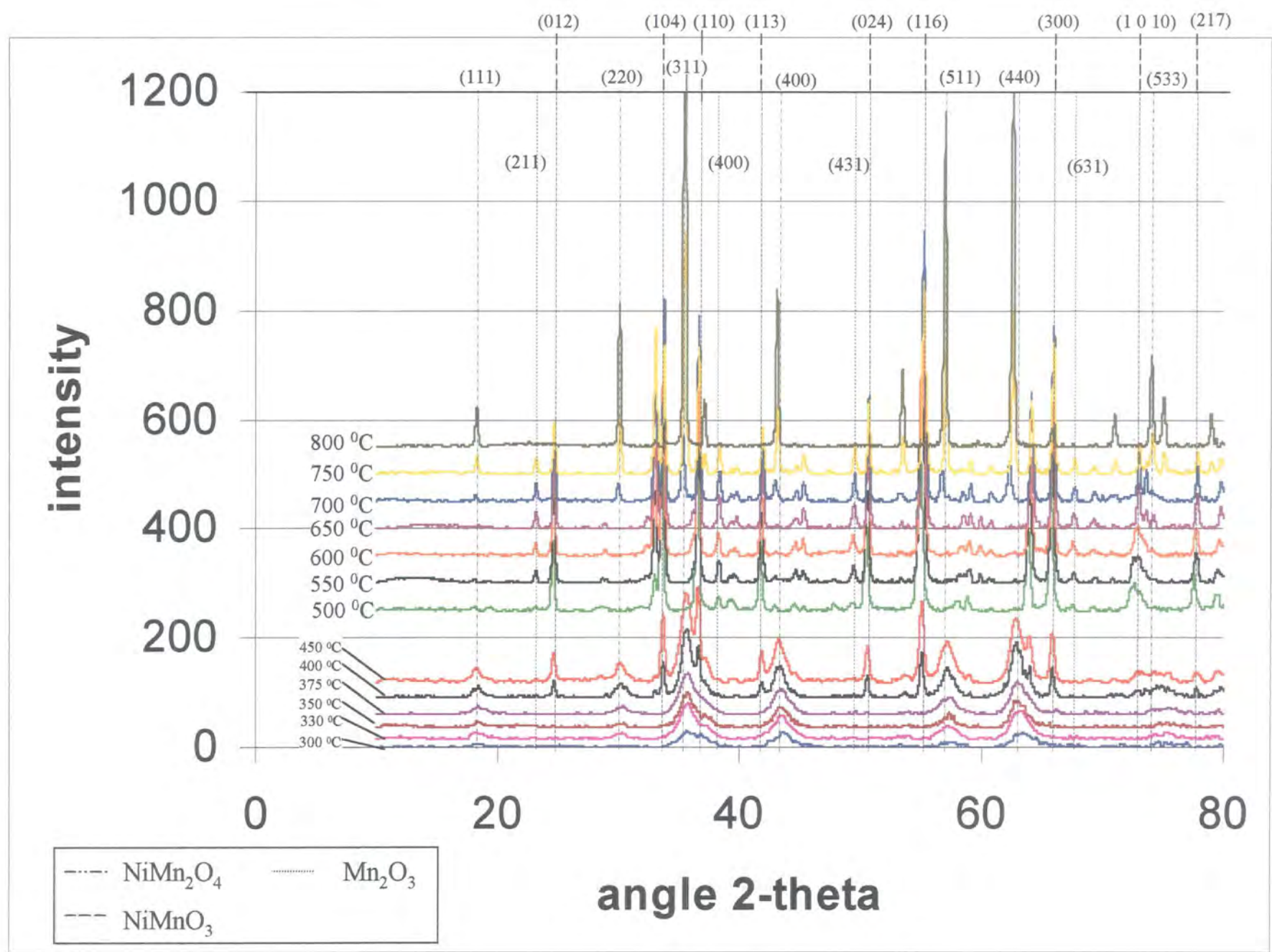
A slow heating rate of 1K/minutes was chosen for heating up to the respective temperature and quench cooling was performed at the end of the heating period by removing the powder from the furnace and leaving at room temperature, in order to retain the phases present at the respective T_d . A slow heating rate was necessary to avoid an abrupt release of the water of hydration in $\text{NiMn}_2(\text{C}_2\text{O}_4)_3 \cdot 6 \text{H}_2\text{O}$, which would lead to the material spilling out of the crucible.

It was previously shown [3] that the heat exposure may be reduced significantly by increasing the heating rate at temperatures where no reactions occur, such as the release of water of hydration, leading to a smaller average grain size. The optimized process was found to be decomposing at 850°C with a minimum holding time of 30 minutes leading to a regular phase pure $\text{NiMn}_2\text{O}_{4+\delta}$ spinel phase.

4.2.2. XRD analysis of decomposed nickel manganese oxalates

Fig. 4.2 shows the XRD scans of decomposed $\text{NiMn}_2(\text{C}_2\text{O}_4)_3 \cdot 6 \text{H}_2\text{O}$ and it can be seen that the powders exhibited 5 different phase compositions dependent on T_d . For 300°C - 375°C a pure spinel $\text{NiMn}_2\text{O}_{4+\delta}$ phase was detected, which is in agreement with the work of Feltz and Töpfer [4] and Tang et al. [5], who claim that a cation deficient meta-stable spinel phase may be present. For T_d values of 400°C - 700°C the above authors found in agreement with Wickham [6] that a mixed phase composition of Mn_2O_3 and NiMnO_3 occurs. The scans in Fig. 4.2 indicate the presence of NiMnO_3 at 400°C and 450°C, but the $\text{NiMn}_2\text{O}_{4+\delta}$ spinel phase is still present and there is little evidence of the predicted Mn_2O_3 phase. Powders processed at 500°C - 650°C seemed to mainly consist of Mn_2O_3 and NiMnO_3 , which is still the case for materials prepared at 700°C and 750°C, although increasing proportion of $\text{NiMn}_2\text{O}_{4+\delta}$ can now be seen. This is clearly not in agreement with the phase diagram given by Wickham [6] (see chapter 2.3), where a mixture of NiMnO_3 and a $\text{NiMn}_2\text{O}_{4+\delta}$ phase was proposed to occur at 700°C and phase pure $\text{NiMn}_2\text{O}_{4+\delta}$ powder at 750°C. The XRD scans for $T_d = 800^\circ\text{C}$ and 850°C (see Appendix C, xiv) clearly indicated the presence of a pure spinel phase, in agreement with Wickham [6].

Fig. 4.2 XRD scans of decomposed oxalates



For clarity of presentation, not all peaks in Fig. 4.2 have been labelled, but the full analysis of selected scans is given in Appendix C.

The occurrence of $\text{NiMn}_2\text{O}_{4+\delta}$ traces at 400°C and 450°C may be the result of the slow heating rate, where $\text{NiMn}_2\text{O}_{4+\delta}$ may have formed at lower temperatures during heating up, but the phase transition from $\text{NiMn}_2\text{O}_{4+\delta}$ to Mn_2O_3 and NiMnO_3 may not have been completed during 6 hours. Higher T_d values of 500°C would be required to achieve this. The Mn_2O_3 and NiMnO_3 impurities at 750°C, where a pure spinel phase was expected, may be well result of the same effect of uncompleted phase transition. It is believed that a faster heating rate would minimise this formation of additional phases during the sweep through lower temperature regions.

Rietveld refinement was carried out for the XRD scans shown in Fig. 4.2, and in addition for the powder decomposed at 850°C in the optimised procedure.

4.2.3. The Rietveld refinement method

The Rietveld refinement method was developed in order to fit a calculated curve to a full XRD scan by refining several parameters [2]. In this work the computer simulation process was carried out using Topas software [7], where detailed information about the crystallographic structure of each compound present in the material under investigation enabled calculation of the geometric and structural factors, which determine the peak intensities in the XRD scan. The fit was performed by using a least squares fitting routine, whereby the following residual sum S_y would be minimised :

$$S_y = \sum_i (y_i - M_i(\hat{x}))^2 ; \quad 4.1$$

where y_i is the observed intensity and $M_i(x)$ is the calculated value from the model.

In Rietveld refinement analysis the R value of weighted parameters R_{wp} is usually defined by (Young, [2]) :

$$R_{wp} = \left\{ \frac{\sum w_i (y_i - M_i(\hat{x}))^2}{\sum w_i (y_i)^2} \right\}^{1/2} ; \quad 4.2$$

where w_i is the weighting factor ($w_i = 1/y_i$). The summations are always taken over all refined data points in the respective fit.

The expected R value R_e is defined by ([2]) :

$$R_e = \left\{ \frac{N - P}{\sum w_i (y_i)^2} \right\} ; \quad 4.3$$

where N is the number of fitting points and P the number of parameters. The goodness of the fit can then be assessed by determining the parameter S , defined by

$$S = \frac{R_{wp}}{R_e} ; \quad 4.4$$

S values between 1 and 1.5 are desirable, values above 1.5 would suggest that the model is inadequate, whereas S values below 1 would indicate that the model contains more parameters than can be justified by the quality of the data [2].

In addition, the goodness of fit for each phase present in the material can be assessed separately by the factor R_{Bragg} , defined as follows [2] :

$$R_{\text{Bragg}} = \frac{\sum |I_K(\text{obs}) - I_K(\text{calc})|}{\sum I_K(\text{obs})}; \quad 4.5$$

where $I_K(\text{obs})$ is the observed intensity of a Bragg peak and $I_K(\text{calc})$ is its intensity calculated from the model. This definition implies that R_{Bragg} factors are not always based on observed intensities, but on those deduced with the help of the model, i.e. one peak in the spectrum could be assigned with the intensities from more than 1 phase. Therefore, R_{Bragg} factors are biased and in favour of the model, but still they give a clear indication of the goodness of fit for each separate phase [2]. R_{Bragg} values between 1 – 2 would indicate an excellent fit, 2 – 5 correspond to a good fit and values above 10 suggest that the results of the respective phase may not be appropriate for taking any main conclusions or interpretations from them.

Additionally, the errors in each single parameter i can be assessed by the estimated standard deviation (e.s.d.) σ_i , defined as [2]:

$$\sigma_i = \left[M_{ii}^{-1} \frac{\sum w_i (y_i - M(\hat{x}))^2}{N - P + C} \right]; \quad 4.6$$

where M_{ii}^{-1} is the diagonal element of an inverse matrix and C the number of constraints applied. Both, M_{ii}^{-1} and C are characteristic for each fit performed by the computer software. However, the σ_i values only give an estimation for errors arising from random errors alone but do not reflect any experimental error. Furthermore, it is important to know that a model inadequacy leading to a systematic error could masquerade as random error in the e.s.d. calculation [2].

In order to perform a reasonable fit, information is required about the phases or compounds present, their crystallographic space-group, unit cell geometry and reasonable starting values for the unit cell parameter(s), lattice angle(s) (if applicable) and the position of each atom inside the unit cell. This information was obtained from a chemical data base (ICSD, [8]) for $\text{NiMn}_2\text{O}_{4+\delta}$, Mn_2O_3 , NiMnO_3 and Mn_3O_4 , where the positions of each atom in the unit cells were expressed as fractions x , y and z of the three unit cell basis vectors with $0 \leq x, y, z \leq 1$.

During the fits performed in this work several global parameters were refined :

- 1.) A mathematical function was chosen to fit the shape of each peak (Pseudo-Voigt) by 6 parameters.
- 2.) The type of background (Chebychev) was specified and was fitted using 1 parameter.
- 3.) An arbitrary scale was used to relate the peak intensities of each phase present, which enabled quantitative specification of the percentage of each compound present in wt.%.
- 4.) The correction term z_{corr} was allowed to compensate for any possible misalignment of sample holder and detector in the XRD device.

The following compound specific parameters were refined:

- 1.) The unit cell parameter(s) $a, (b,c)$ in Å
- 2.) The lattice angle α in angular degree (if applicable)
- 3.) The position of each atom x, y, z was refined, but only a small shift from the original value was regarded as being a reasonable result (complete changes of atom positions would change the unit cell symmetry). Special atom positions such as (0,0,0) were not refined.
- 4.) The thermal factors B_{th} described the changes of the structural factors due to thermal motions of the atoms. The thermal factor B_{th} is defined by

$$B_{th} = 8 \pi^2 U (\text{Å}^2); \quad 4.7$$

where U is the square mean shift of the atom due to thermal motions with respect to the position of equilibrium :

$$U = \langle r'^2 \rangle; \quad 4.8$$

Here, the position of equilibrium is assumed at the origin and r' is the atomic distance to the equilibrium position. Eq. 4.8 is also based on the notion that a scattering event of X-rays involves a much larger time scale than thermal oscillations of atoms around the equilibrium position [9]. B_{th} values between 1 – 10 would be reasonable and usually they should not differ significantly for similar atoms in the same fit.

- 5.) The average crystal size (grain size) L_{cr} was refined (here the peak type had to be changed to FP (= fundamental parameters))

From the compound specific parameters the crystal density ρ_v was calculated in g/cm^3 for each phase.

4.2.4. Rietveld refinement analysis

For all XRD scans of decomposed oxalates Rietveld refinement of the data obtained was performed. The compounds present in each powder were identified from Fig. 4.2 as described in the previous section.

The 350°C – 375°C, 800°C and 850°C XRD scans were analysed assuming only one $\text{NiMn}_2\text{O}_{4+\delta}$ phase present, and the total number of refined parameters was 10. A second fit was performed to determine the crystal size with the peak shape set to FP (fundamental parameters), and the total number of parameters was 6. The atom positions in the $\text{NiMn}_2\text{O}_{4+\delta}$ spinel were refined in a preliminary fit as described in the next section, and it was assumed that the atom positions in the defect spinel (300°C – 375°C) did not change significantly with decomposition temperature and were therefore set to be constant for subsequent fits, as was done for the regular spinel (800°C and 850°C).

At 400°C, 450°C, 700°C and 750°C, 3 phases, NiMnO_3 , Mn_2O_3 , and $\text{NiMn}_2\text{O}_{4+\delta}$ were assumed to be present. The total number of refined parameters was 32 and for the crystal size fit 20. At 500°C – 650°C NiMnO_3 , Mn_2O_3 and Mn_3O_4 were assumed to be present and 33 parameters were refined, for the crystal size scan 21.

The atom positions were again taken as constant determined from preliminary fits, as described in the next section.

4.2.4.1. Refinement of atom positions

It turned out that the simulations did not converge or would not lead to satisfactory S and R_{Bragg} values if too many parameters were refined at the same time, which was the case if three different phases had to be analysed. Therefore, a preliminary refinement of the atom positions in the unit cell was performed from phase pure XRD scans. For $\text{NiMn}_2\text{O}_{4+\delta}$ the atom positions were refined from the scan at 350°C representing the pure defect spinel and again at 800°C for the regular spinel phase. For further refinements it was supposed that at 300°C - 450°C the defect spinel and at 700°C - 850°C the regular spinel was present and the respective atom positions were taken as being constant. The same calibration for the atom positions in Mn_2O_3 and NiMnO_3 was carried out from the 600°C scans, where both compounds were clearly detected.

At 600°C the percentage of the Mn_3O_4 phase was not significant and was first neglected to obtain reasonable atom positions for Mn_2O_3 and NiMnO_3 . The Mn_3O_4 atom positions were then refined thereafter in the same scan.

All refined atom positions are shown in Table 4.1 – 4.5, with the estimated standard deviations σ_i given and the original values from the ICSD data base given in brackets. In the regular $\text{NiMn}_2\text{O}_{4+\delta}$ spinel the refined positions of the second manganese (Mn2) and the nickel (Ni1) atoms showed no difference to the data base, only the oxygen position showed a slight shift.

Table 4.1 Refined atom position of the defect spinel $\text{NiMn}_2\text{O}_{4+\delta}$
(space-group $fd-3m$, point group $m-3m$)

	x	y	z
Mn1	0 (0) not refined	0 (0) not refined	0 (0) not refined
Mn2	0.6276±0.0051 (0.6250)	0.6276±0.0051 (0.6250)	0.6276±0.0051 (0.6250)
Ni1	0.6276±0.0051 (0.6250)	0.6276±0.0051 (0.6250)	0.6276±0.0051 (0.6250)
O1	0.3786±0.0025 (0.3860)	0.3786±0.0025 (0.3860)	0.3786±0.0025 (0.3860)

Table 4.2 Refined atom position of the regular spinel $\text{NiMn}_2\text{O}_{4+\delta}$

	x	y	z
Mn1	0 (0) not refined	0 (0) not refined	0 (0) not refined
Mn2	0.6250±0.00035 (0.6250)	0.6250±0.00035 (0.6250)	0.6250±0.00035 (0.6250)
Ni1	0.6250±0.00035 (0.6250)	0.6250±0.00035 (0.6250)	0.6250±0.00035 (0.6250)
O1	0.3908±0.00041 (0.3860)	0.3908±0.00041 (0.3860)	0.3908±0.00041 (0.3860)

Table 4.3 Refined atom position of Mn_2O_3 (space-group $Pbca$, point group mmm)

	x	y	z
Mn1	0 (0) not refined	0 (0) not refined	0 (0) not refined
Mn2	0.2340±0.0052 (0.285)	0.2259±0.0050 (0.253)	0.0093±0.0068 (0.994)
Mn3	0.9980±0.0055 (0.00462)	0.2385±0.0065 (0.285)	0.2997±0.0024 (0.246)
Mn4	0.2178±0.0055 (0.253)	0.0059±0.0075 (0.00130)	0.2421±0.0081 (0.285)
O1	0.3929±0.022 (0.133)	0.3514±0.019 (0.915)	0.1280±0.020 (0.150)
O2	0.1755±0.030 (0.144)	0.1034±0.025 (0.130)	0.8236±0.020 (0.915)
O3	0.8635±0.018 (0.920)	0.1504±0.024 (0.147)	0.2036±0.014 (0.124)
O4	0.6470±0.024 (0.626)	0.3748±0.023 (0.418)	0.5805±0.024 (0.644)
O5	0.6660±0.022 (0.649)	0.5769±0.025 (0.628)	0.3901±0.020 (0.419)
O6	0.1773±0.027 (0.413)	0.6415±0.019 (0.647)	0.5979±0.033 (0.632)

For the Mn_2O_3 atom positions several values deviated significantly from the data base, which are printed bold. In particular, the first Mn_2O_3 oxygen atom position was shifted, as well as the z - value of the second manganese position Mn2 and the x -value of Mn3. As a result interpretations about the Mn_2O_3 phase have to be considered with care.

The atom positions for NiMnO_3 and Mn_3O_4 matched well with the expected values as shown in Table 4.4 and Table 4.5.

Table 4.4 Refined atom position of NiMnO_3 (space-group R-3r, point group -3)

	x	y	z
Ni1	0.355±0.00038 (0.352)	0.355±0.00038 (0.352)	0.355±0.00038 (0.352)
Mn1	0.156±0.00038 (0.148)	0.156±0.00038 (0.148)	0.156±0.00038 (0.148)
O1	0.549±0.0038 (0.560)	0.946±0.0040 (0.940)	0.250 (0.250) not refined

Table 4.5 Refined atom position of Mn_3O_4

(space-group I41/amd, point group 4/mmm)

	x	y	z
Ni1	0 (0) not refined	0 (0) not refined	0 (0) not refined
Mn1	0 (0) not refined	0 (0) not refined	0.625 (0.625) not refined
O1	0 (0) not refined	0.229±0.014 (0.227)	0.367±0.0096 (0.383)

4.2.4.2. Goodness of fit S , R_{Bragg} , correction term z_{corr} and thermal factors B_{th}

Rietveld refinement was carried out with the atom positions given above and the following S and R_{Bragg} values were obtained indicating the validity of the model:

Table 4.6 S and R_{Bragg} values for $\text{NiMn}_2\text{O}_{4+\delta}$, NiMnO_3 , Mn_2O_3 , Mn_3O_4

	S values	$\text{NiMn}_2\text{O}_{4+\delta}$	NiMnO_3	Mn_2O_3	Mn_3O_4
300	1.11	3.18	-	-	-
330	1.15	4.48	-	-	-
350	1.14	4.08	-	-	-
375	1.15	4.35	-	-	-
400	1.24	5.50	3.61	4.62	-
450	1.22	4.66	3.06	3.01	-
500	1.26	-	4.78	3.36	-
550	1.30	-	4.31	2.72	7.03
600	1.19	-	3.55	2.61	3.82
650	1.20	-	3.72	2.93	4.52
700	1.24	3.83	3.70	4.09	-
750	1.17	4.54	3.11	4.43	-
800	1.20	3.82	-	-	-
850	1.13	3.82	-	-	-

The S values all indicated an acceptable fit ($1 < S < 1.5$) and the R_{Bragg} factors showed all acceptable values, too, except probably for Mn_3O_4 decomposed at 550°C , where the result may be considered with care.

It was attempted to fit all thermal factors B_{th} for each atom position (Mn1, Mn2, etc.) separately, but the values were differing significantly and were open to question. Therefore it was decided to set only one B_{th} value for refinement for each phase without differentiation between Ni, Mn or O atoms. This would lead to a good approximation as B_{th} is not supposed to vary significantly for different atoms.

The fact that thermal factors could not be refined separately from XRD data is in agreement with the literature, where it was suggested that neutron diffraction data should be used for this purpose [2]. The B_{th} values obtained are shown in Table 4.7, together with the estimated standard deviations σ_j .

Table 4.7 B_{th} values of $NiMn_2O_{4+\delta}$, $NiMnO_3$, Mn_2O_3 , Mn_3O_4

	$NiMn_2O_{4+\delta}$	$NiMnO_3$	Mn_2O_3	Mn_3O_4
300	1.961±0.48	-	-	-
330	3.172±0.26	-	-	-
350	2.48±0.27	-	-	-
375	3.048±0.22	-	-	-
400	3.803±0.18	3.876±0.41	11.680±11.23	-
450	3.982±0.20	3.808±0.29	8.176±10.27	-
500	-	4.60±0.12	0.3901±0.62	-
550	-	4.993±0.13	3.474±0.39	9.603±6.56
600	-	4.650±0.13	3.567±0.48	5.048±2.10
650	-	4.560±0.11	4.686±0.29	3.962±1.77
700	4.662±0.35	4.657±0.12	4.842±0.29	-
750	5.314±0.15	5.095±0.16	4.350±0.27	-
800	4.839±0.075	-	-	-
850	4.898±0.074	-	-	-

These values are all in the expected range and rather similar to each other, except for Mn_2O_3 at 400°C - 500°C, for $\text{NiMn}_2\text{O}_{4+\delta}$ at 300°C and for Mn_3O_4 at 550°C. Values that differ significantly to the trend would suggest that the fit was not very good, which was supported by the high σ_i errors of these values.

The z_{corr} terms describing possible misalignments of sample holder and detector were found to be in the range of $-0.13^\circ - 0.08^\circ$, which are reasonably low values and could be explained by variations in the shape and alignment of the different sample holders used for each scan. The σ_i errors in z_{corr} were all smaller than 10%, most of them significantly.

4.2.4.3. Phase composition, unit cell parameter and average grain size

The refined percentages in wt.% of the phases present are shown in Fig. 4.3, where the predicted region of instability of the $\text{NiMn}_2\text{O}_{4+\delta}$ spinel at intermediate temperatures can be seen clearly.

The estimated standard deviations σ_i for the phase percentages are displayed as error bars of the data points, except the σ_i values were too small to be resolved. The phase percentages of Mn_3O_4 were all small and are not displayed in Fig. 4.3. According to the computer model at $T_d = 550^\circ\text{C}$ an amount of $4.87 \pm 0.02\%$ Mn_3O_4 was present, at 600°C $4.84 \pm 0.004\%$ and at 650°C $4.84 \pm 0.003\%$.

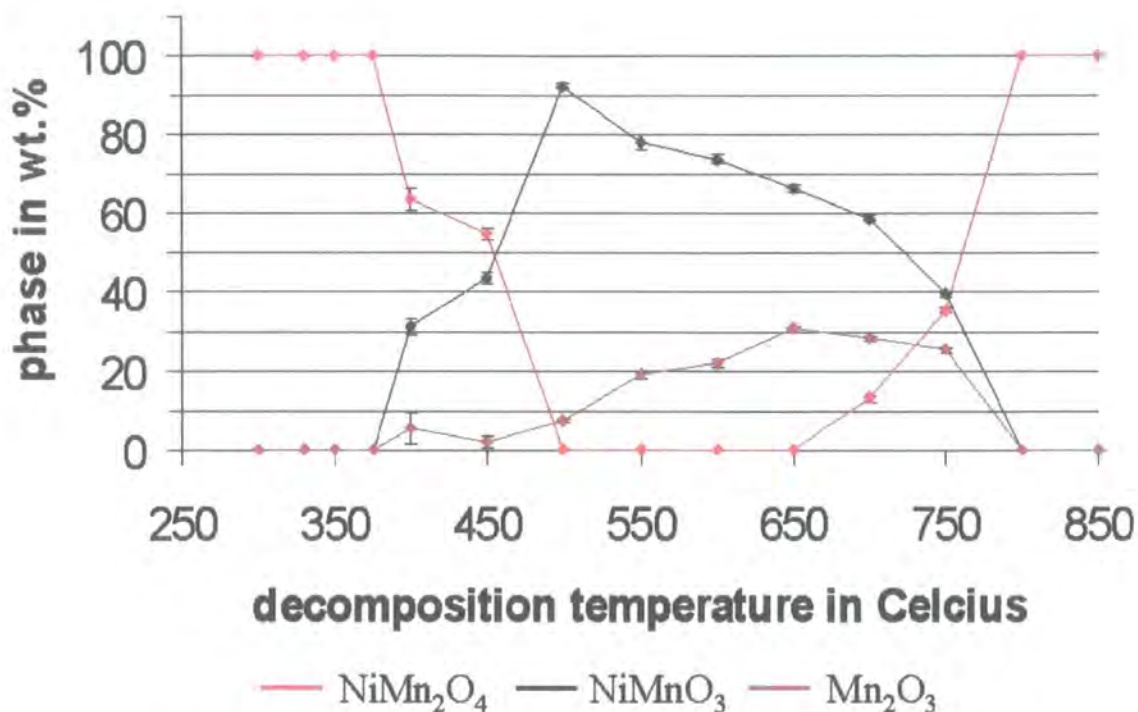


Fig. 4.3 Powder compositions at different decomposition temperatures

In Fig. 4.4 the refined values of the average crystal sizes are shown in nm, together with some σ_i values depending on whether they were large enough to be displayed. It can be seen that the defect spinel $\text{NiMn}_2\text{O}_{4+\delta}$ phase exhibited a very small average grain size in the range of 3 nm – 10 nm. This feature is very interesting and might be of great importance for nano-technological applications of this defect spinel powder.

At $T_d \geq 700^\circ\text{C}$ the grain size of the regular $\text{NiMn}_2\text{O}_{4+\delta}$ spinel increased significantly with increasing T_d as can be seen in the inset of Fig. 4.4. The drop in crystal size for the powder decomposed by the optimised process at 850°C demonstrates the effectiveness of reducing heat exposure for producing smaller grain sizes.

NiMnO_3 exhibited modest increases in grain size with T_d , except at 600°C , where the crystal size reduced with decomposition temperature as was the case at 750°C . This may reflect the fact that at 750°C a significant amount of $\text{NiMn}_2\text{O}_{4+\delta}$ was formed

from NiMnO_3 and Mn_2O_3 grains, reducing their size. Similarly, at 600°C a strong reduction of NiMnO_3 and an increase of Mn_2O_3 concentration is shown in Fig. 4.3, which may suggest that a similar effect occurred.

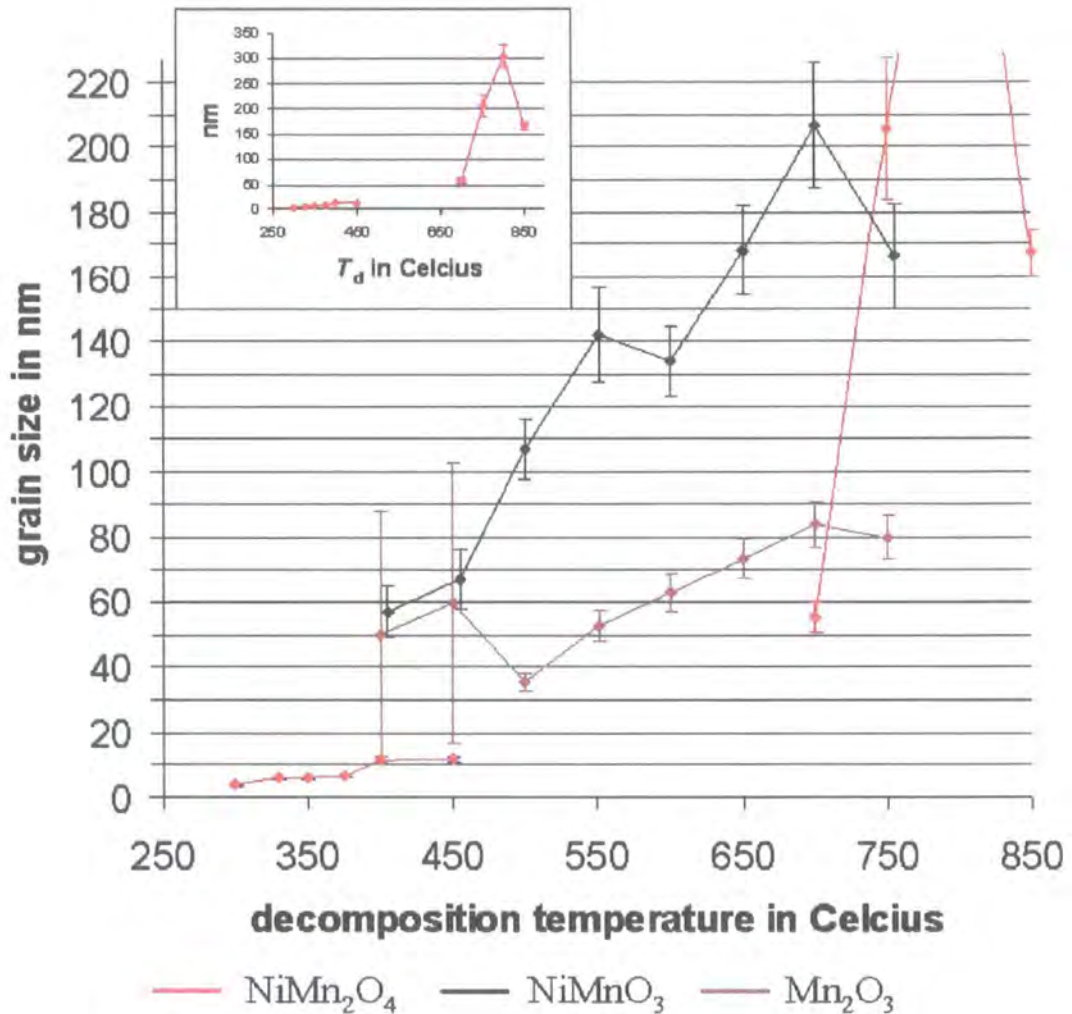


Fig. 4.4 Average grain size at different decomposition temperatures

The crystal size of Mn_2O_3 showed a uniform increase with T_d , except at 400°C and 450°C , where the errors were too high for assessing the trend, and at 750°C , where the corresponding effect as for NiMnO_3 occurred.

In Fig. 4.5 the change in the unit cell parameter a in Å and the crystal density ρ_V in $\text{g}\cdot\text{cm}^{-3}$ are depicted for $\text{NiMn}_2\text{O}_{4+\delta}$. For all unit cell parameters the e.s.d. errors were too small and were therefore not displayed.

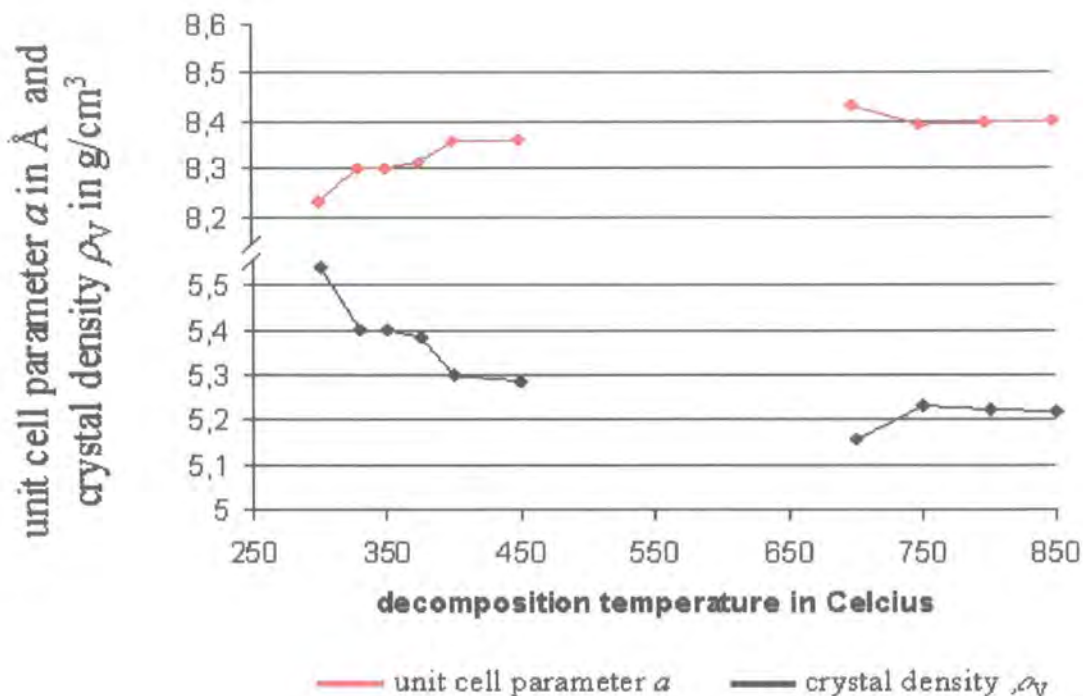


Fig. 4.5 Unit cell parameter a and crystal density ρ_V of $\text{NiMn}_2\text{O}_{4+\delta}$

Due to the cubic unit cell of $\text{NiMn}_2\text{O}_{4+\delta}$ the crystal density ρ_V is proportional to a^{-3} as can be seen in Fig. 4.5. It is also apparent that a increased with increasing temperature with the exception of the material decomposed at 700°C , where it is suggested that a systematic error occurred.

The increase in the unit cell parameter may well be due to differences in the cation distribution as mentioned by Boucher et al. [10]. They reported an increase of the lattice parameter between $8.395 \text{ \AA} - 8.400 \text{ \AA}$ for T_d values between 750°C and 940°C , which is in reasonable agreement with the results obtained. For the defect

spinel, α shows a stronger dependence upon T_d , but no data for comparison can be found in the literature.

The unit cell parameter a and the lattice angle α were refined for NiMnO_3 , and the change of α with T_d is shown in Fig. 4.6.

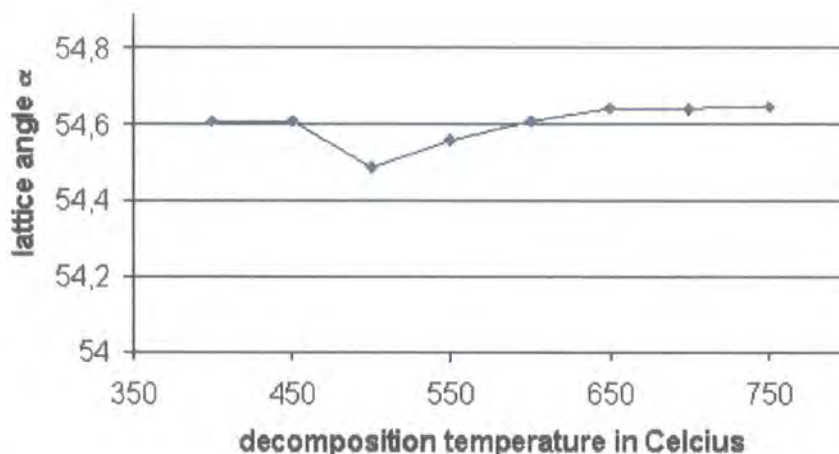


Fig. 4.6 Variation of α with decomposition temperature for NiMnO_3

It can be seen that α varied significantly from the original value (ICSD) of 90° to values of $\sim 54^\circ - 55^\circ$, changing the unit cell geometry from a cubic to a rhombohedral shape. It is believed that this is reasonable, because other data bases (JCPDS [11], no. 48-1330) do suggest a rhombohedral shape. The variations in the lattice angle α are all in the range of 0.3 % and show no systematic trend with the decomposition temperature.

In Fig. 4.7 the unit cell parameter and the crystal density of NiMnO_3 are plotted vs. T_d , and the changes in a and ρ_v are rather small and may well be independent of T_d , too.



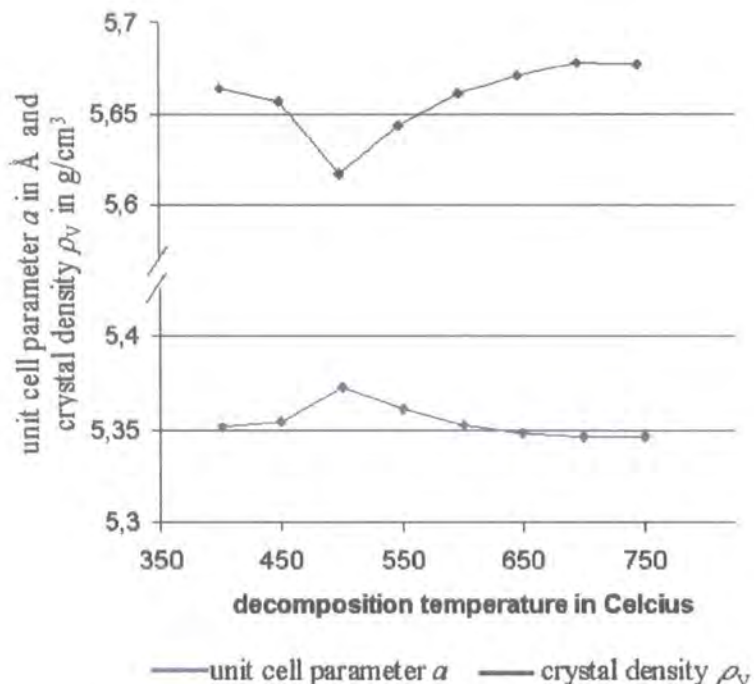


Fig. 4.7 Unit cell parameter a and crystal density ρ_v of NiMnO₃

The refined unit cell parameters a, b and c for Mn₂O₃ are plotted together with the crystal density ρ_v in Fig. 4.8.

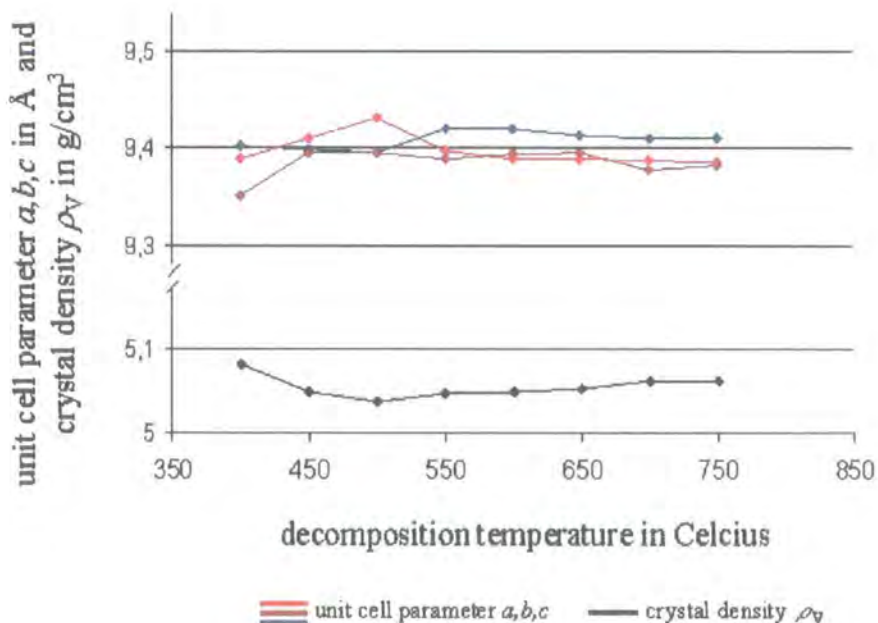


Fig. 4.8 Unit cell parameter a, b, c and crystal density ρ_v of Mn₂O₃

It can be seen that a, b and c varied slightly from each other at T_d values of 400°C - 500°C, but were independent of T_d at higher decomposition temperatures. Since $a \approx b \approx c$, it is suggested that the structure of Mn_2O_3 was cubic, as reported in the literature [11]. The crystal density ρ_v showed no significant T_d dependence at all.

4.3. Screen-printing of thick $\text{NiMn}_2\text{O}_{4+\delta}$ films

4.3.1. Principles of screen-printing

Screen printing is a thick film technique which is used for a wide range of applications, such as printing circuits on board or printing batches and labels on a wide variety of materials including metals, ceramics, textiles or wood [12]. Screen-printing is a direct printing technique where the powder is mixed with carrier material forming a printable paste. The paste is pressed through a screen and deposited directly onto a substrate, which is placed few millimetres beneath the screen (snap-off distance) (Fig. 4.9), thus, no problems with loss of stoichiometry can occur.

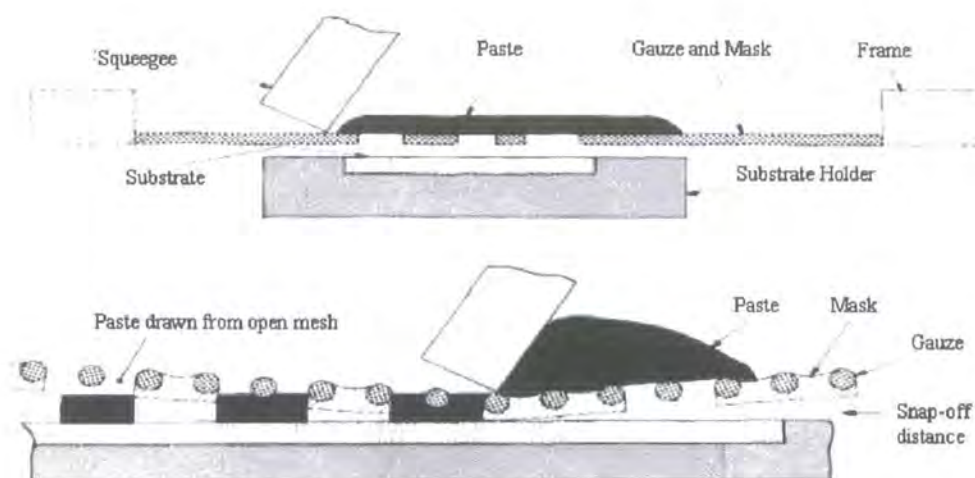


Fig. 4.9 Basic principle of the screen-printing technique, [13]

As can be seen from Fig. 4.9, the paste is first placed on a framed screen consisting of gauze and mask. By applying a print stroke with a squeegee blade the screen is pressed on the substrate and the paste in front of the squeegee blade is forced into the

meshes of the screen. Behind the squeegee the screen snaps off the substrate to its original position, leaving the paste sticking to the substrate. If the paste rheology is correct, it spreads out over the substrate to form an even layer [14], which implies that the viscosity of the paste has to match several conditions. The viscosity must be high enough to avoid the paste dropping through the meshes when distributed on the screen before printing (see Fig. 4.9). Conversely, if any forces are applied to the paste in terms of a shear rate during the print stroke, the paste has to exhibit a lower viscosity in order to move through the screen easily and “flow” together on the substrate to form an even layer (LEVELLING) (Fig. 4.10) [15]. Within a few seconds the paste must regain its original viscosity to form a durable and stable film. Fluids displaying this sort of time-dependent behaviour are called thixotropic.

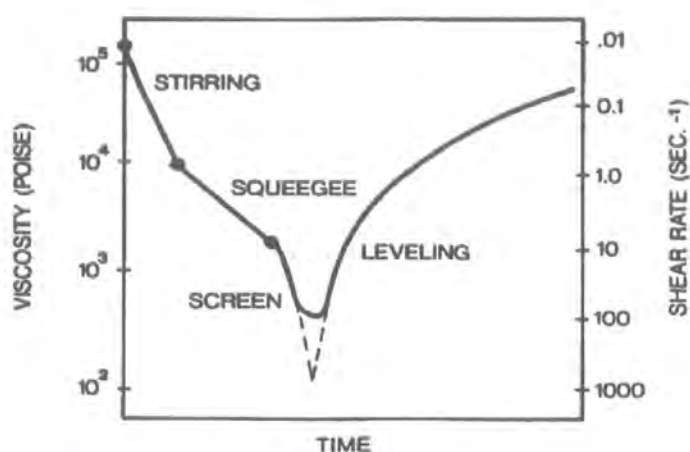


Fig. 4.10 Applied shear rates and viscosity changes during screen-printing, [15]

This specific paste rheology can be obtained by the appropriate mixture of suitable solvents and binders in the vehicle and the solid loading.

Furthermore, a glass phase can be added as well to improve the microstructure of the printed films. After printing a heat treatment is required to evaporate the organic

additives of the vehicle resulting in a sintered film of the original source powder composition (and possibly an additional glass phase). The inclusion of a glass phase allows liquid phase sintering to occur, as at sufficiently high temperatures ($T > 600^{\circ}\text{C}$) the viscosity of the glass becomes low and it can flow between the grains by capillary action. On cooling, this results in a highly compacted film. Adhesion to the substrate is usually improved as well, particularly where Al_2O_3 substrates are used, which also contain a glass phase.

4.3.2. The screen-printing screen

The screen is a crucial element in the screen-printing processes and it is essential to optimise its dimensions and parameters [14]. The screen mesh can be regarded as a volumetric measurement container determining the film thickness.

After printing, the film thickness reduces due to the evaporation of the solvents and densification, but knowing the solid loading of the printing paste this shrinkage can be estimated.

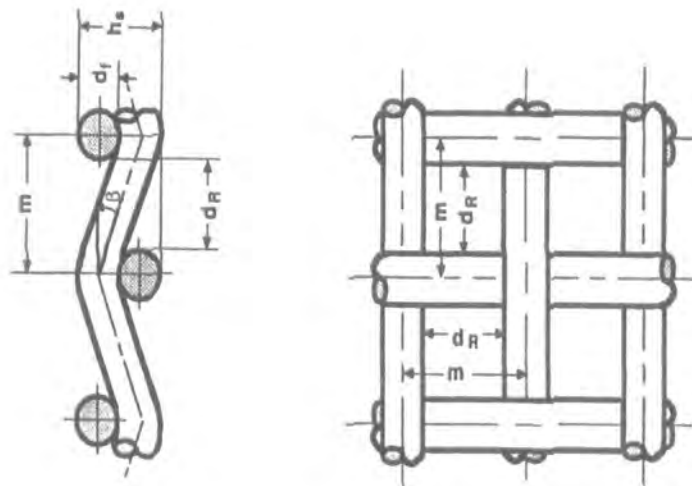


Fig. 4.11 Screen parameter, [14]

Fig. 4.11 shows the main screen parameters from which the theoretical film thickness h_{no} can be calculated. d_f is the thread diameter and m the mesh size. The theoretical film thickness h_{no} is given by :

$$h_{no} = 2d_f \left[1 - \left(\frac{2d_f}{m} - \frac{d_f^2}{m^2} \right) \right]; \quad 4.9$$

During the printing process, a restoring force is necessary for the screen to snap off the substrate and therefore elastic screen materials are used, such as nylon, stainless steel or polyester [16]. With a stainless steel screen a higher resolution of the printing pattern can be achieved, but it can be destroyed easily by applying too high a squeegee force. For a polyester screen this is not the case, but the resolution of the printed pattern is lower.

4.3.3. The screen-printing process

In order to produce an optimum printing paste, resulting in dense and even $\text{NiMn}_2\text{O}_{4+\delta}$ films, several components were added to the source powder. Two types of printing pastes were used, in one, $\text{NiMn}_2\text{O}_{4+\delta}$ powder was mixed with the vehicle, containing organic solvents and organic binder only, and in the second a glass powder and an organic dispersing agent were included additionally.

Table 4.8 shows the compositions of the two pastes before and after the heat treatment.

Table 4.8 Composition of the printing pastes in wt%, [3]

	Before thermal treatment/ Paste without glass	After thermal treatment/ Paste without glass	Before thermal treatment/ Paste with glass	After thermal treatment/ Paste with glass
Dispersing agent	-	-	0.85 %	-
Glass	-	-	6.8 %	8%
Vehicle	15 %	-	15 %	-
NiMn ₂ O ₄ powder	85 %	100 %	77.35 %	92%

For the second set of samples the grains of the pure NiMn₂O_{4+δ} source powder were covered with the commercial dispersing agent “Hypermer” (ICI Surfanctants, Hypermer LP1), which was dissolved in ethanol as a carrier liquid and mixed thoroughly with the NiMn₂O_{4+δ} powder using an ultrasonic probe (KLN, 250/101). The ethanol was then evaporated in an evacuated rotating evaporator (Heidolph, VV200) and the glass phase included by mixing a glass powder (ESL Europe, code 428) to the Hypermer-covered NiMn₂O_{4+δ} grains.

Next, for both sets of samples the powder was dispersed in the vehicle (ESL Europe, type 403) using a petri dish and a spatula, and possible agglomerates destroyed by drum milling (Otto Hermann, 2/7533). The progress was monitored periodically by determining the size of major agglomerates with a grindometer (Simex, PF 50/2) until they were < 10 μm.

The optimised pastes were printed through a 115T-mesh polyester screen onto Al₂O₃ substrates (CeramTec AG, thick film quality Rubalit 708) using a manual screen-printer (DEK, Model 240). The Al₂O₃ substrates contained a glass phase (~ 4%), so stronger bonding of the films to the substrates was achieved for glass containing printing pastes.

For the screen-printing process the optimum distance between screen and substrate (snap off distance) was found empirically to be ~1.5 mm and the printing process was optimised by varying the viscosity of the paste by adding different amounts of vehicle. The optimum viscosity was ~ 10 Pa· s as determined using a viscosimeter (Paar Physica, UDS 200) and Table 4.8 shows the corresponding paste compositions. After printing, the organic components of the films were thermally decomposed (100°C -330°C) and the films sintered at 850°C for 30 min to achieve densification and strong film – substrate bonding. The heat exposure for the heat treatment was minimised in order to prevent extensive grain growth in the printed films, which leaves holes and pores on the film surface as large grains merge together. The phase purity of the printed and fired films was assessed by XRD analysis, while the morphology was examined using SEM (Cambridge Instr., model S250 MK3) and laser profileometry (UBM Messtechnik).

4.3.4. XRD analysis of screen-printed films

Screen-printed films with and without glass phase were examined by XRD analysis after the thermal treatment. For the scans shown in Fig. 4.12 the data was smoothed, the alpha2 intensity stripped out and the background subtracted using Powder-X software [17].

The phase purity of the printed and fired films is clearly demonstrated in the spectra given and for both types of film, with and without glass and dispersing agent, no peak was present which could not be assigned to either $\text{NiMn}_2\text{O}_{4+\delta}$ or the Al_2O_3 substrate material. This is a clear indication for the phase purity of the fired films and it may be concluded that no chemical reactions between $\text{NiMn}_2\text{O}_{4+\delta}$ and the glass

phase or the substrate material had occurred. The films with glass and dispersing agent showed slightly broader XRD peaks, which could be due to increased strain in the crystal or a smaller average grain size. In the next section it will be shown that the latter was the case.

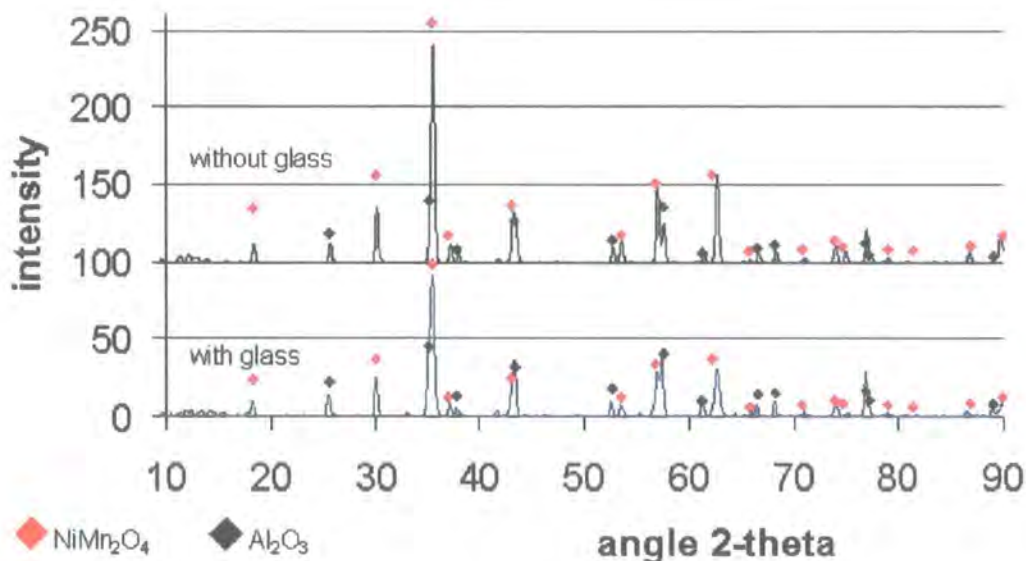


Fig. 4.12 XRD scans for screen printed films, with and without glass phase

4.3.5. Scanning Electron Microscopy (SEM) and surface profilometry

The morphology of the screen-printed and fired films was assessed by SEM and laser profilometry.

The samples containing a glass phase and dispersing agent showed a denser and smoother surface with a lower average grain size. The SEM pictures given in Fig. 4.13 and Fig. 4.15 show the difference in the surface density and the average grain size clearly. It may be concluded that the glass phase contracted the grains during the sintering process leading to a surface with fewer holes and pores. The glass exhibited

a low viscosity at temperatures over 600°C and liquid-phase-sintering occurred enabling a rearrangement of the grains. This is demonstrated in Fig. 4.14 and Fig. 4.16, which show the laser line scans over the surfaces of films prepared with and without glass phase.



Fig. 4.13 SEM image for a film with glass phase, fired at 850°C for 30 min

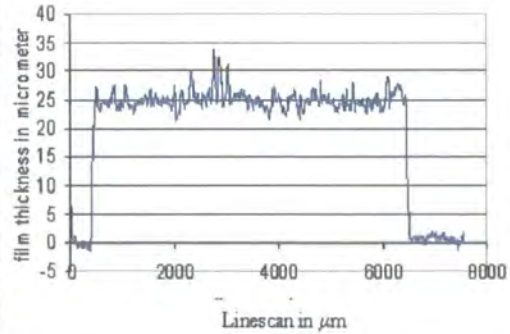


Fig. 4.14 Laser line scan for a film with glass phase, fired at 850°C for 30 min

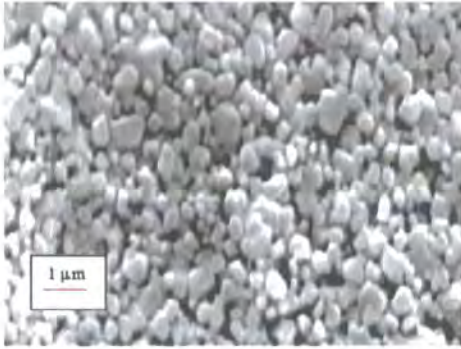


Fig. 4.15 SEM image for a film without glass phase, fired at 850°C for 30 min

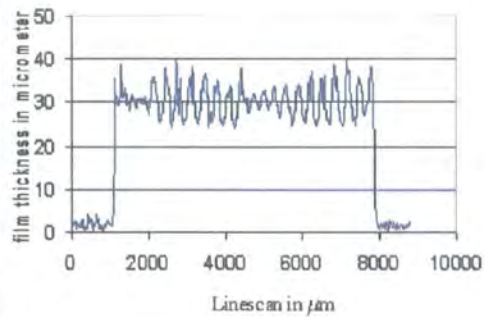


Fig. 4.16 Laser line scan for a film without glass phase, fired at 850°C for 30 min

As can be seen, the surface of the glass containing film was much smoother. The film thickness of the glass containing sample was lower, indicating that the glass phase did result in an improvement of the particle packing as intended, leading to a denser film. The sample with glass was about $25\ \mu\text{m}$ thick, the one without glass $\sim 30\ \mu\text{m}$.

4.4. Conclusions

In this chapter the $\text{NiMn}_2\text{O}_{4+\delta}$ powder production by the thermal decomposition of $\text{NiMn}_2(\text{C}_2\text{O}_4)_3 \cdot 6 \text{H}_2\text{O}$ was described. Several powders decomposed at different temperatures for 6 hours each were examined by XRD analysis and a phase pure $\text{NiMn}_2\text{O}_{4+\delta}$ spinel phase was found for decomposition temperatures of 300°C – 375°C and 800°C - 850°C . At intermediate temperatures mixed phases of Mn_2O_3 and NiMnO_3 were found some of them containing a $\text{NiMn}_2\text{O}_{4+\delta}$ phase as well. Additionally, a small amount of an unpredicted Mn_3O_4 phase was detected at 550°C - 650°C . The percentages of all phases present were determined by Rietveld refinement analysis of the XRD spectra, which was also used to study variations in lattice parameter, lattice angles, atom position and grain size with decomposition temperature for each phase.

Decomposition at 300°C – 375°C resulted in a spinel phase with an average grain sizes of 3 nm – 10 nm. Applications as source powder for screen-printing processes seem promising or as target material for other deposition techniques such as sputtering or other PVD processes.

Source powder production for screen-printing processes by decomposing precursor oxalates at 850°C for 30 min was found to be most advantageous, whereby the heating rate was increased significantly in regions where no reactions would occur. The average grain size of this type of powder was determined using Rietveld analysis giving $0.17 \mu\text{m}$, compared to $0.30 \mu\text{m}$ for the powder decomposed at 800°C for 6 h.

The paste production, the screen-printing process and the post-printing heat treatment were reviewed and the phase purity of the printed films with and without incorporated glass phase was demonstrated by XRD analysis.

Previous results [3] have shown that the addition of a glass phase (5% wt.) lead to higher particle packing in the films and a smoother surface.

Generally, it may be concluded that screen-printing procedures provided reproducible phase pure $\text{NiMn}_2\text{O}_{4+\delta}$ thick films without loss of stoichiometry and a good surface morphology of the films.

4.5. References

1. Schmidt R., *Screen Printing of Coprecipitated NiMn₂O₄ for Production of NTC Thermistors*, 2001, Diploma Dissertation, Department of Material Science III, University of Erlangen-Nuremberg, Erlangen
2. Young R.A., ed. *The Rietveld Method*. IUCr Monographs on Crystallography 5, 1993, Oxford Science Publications, Oxford
3. Schmidt R., Stiegelschmitt A., Roosen A., Brinkman A.W., *Screen Printing of Coprecipitated NiMn₂O₄ for Production of NTC Thermistors*, Journal of the European Ceramic Society, 2003, **23**(10), p. 1549
4. Feltz A., Töpfer J., *Bildung von Defektspinellen und Phasenbeziehungen im System Ni_xMn_{3-x}O₄*, Zeitschrift fuer anorganische und allgemeine Chemie, 1989, **576**, p. 71
5. Tang X.-X., Manthiram A., Goodenough J.B., *NiMn₂O₄ revisited*, Journal of Less-Common Metals, 1989, **156**, p. 357
6. Wickham D.G., *Solid-phase equilibria in the system NiO-Mn₂O₃-O₂*, Journal of Inorganic Nuclear Chemistry, 1964, **26**, p. 1369
7. AXS B., *Topas*, 2000, Bruker AXS, Karlsruhe
8. <http://cds3.dl.ac.uk/dif/icsd/icsdm.htm>, ICSD crystallographic database,
9. Giacovazzo C., *The diffraction of X-rays by crystals*, in *Fundamentals of Crystallography*, Giacovazzo C., Editor, 1992, Oxford Science Publications, Oxford, p. 141
10. Boucher B.P., Buhl R., Perrin M., *Etude cristallographique du manganite spinelle cubique NiMn₂O₄ par diffraction de neutron*, Acta Cryst, 1969, **B25**, p. 2326
11. http://www.ncnr.nist.gov/programs/crystallography/software/icdd_search.html, JCPDS-ICDD crystallographic database,
12. van Duppen J., *Handbuch fuer den Siebdruck*, Lübeck, Verlag Der Siebdruck
13. Schmidt R., Basu A., Brinkman A.W., *Production of NTCR thermistor devices based on NiMn₂O_{4+δ}*, Journal of the European Ceramic society, **In Press**
14. Riemer E., *Ein Beitrag zur Untersuchung der physikalisch-technischen Grundlagen des Siebdruckverfahrens*, PhD Thesis, Fachbereich für Konstruktion und Fertigung, 1988, Berlin, Technische Universität Berlin

15. Trease R., Dietz R.L., *Rheology of pastes in thick-film printing*, Solid State Technology, 1972, **January**, p. 39
16. Franconville F., Kurzweil K., Stalneck S.G., *Screen: essential tool for thick film printing*, Solid State Technology, 1974, **October**, p. 61
17. Dong C., *Powder-X software*, Chinese Academy of Sciences, Institute of Physics, Beijing

Chapter 5

D.c. measurements of $\text{NiMn}_2\text{O}_{4+\delta}$ materials

5.1. Introduction	117
5.2. Theory	118
5.2.1. NNH model	118
5.2.2. VRH models	119
5.2.3. Analysis of Resistance vs. Temperature data	122
5.3. Experimental	125
5.3.1. Contacts	125
5.3.2. Low temperature regime measurements	126
5.3.3. Control software	128
5.3.4. High temperature regime measurements	132
5.4. Results	133
5.4.1. Electron-beam evaporated films	133
5.4.1.1. Thin films on Al_2O_3 substrates	134
5.4.1.2. Thin films on glass substrates	142
5.4.2. Screen-printed films	145
5.4.3. Pellets	148
5.4.4. Summary	150
5.5. Conclusions	152
5.6. References	155

5.1. Introduction

There has been extensive discussion in the literature concerning the model, which describes electrical conduction in NTCR spinel ceramic materials best. The latest contributions report on electron hopping either between neighbouring localised electron states only [1] or regarding the possibility of variable-range-hopping [2]. It has also been pointed out that there might well be a polaron associated with the electron hop [3].

The aim of this chapter is to clarify the type of conduction mechanism in $\text{NiMn}_2\text{O}_{4+\delta}$ for direct currents (d.c.) and resistance versus temperature (R - T) measurements were carried out as the means to achieve this.

In order to display the R - T characteristics in precise detail the accuracy of collecting R - T data was optimised by designing an appropriate computer-controlled data acquisition system. With this system, R - T data was collected for thin electron-beam evaporated and screen printed $\text{NiMn}_2\text{O}_{4+\delta}$ films, and bulk material in the form of pressed pellets over a low temperature regime of 77 K - 350 K (LTR). Measurements at higher temperatures of 300 K – 550K (HTR) were carried out manually.

The slopes of the R - T graphs were analysed in detail to assess, which of the various models was appropriate.

5.2. Theory

In chapter 2 a general expression describing hopping conduction was given (eq. 2.31):

$$\rho = \frac{36 k_B T \pi^3 \rho_V s^5 \hbar^4 \varepsilon_r^2 \varepsilon_0^2 a^4 \exp(\xi_C)}{e^6 n E_1^2 r_{ij}^4 \varepsilon_{ij}} ; \quad 5.1$$

5.2.1. NNH model

For NNH, r_{ij} and ε_{ij} in eq. 5.1 have to be replaced by the dominating hopping length r_C to a nearest neighbour and by the average activation energy ε_3 . Both parameters are temperature independent for NNH. The r dependent part of the percolation threshold ξ_C (eq. 2.11) can be separated and the second term in eq. 2.11, which is energy and temperature dependent, then fully describes the exponential temperature dependence.

$$\rho = C_1 C_2 k_B T \exp\left(\frac{\varepsilon_3}{k_B T}\right) ; \quad 5.2$$

with C_1 containing independent and C_2 material dependent constants. In MKSA units the constants are given by :

$$C_1 = \frac{36 \pi^3 s^5 \hbar^4 \varepsilon_0^2}{e^6} ;$$

$$C_2 = \frac{\rho_V \varepsilon_r^2 a^4 \exp\left(\frac{2 r_C}{a}\right)}{n E_1^2 r_C^4 \varepsilon_3} ; \quad 5.3$$

The charge carrier concentration n would be the concentration of contributing Mn⁴⁺ donor states on octahedral sites, assuming Mn³⁺/Mn⁴⁺ hopping only. If hopping to Mn²⁺ sites occurs as well, n is much more difficult to determine as Mn³⁺ cations would act as both donors and acceptors.

5.2.2. VRH models

For VRH the concentration n of contributing electron states in space varies with temperature as pointed out in chapter 2. n was determined explicitly using the parameterised DOS $g(\varepsilon)$ shown in eq. 2.20:

$$n = R \int_{\varepsilon_F - \varepsilon_{\max}}^{\varepsilon_F + \varepsilon_{\max}} g(\varepsilon) d\varepsilon = \frac{2R}{z+1} \frac{g'}{(\varepsilon')^z} \varepsilon_{\max}^{z+1} ; \quad 5.4$$

$g(\varepsilon)$ is the total DOS per unit energy and unit volume and R is the fraction of sites being donors. Assuming Mn³⁺/Mn⁴⁺ hopping only, this would be: [Mn⁴⁺]/ {[Mn³⁺] + [Mn⁴⁺]}. If hopping to Mn²⁺ sites occurs, R would be more difficult to determine.

In order to obtain a general expression for ρ , n from equation 5.4, $\varepsilon_{ij} = \varepsilon_{\max}$ from eq. 2.24 and $r_{ij} = r_{\max}$ from eq. 2.25 must be substituted into eq. 5.1. Simplification of the above substitutions gives:

$$\rho = C_1 C_2 (k_B T)^{2p} \exp\left(\frac{T_0}{T}\right)^p \quad 5.5$$

where C_1 are independent constants. C_2 are material specific constants, also dependent on the parameter z , i.e. the shape of the DOS. $p = (z+1)/(z+4)$. In MKSA units the constants are given by :

$$C_1 = \frac{288 \pi^3 s^5 \hbar^4 \epsilon_0^2}{e^6} ;$$

$$C_2 = \frac{\rho_V \epsilon_r^2 (2\epsilon')^z (z+1)}{E_1^2 R g'} \left[\frac{21.2}{a^3 g'} (\epsilon')^z (z+1) \right]^{-\frac{z+6}{z+4}} ;$$

$$T_0 = \frac{1}{k_B} \left(\frac{21.2}{a^3 g'} (\epsilon')^z (z+1) \right)^{\frac{1}{z+1}} ; \quad 5.6$$

The temperature dependence of the exponential and pre-exponential term in 5.5 is in agreement with the expressions given by Mansfield [4].

For an uniform DOS $z = 0$, $p = 1/4$, $\epsilon' = 1$ and $g' = g(\epsilon_F)$, with $g(\epsilon_F)$ being the DOS at all energies in real and energy space.

Basu et al. found by using STM/STS that the DOS $g(\epsilon)$ in NiMn₂O_{4+δ} has a parabolic shape and the parameter z would be 2. The resistivity in NiMn₂O_{4+δ} would then be described by the following expression:

$$\rho = 1.166 \cdot 10^{-30} \frac{\rho_V a^4 \epsilon_r^2}{E_1^2 R} \frac{(g')^{1/3}}{(\epsilon')^{2/3}} k_B T \exp\left(\frac{T_0}{T}\right)^{1/2}; \quad 5.7$$

where T_0 would be given by:

$$T_0 = 3.99 \frac{1}{k_B} \frac{(\epsilon')^{2/3}}{a(g')^{1/3}}; \quad 5.8$$

Setting $z = 2$ in expression 2.26 gives:

$$\epsilon_{\max} = (k_B T_0)^{1/2} (k_B T)^{1/2}; \quad 5.9$$

ϵ_{\max} clearly increases with increasing temperature according to $\epsilon_{\max} \sim T^{1/2}$.

A parabolic DOS might well be the manifestation of a Coulomb type gap around the Fermi level. Shklovskii and Efros [5] have proposed the following expression for the DOS in the presence of a Coulomb gap:

$$g(\epsilon) = \frac{3\epsilon_1^2 \kappa^3}{\pi e^6}; \quad 5.10$$

ϵ_1 is the energy of electrons with the zero level set to coincide with the Fermi level ϵ_F and $\kappa = 4\pi \epsilon_r \epsilon_0$. Comparison with eq. 2.20 indicates that ϵ_1 would correspond

to $|\varepsilon - \varepsilon_r|$, $z = 2$, ε' would be 1 and g' equals the constants in 5.10. Applying this specific parameterisation of $g(\varepsilon)$ to T_0 in eq. 5.8 gives :

$$k_B T_0 = \frac{\beta_1 e^2}{\kappa a} = \frac{\beta_1 e^2}{4\pi \varepsilon_r \varepsilon_0 a} ; \quad 5.11$$

where β is a numerical coefficient. Eq. 5.11 is in agreement with T_0 proposed by Shklovskii and Efros [5] for a DOS with a Coulomb gap present except that here $\beta_1 = 3.99$ rather than 2.8. In eq. 5.11 ε_r is the dielectric constant and a the effective Bohr's radius of the electrons participating on the hopping process.

5.2.3. Analysis of $R - T$ data

Direct current $R - T$ characteristics were measured for NiMn₂O_{4+δ} pellets, electron-beam evaporated and screen-printed films. For all three types of NiMn₂O_{4+δ} materials the $R - T$ data was analysed by a sophisticated procedure, developed by Shklovskii and Efros [5], and proved to be applicable to real systems by Zabrodskii [6]. The method enables the parameter $p [= (z+1)/(z+4)]$ to be determined and therefore to decide which VRH model provides a better description of the $R-T$ behaviour or if NNH occurs.

The starting point for the data analysis are the general VRH and NNH models from eq. 5.2 and 5.4 given in generalised form. It is believed that all other models described in section 2.5.9. are lacking theoretical justification and have not been considered.

$$R = C T^{2p} \exp\left(\frac{T_0}{T}\right)^p ; \quad (\text{VRH}) \quad 5.12$$

$$R = C T \exp\left(\frac{T_0}{T}\right) ; \quad (\text{NNH}) \quad 5.13$$

First, VRH (eq. 5.12) will be considered. Taking the natural logarithm of 5.12 gives:

$$\ln R = \ln C + 2p \ln T + \left(\frac{T_0}{T}\right)^p ; \quad 5.14$$

It is useful to define the parameter W :

$$W = \frac{1}{T} \frac{d(\ln R)}{d(T^{-1})} = -2p + p\left(\frac{T_0}{T}\right)^p ; \quad 5.15$$

W was calculated by differentiating 5.14 according to $d(\ln R)/d(\ln T^{-1})$. Note that W can be regarded as the slope of the $\ln R$ vs. $1/T$ plot multiplied by T^{-1} .

The following assumption can be made to a good approximation:

$$|-2p| \ll p\left(\frac{T_0}{T}\right)^p ; \quad 5.16$$

At a later stage in this chapter at the results section it will be shown that this assumption was a good approximation for the data obtained. By neglecting $|2p|$, the natural logarithm of W is given by:

$$\ln W \cong \ln p + p \ln T_0 - p \ln T = C^* - p \ln T ; \quad 5.17$$

C^* comprises all parameters independent of temperature T . By calculating $\ln W$ from the data obtained and plotting $\ln W$ vs. $\ln T$ the slope of the graph equals $-p$.

It can be shown readily that using the same approach for the NNH in eq. 5.13 the plot $\ln W$ vs. $\ln T$ would exhibit the slope -1 , if the following assumption is made:

$$|-1| \ll \frac{T_0}{T} ; \quad 5.18$$

Clearly, by plotting $\ln W$ vs. $\ln T$ the parameter p can be determined independently of the pre-exponential factor providing a way to discriminate between the VRH models ($p = 0.5$ or $p = 0.25$) and the NNH model ($p = 1$). The characteristic temperature T_0 of the models in 5.12 and 5.13 can be determined from the slope of a $\ln(R/T^{2p})$ vs. $1/T^p$ plot for VRH and from a $\ln(R/T)$ vs. $1/T$ plot for NNH. For a NNH model T_0 is directly connected to the average activation energy by $\varepsilon_3 = k_B T_0$. For VRH the activation energy changes with temperature and is connected to T_0 via eq. 2.26.

5.3. Experimental

5.3.1. Contacts

In order to measure the R - T characteristics by two-point-measurements, two contacts were deposited onto the films and pellets. It was necessary to ensure that the work function of the contact material was lower than for $\text{NiMn}_2\text{O}_{4+\delta}$ in order to avoid a Schottky barrier forming at the contact-sample interface [7]. Aluminium contacts were found to lead to Ohmic behaviour, so for each film two aluminium point contacts of 1 mm diameter and a distance of 7 mm apart were evaporated onto the film surface using a standard coating unit (Edward Ltd., USA, model 6E4). For the pellets the circular surface areas on both sides were fully covered and the edges polished to remove any possible traces of aluminium, which could short-circuit the pellet.

The contacts were covered with quick drying silver paint (Agar Scientific Ltd., UK) immediately after deposition in order to avoid oxidation of the aluminium. The silver paint was allowed to dry in air overnight. Two copper wires were soldered to the contacts and ohmic behaviour was confirmed over the temperature range of interest by measuring the voltage vs. current (I/V) characteristics using a programmable electrometer (Keithley Instruments, 617 programmable electrometer) operating in “ohms I/V “ mode. In Appendix D the $I - V$ characteristics at 3 representative temperatures (350 K, 293 K, 150 K) are given explicitly. They were recorded by applying voltages between 0.5 – 100 V, which showed linear current responses at 350 K and 293 K.

5.3.2. Low temperature regime (LTR) measurements

For R - T measurements between 77 K and 350 K the samples were placed in the cryostat system (Oxford Instruments Ltd., DN1704) shown in Fig. 5.1.

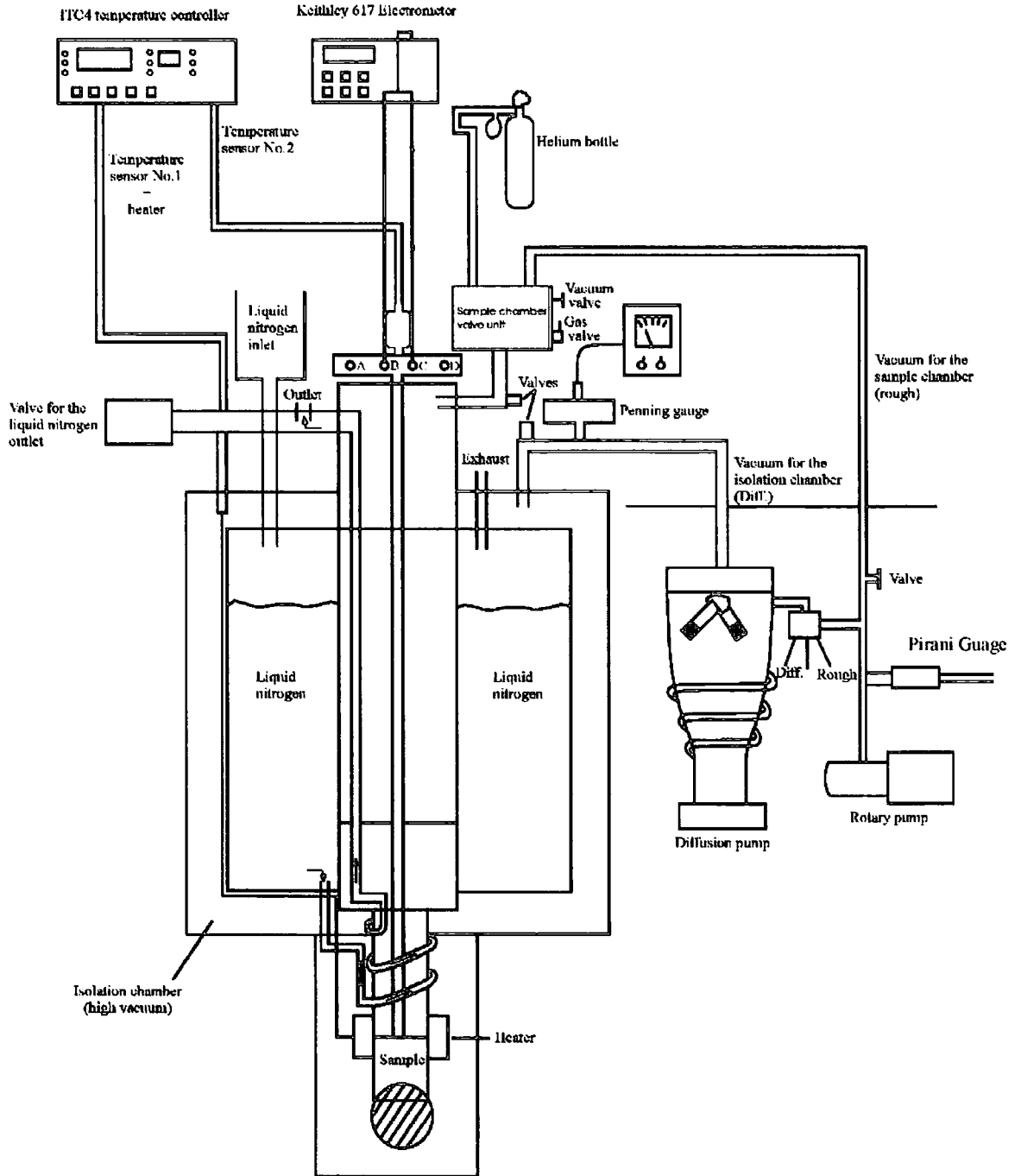


Fig. 5.1 Cryostat system used for two-point R - T measurements

The two contacts on the sample were connected to the electrometer (Keithley Instruments, 617 programmable electrometer), operating in “Resistance “ mode, via the sample holder, which was equipped with four pins, each connected to the electrometer via coax cables. The accuracy of the electrometer was $\pm 2\%$ as an upper limit. The resistance between the pins on the sample holder of the cryostat was determined to be $\sim 1 \cdot 10^{11}$ Ohm. Therefore, reliable measurements could be taken up to $\sim 1 \cdot 10^{10}$ Ohm with a leakage current $< 10\%$.

The cryostat system was linked to a temperature controller (Oxford Instruments Ltd., ITC4) capable of setting and controlling the temperature in the sample chamber by resistive heaters embedded in a heat exchanger block attached to the sample chamber. Liquid nitrogen from an isolated reservoir was passed around the sample chamber to provide cooling and the temperature created by this interplay of resistive heater and liquid nitrogen was measured using a standard Pt resistance thermometer (sensor 1). The accuracy was ± 0.2 K as an upper limit.

The exact temperature of the sample could be measured using a second platinum resistance thermometer inside the sample chamber placed right beneath the sample (sensor 2), also connected to the temperature controller.

The sample chamber was evacuated before measurements by a rotary pump to remove moisture and dust particles and was then flushed with helium gas. The procedure was repeated several times and the measurements were then conducted with the sample chamber filled to enable good heat exchange.

The temperature controller was connected to a personal computer (PC) via a RS232 data line and the Electrometer via an IEEE interface as can be seen in Fig. 5.2. IEEE hardware was installed on the PC for this purpose (Keithley, KPC-488.2 IEEE – 488EX interface) accompanied by the appropriate software (Keithley, GPIB CEC

488 drive) to access the interface from a VisualBasic6.0 program, which allowed automated data acquisition as described in the next section.

The RS232 connection was established over the RS232 port of the PC and no additional software was required as VisualBasic6.0 has an integrated function enabling access to a RS232 port.

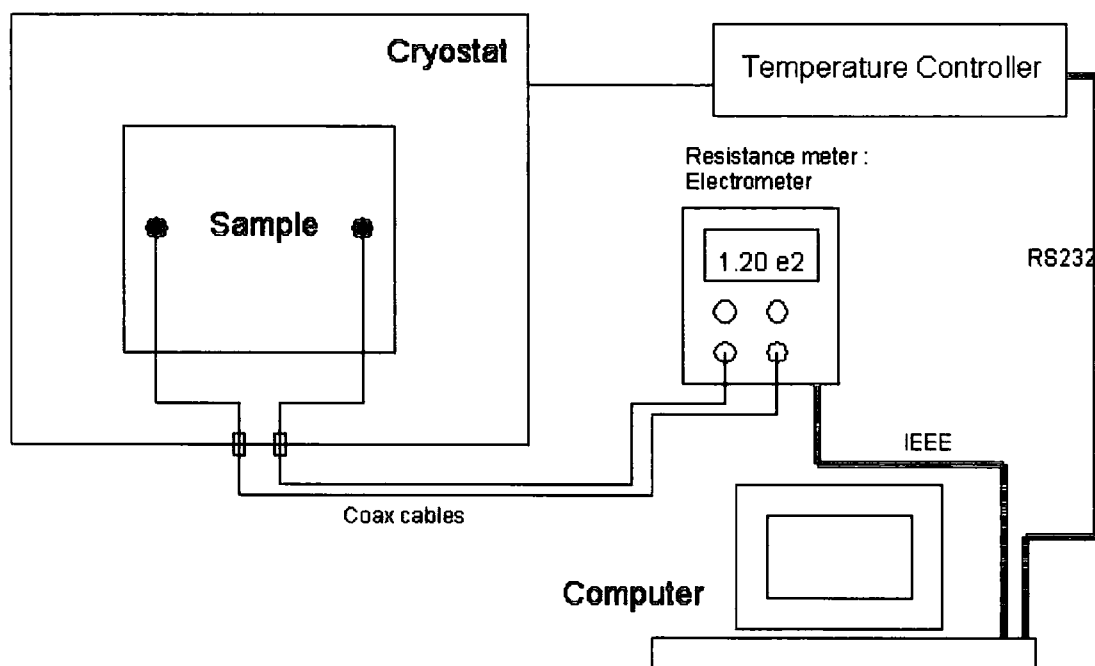


Fig. 5.2 Principle of computer controlled two-point measurements

5.3.3. Control software

The computer program consisted of two main components. A data input section allowed the user to set the measurement parameters and the second control section carried out the measurement allowing the user to monitor the experiment on two R - T

output graphs on different scales. The basic schematic principle underlying the program is depicted in Fig. 5.3 and is listed in full in Appendix E. As indicated, the program follows consecutively several stages with associated windows.

First, the user is informed in detail about the experimental set-up, how to connect the sample and to flush the sample chamber with helium (**Introduction**). Fig. 5.1 is shown in this section.

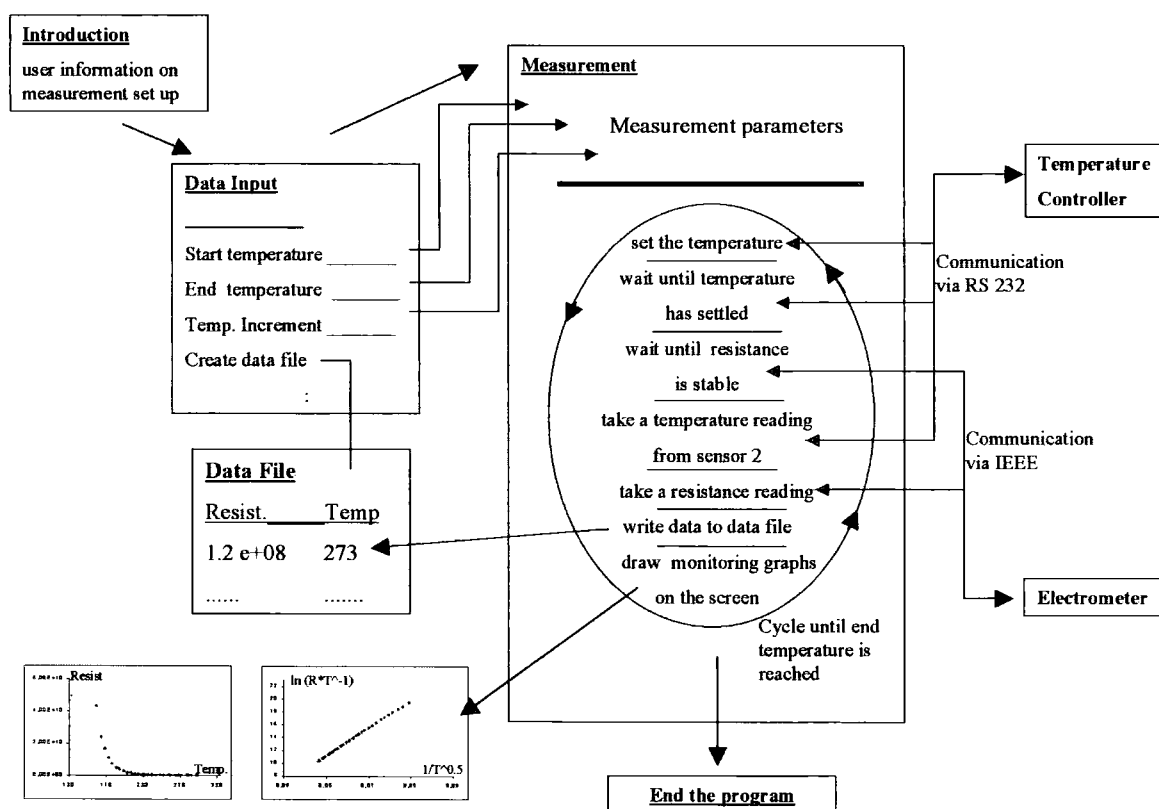


Fig. 5.3 Schematic principle of the computer program

The second window (**Data Input**) allows the user to provide details of the measurement procedure; the start and end temperatures of the measurement, the temperature increment, i.e. the temperature interval between 2 measurement points, and the name and path of the data file.

Another option (not shown in Fig. 5.3) provides a selection of measurement programs, which allow the resistance to be measured during cooling down or heating, or during a cooling and heating cycle or vice versa. The conduction mechanism expected can be specified to adjust the scale of the logarithmic monitoring plot, by specifying the parameters A and B in the following equation :

$$R = C T^A \exp\left(\frac{T_0}{T}\right)^{\frac{1}{B}} \quad 5.19$$

The monitoring plots are shown on a linear scale (R vs. T) and also on a logarithmic scale $\ln(R/T^A)$ vs. $(1/T)^{1/B}$, enabling the user to assess the linearity of the graph and thus the validity of the model chosen.

The program performs several steps to ensure a stable temperature and resistance reading. The first step in the measurement cycle is to set the temperature of the heat exchanger block via sensor 1. In order to ensure complete stability, the program takes pairs of readings from sensor 1, 3 seconds apart. Only if these two readings do not differ by more than 0.5 Kelvin and are within 1 Kelvin from the set temperature is the next step initiated, otherwise the program repeats the readings after 1 minute.

Once the reading from sensor 1 is stable, the program takes a reading from sensor 2 and the heat exchange is regarded to be accomplished if the readings from sensor 1 and sensor 2 do not differ by more than 3 Kelvin, which can take several minutes.

The temperature of sensor 2 is determined by taking 3 readings at 3 second intervals and it is ensured that the values do not differ by more than 0.5 Kelvin to guarantee temperature stability.

The stability of resistance is then assessed by taking two resistance readings from the sample within 9 seconds to ensure that they do not differ by more than 1%. This is to account for a possible response time of several seconds that NiMn₂O_{4+δ} sensors are expected to exhibit, i.e. a change in temperature is not instantly reflected by a change of resistance. However, experience indicated that the limiting factor would be the response of the Electrometer and it took about 1 or 2 minutes until the electrometer reading stabilised following a change in resistance.

In taking a ‘single’ measurement of resistance, the program actually carries out 30 resistance readings, all within about 2 seconds, and averages the reading in order to eliminate statistical effects and to significantly reduce the uncertainty in the resistance under 2%.

When the temperature and resistance readings are stable, one temperature reading from sensor 2 and a resistance reading (an average of only 20 readings now) are taken in short sequence. The data is written to the data file (**Data File**) and the two monitoring graphs updated, changing the scale of the axes if necessary.

The program then sets the next temperature and the process is repeated until the end temperature is reached. The program can be finished by the user on the “**End the program**” window. The user also has the option of terminating the program at any time, either after completing the current temperature cycle or immediately. In both cases the data obtained so far is available in the data file.

It is believed that the procedures employed to ensure thermal equilibrium, stable resistance and minimisation of statistical errors, resulted in high accuracy in the *R-T* measurements, which was achieved by fully exploiting the advantages of automated data acquisition.

5.3.4. High temperature regime (HTR) measurements

Additionally, two-point measurements were carried out at higher temperatures between 300 K and 550 K. For this purpose the samples were placed in a heat resistive PTFE sample holder with two stainless steel drop down contacts. A chromel-alumel thermocouple was connected to the sample holder allowing the top of the thermocouple to touch the sample surface and the whole arrangement was placed in an insulated furnace as can be seen in Fig. 5.4. The heater supply was controlled by a temperature controller (Eurotherm, UK, Cal 9900) linked to the thermocouple, such that the temperature was adjusted manually with an accuracy of ± 0.2 K. The resistance readings were then taken with the electrometer operating in “Ohms” mode. The inaccuracy of the device was corresponding to the LTR measurements below 2%.

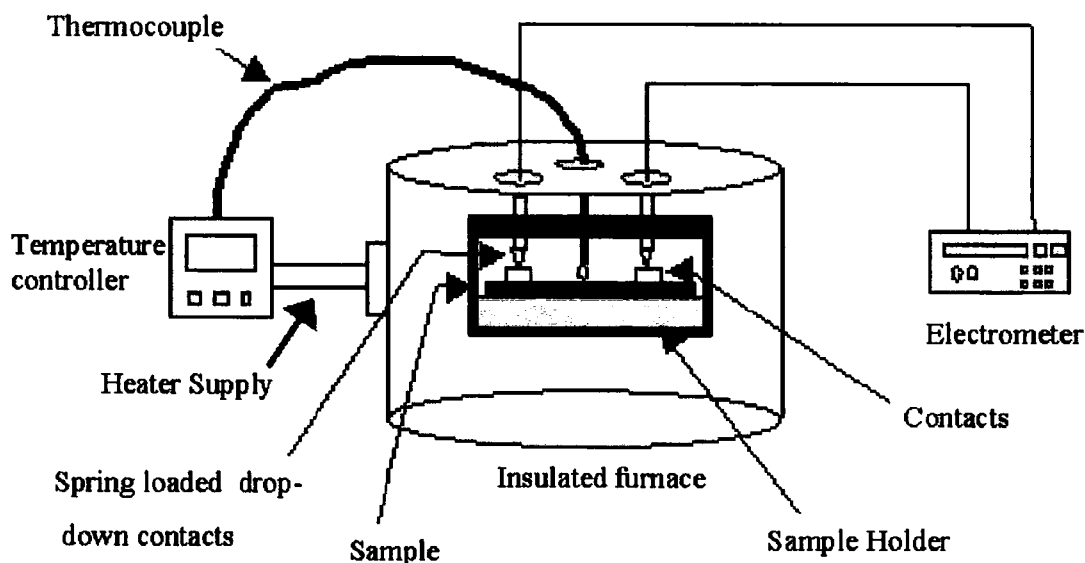


Fig. 5.4 Insulated furnace used for two-point R - T measurements

5.4. Results

R - T data for NiMn₂O_{4+δ} electron-beam evaporated and screen printed films, and for pressed pellets as a reference for bulk materials, were examined using the p -factor analysis described in section 5.2.3. The respective trends are presented in detail for each type of NiMn₂O_{4+δ} material separately. The experimental uncertainty in the temperature measurement was $\sim \pm 0.2$ K, which was too low to be displayed as error bars in any of the subsequent graphs in this chapter. This was also the case for the uncertainty in the resistance R , which was estimated to be below 2%, for the LTR significantly. For the LTR measurements it was believed that the averaging over 20 resistance readings in order to obtain one accurate value lead to an effective reduction in the uncertainty in R far below 5%, as mentioned in section 5.3.3.

The growth of electron-beam evaporated films on different substrate materials was described in chapter 3, the production of screen-printed films with and without an incorporated glass phase in chapter 4. NiMn₂O_{4+δ} pellets were obtained from elsewhere [8] and were used here as a reference for the films. They were produced from NiMn₂O_{4+δ} powder, synthesized from the mixed oxalate route. The powder was pressed into pellets in a standard procedure, and the pellets were sintered at 1000°C for 24 hours, annealed at 800°C for 40 hours and then electrically characterised [8].

5.4.1. Electron-beam evaporated films

Thin electron-beam evaporated films grown on Al₂O₃ substrates with pre-digitated aluminium contacts (sample 1 and sample 2) and on soda lime glass slides (sample 3)

were examined. The p -values were determined from the slope of the best linear fit to $\ln W$ vs. $\ln T$ data, whereby the fit was performed using a least-squares fitting routine. The data was fitted to a linear line described by ($y = A + Bx$), where y would correspond to $\ln W$, x to $\ln T$ and B would give the negative p -value. Analysis of the intercepts A corresponding to C^* in eq. 5.17 was not carried out.

5.4.1.1. Thin films on Al_2O_3 substrates

The $\ln W$ vs. $\ln T$ plots of sample 1 in the as-deposited and post deposition annealed state are shown in Fig. 5.5. Annealing was carried out at 200°C, 300°C and 500°C for 30 min.

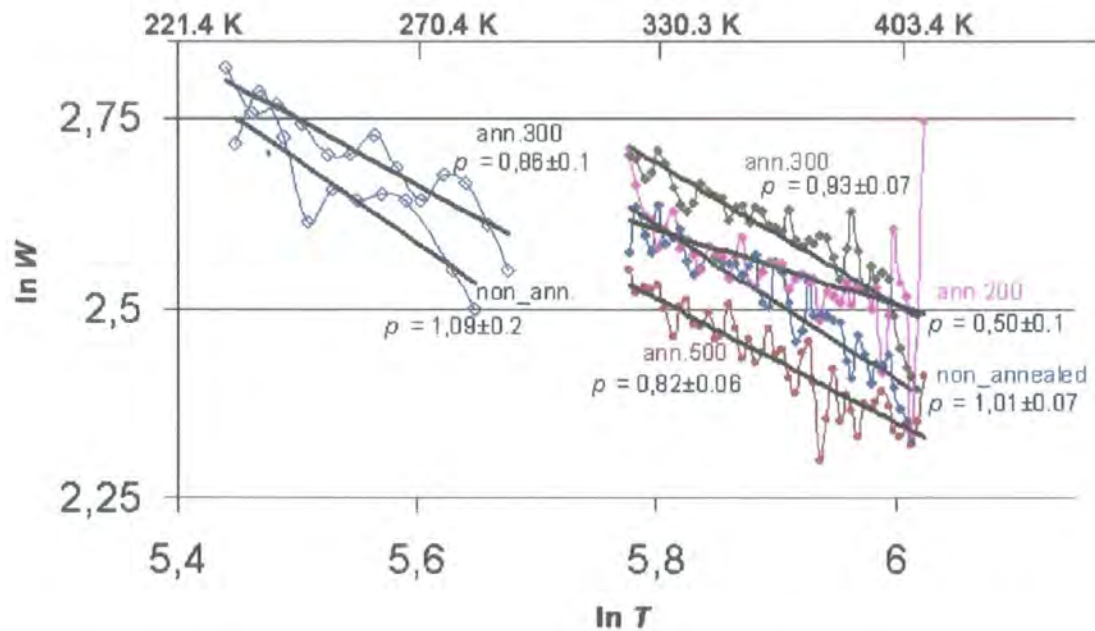


Fig. 5.5 $\ln W$ vs. $\ln T$ graphs for sample 1, annealed at different temperatures for 30 min, HTR and LTR

From Fig. 5.5 it may be concluded that conduction was by NNH as p tended to 1 for the HTR and the LTR, except when annealed at 200°C the specimen measured at the HTR showed a significant shift to a lower value of $p = 0.5$.

The uncertainty in p was calculated according to the definition given by Taylor [9] using the uncertainty σ_B in the B value from the linear least-square fitting routine. The values of $p \pm \sigma_B$ are shown in Fig. 5.5 for each graph and were all in an acceptable range. The uncertainty in p was higher in the LTR due to the lower number of data points and to a higher degree of scattering of the data points. Nevertheless, NNH was believed to be identified, with the exception of the sample annealed at 200°C, where p was close to 0.5, as expected for a VRH with a parabolic DOS. No physical explanation of this p -value seems reasonable and it may well have been subject to a systematic experimental error. The scatter in the data especially at higher temperatures was significant, possibly due to high temperature fluctuations during the measurement. Such high level of scatter reflects the fact that the curves are of differentiated data and therefore particularly susceptible to noise.

Fig. 5.5 shows that the alignment between the data obtained from the HTR and LTR was less than ideal. The contacts had been changed for measurements at different temperature regimes, but still the discrepancy was rather high and the experimental accuracy was open to question.

In Fig. 5.6 the $\ln W$ vs. $\ln T$ plots are given for sample 2, which seemed to display NNH as well, although the specimen annealed at 400°C (for 30 min) deviated slightly from the NNH value and the correspondence between high and low temperature data was again rather poor.

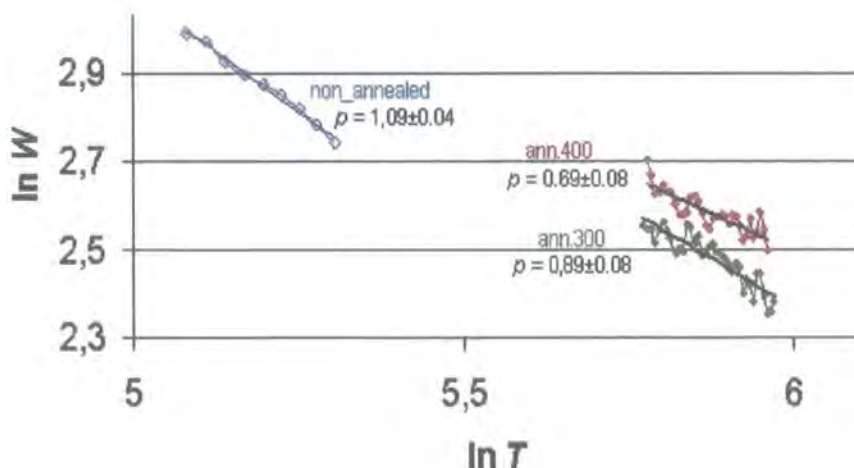


Fig. 5.6 $\ln W$ vs. $\ln T$ plots for sample 2, annealed at different temperatures for 30 min, HTR and LTR

Here the uncertainty in p was reasonably low again and despite the experimental uncertainties, a clear trend towards NNH was observed in sample 2 as well as in sample 1.

In section 5.2.3. it was noted that the p -analysis for NNH rested on the assumption that

$$|-1| \ll \frac{T_0}{T}; \quad 5.18$$

For the samples investigated in the LTR this was indeed a good approximation as T_0/T was in the range of 16.8 – 20.9. For HTR measurements the approximation was less good as T_0/T was 10.9 – 17.5. It is clear that especially at the HTR the p -value might contain a perceptible error, but it is believed that the approximation was good enough nevertheless to enable a clear distinction between different hopping mechanisms in both temperature regimes.

As sample 1 and sample 2 were believed to exhibit NNH, the R - T data were plotted on $\ln(R/T)$ vs. $1/T$ axes shown in Figs. 5.7 and 5.8.

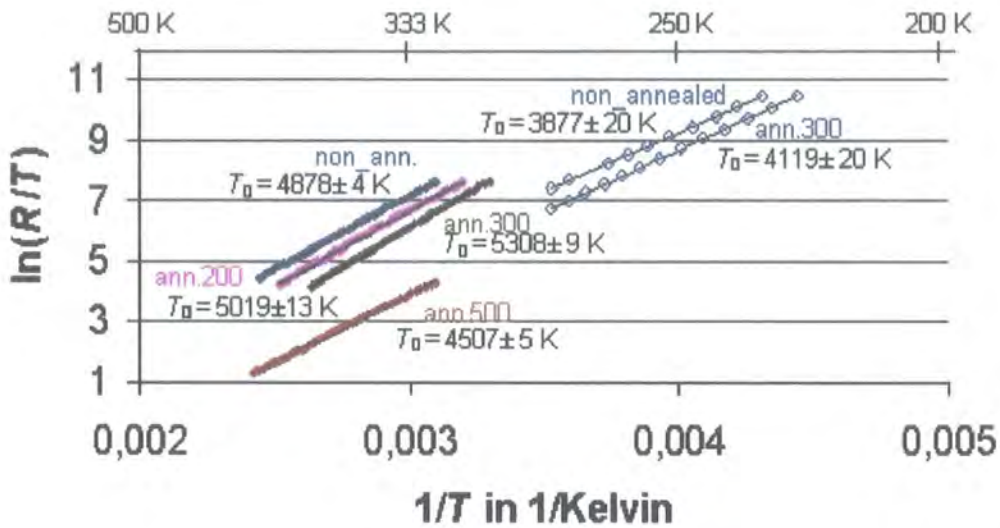


Fig. 5.7 $\ln(R/T)$ vs. $1/T$ for sample 1, annealed at different temperatures for 30 min, HTR and LTR; the graphs in the HTR for the films annealed at 200°C and 300°C were shifted by 0.0001 and 0.0002 on the $1/T$ axis for demonstration purposes

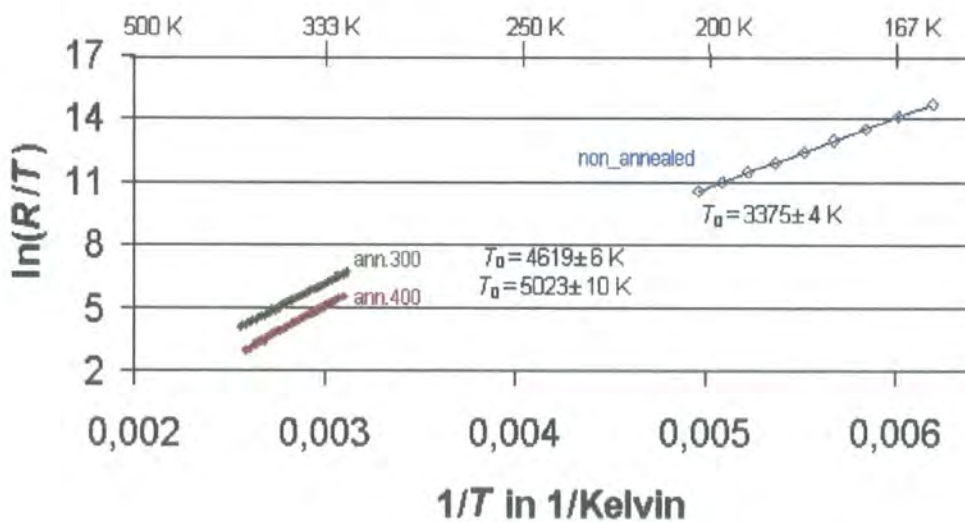


Fig. 5.8 $\ln(R/T)$ vs. $1/T$ for sample 2, annealed at different temperatures, HTR and LTR

In Fig. 5.7 it can be seen that the absolute conductivity at the HTR of the non-annealed, and the 200°C and 300°C annealed films were all comparable, despite the differences in T_0 , but a change in the conduction mechanism for the sample annealed at 500°C was obvious. Fig. 5.8 shows that sample 2 annealed at 400°C showed a modest increase in conductivity, too.

The characteristic temperature T_0 ($=\varepsilon_3/k_B$) was determined from the slope of the best linear fit to the graphs in Figs. 5.7 and 5.8 and the values obtained are summarised in Table 5.1. The fit was again performed using a linear least-squares fitting routine of the form ($y = A + Bx$), where y would correspond to $\ln(R/T)$, x to $1/T$ and B would give the characteristic temperature T_0 . The uncertainty in T_0 was calculated as the uncertainty in the B-value σ_B and is given for each graph in Figs. 5.7 and 5.8. It is shown that the σ_B values indicated an excellent fit, only in sample 1 at the LTR σ_B was slightly higher than desired.

Table 5.1 : Characteristic temperature T_0 in K and activation energy ε_3 (in brackets) in eV from $\ln(R/T)$ vs. $1/T$ plots

	LTR non-ann.	300	HTR non ann.	200	300	400	500
sample1	$3.9 \cdot 10^3$ (0.33)	$4.1 \cdot 10^3$ (0.36)	$4.9 \cdot 10^3$ (0.42)	$5.0 \cdot 10^3$ (0.43)	$5.3 \cdot 10^3$ (0.46)		$4.5 \cdot 10^3$ (0.39)
sample2	$3.4 \cdot 10^3$ (0.29)				$4.6 \cdot 10^3$ (0.40)	$5.0 \cdot 10^3$ (0.43)	

The T_0 and ε_3 values given in Table 5.1 are consistent with previous findings for bulk material. Brabers and Terhell [10] gave $\varepsilon_3 = 0.37$ eV for measurements between 385 K and 550 K and Feltz et al. [11] gave $T_0 = 3.8 \cdot 10^3$ K for temperatures of 273 K – 343 K.

From Table 5.1 it is obvious that the characteristic temperature T_0 showed generally higher values for the HTR than for the LTR. This shift in T_0 towards higher values with increasing temperature could indicate that conduction was transitional between NNH and VRH behaviour. Electron-beam evaporated films on glass substrates, screen printed films and pellets all exhibited VRH as discussed later, so in the films there might well be a limited VRH component, although the full mechanism was clearly better described by a NNH model as the p -values were close to 1. A VRH component would indeed lead to an increase of T_0 with increasing temperature, because the average activation energy in VRH increases according to $\varepsilon_{\max} \sim T^{1/2}$ (eq. 5.9). This explanation is supported by the fact that only 3 of a total of 9 p -values analysed were marginally higher than 1. All other p -values were lower than 1, some of them significantly.

Furthermore, it is obvious from Table 5.1 that the characteristic temperature T_0 also changed with annealing temperature, as is illustrated in Fig. 5.9.

In Fig. 5.9, T_0 was estimated at the HTR for sample 2 for the non-annealed state from the corresponding value at the LTR. For other samples T_0 seemed to be about 1000 K higher at the HTR than for the LTR as could be seen in Table 5.1. The uncertainties in the T_0 - values were small as mentioned above and could therefore not be displayed as error bars in the graphs shown in Fig. 5.9.

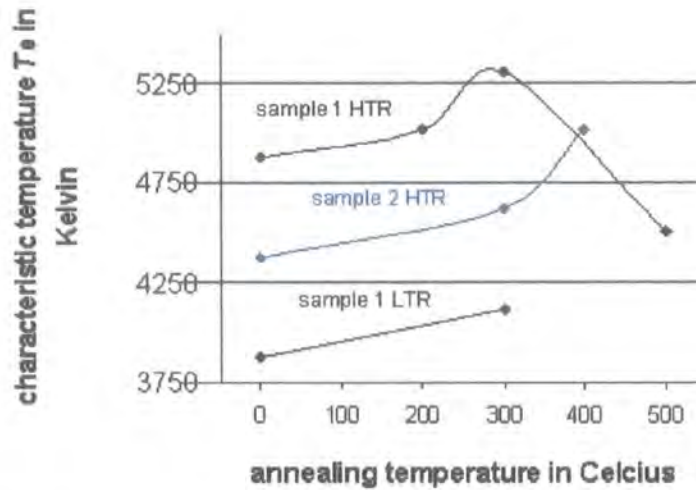


Fig. 5.9 Characteristic temperature T_0 vs. annealing temperature

It is clear that T_0 increased with increasing annealing temperature up to 400°C , which might be due to improved crystallinity at higher annealing temperatures, as demonstrated by the SEM images of sample 1, shown in chapter 3.4.4. It was believed that an amorphous-like phase may be present in the as-deposited state, and with improving crystallinity and the formation of the typical spinel phase the conduction mechanism might well be transitional. The grain growth seemed to be more pronounced at temperatures of $300^\circ\text{C} - 400^\circ\text{C}$, which is reflected by a non-linear increase of T_0 .

The activation energy could also be affected by a change in oxygen content δ in $\text{NiMn}_2\text{O}_{4+\delta}$ at different annealing temperatures, but the variations in ε_3/T_0 are rather high and may not be fully explained by this possible effect.

A significant reduction in T_0 was observed for sample 1 with an annealing temperature of 500°C and it is believed that this occurred due to phase transitions at higher temperatures and possibly a different grain structure. In chapter 2 it was pointed out that $\text{NiMn}_2\text{O}_{4+\delta}$ is not stable at temperatures in the range of $400^\circ\text{C} -$

700°C and at high annealing temperatures of 500°C NiMn₂O_{4+δ} may have decomposed to form NiMnO₃ and Mn₂O₃, resulting in a significant change in the electrical transport mechanism. This is supported by the fact that not only the characteristic temperature but also the absolute resistivity was reduced significantly compared to the other samples, as can be seen in Fig. 5.7. However, this trend is less clear in sample 2 annealed at 400°C, where the absolute resistivity decreased slightly, but no reduction in T_0 could be observed. It is believed that the phase separation initiated at 400°C and its effects were much weaker and reflected less conclusively than for the sample annealed at 500°C.

In addition to the T_0 values, the pre-exponential factors C (eq. 5.13) were determined as $\ln C$, corresponding to the A values ($y = A + Bx$) in the linear least-squares fit, together with their uncertainties σ_A calculated according to the definition given by Taylor [9]. The trend of $1/C$ vs. annealing temperature is displayed in Fig. 5.10. The uncertainties calculated were in the range of 1.2 % – 3.7 %, except for sample 1 at the LTR, where 7.6 % and 6.3 % was obtained, but still the values were too small to be displayed as error bars in Fig. 5.10.

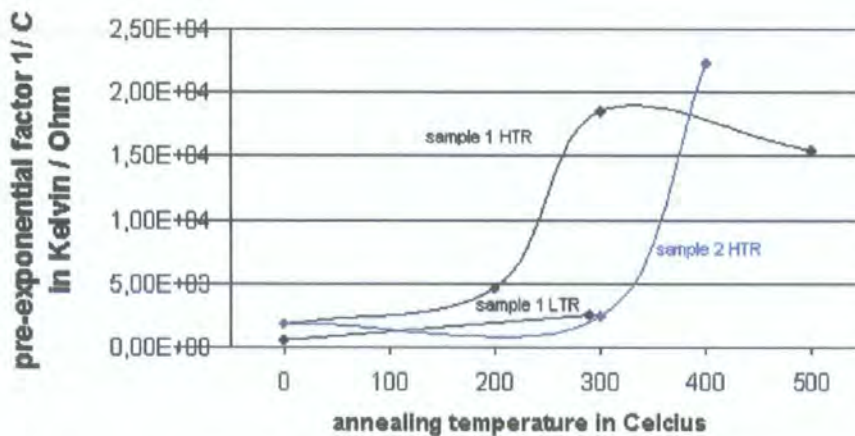


Fig. 5.10 Pre-exponential factor $1/C$ vs. annealing temperature

Comparison with Fig. 5.9 indicates that $1/C$ followed a similar trend observed for T_0 . This can be understood regarding eq. 5.3, where it can be seen that C is proportional to $1/\varepsilon_3$ ($T_0 = \varepsilon_3/k_B$). It may well be possible that non of the parameters in C (eq. 5.3, $C = C_1 \cdot C_2$) changed significantly with annealing temperature, except ε_3 . On the other hand, the ratio of the absolute values of $1/C$ seemed to be altered, suggesting that the parameters in C varied in the different samples.

5.4.1.2. Thin films on glass substrates

The $\ln W$ vs. $\ln T$ plots for sample 3, thin films grown on soda lime glass substrates, are given in Fig. 5.11.

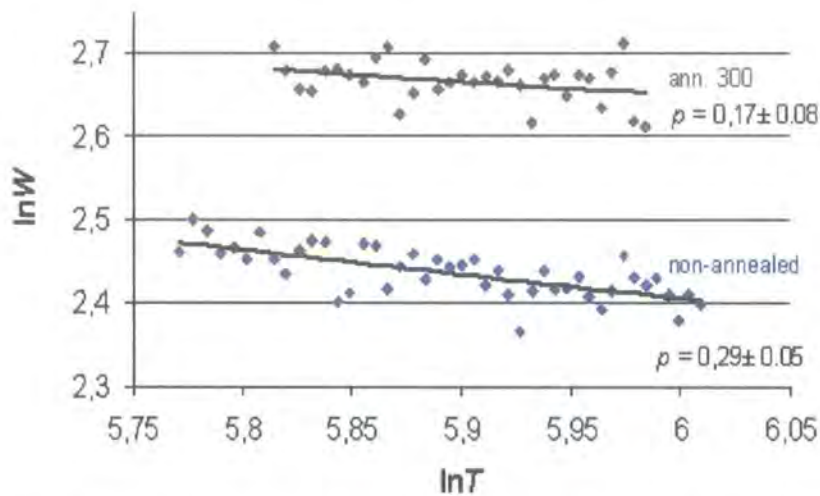


Fig. 5.11 $\ln W$ vs. $\ln T$ for sample 3, non-annealed and at 300°C for 30 min, HTR

Sample 3 exhibited p -values close to 0.25 suggesting that VRH with a constant DOS occurred. The uncertainty in p was low enough to exclude any ambiguities in identifying the conduction mechanism.

The p -value analysis for VRH rested on the assumption given in 5.2.3. :

$$|-2p| \ll p \left(\frac{T_0}{T} \right)^p ; \quad 5.16$$

With p being 0.25 the expression on the left hand side of 5.16 is 0.5 and for the samples investigated at the HTR the right hand side was in the range of 11.5 – 15.4, indicating that the approximation was valid.

The reason why conduction in sample 3 was by Mott VRH is not clear, but may reflect differences in possibly the film composition and crystallinity. The different substrate materials used or variations in the target temperature might be possible explanations for this. However, a change from NNH to VRH would imply that the differences mentioned lead to a reduction in the average distance between electron states r , and/or a variation in the shape of the electron wave functions dependent on a , as described in chapter 2.5.5./2.5.6. (eq. 2.8).

In this context it should also be considered that electron-beam evaporated films were nickel-rich and that the nickel content varied significantly between different samples in an uncontrollable way. An increase of nickel concentration would clearly reduce the manganese, or in particular the Mn³⁺ and Mn⁴⁺ concentration leading to a higher average distance between donors and acceptors, and NNH could then be favourable rather than VRH.

The corresponding $\ln(R/T^{0.5})$ vs. $1/T^{0.25}$ plots for sample 3 are given in Fig. 5.12.

The slope of the graphs represents the characteristic temperature according to $(T_0)^{0.25}$ and an increase in T_0 with annealing temperature can be seen, which is consistent with the previous findings for thin films exhibiting NNH. The slope B and the intercepts A were determined again by a linear least-squares fit, given in Fig. 5.12 as T_0 and C together with the uncertainties.

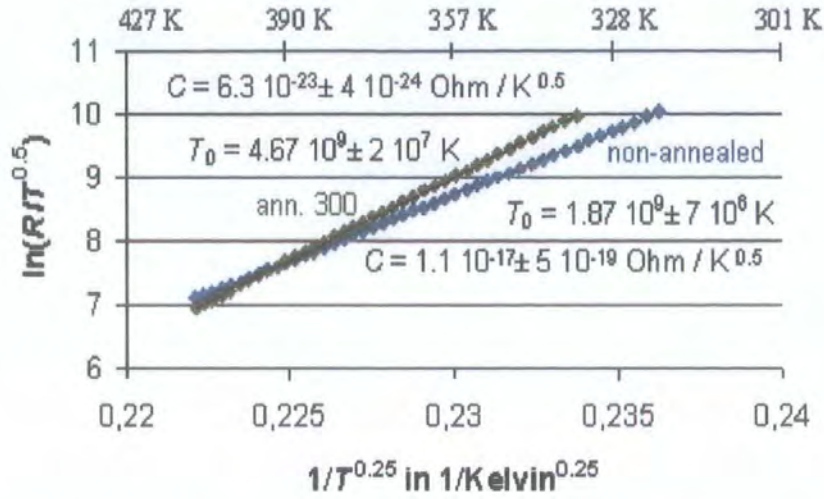


Fig. 5.12 $\ln(R/T^{0.5})$ vs. $1/T^{0.25}$ plots for sample 3, non-annealed and at 300°C for 30 min, HTR

For VRH with a constant DOS the characteristic temperature T_0 is connected to the uniform DOS $g(\varepsilon_F)$ as can be seen in eq. 5.6 . The explicit relation is

$$T_0 = \frac{1}{k_B} \frac{21.2}{a^3 g(\varepsilon_F)} ; \quad 5.20$$

In eq. 5.20, the upper limit of the Bohr's radii a can be obtained from a hard sphere model, where the radii of participating manganese cations on octahedral sites were given by 0.72 Å for Mn³⁺ (low spin) and 0.67 Å for Mn⁴⁺ as an upper limit [12]. In fact the radii may well be below these values and at the end of chapter 6.4.3. it will be shown that $a = 0.3$ Å is a reasonable estimation.

$g(\varepsilon_F)$ was then determined to be $4.87 \cdot 10^{21} \text{ cm}^{-3} (\text{eV})^{-1}$ for the non-annealed film and $1.95 \cdot 10^{21} \text{ cm}^{-3} (\text{eV})^{-1}$ for the film annealed at 300°C.

However, the $g(\varepsilon_F)$ values obtained are low compared to crystalline Ge at the conduction band edge, where $g(\varepsilon_F)$ is in the order of $10^{22} \text{ cm}^{-3} (\text{eV})^{-1}$ [13]. On the

other hand, the density of states in amorphous H-doped silicon at low temperatures in the impurity conduction regime is in the order of $10^{17} - 10^{18} \text{ cm}^{-3} (\text{eV})^{-1}$ [14], and the values obtained for NiMn₂O_{4+δ} are more close to the crystalline reference.

5.4.2. Screen-printed films

The p -factor analysis for screen-printed films clearly indicated that VRH occurred with a parabolic shape of the DOS $g(\varepsilon)$. The factors p were shown to be very close to 0.5, and the uncertainties in p were reasonably low. A p -value of 0.5 implies that $z = 2$ (i.e. $p = (z+1)/(z+4)$), where z describes the energy dependence of the DOS according to $g(\varepsilon) \sim \varepsilon^z$.

The $\ln W$ vs. $\ln T$ plots for screen-printed films with and without glass phase are given in Fig. 5.13. It can be seen that there was close agreement of the $\ln W$ vs. $\ln T$ plots for films with and without the glass phase and, unlike the electron-beam evaporated films, the correspondence in the data obtained at the LTR and HTR was very good.

It is interesting to note that the data for samples with glass phase was less scattered and more linear in the $\ln W$ vs. $\ln T$ graph, indicating that the R - T measurements for the samples with glass phase were more reliable.

Again, the p -value analysis rested on the assumption 5.16 given above. With p being 0.5 the expression on the left hand side of 5.16 is 1 and for the samples investigated at the LTR the right hand side was in the range of 12.4 – 18.8. For the HTR it was 9.2 – 12.5. Especially at high temperatures the p -value might display an error, but the conduction mechanism was again believed to be identified unambiguously.

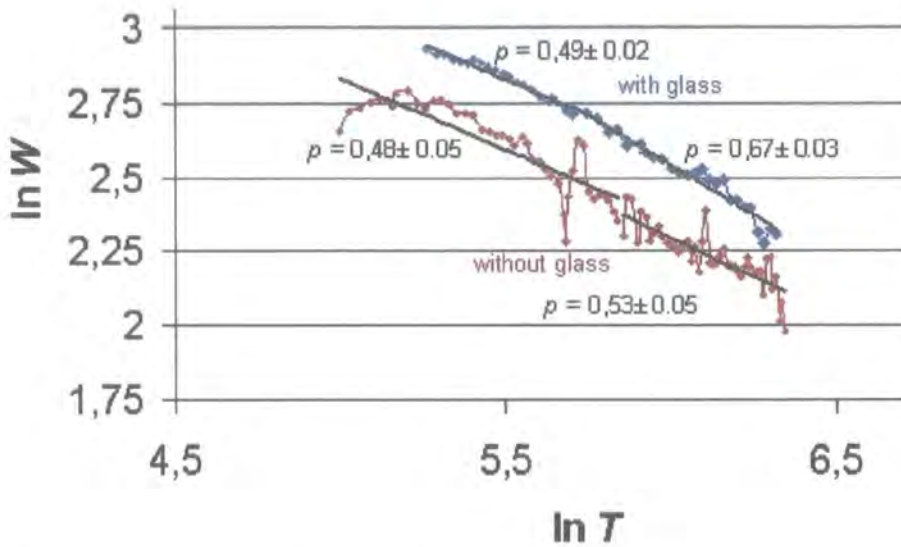


Fig. 5.13 $\ln W$ vs. $\ln T$ plots for screen-printed films, sintered at 850°C for 30 min, HTR and LTR, the graphs obtained for samples with glass are shifted by 0.25 on the $\ln W$ axis for demonstration purposes

The R - T data of screen-printed films was plotted as $\ln(R/T)$ vs. $1/T^{0.5}$ (appropriate for a VRH model with a parabolic DOS), as shown in Fig. 5.14.

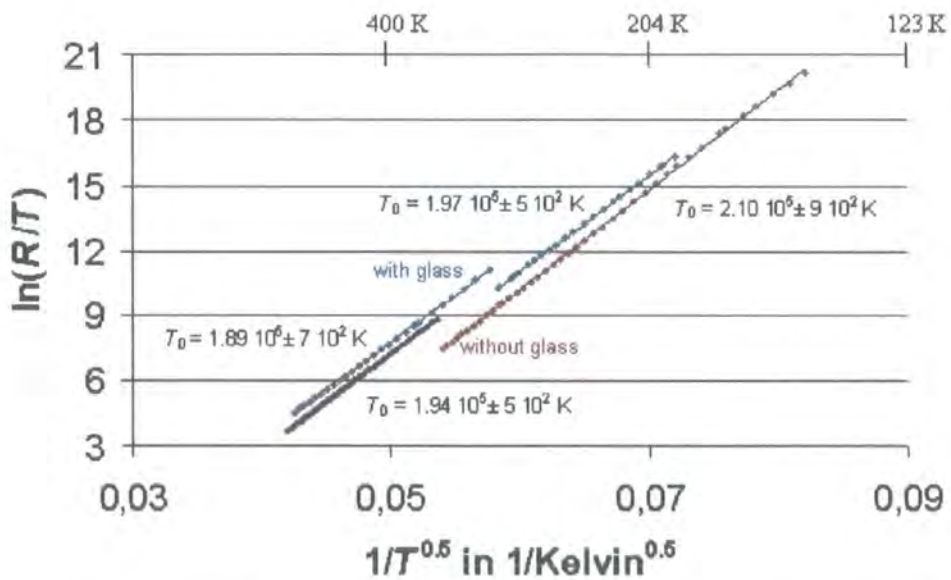


Fig. 5.14 $\ln(R/T)$ vs. $1/T$ plots for screen-printed films with and without glass phase, sintered at 850°C for 30 min, HTR and LTR

The resistance for samples with glass phase was about a factor of 2 higher than those without glass and presumably was a consequence of the low conductivity of the glass. The characteristic temperatures T_0 were determined from the slope of the graphs in Fig. 5.14 by least-squares fitting and are summarised in Table 5.2.

The values of T_0 were all similar regardless of whether a glass phase had been included, but a difference could be seen as T_0 decreased with increasing temperature regime.

Table 5.2 Characteristic temperature T_0 in K from $\ln(R/T)$ vs. $1/T^{0.5}$ plots

	LTR	HTR
with glass	$1.97 \cdot 10^5 \pm 4.5 \cdot 10^2$	$1.89 \cdot 10^5 \pm 7.0 \cdot 10^2$
without glass	$2.10 \cdot 10^5 \pm 8.7 \cdot 10^2$	$1.94 \cdot 10^5 \pm 4.7 \cdot 10^2$

If it is assumed that a Coulomb type gap in the DOS is present at the Fermi level, the product $\epsilon_r \cdot a$ can be determined from the characteristic temperature T_0 (eq. 5.11). The values for $\epsilon_r \cdot a$ obtained were 2.78Å – 3.09Å. As mentioned before, the upper limit for the Bohr's radii of Mn³⁺/Mn⁴⁺ cations participating on the hopping was 0.72 Å and 0.67 Å respectively, which leads to a lower limit for the dielectric constant ϵ_r in NiMn₂O_{4+δ}: $\epsilon_r \geq 3.9$.

The intercepts A of the linear least-squares fit in Fig. 5.14 were determined and the constant C (eq. 5.13) calculated, given in Table 5.3. It can be seen that C increases with increasing temperature regime, contrarily to the characteristic temperature T_0 , which confirms the notion that the pre-exponential factor C (eq. 5.12), here consisting of all pre-exponential constants in eq. 5.7, is proportional to $1/T_0$ (eq. 5.8).

Table 5.3 Constant C in Ohm / K from $\ln(R/T)$ vs. $1/T^{0.5}$ plots

	LTR	HTR
with glass	$1.7 \cdot 10^{-7} \pm 5.6 \cdot 10^{-9}$	$8.6 \cdot 10^{-7} \pm 3.5 \cdot 10^{-8}$
without glass	$3.1 \cdot 10^{-8} \pm 2.0 \cdot 10^{-9}$	$3.8 \cdot 10^{-7} \pm 9.7 \cdot 10^{-9}$

It is remarkable that the VRH model is still valid at higher temperatures, whereas in the literature VRH is reported to occur mainly as impurity conduction of semiconductors at very low temperatures only. It can be concluded that the first term on the right hand side in eq. 2.8 must be sufficiently small even at higher temperatures, which would require a small distance r_{ij} between acceptor and donor. The Mn³⁺ and Mn⁴⁺ concentration in NiMn₂O_{4+δ} is some orders of magnitude higher than any impurity concentration in semiconductors and r_{ij} would be indeed comparably small in consequence. This is consistent with the findings in section 5.4.1.2., where it was suggested that the DOS in thin films on glass substrates is several orders of magnitudes higher than in a typical semiconductor impurity conduction regime.

It might also be possible that electron hopping is influenced by double-exchange effects via oxygen atoms, which has been reported to occur in manganate perovskite structures [15].

5.4.3. Pellets

The measurement for a pellet was carried out in the LTR and the p -value was close to 0.5 with a low uncertainty, suggesting that a similar VRH mechanism with a

parabolic DOS was predominant as in screen-printed films. This finding is identical with the one obtained by Basu [8].

The $\ln W$ vs. $\ln T$ graph is given in Fig. 5.15, where the pressed pellet seemed to show agreement in the conduction mechanism with screen-printed films, leading to the conclusion that screen-printed films may exhibit bulk material rather than typical film properties, although the absolute resistance was a factor of 10^4 Ohms higher in films due to the different dimensions of films and pellets. The corresponding $\ln(R/T)$ vs. $1/T^{0.5}$ plot is given in Fig. 5.16.

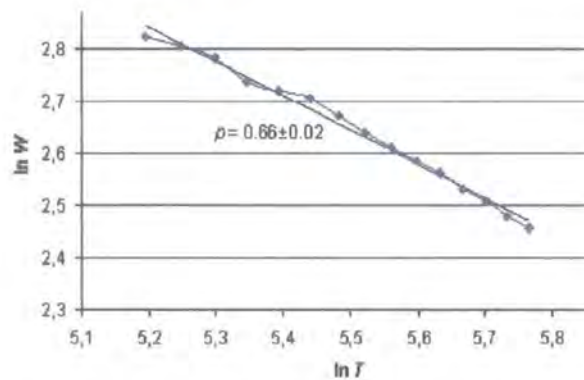


Fig. 5.15 $\ln W$ vs. $\ln T$ graph for a pressed pellet, sintered at 1200°C for 24 h and annealed at 800°C for 40 h, LTR

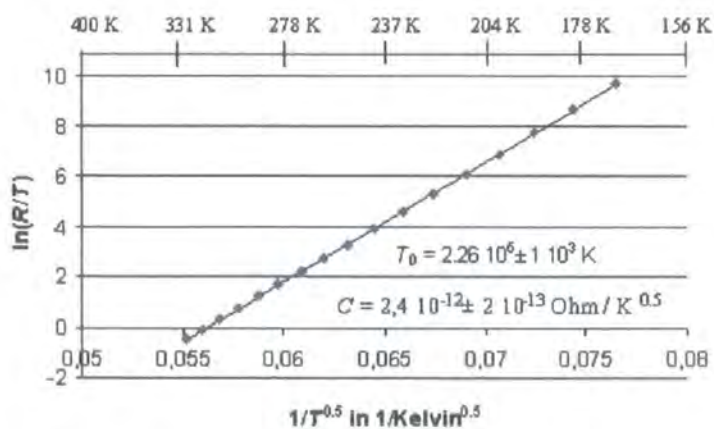


Fig. 5.16 $\ln(R/T)$ vs. $1/T^{0.5}$ plot for a pressed pellet, sintered at 1200°C for 24 h and annealed at 800°C for 40 h, LTR

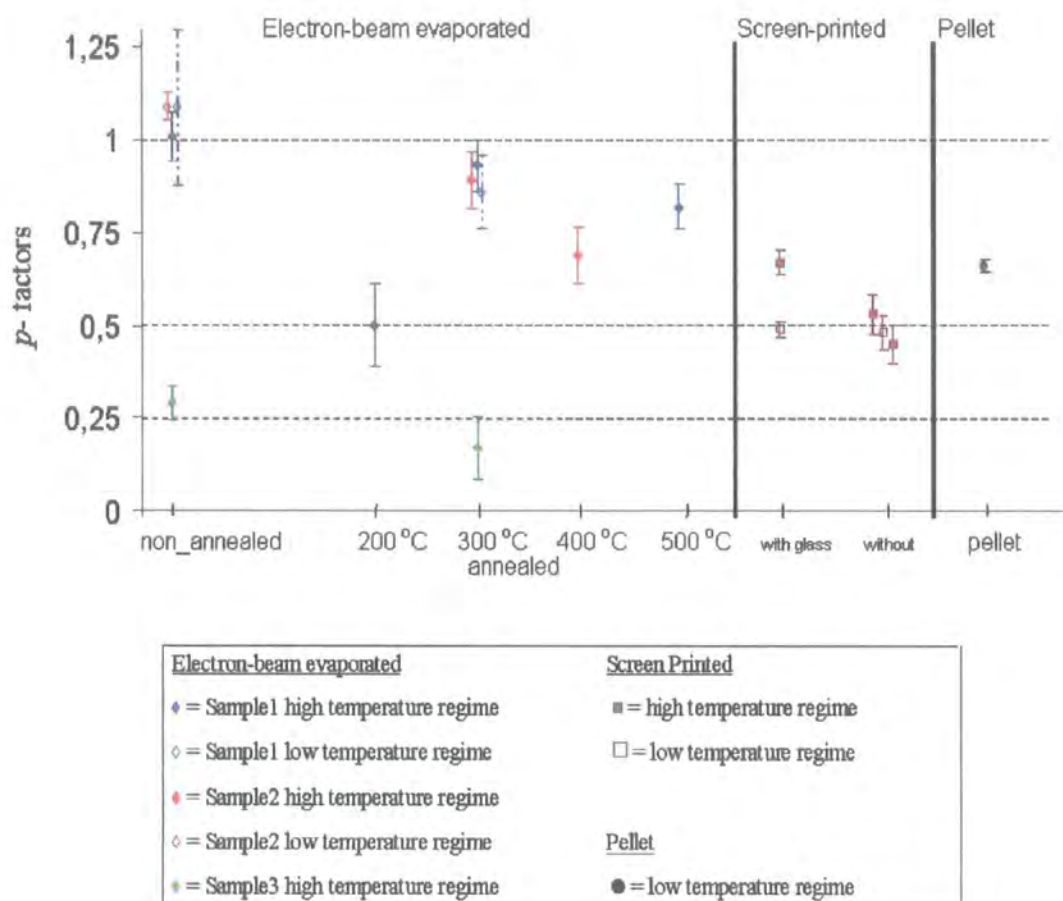
The characteristic temperature T_0 proved to be slightly higher than for screen-printed films suggesting a lower $\varepsilon_r \cdot a$ product, which in turn may correspond to a smaller overlap of the wave functions of donor and acceptor. The T_0 value obtained by Basu [8] was $2.23 \cdot 10^5$ K in very good agreement. The constant C in the pellet showed a significant shift compared to the films, suggesting that significant differences in the pre-exponential constants (eq. 5.7), described by C , occurred.

5.4.4. Summary

All p -factors determined for pellets, electron-beam evaporated films annealed in air at different temperatures and for screen-printed films with and without incorporated glass phase are summarised in Fig. 5.17. As can be seen the p -values for the electron-beam evaporated films varied significantly, although in most samples NNH occurred. In contrast, all screen-printed films and pellets clearly followed a VRH model with $p = 0.5$.

By investigating the trend of p -values for sample 1 and sample 2 it might be concluded that the p -values tended to lower values with higher annealing temperatures. Previously, an increase of the annealing temperature was associated with an increase in crystallinity and it is suggested that the transition from an amorphous to a more crystalline phase could be accompanied by a transition from NNH to VRH.

The uncertainties in p are all displayed in Fig. 5.17 as error bars and especially for the screen-printed films high confidence may be placed in the identification of VRH with a parabolic DOS.

Fig. 5.17 p -factors for different samples

5.5. Conclusion

For all types of NiMn₂O_{4+δ} materials a strong NTCR effect was observed over the full range of temperatures (130K – 550K) as expected. In screen-printed films and pressed pellets the conduction was described best by a variable-range hopping model, assuming a parabolic DOS, as reported by Basu [8]. The resistance was best described by the following equation :

$$R = C T \exp\left(\frac{T_0}{T}\right)^{1/2}; \quad 5.21$$

In most electron-beam evaporated films conduction appeared to be by NNH with the following *R-T* behaviour:

$$R = C T \exp\left(\frac{T_0}{T}\right); \quad 5.22$$

In some of the electron-beam evaporated films conduction followed a VRH model with a constant DOS for which the *R-T* behaviour is described by :

$$R = C T^{1/2} \exp\left(\frac{T_0}{T}\right)^{0.25}; \quad 5.23$$

The p -factor analysis for screen-printed films and pellets gave a very convincing indication for VRH with a parabolic DOS, whereas for electron-beam evaporated films there was considerable scatter in the p -values. The identification of NNH and VRH regimes was correspondingly less certain. The production of screen-printed films could be achieved with better control on all process and material parameters as described in chapter 4, whereas the production of electron-beam evaporated films was less controllable as described in chapter 3. It is believed that it was the better reproducibility of the production process that was leading to the greater consistency in the p -values as well as in the characteristic temperatures T_0 .

It was pointed out in previous chapters that the glass phase enabled better mechanical properties of the films, whereas in this chapter the electrical properties seemed to be only marginally affected by the glass phase. The characteristic temperature seemed to be slightly lower for glass containing films, leading to less temperature dependent devices. However, the sensor performance would not be impaired and it may be concluded that a reliable temperature sensing device can be obtained by screen-printing of NiMn₂O_{4+δ} materials including a glass phase.

Determining the characteristic temperature T_0 of screen-printed films enabled the specification of a lower limit of the dielectric constant ϵ_r in NiMn₂O_{4+δ} ($\epsilon_r \geq 3.9$), whereby a hard sphere model of the crystal atoms was assumed.

The conduction mechanism in pellets was found to be very similar to the screen-printed films, suggesting that screen-printed films with a thickness of $\sim 20 - 25 \mu\text{m}$ exhibit bulk rather than typical film properties.

The characteristic temperatures T_0 (thermistor constant) of electron-beam evaporated films (3370 – 5310 K) were higher than for commercial bulk thermistors (2750 – 4100 K). The resistance tolerance of $\sim 5\%$ - 10% in commercial devices could not be

compared due to different film thickness in samples 1,2 and 3. For screen-printed films the absolute resistance varied by $\sim 50\%$ between samples with and without glass phase, but no data was taken to compare samples of the same sort. No assessment of the thermistor constants could be achieved for screen-printed films and pellets, as the values given for commercial devices are based on a $R-T$ scale used for NNH.

It was noted that in electron-beam and screen-printed films NNH and VRH models might be both valid in a transitional range of an intermediate type of electrical conduction, for example in the transition range from an amorphous to a more crystalline phase.

5.6. References

1. Fritsch S., Sarrias J., Brieu M., Couderc J.J., Baudour J.L., Snoeck E., Rousset A., *Correlation between the structure, the microstructure and the electrical properties of nickel manganite negative temperature coefficient (NTC) thermistors*, Solid State Ionics, 1998, **109**, p. 229
2. Baliga S., Jain A.L., *Hopping conduction in sputtered Ni-Co-Mn-O spinel films*, Materials Letters, 1991, **11**(5,6,7), p. 226
3. Baliga S., Jain A.L., Zachofsky W., *Sputter deposition and characterisation of Ni-Mn-O and Ni-Co-Mn-O spinels on polyamide and glass substrates*, Applied Physics A : Solids and Surfaces, 1990, **50**, p. 472
4. Mansfield R., *Hopping conduction in III-V compounds*, in *Hopping transport in Solids*, Pollak M., Shklovskii B., Editors, 1991, Elsevier Science, Amsterdam, p. 349
5. Shklovskii B.I., Efros A.L., *Electronic properties of doped semiconductors*, Solid State Sciences 45, 1984, Berlin, Springer - Verlag
6. Zabrodskii A.G., *Electrical conductivity of heavily doped compensated n-type germanium produced by neutron doping*, Sov.Phys.Semicond., 1980, **14**(6), p. 670
7. McKelvey J.P., *Solid State and Semiconductor Physics*, 1966, New York, Harper&Row
8. Basu A., *Deposition and Characterisation of Sputtered Nickel Manganate Thin Films*, PhD Thesis, Department of Physics, 2002, Durham, University of Durham
9. Taylor J.R., *An Introduction to Error Analysis*, A Series of Books in Physics, ed. Commins E.D., 1982, Mill Valley, University Science Books, p. 159
10. Brabers V.A.M., Terhell J.C.J.M., *Electrical conductivity and cation valencies in nickel manganite*, Physica Status Solidi (A), 1982, **69**, p. 325
11. Feltz A., Töpfer J., Schirrmeister F., *Conductivity data and preparation routes for NiMn₂O₄ thermistor ceramics*, Journal of the European Ceramic Society, 1992, **9**, p. 187
12. O'Neill H.S.C., Navrotsky A., *American Mineralogist*, 1983, **68**, p. 181
13. Ibach H., Lüth H., *Festkörperphysik*, p.145, 1995, Berlin, Springer Verlag
14. Mott N.F., *Conduction in Non-Crystalline Materials*, 1993, Oxford, Clarendon Press, Oxford Science Publications, p. 91

15. Zener C., *Interaction between d-Shells in the Transition Metals. II. Ferromagnetic Compounds of Manganese with Perovskite Structure*, Physical Review, 1951, **82**(3), p. 403

Chapter 6

A.c. impedance spectroscopy of screen-printed films with glass phase

6.1. Introduction	158
6.2. Theoretical Review	159
6.2.1. Basic principle of impedance spectroscopy	159
6.2.2. Data analysis and equivalent circuit modelling	161
6.2.3. A.c. impedance of hopping processes	165
6.3. Experimental techniques	169
6.4. Results/ Discussion	171
6.4.1. Impedance spectroscopy data presented as Z' - Z'' complex plane loci	171
6.4.2. Interpretation of Z' - Z'' complex plane loci	174
6.4.3. Data analysis by modulus M' vs. frequency plots	177
6.4.4. Data analysis by Z' vs. f and Z'' vs. f plots	181
6.4.5. A.c. conductivity of the hopping mechanism	184
6.4.5.1. Extended Pair Approximation (EPA)	184
6.4.5.2. Impedance vs. temperature plots	186
6.4.6. Equivalent circuit modelling	191
6.4.6.1. Z' behaviour in respect to the equivalent circuit model	192
6.4.6.2. Z'' behaviour in respect to the equivalent circuit model	194
6.5. Conclusions	196
6.6. References	198

6.1. Introduction

Impedance spectroscopy is a powerful tool to investigate the electrical characteristics of specimens of various kinds. Originally, alternating current (a.c.) impedance spectroscopy was developed to analyse electrolytic solutions in order to gain separate information about cathode and anode reactions [1]. Since then the technique has been also applied to the analysis of solid electrolytes and solid materials in general, to distinguish between bulk, grain boundaries and sample – electrode interface effects. Possible effects of minor secondary phases or surface layers may be identified and analysed as well. The principles for using a.c. impedance spectroscopy with ceramic materials have been described by Macdonald [1] and more particularly by Irvine et al. [2]. The first a.c. impedance spectroscopy experiments were carried out using single capacitance bridges, which were restricted to small frequency ranges. Nowadays, with the development of sophisticated impedance analysers, the application of a.c. impedance spectroscopy allows automated data collection of sample responses to an a.c. signal of frequencies between 10^{-2} Hz up to 10^7 Hz.

Impedance spectroscopy enables a qualitative analysis of the electric behaviour leading to an equivalent circuit model for the sample under investigation, and the quantitative contributions of the respective circuit elements to the overall impedance can be determined. In consequence, a.c. impedance spectroscopy is well suited to the examination and specification of possible effects of grain boundaries and bulk material on the conduction mechanism in thick $\text{NiMn}_2\text{O}_{4+\delta}$ films and for the development of an equivalent circuit model. In general, the electronic properties of $\text{NiMn}_2\text{O}_{4+\delta}$ may be further elucidated and the understanding of a.c. hopping extended.

6.2. Theoretical review

6.2.1. Basic principle of impedance spectroscopy

The basic impedance spectroscopy experiment is carried out by applying an alternating voltage signal to the sample under investigation: $V(t) = V_m \sin (2\pi f t)$. $V(t)$ is the time (t) dependent voltage, V_m the amplitude and f the frequency of the applied signal. The resulting current through the sample $I(t) = I_m \sin (2\pi f t + \theta)$ is measured with I_m being the amplitude and θ the phase shift. The impedance \tilde{Z} of the sample is defined as $\tilde{Z}(f) \equiv V(t)/I(t)$ and its magnitude is $|\tilde{Z}| = V_m / I_m$ [1].

\tilde{Z} can be represented as a complex number, where the real part Z' is the resistive component and the imaginary part Z'' the reactive component of the overall impedance \tilde{Z} . The complex impedance \tilde{Z} is given on the complex plane in Fig. 6.1.

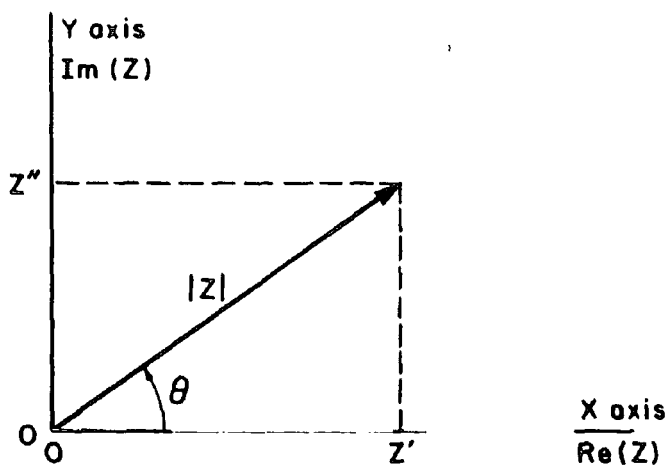


Fig. 6.1 Complex plane showing $|\tilde{Z}|$, Z' ($\text{Re}(\tilde{Z})$), Z'' ($\text{Im}(\tilde{Z})$) and θ , [1]

The corresponding relations between $|\tilde{Z}|$, Z' , Z'' and θ are listed in 6.1, 6.2 and 6.3.

$$|Z| = [(Z')^2 + (Z'')^2]^{1/2}; \quad 6.1$$

$$\tan \theta = (Z'' / Z'); \quad 6.2$$

$$Z' = |Z| \cos(\theta); \quad Z'' = |Z| \sin(\theta); \quad 6.3$$

Instead of applying a voltage signal, a current signal may be used and the voltage response measured. This is an equivalent experiment and leads to the same results. A.c. impedance spectra are obtained by measuring the impedance with signals of different frequencies f over as wide a range as possible, typically 10^{-2} Hz – 10^7 Hz.

The parameters Z' and Z'' can be related to the complex dielectric constant $\tilde{\epsilon}$ with real and imaginary parts ϵ' and ϵ'' , \tilde{Y} is the conductance.

$$2\pi f iC_0 (\epsilon' - i\epsilon'') = \frac{1}{\tilde{Z}} = \frac{1}{Z' + iZ''} = \tilde{Y}; \quad 6.4$$

C_0 is the capacitance of the empty measuring cell, i.e. $C_0 = \epsilon_0 A/l$, where l is the length and A the cross section of the conductive path in the sample. In a crude approximation for samples of film type, A may be the diameter of the contacts multiplied by the film thickness d , and the conducting length l is the distance between contacts.

However, it is believed that \tilde{Z} is only related to the dielectric constant $\tilde{\epsilon}$, if electrical conduction takes place due to ion conduction as in an electrolyte or an ion conductor. If electrical conduction is based on electron transport, the dielectric

constant of the material is believed to have no significant influence on the transport of free or quasi-free electrons as $\tilde{\epsilon}$ describes the polarisability of the material. For the analysis of a.c. impedance data it is useful to define the modulus function \tilde{M} as follows:

$$\tilde{M} = M' + iM'' = 2\pi f iC_0 \tilde{Z} = \frac{1}{\tilde{\epsilon}} = \frac{1}{\epsilon' - i\epsilon''} ; \quad 6.5$$

The use of M'' for data analysis is described in the next section.

6.2.2. Data analysis and equivalent circuit modelling

In order to interpret the sample response to a stimulating a.c. signal it is common practice to develop an equivalent circuit model consisting of ideal resistive, capacitive and in rare cases inductive components. The theoretical a.c. impedance of possible equivalent circuit models may be calculated and compared to experimental findings.

In a conventional equivalent circuit model, a resistive component (R) and capacitive component (C) in parallel (RC element) describe a relaxation time τ for a certain process; e.g. grain boundaries, bulk or electrode conduction. The complex impedance of such a RC element is given by

$$\tilde{Z} = \frac{R}{1 + (2\pi f CR)^2} - i \frac{2\pi f CR^2}{1 + (2\pi f CR)^2} = \frac{R}{1 + (\omega\tau)^2} - i \frac{\omega R\tau}{1 + (\omega\tau)^2} ; \quad 6.6$$

In eq. 6.6 the time constant τ of the corresponding process was substituted for $R \cdot C$ ($\tau = R \cdot C$). In the literature inductive components (L) are hardly ever used in equivalent circuits and all recent publications describe models restricted to RC elements in series, each representing either bulk, grain boundary or electrode effects [2], [3].

One of the most common ways to present a.c. impedance spectroscopy data are as a Cole-Cole complex plane locus with frequency of the imaginary part of the dielectric constant $-\varepsilon''$ vs. the real part ε' [4], or, more appropriately for solid materials, as a Z'' - Z' complex plane locus of the imaginary part of the impedance $-Z''$ vs. the real part Z' [2]. By convention, both ε'' and Z'' are plotted on the positive vertical axis even though they are in fact negative quantities for a RC element.

In the ideal case, for every specific relaxation time τ (i.e. RC element) a perfect semicircle occurs in both, ε'' - ε' and Z'' - Z' loci. Fig. 6.2 shows a standard equivalent circuit with the corresponding Z'' - Z' complex plane locus.

In a RC element, the resistive component R is the real resistance of the bulk, grain boundary or electrode resistance. At low enough frequencies the electrons move through the whole sample during each half cycle. The capacitive reactance of the RC elements representing the electrode, grain boundary and bulk components (Fig. 6.2) would all be large and the impedance is effectively just the series resistance $R_{gb} + R_b + R_{el}$. As the frequency is increased, the reactance of the capacitive elements start to decrease and eventually short circuit the parallel resistive elements.

From Fig. 6.2. it is clear that, as the frequency increases, each resistive element gets by-passed successively according to the reactance of its parallel capacitive component, whereby the capacitance C describes the capacitive effects involved with the process.

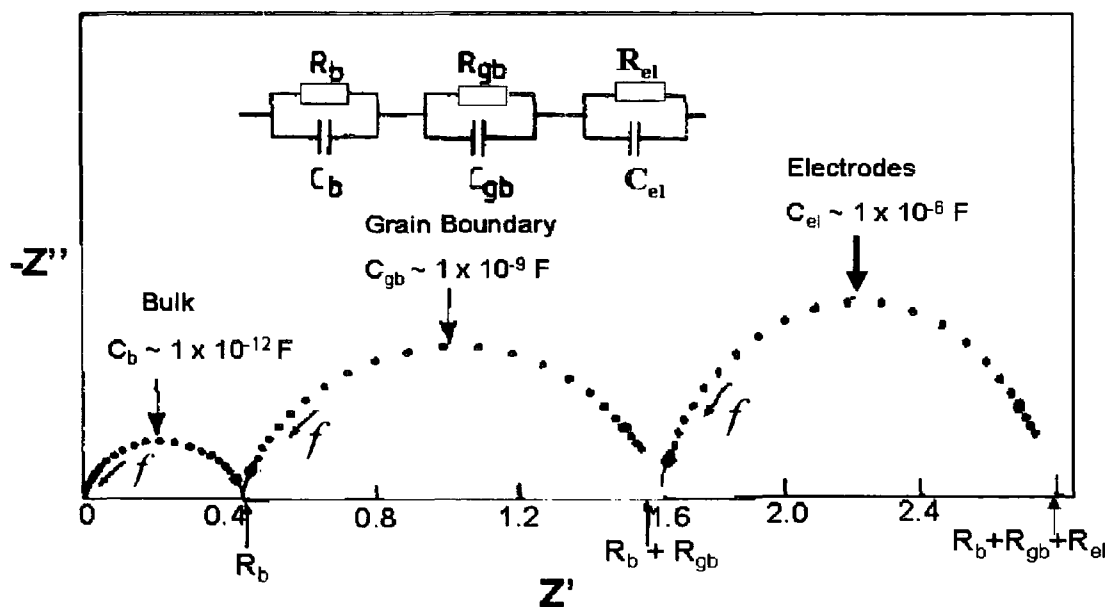


Fig. 6.2 Equivalent circuit model with the corresponding Z'' - Z' locus, [2]

For conductors or semi-conductors with delocalised electrons the bulk resistance may break down completely if the frequency becomes high enough leading to a conduction path significantly shorter than the mean free path of electrons due to scattering events (see high frequency end in Fig. 6.2). However, this may not be valid for electron hopping between localised states as discussed in the next section.

As the main advantage of such equivalent circuit modelling based on RC elements, calculation of the resistance and the capacitance of the respective RC element is possible from the semicircle in the Z'' - Z' loci. It can be readily shown that the frequency f_{\max} at which the imaginary part of the impedance ($-Z''$) is a maximum is given by:

$$f_{\max} = \frac{1}{2\pi \tau} = \frac{1}{2\pi RC} \quad 6.7$$

The radius of the semicircle equals the resistance $R/2$, because $-Z''(f_{\max}) = R/2$ and C can be determined knowing f_{\max} .

Irvine et al. [2] have pointed out that, for ceramic materials, grain boundary, bulk or electrode contributions normally show clearly different magnitudes of the capacitance and each semicircle can be attributed to one of those effects in this way.

However, there are some problems involved with equivalent circuit modelling approaches. Two different circuits can display exactly the same impedance at all frequencies, so ambiguities may occur and experience and physical intuition are needed to find the appropriate model. Usually, the data is compared with theoretical calculations of M' , Z'' or Z' vs. f behaviour for different suggested equivalent circuits.

Furthermore it is important to note that two different RC elements may have similar time constants and the corresponding semicircles may overlay each other making the analysis difficult. If a RC element and another L containing element overlay each other, the complex plane locus may become even more complicated, because Z'' for an L containing component can be of different sign to that for a capacitive component. Therefore, another method based on the modulus function \tilde{M} (eq. 6.5) has been developed to distinguish RC elements according to their capacitance C and to help identify L containing components. From eq. 6.5 and 6.6 the imaginary part of \tilde{M} for a RC element is:

$$M''(f) = 2\pi f C_0 Z' = C_0 \frac{2\pi f R}{1 + (2\pi f RC)^2}; \quad 6.8$$

M'' exhibits a maximum at the same frequency f_{\max} as Z'' (eq. 6.7), when 6.8 reduces to:

$$M''(f_{\max}) = \frac{C_0}{2C} ; \quad 6.9$$

The value of M'' at the peak is dependent on C , and this often allows overlapping RC elements to be more readily separated according to their capacitance. Identification of an L containing component is possible, because M'' is connected to the resistive part of the impedance (eq. 6.5), which is of the same sign (positive) for all C and L containing components.

The graphs of $-Z''$ vs. $\log f$, Z' vs. $\log f$ and M'' vs. $\log f$ may contain additional information needed for equivalent circuit modelling, particularly where the modelling requires more than a series connection of simple RC elements. Often the behaviour at limiting values of $f \rightarrow 0$ and $f \rightarrow \text{infinity}$ give a clear indication for the validity of a possible model.

6.2.3. A.C. impedance of hopping processes

Generally, the a.c. signal response of a hopping system exhibits 3 distinct frequency regimes [5], here termed Low (LFR), Intermediate (IFR) and High Frequency Regime (HFR). Different models have been proposed for all 3 regimes for NNH and VRH hopping mechanisms, although all models for VRH found in the literature were restricted to Mott's $(T_0/T)^{1/4}$ case.

In the LFR electrons move through the sample completely during each half cycle, thus the percolation threshold coincides with the d.c. threshold and Z' vs. temperature characteristics show equivalent behaviour to the d.c. R - T characteristics. Therefore, the same models applied for d.c. resistivity are valid at these frequencies and the real part of the impedance is frequency independent here ($Z'(\omega \rightarrow 0) = R$). Fig. 6.3 shows a representative $\log Z'$ vs. $\log f$ plot for 3 different temperatures at the LFR, IFR and HFR.

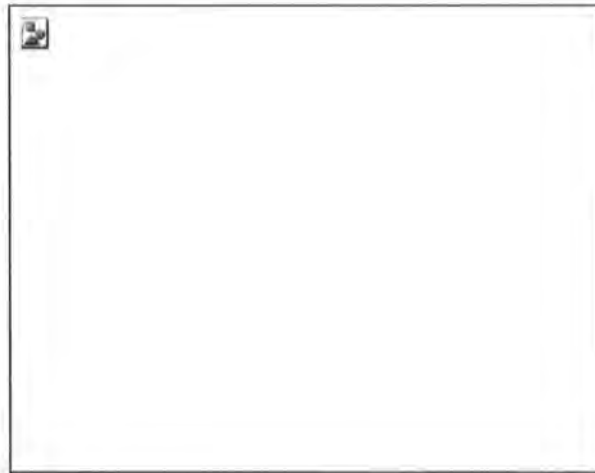


Fig. 6.3 $\log Z'$ vs. $\log f$ for NNH hopping type conduction at different temperatures

Several theoretical models for the IFR, where Z' first starts to drop with frequency, are based on cluster theories. With increasing frequency the infinite resistor network is assumed to break up and electrons are restricted to finite clusters of decreasing size where the percolation threshold ξ_c decreases with decreasing cluster size [6].

Zyvagin [6] has considered the general case of a.c. response for hopping systems in the IFR from where explicit expressions for NNH or VRH may be derived. Alternative approaches have been undertaken by Movaghar et al. [7], who used a Random-Walk model, and by Summerfield and Butcher [8], who developed an

extended pair approximation (EPA). This EPA model by Summerfield and Butcher is not only restricted to the IFR, but holds in the HFR as well. In order fit the real part of the a.c. conductivity $\sigma_1(\omega, T)$ at all temperatures and all frequencies in one curve the following equation was developed by Summerfield [9]:

$$\frac{\sigma_1(\omega, T)}{\sigma_1(0, T)} = 1 + \left(\frac{A e^2 \omega}{a k_B T \sigma_1(0, T)} \right)^{0.725} = 1 + \left(C_{EPA} \frac{\omega}{T \sigma_1(0, T)} \right)^p ; \quad 6.10$$

where $\sigma_1(0, T)$ is the real part of the a.c. conductivity in the LFR ($f \rightarrow 0$), where the conductivity is independent of frequency, a is the wave function parameter and A a numerical parameter characteristic of the fit. In the more generalised form with the parameters C_{EPA} and p , eq. 6.10 is able to explain the LFR data as well, where p would be 0. At the IFR and HFR p was reported to be 0.725 for impurity conduction in n-type semiconductors at very low temperatures [10]. For hopping conduction in NTCR thermistors p and C_{EPA} have not been examined yet.

Furthermore, it has not been considered by any author that with increasing frequency a transition of the average cluster size beyond the average grain size would occur, which may effect the impedance. It is suggested that this could result in a drop in ξ_C as hopping over grain boundaries no longer contributes significantly to the conductivity.

In the HFR (~ 50 kHz – 3 MHz) the real part of the impedance is reported to drop with increasing frequency [5] and the temperature dependence of Z' becomes much less pronounced, such that the $\log Z'$ vs. $\log f$ graphs seem to almost coincide (see Fig.

6.3). Pollak and Geballe [11] assumed that the total a.c. response in the HFR consists of the sum of the individual responses of pairs of sites randomly distributed throughout the material (pair approximation).

At even higher frequencies of $\sim 3 - 10$ MHz (i.e. an Ultra High Frequency Regime (UHFR)), no data is available in the literature to determine whether this trend still holds here.

It is clear that in the HFR/UHFR at high enough frequencies electrons will be confined to hops only between pairs of electron states, i.e. a constant cluster size . Therefore, it may be possible that Z' may not continue to decrease with frequency at the UHFR as an increasing number of electrons could be prevented to hop within one test signal period, if the frequency becomes higher than the average time interval needed for an electron to perform an oscillation between two localised states. Z' could instead tend to a constant value or even increase.

6.3. Experimental techniques

Thick $\text{NiMn}_2\text{O}_{4+\delta}$ films (20-25 μm) containing a glass phase were printed onto Al_2O_3 substrates and sintered at 850°C for 30 min, as described in detail in chapter 4.

Al contacts were evaporated onto the film surface and covered with silver paint to prevent oxidation (for contact deposition see chapter 5.3.1.). The samples were placed in a ceramic purpose-built sample holder equipped with spring loaded drop-down contacts, which it has been reported to minimise the contact resistance, so that electrode - sample interface effects in the impedance spectra can be neglected [3].

The sample holder was placed in an insulated heat calorimeter equipped with an Eurotherm temperature controller in the same arrangement as described in chapter 5.3.4. The temperature was manually adjusted between measurements and allowed to settle down for at least 15 minutes. Complete thermal equilibrium was required, because even tiny temperature fluctuations would cause a significant change of the impedance due to the strong NTCR effect in $\text{NiMn}_2\text{O}_{4+\delta}$.

Impedance spectroscopy was carried out using a Hewlett/Packard 4192A LF Impedance Analyser with computer controlled automated data collection (“Integrated Impedance Analyser Programme”, Version #2.6, 1991). Measurements were carried out between 5 Hz – 6 MHz and the frequency increased logarithmically. The accuracy in the frequency was better than $\pm 0.02\%$.

The alternating test voltage had an amplitude of 3V and a 30V d.c. bias voltage was applied additionally in order to reduce noise. Spectra were collected over the temperature range of 60°C - 220°C in 20°C intervals.

First, an open circuit calibration was carried out with all test wires in place, but with the sample not connected in order to measure parasitic contributions. The calibration

values were recorded by the computer program and later used to correct the data obtained from the sample. The impedance values were measured with an uncertainty of not more than $\pm 1\%$, for both reactive and resistive part of the impedance.

6.4. Results and Discussion

6.4.1. Impedance spectroscopy data presented as Z'' - Z' complex plane loci

As described in section 6.2.2., $-Z''$ vs. Z' loci on the complex plane give information about different relaxation times in the sample. In Fig. 6.4 the Z'' - Z' loci for screen-printed films with the glass phase are presented. The data was collected at different temperatures as indicated. The uncertainty in the Z'' and Z' was below 1%, as mentioned in 6.3., and no error bars could be displayed. The accuracy of the frequency values was extremely high as well ($\sim 0.02\%$) and again no errors were indicated.

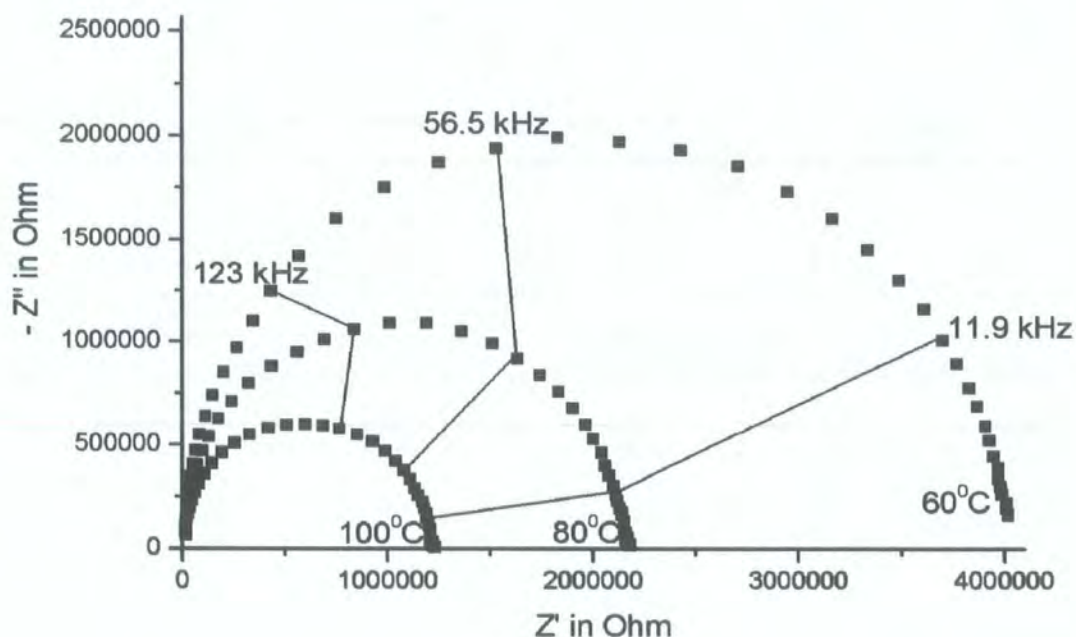


Fig. 6.4 (a) $-Z''$ vs. Z' complex plane locus, $60^{\circ}\text{C} - 100^{\circ}\text{C}$;

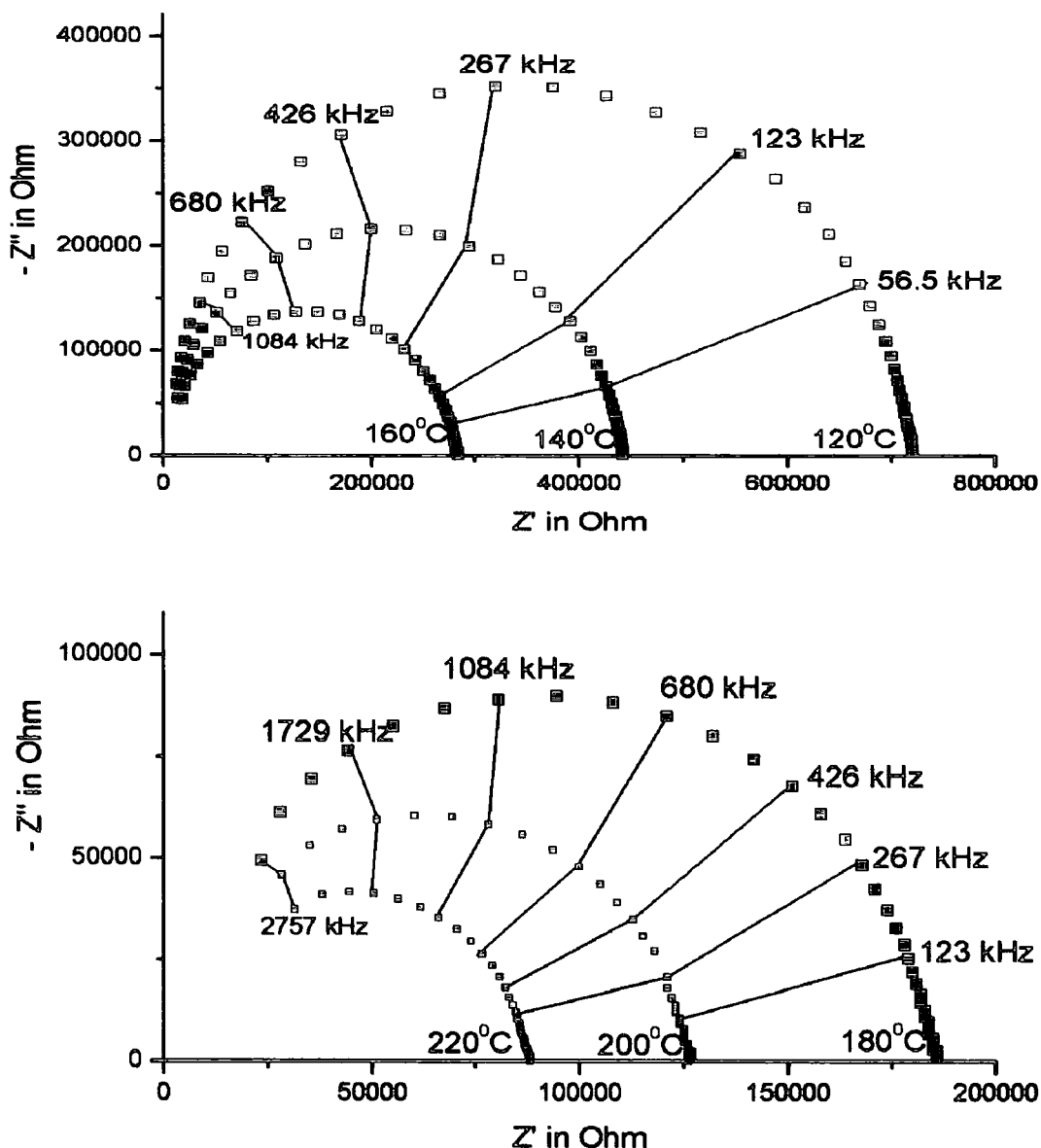


Fig. 6.4 (b),(c) $-Z''$ vs. Z' loci for screen-printed, fired and glass incorporated samples at different temperatures; (b) 120°C - 160°C; (c) 180°C - 220°C;

In Fig. 6.4 (a),(b) and (c) it can be seen that the Z'' - Z' loci for different sample temperatures all showed one almost perfect semicircle over the frequency range shown (5 Hz - 2757 kHz), indicating the presence of a single RC element describing one time constant in the sample. As the radius of the semicircle corresponds to the

resistance $R/2$ of the RC element, the decreasing size of the semicircle with increasing temperature was interpreted as the NTCR effect of the sample.

The semicircle maximum (f_{\max}) was determined and the time constant τ calculated (eq. 6.7). Fig. 6.5 shows the variation of τ with temperature.

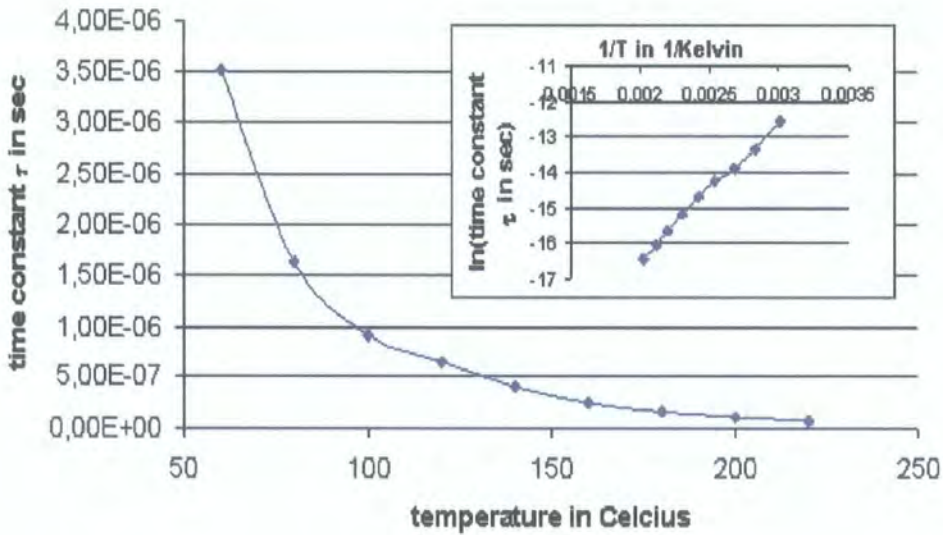


Fig. 6.5 Time constant τ vs. temperature and $\ln(\tau)$ vs. $1/\text{temperature}$

It can be seen from the inset in Fig. 6.5, that the time constant τ increased exponentially with inverse temperature, although there was a shift in the characteristics at a temperature of $\sim 100^\circ\text{C}$. It may be possible that adsorbed water on the film surface was present under 100°C and evaporated at higher temperatures, leading to a small shift in the $\ln(\tau)$ vs. $1/T$ characteristics.

The Z'' - Z' loci shown in Fig. 6.4 (a),(b),(c) were regular only for the range of frequencies shown; i.e. below 2757 kHz. A representative example for a Z'' - Z' locus over the full frequency regime recorded is given in Fig. 6.6.

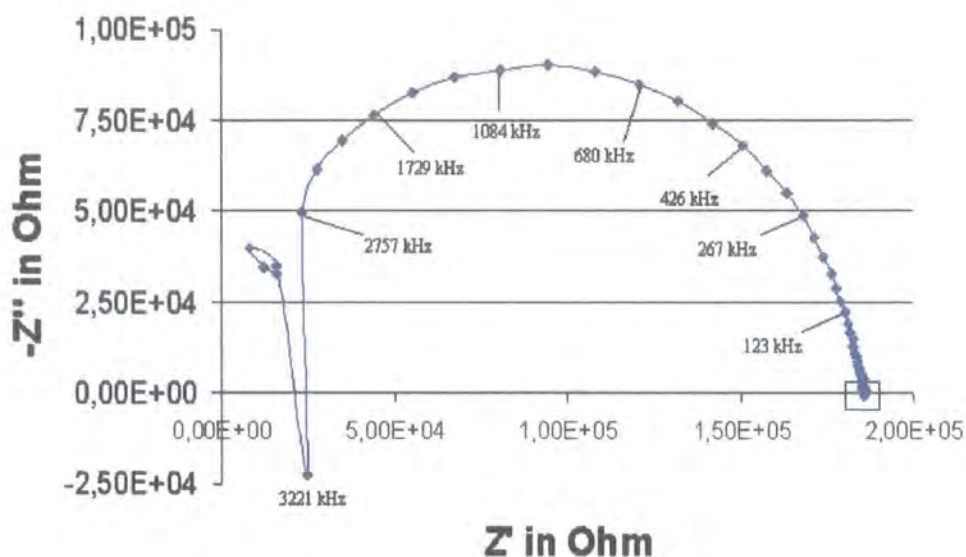


Fig. 6.6 $-Z''$ vs. Z' locus, full frequency range, sample temperature: 180 °C

It can be seen that for higher frequencies ($f > 2757$ kHz) the plot appears to become erratic, with an abrupt change of sign at 3221 kHz. At the low frequency end (represented by the square in Fig. 6.6) the data points exhibited a high level of scatter most probably due to noise in the response signal, but no hint of a second semicircle could be found.

6.4.2. Interpretation of Z'' - Z' complex plane loci

In section 6.2.2. it was pointed out that the resistance R of a specific RC element, representing electrode, grain boundary or bulk contributions, can be determined from the corresponding Z'' - Z' semicircle (radius = $R/2$). An R - T characteristic from the a.c. data at different temperatures was obtained in this way and the p -factor analysis described in chapter 5.2.3. was carried out by calculating $\ln W$ vs. $\ln T$ as shown in Fig. 6.7.

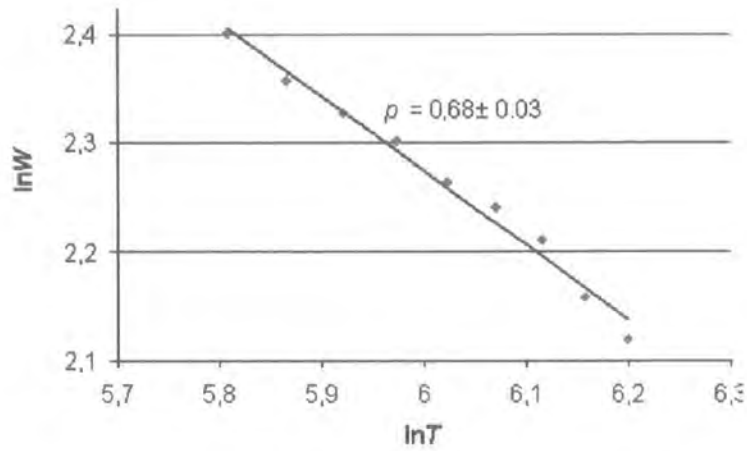


Fig. 6.7 $\ln W$ vs. $\ln T$ plot for a.c. data of a film screen-printed with glass phase

The p -value of 0.68 is in good agreement with the d.c. value of 0.67 with the linearity of the graph being good as indicated by the low uncertainty in p , which suggests that a high degree of confidence may be placed in the impedance spectroscopy measurements.

The R - T data was well described by the same VRH model discussed earlier in chapter 5.3 for the d.c. behaviour of screen-printed films and in Fig. 6.8 the corresponding plot of $\ln(R/T)$ vs. $(1/T^{0.5})$ is given.

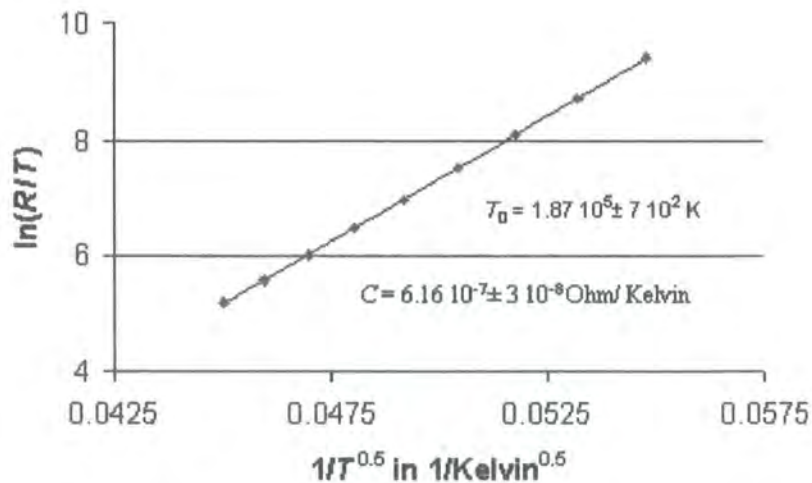


Fig. 6.8 $\ln(R/T)$ vs. $(1/T^{0.5})$, 60°C - 220°C

The slope of the graph represents the characteristic temperature $(T_0)^{1/2}$ yielding a value for T_0 of $1.87 \cdot 10^5$ K in very good agreement with $1.89 \cdot 10^5$ K from d.c. measurements. The value of $6.16 \cdot 10^{-7}$ Ohm/K for the pre-exponential factor C corresponds well to the d.c. value of $8.65 \cdot 10^{-7}$ Ohm/K. The uncertainties in T_0 and C are reasonably low and the results indicate that the conduction process is well represented by an ideal RC element for $f \leq 2757$ kHz and the underlying hopping process may well dominate the d.c. conduction in screen-printed $\text{NiMn}_2\text{O}_{4+\delta}$ films.

As described in section 6.2.2. electrode, grain boundary and bulk contributions can in principle be distinguished by the capacitance of the corresponding RC element, ideally represented as a semicircle in the Z'' - Z' loci. The capacitance was calculated from the frequency f_{\max} where $-Z''$ is a maximum and from the resistance of the corresponding Z'' - Z' semicircle (radius = $R/2$) (eq. 6.7). The capacitance is plotted vs. temperature in Fig. 6.9.

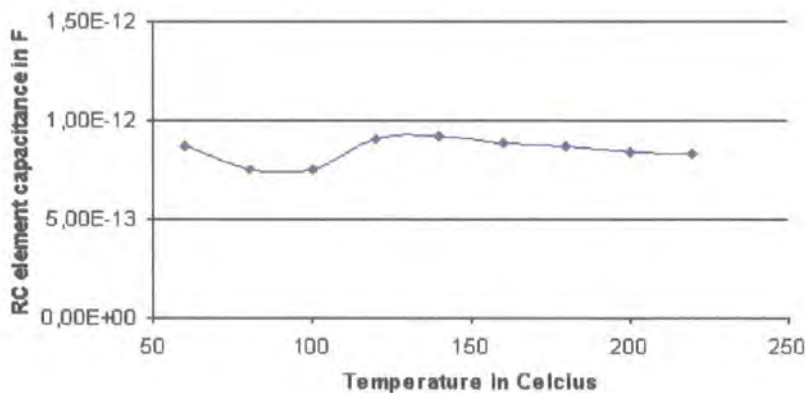


Fig. 6.9 RC element capacitance vs. temperature

According to Irvine et al. [2] bulk effects exhibit a capacitance with an order of magnitude of $\sim 10^{-12}$ F, which was the case at all temperatures in the sample investigated, shown in Fig. 6.9. It is strongly indicative that the hopping process

through the overall sample could be described by one time constant τ , i.e. one RC element, where the capacitance seemed to be connected to bulk effects. As no additional time constant due to grain boundary effects could be observed, it may be concluded that a high film density with good inter-granular contact was achieved in the investigated films with incorporated glass phase.

As pointed out before (chapter 2.5.3.) the sample may be regarded as a random resistor network where localised electron states i and j are connected by a resistor R_{ij} , which may well be a valid picture here over the whole dimensions of the $\text{NiMn}_2\text{O}_{4+\delta}$ film sample. Electron hopping between sites separated by a grain boundary may not be involved with any capacitive effect and may show little difference to neighbouring electron states within a grain, but may exhibit a higher separation in energy and possibly real space. With good crystallinity the grain boundaries in the sample might be distinct and the difference in energy and real space separation more pronounced.

From Fig. 6.9 it is also obvious that at lower temperatures of $60^\circ\text{C} - 100^\circ\text{C}$ the graph is less uniform, again suggesting an effect disturbing the regular impedance as mentioned before.

6.4.3. Data analysis by modulus M'' vs. frequency plots

In order to reveal a possible additional time constant in the frequency range investigated, the complex modulus function M'' was determined and plotted vs. $\log(\text{frequency})$ in Fig. 6.10 and against frequency on a linear scale in Fig. 6.11.

Fig. 6.10 shows that 2 maxima and 2 minima were present at all temperatures. The first maximum at intermediate frequencies clearly showed a progressive shift to

higher frequencies with increasing temperature, although a uniform trend was observed only at temperatures over 100°C. This is consistent with the results presented before, where it was suggested that adsorbed water on the films may have affected the results.

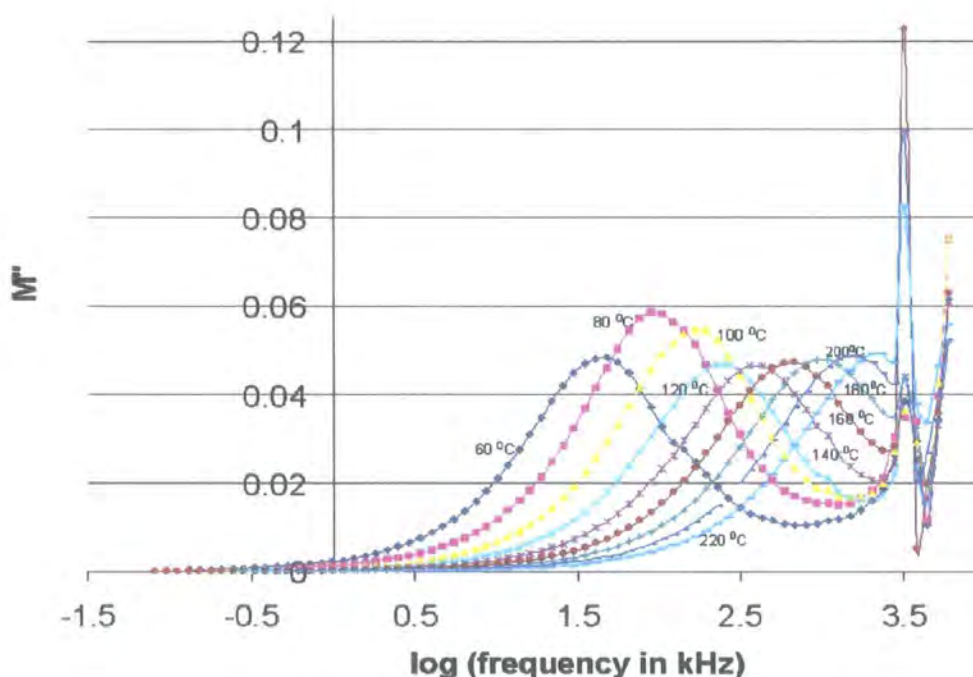


Fig. 6.10 Modulus M'' vs. $\log f$ (frequency)

The first maximum could be assigned to the bulk hopping effects as it clearly corresponds to the semicircle observed in the Z'' - Z' loci. There is no additional peak at the low frequency regime present and a significant contribution from grain boundary or electrode effects may be excluded, in the latter case justifying the use of spring-loaded drop down probes.

Concerning the second maximum in Fig. 6.10 and 6.11, it is indicative that in the UHFR a second mechanism appeared to predominate and electron hopping may not be described by a simple RC element anymore.

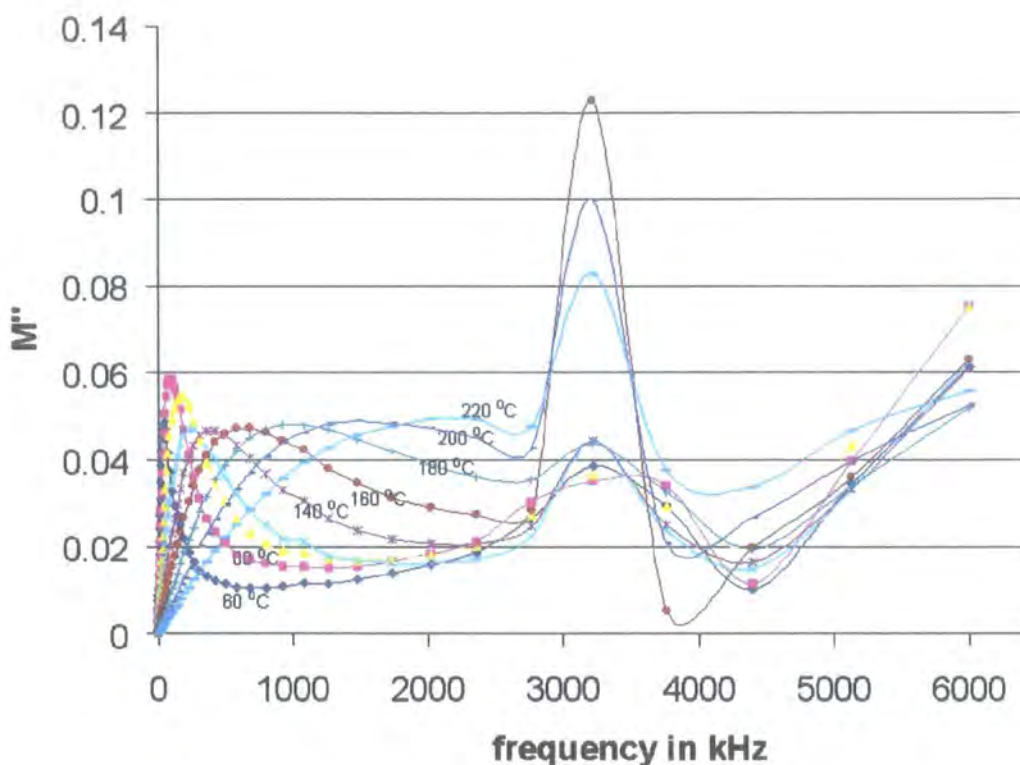


Fig. 6.11 Modulus M'' vs. frequency

It is interesting to note that for all temperatures the reactive component Z'' showed a change of sign and was positive at the second M'' peak frequency of 3221 kHz, and negative at all other frequencies, which would imply a change from a capacitive to inductive type behaviour. Experimental error at the maximum frequency for this single point would seem unlikely as the peak is apparent in the modulus spectrum over a significant range of frequency.

The second maximum in Fig. 6.11 showed no temperature dependence, although a small peak shift with temperature might not have been resolved as the data was collected in logarithmic frequency intervals. The fact that the height of the peak changed significantly with temperature supports this suggestion.

At the high frequency end M'' seemed to increase monotonically with little indication of a third maximum. A linear increase of M'' with increasing frequency is

consistent with an equivalent circuit model containing an inductive-like component and it is also consistent with the theoretical considerations described in section 6.2.3. Hopping of electrons between 2 sites might not follow high frequencies easily and the resistive component Z' could then be expected to approach a constant value at high frequencies, as Z' is directly proportional to M''/f .

The implication is that a possible equivalent circuit model may contain an RC element and an additional element, most probably including an inductive component. In the following discussion, reference to an 'inductive component' is intended to be a convenient notation for a reactive impedance, whose magnitude is directly proportional to the frequency. It is not intended that the inductive component is a 'real' or conventional inductor arising out of magnetic field effects.

The capacitance of the RC element corresponding to the first maximum in the M'' spectra was calculated from eq. 6.9 and is plotted in Fig. 6.12 together with the capacitance previously obtained from the maximum in Z'' (Fig. 6.9).

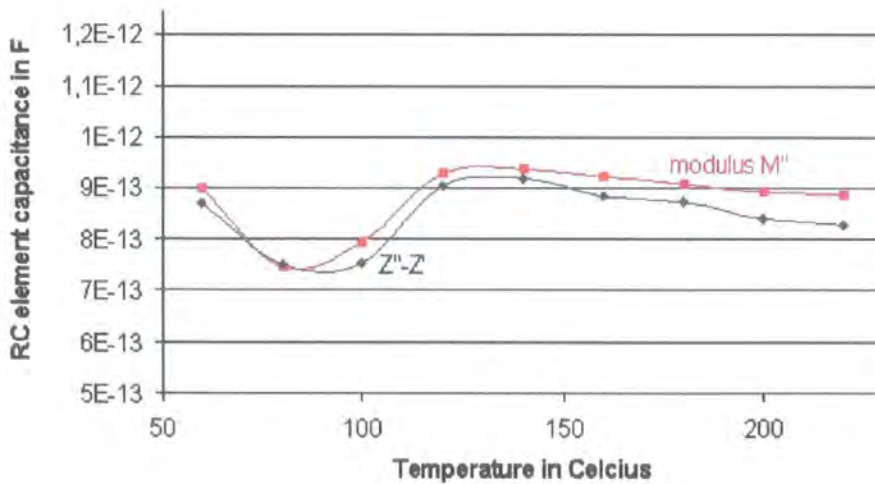


Fig. 6.12 RC element capacitance vs. temperature in Celcius

From Fig. 6.12 it can be seen that the capacitance obtained from the modulus plots was in the same range and the trend of the graphs was very similar. Obviously, the components Z' ($\sim f \cdot M''$) and Z'' measured are connected to each other justifying the description of the semi-circle by a RC element.

The dielectric constant ϵ_r was calculated as $\epsilon_r = 1/(2 \cdot M''(f_{\max}))$, (according to $C = \epsilon_r \cdot C_0$ and eq. 6.9) and was found to vary from 10.2 - 10.7 between 120°C – 220°C. In chapter 5.4.2. the lower limit for ϵ_r in $\text{NiMn}_2\text{O}_{4+\delta}$ was given by $\epsilon_r \geq 3.9$, which is consistent with the values obtained here. The lower limit was calculated assuming a hard sphere model where the radii of the spheres were interpreted as an upper limit for the Bohr's radii of the respective atoms. If the ϵ_r values of 10.2 – 10.7 are taken as a more precise estimation, the Bohr's radii of the manganese atoms in screen-printed films can be determined to be in the range of 0.260 Å – 0.303 Å.

6.4.4. Data analysis by Z' vs. f and Z'' vs. f plots

For developing an equivalent circuit model, besides the behaviour of M'' , also Z'' and Z' was plotted vs. frequency and analysed at extreme frequency values.

In Fig. 6.13 and Fig. 6.14 the real and imaginary parts of the impedance were plotted vs. f on double-logarithmic scales.

Fig. 6.13 shows that at low frequencies Z' was independent of frequency, but strongly dependent on temperature, which may well be the NTCR effect. The temperature dependence of Z' at different frequencies will be discussed in more detail in the subsequent section.

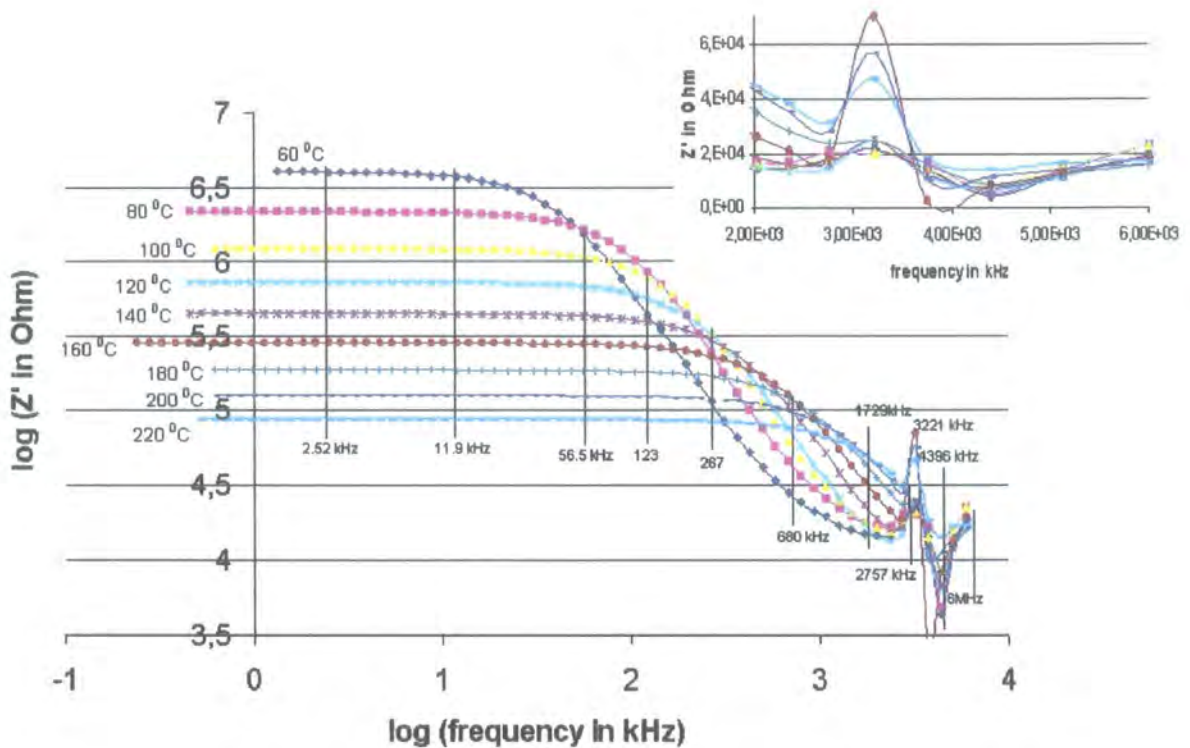


Fig. 6.13 Z' vs. $\log f$ at different temperatures

At the HFR, Z' dropped with frequency (approx. $\sim f^{-2}$) and the temperature dependence became less pronounced. This is in general agreement with theoretical predictions for the LFR, IFR and HFR as described in section 6.2.3. Additionally all curves showed a sharp maximum at 3221 kHz, corresponding to the maxima in the M'' plots. This and higher frequencies may represent a UHFR. At the high frequency end Z' seemed to approach a constant value as expected for an L containing equivalent circuit. This trend is illustrated in the inset in Fig. 6.13, where Z' was plotted vs. f on linear scales.

Fig. 6.14 shows that the imaginary part ($-Z''$) increased linearly ($\sim f$) at low frequencies, reaching a turning point at f_{\max} , as expected for an impedance described by a single dominant RC element.

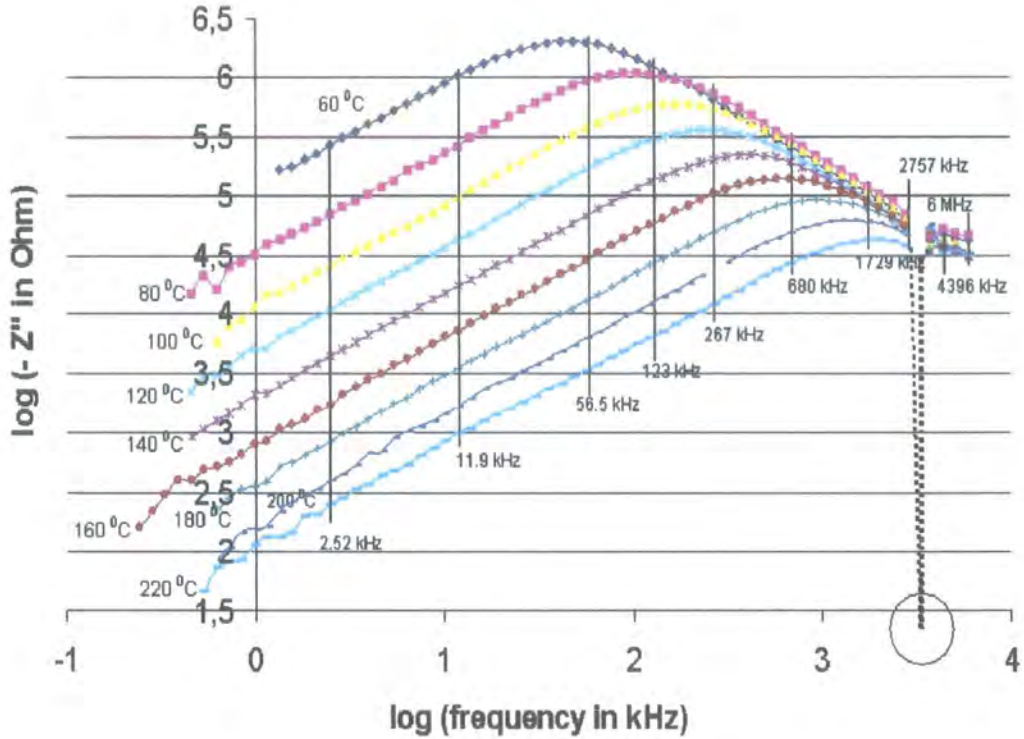


Fig. 6.14 - Z'' vs. $\log f$ at different temperatures

The maximum occurred at progressively higher frequencies as the temperature was increased and at frequencies above f_{\max} , Z'' became inversely proportional to the frequency ($\sim f^{-1}$), such that the Z'' - f characteristics tended to coincide at $f > f_{\max}$ and the temperature dependence of Z'' became significantly less pronounced.

In the UHFR at $f = 3221$ kHz, Z'' changed sign becoming positive. This point could not be plotted on a graph of $\log(-Z'')$ and so it has been represented as a gap in the characteristics. At still higher frequencies, Z'' may well have continued to drop in proportion to f^{-1} , although this could not be established definitely.

6.4.5. A.c. conductivity of the hopping mechanism

6.4.5.1. Extended Pair Approximation (EPA)

In section 6.2.3. it was mentioned that the real part of the a.c. conductivity σ_1 may be plotted at all frequencies and all temperatures in one curve, which was described by eq. 6.10 based on the EPA theory. In order to test the validity of this expression $[\sigma_1(\omega)/\sigma_1(0,T)]$ on a logarithmic scale vs. $\log [(C_{EPA} \cdot \omega)/(T \cdot \sigma_1(0,T))]$ was plotted in Fig. 6.15, where the slope of the graph would give the exponential parameter p . Here σ_1 was replaced by the a.c. conductance $1/Z'$ as the conductivity could not be calculated precisely for film type samples. It was believed that this would only alter the constant C_{EPA} , but the frequency and temperature dependence would remain valid. In Fig. 6.15 a.c. data at the LFR, IFR and HFR was plotted.

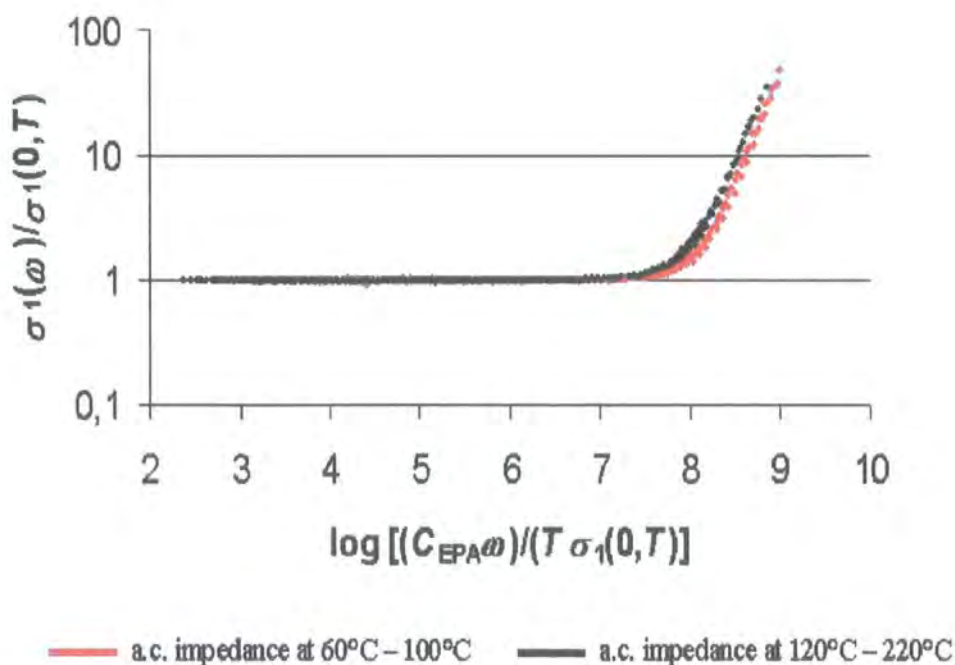


Fig. 6.15 $[\sigma_1(\omega)/\sigma_1(0,T)]$ vs. $\log [(C_{EPA} \cdot \omega)/(T \cdot \sigma_1(0,T))]$ plot at LFR, IFR and HFR

Fig. 6.15 clearly shows that the conduction mechanism was different for temperatures of 60°C - 100°C, possibly due to adsorbed water on the films, which had evaporated at elevated temperatures. Furthermore, it is obvious that at lower frequencies the factor $\sigma_1(\omega)/\sigma_1(0,T)$ exhibited the value 1, as expected for the LFR. At the HFR the graph showed a good linearity for both temperature regions, 60°C - 100°C and 120°C - 180°C. The slope of the graph was calculated using a least-square fitting procedure and the factor p was determined to be 1.68 ± 0.03 for 60°C - 100°C, and 1.50 ± 0.02 for 120°C - 180°C. These results are clearly different to the value of 0.725 reported for a.c. hopping conduction between impurity ions in n-type semiconductors at very low temperatures [10].

The values of the constant C_{EPA} were determined to be $4.08 \cdot 10^{-10}$ and $6.26 \cdot 10^{-10}$ in MKSA units respectively but are rather meaningless as in Fig. 6.15 the a.c. conductance was plotted instead of the conductivity.

However, the trend of the HTR did not hold in the UHFR as is shown in Fig. 6.16, where the data was plotted on the same axis but over the full frequency range.

Fig. 6.16 shows that the curves deviated from linearity at the UHFR. The data point at each graph where the curve starts to deviate from linearity first, strictly corresponds to the first minima in the M'' vs. $\log f$ graphs shown in Fig. 6.10. This shift off frequency may well be regarded as the transition from the HFR to the UHFR.

The UHFR behaviour is clearly not in agreement with the EPA theory and it could be confirmed that a modified type of hopping occurred.

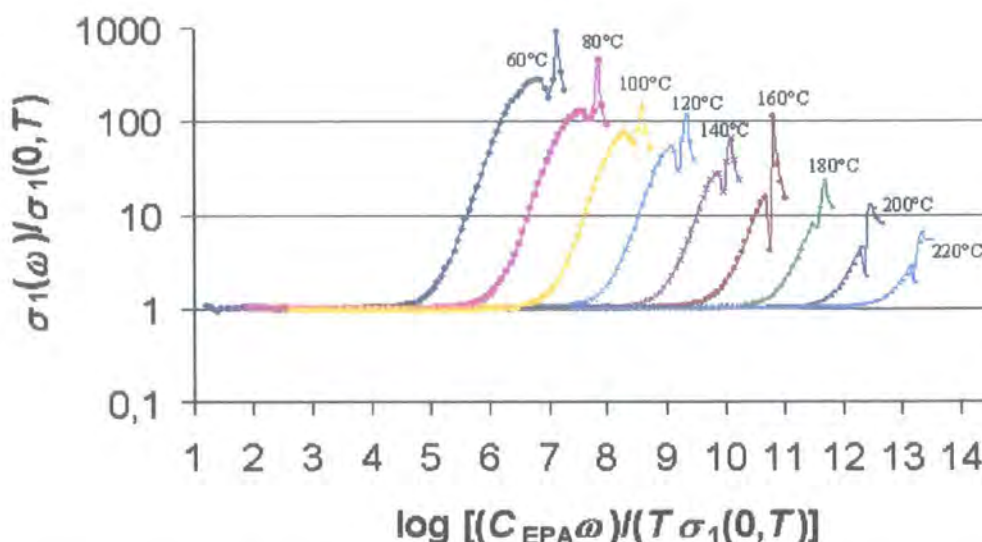


Fig. 6.16 $[\sigma_1(\omega)/\sigma_1(0,T)]$ vs. $\log [(C_{EPA}\omega)/(T\sigma_1(0,T))]$ plot over the full frequency range at different temperatures. The data at 120°C is original, all other graphs were shifted by 1 unit on the x -axis in respect to the neighbouring graph

6.4.5.2. Impedance vs. temperature plots

In order to gain more information about the conduction mechanism, the temperature dependence of Z' and Z'' was examined by plotting Z' and Z'' vs. temperature at different frequencies. Fig. 6.17 indicates an approximately exponential temperature dependence of Z' on T at lower frequencies as expected, whereas at higher frequencies this dependence was much less pronounced. The Z' vs. T graph at 3221 kHz did not show any regular trend and it may be concluded that the shape and position of the Z' peak at 3221 kHz was not sufficiently well resolved on the logarithmic data scale to enable the observation of any temperature dependence. At frequencies below 11.92 kHz the $\log Z'$ vs. T graphs in Fig. 6.17 show d.c. behaviour and in order to gain a better understanding of the a.c. hopping conduction, the data

plotted in Fig. 6.17 is shown again in Fig. 6.18 on a $\log(Z \cdot T^{-1})$ vs. $1/T^{0.5}$ scale, as used for the d.c. conduction mechanism.

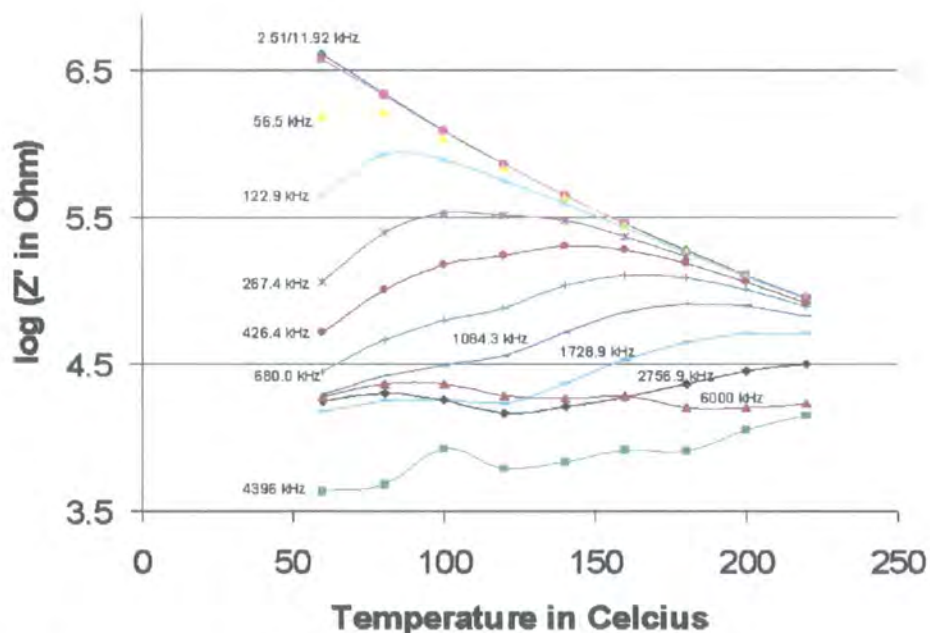


Fig. 6.17 $\log(Z'$ in Ohm) vs. temperature in Celcius at different frequencies

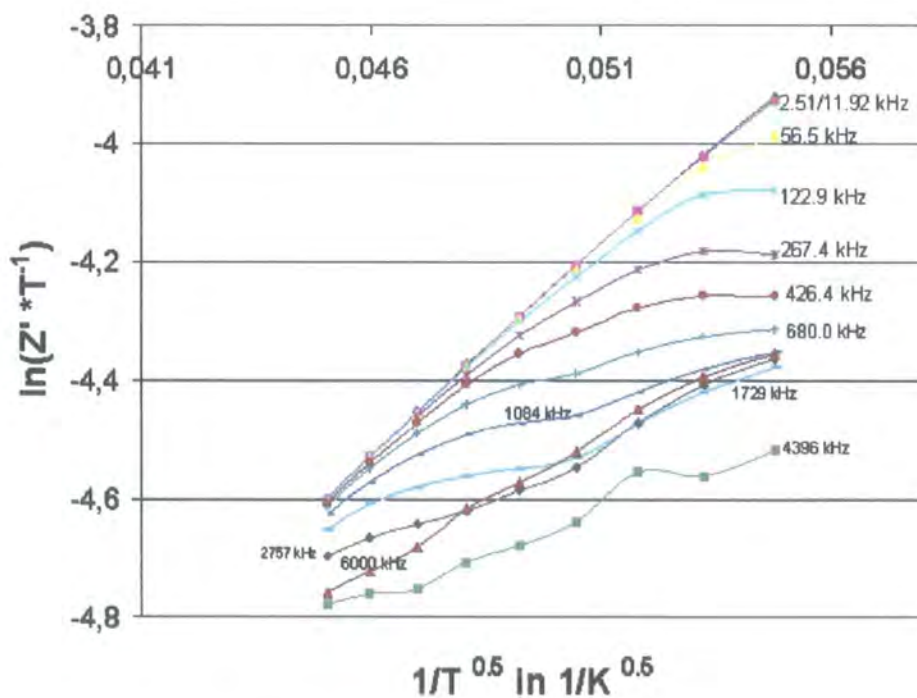


Fig. 6.18 $\log(Z' \cdot T^{-1})$ vs. $1/T^{0.5}$ at different frequencies

The slope of the graph at 2.51 kHz gave a characteristic temperature T_0 of $1.86 \cdot 10^5$ K, in good agreement with the value of $1.87 \cdot 10^5$ K obtained from plotting the radius of the Z'' - Z' loci semicircle and with $1.89 \cdot 10^5$ K from d.c. measurements. The good agreement of all 3 values confirms that in the LFR Z' may well approach the d.c. behaviour.

At frequencies over 11.92 kHz the Z'' - T characteristics departed from the d.c. limit and tended to a constant value at lower temperatures as has been reported by Long [5]. The results also suggested that at lower temperatures the electron hopping becomes independent of temperature and highly dependent on frequency, although the reasons for this change in behaviour are not fully understood. However, this tendency became less clear at frequencies over 1729 kHz and the graphs plotted in Fig. 6.18, assuming VRH with a parabolic density of states, may not be in agreement with the predicted a.c. hopping conduction.

When plotted on $\log(Z'/T)$ vs. $1/T$, as used to indicate a NNH mechanism, or on $\log(Z'/T^{0.5})$ vs. $1/T^{0.25}$ indicating a VRH behaviour with constant density of states, the graphs were inconsistent with theoretical predictions and it is suggested that the a.c. conductivity is most correctly displayed on a $\log(Z' \cdot T^{-1})$ vs. $1/T^{0.5}$ plot here, indicating the validity of the VRH model with a parabolic density of states in the LFR, IFR and HFR.

It is suggested that at $f > 1729$ kHz a regime of different hopping type conduction was present, corresponding to the UHFR features analysed in the previous sections. In the literature no conclusive explanations could be found in terms of possible physical effects underlying these features.

As mentioned before, as the frequency is increased the percolation area would eventually fall below the average grain size, and this transition might be reflected in

the impedance at the respective frequency. The UHFR behaviour may also be influenced by effects occurring out of pair hopping, where at high enough frequencies electron transfer is restricted to pairs of electron states, possibly between nearest-neighbours only. The possibility that electrons could be prevented to hop might contribute to the UHFR impedance, as with increasing frequency a decreasing fraction of the electrons would be able to follow the applied alternating voltage, whereas the percolation area stayed constant, i.e. pairs of electron states.

In Fig. 6.17 it is shown that at the highest frequency, 6000 kHz, Z' remained approximately constant with temperature over the measurement range, but was higher than corresponding values at the lower frequency of 4396 kHz. This was a reversal of the previous behaviour where Z' decreased with increasing frequency, but which is consistent with pair hopping.

Furthermore, from Fig. 6.18 it can be seen that the $Z'-T$ graphs departed from the d.c. characteristics at different temperatures, here termed 'shift-off temperature', which seemed to have increased with increasing frequency, as illustrated in Fig. 6.19.

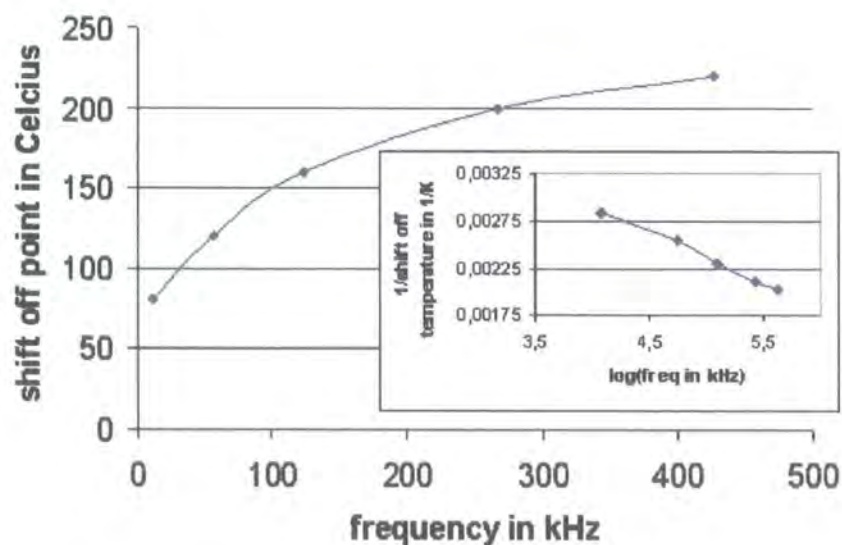


Fig. 6.19 Shift off temperature vs. frequency/ log(freq.) vs. 1/shift off T

The shift off temperature appeared to increase logarithmically with increasing temperature, as indicated by the imbedded graph.

The imaginary part Z'' of the impedance was plotted as a function of temperature at different frequencies as shown in Fig. 6.20. It shows that with increasing frequency the dependence of Z'' on temperature vanished, i.e. Z'' tended to be independent of temperature. This implies that at the UHFR a temperature independent reactive component may dominate the imaginary part of the impedance.

By analogy with the Z' vs. T plots, the Z'' - T curves tended to deviate from the low frequency characteristic at lower temperatures first.

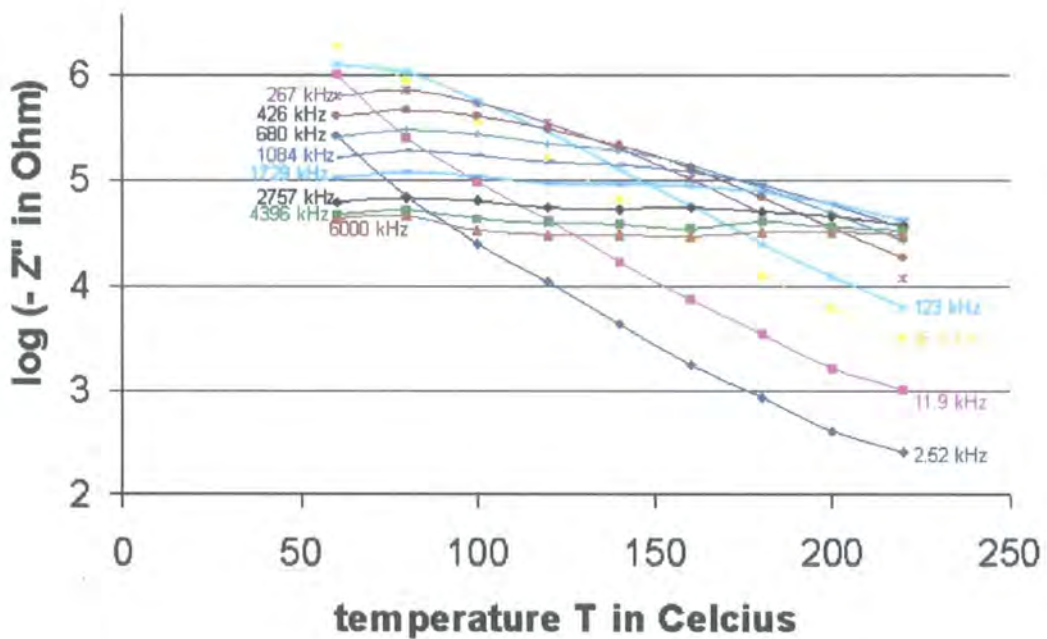


Fig. 6.20 $\log(-Z'')$ vs. temperature in Celcius

6.4.6. Equivalent circuit modelling

Several equivalent circuit models were considered and the model drawn in Fig. 6.21 was found to explain the features of the Z' vs. f , Z'' vs. f and M'' vs. f plots best. One RC element (R_1, C_1) was associated with regular electron hopping in the LFR, IFR and HFR, and the UHFR features in the Z' , Z'' and M'' vs. f plots were reasonably well described by a CRL element (C_2, R_2, L_2), associated with a modified hopping behaviour.

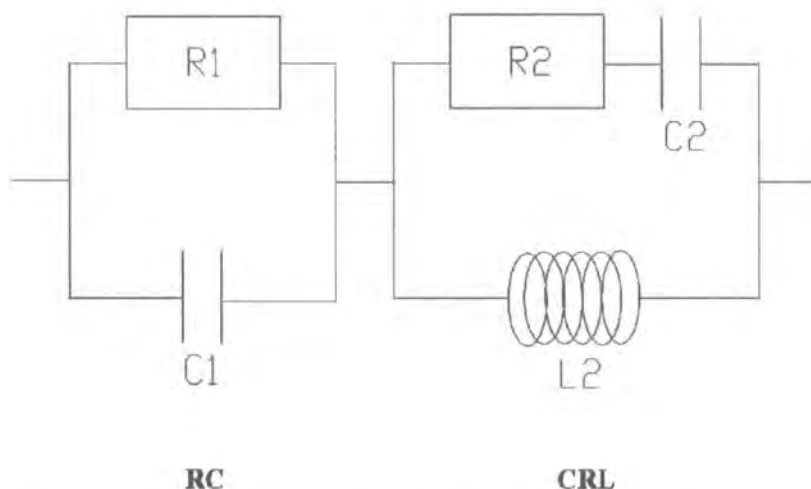


Fig. 6.21 Equivalent circuit model proposed for screen-printed samples with glass phase

The Z'' - Z' loci in Fig. 6.4 a,b,c implied that in the LFR, IFR and HFR, the CRL section played no significant effect. The inductance L_2 must have been sufficiently low and the corresponding impedance small, in order to bypass R_2 and C_2 . In the UHFR the impedance of L_2 ($\tilde{Z} = i\omega L_2$) became significant and the UHFR effects seen in the respective frequency plots would then be described by the CRL section.

The equivalent circuit model in Fig. 6.21 was chosen from several models under consideration, all containing one RC element and a second element in series containing an inductive component L. The complex impedance \tilde{Z} was calculated for all models and analysed using Maple® [12]. The trends of Z' , Z'' and M'' at $\omega \rightarrow 0$ and $\omega \rightarrow$ infinity and the extrema of the respective functions of frequency were examined and compared with the measurements.

For the full model chosen (Fig. 6.21) no solutions for extrema could be found by using Maple® due to the complexity of the equations analysed, nor were there any references for a description of this CRL type element as a standard analogue filter element in the literature [13], [14].

Therefore, the RC and the CRL elements were analysed separately, which was believed to be a valid approach as long as the two different branches were dominant at different frequencies as appeared to be the case here. The first maximum in the Z'' or M'' spectra, corresponding to the RC element, would probably have very little influence on the UHFR features of the resulting spectrum and vice versa.

6.4.6.1. Z' behaviour in respect to the equivalent circuit model

For the model in Fig. 6.21 the real part Z' was determined as the sum of the real parts of its constituents, i.e. the contribution from the RC and the CRL elements:

$$Z'(\omega) = \frac{R_1}{1 + (\omega R_1 C_1)^2} + \frac{\omega^4 R_2 C_2^2 L_2^2}{(1 - \omega^2 L_2 C_2)^2 + (\omega C_2 R_2)^2} ; \quad 6.11$$

It is easily seen that $Z' \rightarrow R_1$ as $\omega \rightarrow 0$ and $Z' \rightarrow R_2$ as $\omega \rightarrow$ infinity. In Fig. 6.13 it was shown that for low frequencies Z' was indeed constant and may well have been approaching a constant value at the high frequency end. From the inset of Fig. 6.13, R_2 could be estimated to be $\sim 2.0 \cdot 10^4$ Ohm and the temperature dependence of R_2 seemed to be rather weak.

No extremum of Z' is present for a RC section, for the CRL element the following extremum was found at ω_{\max} :

$$\omega_{\max} = \frac{2}{\sqrt{4C_2 L_2 - 2C_2^2 R_2^2}} ; \quad 6.12$$

This is a real number under the following condition:

$$R_2^2 < \frac{2L_2}{C_2} ; \quad 6.13$$

In Fig. 6.13 one maximum could be seen, which may be associated with the CRL element, and therefore R_2 , L_2 and C_2 might well fulfil relation 6.13. The second derivative of Z' indicated a maximum [$(Z')''(\omega_{\max}) < 0$], if the same relation shown in 6.13 is valid.

The value of Z' at ω_{\max} was found to be

$$Z'(\omega_{\max}) = \frac{4L_2^2}{C_2 R_2 (4L_2 - C_2 R_2^2)} ; \quad 6.14$$

If relation 6.13 is valid, this is always a positive number. Unfortunately C_2 and L_2 can not be determined separately from 6.14, only a limit for C_2 could be determined by using 6.13, but $Z'(\omega_{\max})$ would have to be determined from the poorly resolved UHFR peak in Fig. 6.13 and this was thought to be too inaccurate.

In Fig. 6.13, two minima in Z' occurred as well. The first minimum at lower frequencies may be understood in terms of the interaction between the RC and CRL elements. For the RC element $Z' \rightarrow 0$ as $\omega \rightarrow$ infinity and for the CRL element $Z' \rightarrow 0$ as frequency $\rightarrow 0$. Both elements were dominant at different frequency regimes, so at intermediate frequencies the overlap would lead to a minimum in the overall Z' . The second minimum could not be explained by the model, but all other features of the data showed qualitative agreement.

6.4.6.2. Z'' behaviour in respect to the equivalent circuit model

The imaginary part Z'' of the model in Fig. 6.21 was determined, again as the sum of the contributions from the RC and CRL element :

$$Z''(\omega) = -\frac{\omega C_1 R_1^2}{1 + (\omega C_1 R_1)^2} + \omega L_2 \frac{1 - \omega^2 L_2 C_2 + \omega^2 R_2^2 C_2^2}{(1 - \omega^2 L_2 C_2)^2 + \omega^2 R_2^2 C_2^2}; \quad 6.15$$

Here $Z'' \rightarrow 0$ as $\omega \rightarrow 0$ and increases linearly with ω at low frequencies, and Z'' decreases $\sim \omega^{-1}$ as $\omega \rightarrow$ infinity. This is clearly in agreement with the experimental findings in Fig. 6.14.

The RC and the CRL element were examined separately again. The extremum of Z'' for an RC element is straightforward and was used for data analysis earlier in this chapter (section 6.4.2.). At 3221 kHz, a change in sign of Z'' was observed, which was assumed to be associated with the CRL element. Several Z'' extrema were found for the CRL element, but the expressions obtained from Maple® were far too complicated to draw any conclusion from them. Nevertheless, useful information could be obtained by analysing Z'' of the CRL element qualitatively and it could be shown that a change of sign in Z'' occurs at

$$\omega_0 = \frac{1}{\sqrt{L_2 C_2 - R_2^2 C_2^2}} ; \quad 6.16$$

This is a real positive number under the following condition:

$$R_2^2 < \frac{L_2}{C_2} ; \quad 6.17$$

Here, the range of R_2 is more restricted than in 6.13, but both relations were assumed to be valid. It could also be shown that Z'' is positive for angular frequencies lower than ω_0 and negative otherwise. As $Z'' \rightarrow 0$ as $\omega \rightarrow 0$ and $Z'' \rightarrow 0$ as $\omega \rightarrow$ infinity, it could be concluded that at least one maximum for $\omega < \omega_0$ and one minimum for $\omega > \omega_0$ was present. In Fig. 6.14 they appear as a minimum and a maximum respectively. Fig. 6.14 showed features, which allowed this interpretation and the data might well conform with the model.

6.5. Conclusions

In this chapter it was shown that the a.c. conduction mechanism in screen-printed NiMn_2O_4 films with incorporated glass phase was dominated by a hopping process, which could be described by a conventional RC element. The Z'' - Z' loci showed the typical semicircle and in the LFR, IFR and HFR the behaviour of the Z' vs. f and the Z'' vs. T plots were in agreement with theoretical predictions for a.c. electron hopping processes.

The capacitance of the RC element was in the range of 10^{-12} F, which is a typical value for bulk effects, which implied that grain boundary effects were not significant, an implication which was confirmed by analysing M'' vs. f data.

In the LFR, Z' followed the same variable-range hopping model observed for d.c. measurements as expected and the $\ln(Z' \cdot T^{-1})$ vs. $1/T^{0.5}$ plot revealed a characteristic temperature T_0 of $1.87 \cdot 10^5 \pm 7.0 \cdot 10^2$ K, which was in good agreement with the value of $1.89 \cdot 10^5 \pm 7.0 \cdot 10^5$ K derived from d.c. measurements.

At the LFR, IFR and HFR the data was found to be consistent with the EPA model of Summerfield and Butcher [8], although the exponential dependence of ω and other parameters was found to be 1.68 ± 0.03 at temperatures of $60^\circ\text{C} - 100^\circ\text{C}$, and 1.50 ± 0.02 for $120^\circ\text{C} - 180^\circ\text{C}$, which is in contrast to values of 0.725 reported in the literature for impurity hopping conduction in semiconductors [10].

In the UHFR the EPA theory no longer holds and it was shown that at frequencies over 2.8 MHz, the Z'' - Z' loci became complicated with a different mechanism being predominant, which was better described by a CRL element.

An equivalent circuit model consisting of a RC and a CRL element in series described most of the experimental values reasonably well. It is believed that above a

critical frequency in the UHFR, electrons are confined to hops between pairs of electron states, but the exact physical effects underlying the UHFR impedance remained unclear.

All data was collected on a logarithmic frequency scale and the resolution in the UHFR was insufficient to allow for a more precise analysis of the high frequency hopping mechanism.

It was suggested that at temperatures between 60°C and 100°C the electronic properties were affected by adsorbed water on the films. For future experiments it is suggested that the sample under investigation should undergo a drying process first.

6.6. References

1. Macdonald, ed. *Impedance spectroscopy*. 1987, John Wiley & Sons, New York
2. Irvine J.T.S., Sinclair D.C., West A.R., *Electroceramics: Characterization by Impedance Spectroscopy*, *Advanced Materials*, 1990, **2**(3), p. 132
3. Hwang J.-H., Kirkpatrick K.S., Mason T.O., Garboczi E.J., *Experimental limitations in impedance spectroscopy: part IV. electrode contact effects*, *Solid State Ionics*, 1997, **98**, p. 93
4. Cole K.S., Cole R.H., *Dispersion and Absorption in Dielectrics. I. Alternating Current Characteristics*, *Journal of Chemical Physics*, 1941, **9**, p. 341
5. Long A.R., *Hopping Conductivity in the Intermediate Frequency Regime*, in *Hopping transport in Solids*, Pollak M., Shklovskii B.I., Editors, 1991, Elsevier Science, Amsterdam, p. 207
6. Zvyagin I.P., *A percolative approach to the theory of the AC hopping conductivity*, *Phys. stat. Sol. (b)*, 1980, **97**, p. 143
7. Movaghar B., Pohlmann B., Schirmacher W., *Theory of electronic hopping transport in disordered materials*, *Phil. Mag. B*, 1980, **41**, p. 41
8. Summerfield S., Butcher P.N., *A unified equivalent-circuit approach to the theory of AC and DC hopping conductivity in disordered systems*, *J. Phys. C: Solid State Phys.*, 1982, **15**, p. 7003
9. Summerfield S., *Universal low-frequency behaviour in the a.c. hopping conductivity of disordered systems*, *Phil.Mag. B*, 1985, **52**(1), p. 9
10. Abboudy S., Fozooni P., Mansfield R., Lea M.J., *Finite frequency scaling of hopping conductivity in n-InSb*, *Phil.Mag.Lett.*, 1988, **57**(5), p. 277
11. Pollak M., Geballe T.H., *Low Frequency Conductivity Due to Hopping Processes in Silicon*, *Physical Review*, 1961, **122**(6), p. 1742
12. *Maple*, 2002, Waterloo Maple Inc.
13. van Valkenburg M.E., *Analog Filter Design*, 1982, New York, CBS College publishing, Holt, Rinehart and Winston
14. Williams E., *Electric filter circuits*, 1963, London, Sir Isaac Pitman & Sons Ltd.

Chapter 7

Conclusions

7.1. Conclusions

The aim of this work was to produce reliable film type NTCR thermistors based on $\text{NiMn}_2\text{O}_{4+\delta}$ and investigate their electrical properties in a detailed study.

First, several general properties of the $\text{NiMn}_2\text{O}_{4+\delta}$ spinel system were reviewed in chapter 2, in particular the basic crystal lattice structure, the cation distribution and the oxygen content. The electrical conduction could be related to these features and a detailed consideration of the hopping mechanism present in $\text{NiMn}_2\text{O}_{4+\delta}$ was given. Furthermore, the phase stability and, depending on this, possible production routes of $\text{NiMn}_2\text{O}_{4+\delta}$ were discussed. The most recent advances in including dopants into the system were reviewed, too.

Electron-beam evaporation procedures have been applied to produce thin film NTCR thermistors. In chapter 3 the production of phase pure $\text{NiMn}_2\text{O}_{4+\delta}$ target material via a traditional ceramic precursor oxide route, the set-up of electron-beam evaporation experiments and the optimisation of the process parameters, yielding a film thickness in the range of 1 – 10 μm , were described in detail.

The thickness distribution of evaporated films was investigated and showed good agreement with a theoretical model, derived from evaporation theory, and the

sticking coefficient of the vapour on the substrates was estimated in this approach to be $80\% \pm 1.5\%$.

The composition of the films was analysed in terms of the phase purity and the Ni : Mn ratio. It was found that both compositional parameters could not be controlled in this PVD type process; no pure $\text{NiMn}_2\text{O}_{4+\delta}$ phase was detected in the films using XRD despite post-deposition annealing, and the Ni : Mn ratio, as determined using EDAX, varied in an uncontrollable way. In addition, SEM revealed that the microstructure of the samples was poor in the as-deposited state and improved with increasing annealing temperature.

It was concluded that electron-beam evaporation may not be appropriate for the production of films based on complex ternary compounds such as $\text{NiMn}_2\text{O}_{4+\delta}$. Dissociation of the target material and preferential sublimation of Ni- rich material probably occurred, leading to an excess of Ni in the films.

In order to circumvent these problems it was decided to develop thick film $\text{NiMn}_2\text{O}_{4+\delta}$ NTCR thermistors via direct screen-printing as an alternative film production technique. Screen-printed $\text{NiMn}_2\text{O}_{4+\delta}$ film samples were obtained from elsewhere [1] and the synthesis of the source powder, the production of the printing-paste, the screen-printing process itself and the post-printing sintering procedure were reviewed in chapter 4. Evidence of good surface morphology and phase purity of $\text{NiMn}_2\text{O}_{4+\delta}$ films, screen-printed with the inclusion of a glass phase and decomposable dispersing agent, was given.

In the earlier study it had been concluded that an optimised decomposition process of co-precipitated $\text{NiMn}_2(\text{C}_2\text{O}_4)_3 \cdot 6 \text{H}_2\text{O}$ at 850°C for 30 minutes may be used to

produce $\text{NiMn}_2\text{O}_{4+\delta}$ powder exhibiting a minimum grain size with a narrow distribution as required for screen-printing.

Here, the formation of appropriate $\text{NiMn}_2\text{O}_{4+\delta}$ source powder was studied in more detail. The wet chemical process used was involved with the co-precipitation of oxalates from ionic Ni, Mn and oxalate stock solutions of well known concentrations, as determined by titration methods. The oxalates were thermally decomposed at different temperatures for 6 hours and the powders obtained were analysed by XRD. It was found that a regular spinel phase can be obtained by decomposing at 800°C or higher and additionally for decomposition temperatures between 300°C and 375°C . The low temperature spinel phase found was suggested by other authors to be a cation deficient meta-stable spinel [2], [3].

Rietveld refinement was carried out for all XRD data and the defect spinel phase was found to exhibit an average grain size of 3 nm – 10 nm. This very interesting feature would enable use in nano-technological applications and it is suggested that this type of powder may be used in the future for screen-printing processes.

Furthermore, Rietveld refinement analysis confirmed that the previously determined optimised decomposition process of oxalates leads to an efficient reduction in grain size as intended by minimising the heat exposure as far as possible during decomposition.

As the main focus of this work, electrical characteristics were measured for thin and thick films and pellet, in order to gain a better understanding of electrical conduction in these materials.

For this purpose, in chapter 2 hopping conductivity was discussed in a general sense.

It was assumed that a polaron is associated with the electron transfer in $\text{NiMn}_2\text{O}_{4+\delta}$

materials [4] and a “Small-Polaron hopping” model [5] was used to give a general expression for all types of hopping resistivity ρ , in terms of several pre-exponential factors, some being material specific parameters and some depending on the type of electron hopping occurring, i.e. the hopping length r_{ij} and the activation energy ε_{ij} . The exponential dependency of resistivity was described by the percolation threshold ξ_C , which in turn was determined by the parameters r_{ij} and ε_{ij} . The percolation threshold ξ_C was derived explicitly for two different types of hopping, NNH and VRH with a parameterised density of states, from a detailed consideration of percolation theory [6].

In chapter 5 the appropriate parameters for NNH and VRH were substituted into the general formula for ρ , to give expressions for VRH, where the parameterised density of states was specified in terms of two physically meaningful cases, a constant and a parabolic density of states.

The R - T data obtained from electron-beam evaporated films on different substrates, screen-printed films with and without incorporated glass phase and from pellets were characterised using p -analysis to identify the mode of hopping. For screen-printed films and pellets, a p -value of 0.5 was identified indicating VRH with a parabolic density of states where $R \sim \exp(T_0/T)^{0.5}$, according to the Shklovskii and Efros model [6]. For these samples the p -values were uniformly close to 0.5, which was taken to indicate that production processes for screen-printed films and pellets were well controlled.

Production of electron beam evaporated films was less well controlled and there was considerable scatter in the p -values. Given this uncertainty, two modes of hopping conduction were tentatively identified; NNH ($R \sim \exp(T_0/T)$) and Mott hopping ($R \sim \exp(T_0/T)^{0.25}$) [7]. It is believed that the hopping mechanisms detected in E-beam

films differ from the VRH in thick films and pellets due to the Ni-rich composition of E-beam films, and/or due to differences in crystallinity. Hopping in an amorphous-like disordered system might well be different from that in the regular (poly-) crystalline $\text{NiMn}_2\text{O}_{4+\delta}$ spinel phase.

Comparison of screen-printed films with and without an incorporated glass phase indicated no changes in the conduction mechanism, and only slight quantitative variations in the characteristic temperature T_0 and absolute resistivity were found.

Due to the better surface density and particle packing in films with the glass phase, they are suggested to be an excellent solution for the production of NTCR thermistor devices. Other film deposition techniques have been suggested in the literature [8], [9], but especially screen-printing processes are well established for high volume low cost commercial applications and therefore, it is suggested that for industrial requirements screen-printed films with glass phase may be the most advantageous.

The film and pellet R - T characteristics examined were obtained for a LTR (130 K – 350 K) with an automated data acquisition system. A sophisticated VisualBasic 6.0 computer program was developed enabling control of the temperature and resistance measurement devices, ensuring thermal equilibrium and stable resistance measurements. Statistical errors were minimised by averaging multiple readings, which was believed to lead to very accurate R - T data. Manual R - T readings were carried out to obtain HTR (300 K – 550 K) characteristics, but were probably less precise.

For screen-printed films with glass phase the electrical conduction mechanism was further analysed using a.c. impedance spectroscopy, as described in chapter 6.

It was found that electrical conduction in the films is dominated by one specific time constant, which was associated with the VRH hopping also found for d.c. measurements. For $f < 2.76$ MHz, the a.c. data was in agreement with theoretical predictions for hopping conductivity, and the low frequency behaviour ($f < 11.9$ kHz) of Z' was virtually identical with the d.c. characteristics. Conduction for $f < 2.76$ MHz could be described by an equivalent circuit containing a single RC element and the R - T characteristics obtained from the semicircle in the Z' - Z'' loci clearly indicated VRH with a parabolic density of states. The order of magnitude of the capacitance in the RC element was determined as well and indicated a typical bulk effect.

The VRH mechanism with a parabolic density of states was confirmed again by plotting the real part Z' of the complex impedance vs. T as a $\log(Z' \cdot T^{-1})$ vs. $1/T^{0.5}$ plot, which showed the same d.c. behaviour at low frequencies ($f < 11.9$ kHz) as found from the semicircle radii and from d.c. measurements. For $f < 1729$ kHz the $\log(Z' \cdot T^{-1})$ vs. $1/T^{0.5}$ plots were in good agreement with theoretical predictions for a.c. hopping [10], whereas corresponding plots on different scales appropriate for alternative hopping mechanisms were clearly not. This was further strong evidence that conduction was by VRH with a parabolic density of states. At the LFR, IFR and HFR the a.c. data was consistent with the Extended Pair Approximation theory proposed by Summerfield and Butcher [11].

At lower frequencies no additional time constant was detected, as might have been expected for a possible grain boundary or electrode contribution. Therefore, it may be concluded that hopping in $\text{NiMn}_2\text{O}_{4+\delta}$ thick films can be regarded as uniform throughout the sample at these frequencies, no matter whether hopping took place over grain boundaries or within grains.

At higher frequencies in a UHFR a different contribution to the impedance was detected which was best described by a CRL element. This contribution seemed to have no influence on the d.c. behaviour and from the a.c. data presented it is believed that it was not a standard hopping process and may not be described by a simple VRH model.

At higher frequencies electron hopping would probably be restricted to hopping between pairs of electron states. Pair hopping associated with a polaron should exhibit some time dependence, such that the hopping probability would decrease with increasing frequency, leading to the UHFR effects observed. The hopping between pairs of electron states would be restricted to nearest-neighbour hops, and clearly VRH models would no longer apply, which may lead to a modified hopping type conduction described by the CRL element.

7.2. Scope for future work

Generally, future work should be mainly focussed on the inclusion of different dopants into the $\text{NiMn}_2\text{O}_{4+\delta}$ spinel system, such as Co or Cu, to improve conductivity and minimise ageing effects. A promising method for doping would be the co-precipitation of oxalates, as Co and Cu oxalates exhibit a very low solubility, comparable to Ni and Mn oxalates [12].

Low decomposition temperatures of $\sim 350^\circ\text{C}$ may be chosen to obtain a nano-sized powder, which could be mixed and dispersed with a nano-scale glass powder, enabling screen-printing processes leading to very dense and even films.

In general, the amount of glass phase would need more careful adjustment to give optimum capillary actions between single grains, which would ideally compact the films, so that it would leave a minimum number of pores and holes on the film surface.

It is believed that the conduction mechanism in $\text{NiMn}_2\text{O}_{4+\delta}$ should be further investigated through the use of combined Scanning Tunneling Spectroscopy (STS) and Scanning Tunneling Microscopy (STM). In a recent STM/STS study [13], [14] the shape of the density of states in $\text{NiMn}_2\text{O}_{4+\delta}$ was examined and it seems to be possible that electron hopping between two impurity bands separated by the Fermi-level may occur, one impurity band corresponding to electron states consisting of Mn^{3+} donors and one consisting of Mn^{4+} acceptors. The two impurity bands were situated in a large band gap, as expected for insulating material, and showed a parabolic shaped gap around the Fermi-level, which would explain the validity of a variable range hopping model with a parabolic density of states. However, these

findings need far more detailed analysis and have to be confirmed in similar experiments. Photoelectron spectroscopy may be a powerful tool to obtain more precise information on the structure of the density of states in film type $\text{NiMn}_2\text{O}_{4+\delta}$ [15].

Furthermore, the possibility of double-exchange effects occurring in $\text{NiMn}_2\text{O}_{4+\delta}$ should be considered in context with the electrical conduction. Perovskite structured manganese oxides do exhibit double-exchange effects between Mn^{3+} and Mn^{4+} cations [16]. This leads to a rather high conductivity if a considerable amount of Mn^{3+} cations change their valence state to Mn^{4+} , as accomplished by introducing dopants of double or single charged cations [17]. Electrical conductivity in $\text{NiMn}_2\text{O}_{4+\delta}$ is at least 2 orders of magnitude lower than in these perovskite compounds and the occurrence of double-exchange effects is not at all clear. Double-exchange effects in perovskite manganites were found to rely on a ferromagnetic coupling of Mn^{3+} and Mn^{4+} cations [18]. In $\text{Ni}_{0.5}\text{Cu}_{0.5}\text{Fe}_2\text{O}_4$ spinels this type of ferromagnetic interaction of outer shell electrons was detected for intra-sublattice exchange interactions on octahedral sites, and anti-ferromagnetic interactions were found on all inter-sublattice interactions and for intra-sublattice interactions on tetrahedral sites [19]. Mössbauer spectroscopy is the appropriate method to determine these interactions qualitatively and quantitatively, and should be carried out for pure $\text{NiMn}_2\text{O}_{4+\delta}$ as well. This would lead to a clear understanding of the dimensions of these interactions and possibly, the occurrence of double-exchange effects could be supported or negated. Furthermore, pure Mn^{3+} and Mn^{4+} hopping on octahedral sites or the involvement of Mn^{2+} cations on tetrahedral sites in the hopping process could also be identified.

For an explicit understanding of the quantitative correlation of resistivity on cation distribution in $\text{NiMn}_2\text{O}_{4+\delta}$ it is believed that a comprehensive study would be required. Besides the possible involvement of Mn^{2+} cations on tetrahedral sites, one set of samples of varying composition has to be investigated, specifying the number of possible Mn^{2+} cations occurring on octahedral sites, as previously determined using neutron diffraction data [20], the oxygen content must be examined using titration methods as demonstrated by Feltz and Töpfer [2], and the absolute ratios of Mn^{2+} , Mn^{3+} and Mn^{4+} have to be obtained preferably using XPS [21], [22]. Only if all these experiments were to be carried out for the same set of samples, could the resistivity of these be connected to the cation distribution.

Additionally, it is suggested that further electrical characterisations should be carried out using a.c. impedance spectroscopy over a larger range of frequency to confirm the findings presented and examine the high frequency behaviour of $\text{NiMn}_2\text{O}_{4+\delta}$ materials in more detail. Measurements for pellets, thin electron-beam evaporated or sputtered films and screen-printed films without a glass phase should be carried out as well.

As a final conclusion it is stated that reliable NTCR thermistors, based on $\text{NiMn}_2\text{O}_{4+\delta}$, were produced using screen-printing methods with an included glass phase. The d.c. and a.c. characteristics of the films were described and specified.

7.3. References

1. Schmidt R., *Screen Printing of Coprecipitated NiMn₂O₄ for Production of NTC Thermistors*, 2001, Diploma Dissertation, Department of Material Science III, University of Erlangen-Nuremberg, Erlangen
2. Feltz A., Töpfer J., *Bildung von Defektspinellen und Phasenbeziehungen im System Ni_xMn_{3-x}O₄*, Zeitschrift fuer anorganische und allgemeine Chemie, 1989, 576, p. 71
3. Tang X.-X., Manthiram A., Goodenough J.B., *NiMn₂O₄ revisited*, Journal of Less-Common Metals, 1989, 156, p. 357
4. Fritsch S., Sarrias J., Brieu M., Couderc J.J., Baudour J.L., Snoeck E., Rousset A., *Correlation between the structure, the microstructure and the electrical properties of nickel manganite negative temperature coefficient (NTC) thermistors*, Solid State Ionics, 1998, 109, p. 229
5. Tuller H.L., Nowick A.S., *Small polaron electron transport in reduced CeO₂ single crystals*, Journal of Physics and Chemistry of Solids, 1977, 38, p. 859
6. Shklovskii B.I., Efros A.L., *Electronic properties of doped semiconductors*, Solid State Sciences 45, 1984, Berlin, Springer - Verlag
7. Mott N.F., *Conduction in glasses containing transition metal ions*, J. Non-Crystal.Solids, 1968, 1, p. 1
8. Schmidt R., Basu A., Brinkman A.W., *Production of NTCR thermistor devices based on NiMn₂O_{4+δ}*, Journal of the European Ceramic society, In Press
9. Baliga S., Jain A.L., Zachofsky W., *Sputter deposition and characterisation of Ni-Mn-O and Ni-Co-Mn-O spinels on polyamide and glass substrates*, Applied Physics A : Solids and Surfaces, 1990, 50, p. 472
10. Long A.R., *Hopping Conductivity in the Intermediate Frequency Regime*, in *Hopping transport in Solids*, Pollak M., Shklovskii B.I., Editors, 1991, Elsevier Science, Amsterdam, p. 207
11. Summerfield S., Butcher P.N., *A unified equivalent-circuit approach to the theory of AC and DC hopping conductivity in disordered systems*, J. Phys. C: Solid State Phys., 1982, 15, p. 7003
12. Weast R.C., ed. *CRC Handbook of Chemistry and Physics*. 1977/1978, CRC Press, Cleveland

13. Basu A., Brinkman A.W., Hase T.P.A., Klusek Z., Datta P.K., Pierzgalski S., *In situ study of the effect of temperature on electronic structure of $Ni_xMn_{3-x}O_{4+\delta}$ thin films using scanning tunnelling spectroscopy*, Journal of Applied Physics, 2002, **92**, p. 4123
14. Basu A., Brinkman A.W., Schmidt R., Klusek Z., Kowalczyk P., Datta P.K., *A study of electronic states of $Ni_xMn_{3-x}O_{4+\delta}$ thin films using scanning tunneling microscopy and current imaging tunneling spectroscopy*, Journal of the European Ceramic society, in Press
15. <http://www.fkp.uni-erlangen.de/welcome.html>, *Photoelectron spectroscopy*,
16. Zener C., *Interaction between d-Shells in the Transition Metals. II. Ferromagnetic Compounds of Manganese with Perovskite Structure*, Physical Review, 1951, **82**(3), p. 403
17. Troyanchuk I.O., Kolesova I.M., Szymczak H., Nabialek A., *Preparation, magnetic and transport properties of $A_{0.66}Ba_{0.34}MnO_{3-\gamma}$ ($A=Pr, Nd, Sm, Eu, Gd$) perovskites*, Journal of Magnetism and Magnetic Materials, 1997, **176**, p. 267
18. Gennes P.-G.d., *Effects of Double Exchange in Magnetic Crystals*, Physical Review, 1960, **118**(1), p. 141
19. Kim W.C., Kim S.J., Kim C.S., *Mössbauer studies of superexchange interaction in $Ni_{0.5}Cu_{0.5}Fe_2O_4$* , Journal of Magnetism and Magnetic Materials, 2002, **239**, p. 82
20. Boucher B.P., Buhl R., Perrin M., *Etude cristallographique du manganite spinelle cubique $NiMn_2O_4$ par diffraction de neutron*, Acta Cryst, 1969, **B25**, p. 2326
21. Hashemi T., Brinkman A.W., *X-ray photoelectron spectroscopy of nickel manganese oxide thermistors*, Journal of the Materials Research Society, 1992, **7**(5), p. 1278
22. Brabers V.A.M., Van Setten F.M., Knapen P.S.A., *X-ray photoelectron spectroscopy study of the cation valencies in nickel manganite*, Journal of Solid State Chemistry, 1983, **49**, p. 93

Appendix A

List of Publications

Journal articles

1.) R. Schmidt, A. Stiegelschmitt, A. Roosen, A.W. Brinkman, *Screen Printing of Co-precipitated NiMn₂O₄ for Production of NTC Thermistors*, Journal of the European Ceramic Society, **23**, Issue 10, 2003, 1549 - 1558

Conference proceedings

E-MRS – IUMRS – ICEM Conference, Strasbourg, May 2000

2.) R. Schmidt, A.W. Brinkman, *Preparation and characterisation of NiMn₂O₄ films*, International Journal of Inorganic Materials, **3**, 2001, 1215-1217,

7th Conference of the European Ceramic Society, Bruges, September 2001

3.) R. Schmidt, A. Stiegelschmitt, A. Roosen, A.W. Brinkman, *Preparation and Performance of Thick Film NTC Thermistors*, Key Engineering Materials, **206-213**, 2002, 1417-1420

4.) R. Schmidt, A. Basu, A.W. Brinkman, *Production of NTCR thermistor devices based on $NiMn_2O_{4+\delta}$* , Journal of the European Ceramic Society, **in Press**

5.) A. Basu, A.W. Brinkman, R. Schmidt, *Effect of oxygen partial pressure on the NTCR characteristics of sputtered $Ni_xMn_{3-x}O_{4+\delta}$ thin films*, Journal of the European Ceramic Society, **in Press**

6.) A. Basu, A.W. Brinkman, R. Schmidt, Z. Klusek, P. Kowalczyk, P.K. Datta, *A study of electronic states of $Ni_xMn_{3-x}O_{4+\delta}$ thin films using scanning tunnelling microscopy and current imaging tunnelling spectroscopy*, Journal of the European Ceramic Society, **in Press**

Appendix B

XRD reference patterns from JCPDS data base

B1	NiMn ₂ O ₄ ; JCPDS 71-852
B2	NiMnO ₃ ; JCPDS 48-1330
B3	NiO ; JCPDS 44-1159
B4	Mn ₂ O ₃ ; JCPDS 24-508
B5	Al ; JCPDS 4-787
B6	Al ₂ O ₃ ; JCPDS 46-1212
B7	MnO ; JCPDS 7-230
B8	Ni ₆ MnO ₈ ; JCPDS 42-479
B9	Mn ₃ O ₄ ; JCPDS 24-734

NiMn₂O₄ ; JCPDS 71-852

d-space	angle 2-th	intensity	h	k	l
4,85	18,27735	20	1	1	1
2,97	30,06417	34	2	2	0
2,53	35,45208	100	3	1	1
2,425	37,04162	8	2	2	2
2,1	43,03791	21	4	0	0
1,71	53,54733	8	4	2	2
1,62	56,78294	31	5	1	1
1,49	62,25968	34	4	4	0
1,42	65,70308	1	5	3	1
1,33	70,78468	2	6	2	0
1,28	73,99728	6	5	3	3
1,27	74,67871	3	6	2	2
1,21	79,07911	2	4	4	4

NiMnO₃ ; JCPDS 48-1330

d-space	angle 2-th	intensity	h	k	l
3,59	24,78036	40	0	1	2
2,65	33,79721	100	1	0	4
2,45	36,65013	80	1	1	0
2,28	39,49193	5	0	1	5
2,26	39,85615	7	0	0	6
2,15	41,98903	25	1	1	3
2,08	43,47269	6			
2,02	44,83294	10	2	0	2
1,8	50,67429	40	0	2	4
1,66	55,29564	80	1	1	6
1,57	58,76483	4			
1,56	59,17885	5	0	1	8
1,45	64,17864	30	2	1	4
1,416	65,91222	20	3	0	0
1,293	73,1316	20	1	0	10
1,285	73,66167	5	1	1	9
1,236	77,10321	10	2	1	7

NiO ; JCPDS 44-1159

d-space	angle 2-th	intensity	h	k	l
2,41	37,28063	61	1	0	1
2,09	43,25418	100	0	1	2
1,48	62,72788	35	1	1	0
1,26	75,37413	13	1	1	3
1,21	79,07911	8	2	0	2
1,04	95,5774	4	0	2	4

Mn₂O₃ ; JCPDS 24-508

d-space	angle 2-th	intensity	h	k	l
3,84	23,14394	18	2	1	1
2,72	32,90235	100	2	2	2
2,52	35,59746	2	3	2	1
2,35	38,269	11	4	0	0
2,01	45,06821	9	3	3	2
1,85	49,21223	10	4	3	1
1,72	53,21143	2	5	2	1
1,66	55,29564	27	4	4	0
1,61	57,16799	2	4	3	3
1,53	60,4588	2	6	1	1
1,45	64,17864	4	5	4	1
1,42	65,70308	11	6	2	2
1,39	67,3074	3	6	3	1
1,36	68,99862	3	4	4	4
1,08	90,99826	2	6	6	2

Al ; JCPDS 4-787

d-space	angle 2-th	intensity	h	k	l
2,3379	38,47483	100	1	1	1
2,02372	44,74606	47	2	0	0
1,43117	65,12649	22	2	2	0
1,22086	78,24018	24	3	1	1
1,16895	82,44221	7	2	2	2
1,01236	99,08621	2	4	0	0

Al₂O₃ ; JCPDS 46-1212

d-space	angle 2-th	intensity	h	k	l
3,48003	25,57648	45	1	1	0
2,55044	35,15865	100	2	1	1
2,38001	37,76806	21	1	0	-1
2,08554	43,35136	66	2	1	0
1,74002	52,55198	34	2	2	0
1,60125	57,50945	89	3	2	1
1,51088	61,30564	14	3	3	2
1,40466	66,51302	23	3	1	0
1,37357	68,22238	27	1	1	-2
1,23933	76,85805	29	4	3	3
1,23448	77,21569	12	4	3	2
1,09901	88,99893	9	4	4	2

MnO ; JCPDS 7-230

d-space	angle 2-th	intensity	h	k	l
2,56803	34,91006	60	1	1	1
2,22246	40,55868	100	2	0	0
1,57	58,76483	60	2	2	0
1,34	70,17826	20	3	1	1
1,28	73,99728	14	2	2	2
1,11	87,88929	12	4	0	0
1,02	98,08484	10	3	3	1

Ni₆MnO₈ ; JCPDS 42-479

d-space	angle 2-th	intensity	h	k	l
4,80188	18,4621	25	1	1	1
4,1626	21,32837	14	2	0	0
2,94042	30,37386	13	2	2	0
2,50673	35,79226	13	3	1	1
2,39953	37,44934	65	2	2	2
2,07708	43,53692	100	4	0	0
1,906	47,67503	2	3	3	1
1,8576	48,99762	10	4	2	0
1,69607	54,0227	9	4	2	2
1,59875	57,6078	10	5	1	1
1,4681	63,2949	45	4	4	0
1,40418	66,53871	9	5	3	1
1,38519	67,57251	5	6	0	0
1,26693	74,89069	25	5	3	3
1,19906	79,94488	20	4	4	4
1,03801	95,81987	13	8	0	0

Mn₃O₄ ; JCPDS 24-734

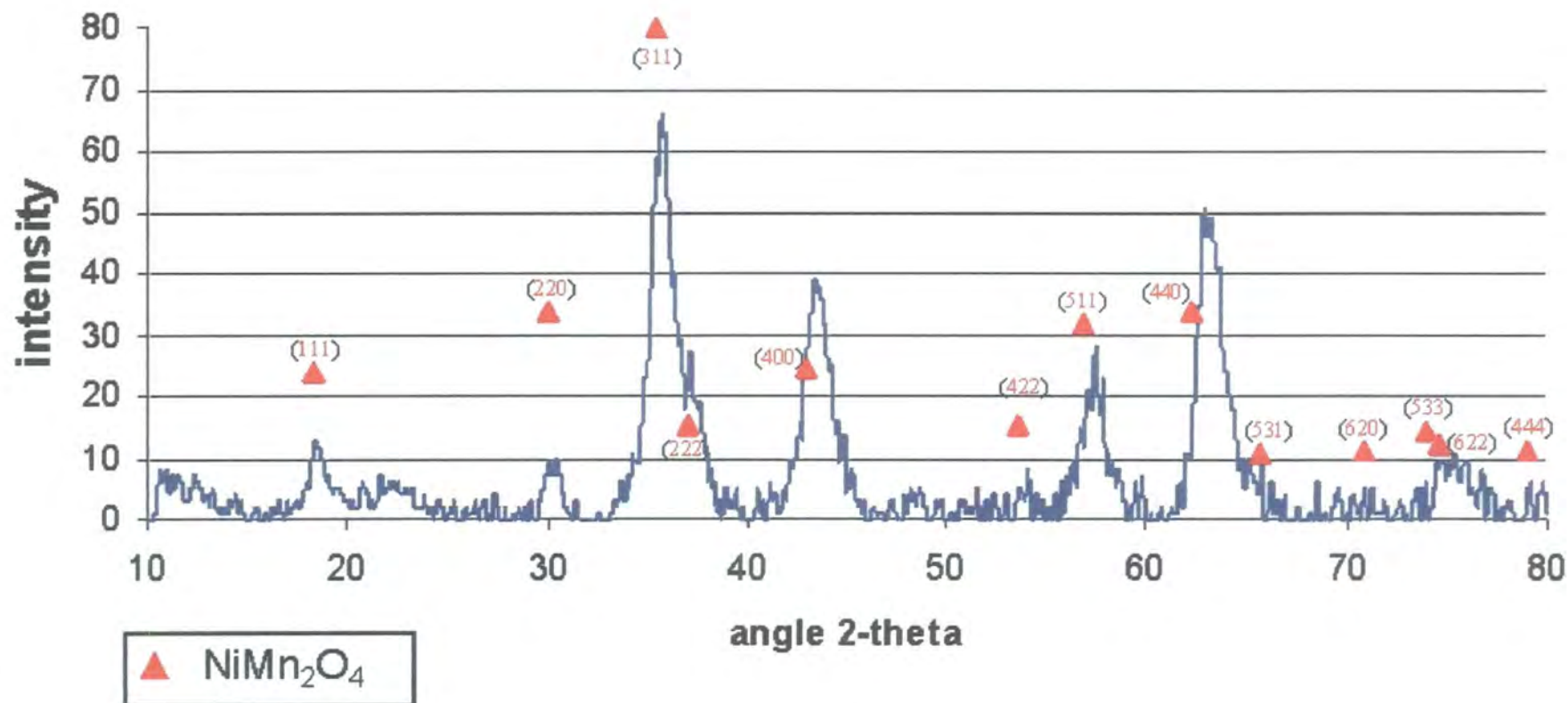
d-space	angle 2-th	intensity	h	k	l
4,92308	18,00376	30	1	0	1
3,08899	28,88038	40	1	1	2
2,88045	31,02197	17	2	0	0
2,768	32,31601	85	1	0	3
2,487	36,08594	100	2	1	1
2,463	36,44987	20	2	0	2
2,37	37,93366	20	0	0	4
2,037	44,43873	20	2	2	0
1,829	49,81551	7	2	0	4
1,799	50,70445	25	1	0	5
1,701	53,85346	10	3	1	2
1,64	56,02894	8	3	0	3
1,576	58,51933	25	3	2	1
1,544	59,85428	50	2	2	4
1,526	60,63391	2	2	1	5
1,472	63,10787	3	1	1	6
1,441	64,62797	20	4	0	0
1,426	65,39201	3	3	2	3
1,384	67,63845	4	2	0	6
1,382	67,74958	2	4	1	1
1,349	69,64205	6	3	0	5
1,289	73,39559	2	4	2	0
1,278	74,13247	10	4	1	3
1,243	76,58986	6	4	2	2
1,23	77,54936	5	4	0	4
1,198	80,0299	5	2	1	7
1,193	80,4337	4	3	1	6
1,183	81,25526	4	0	0	8
1,144	84,65048	2	4	3	1
1,131	85,85585	4	4	2	4
1,124	86,52146	8	4	1	5
1,099	88,99996	2	5	1	2
1,083	90,67572	8	4	3	3
1,063	92,87886	3	5	2	1
1,033	96,437	5	3	2	7
1,023	97,69843	3	2	2	8
1,018	98,34455	6	4	4	0

Appendix C

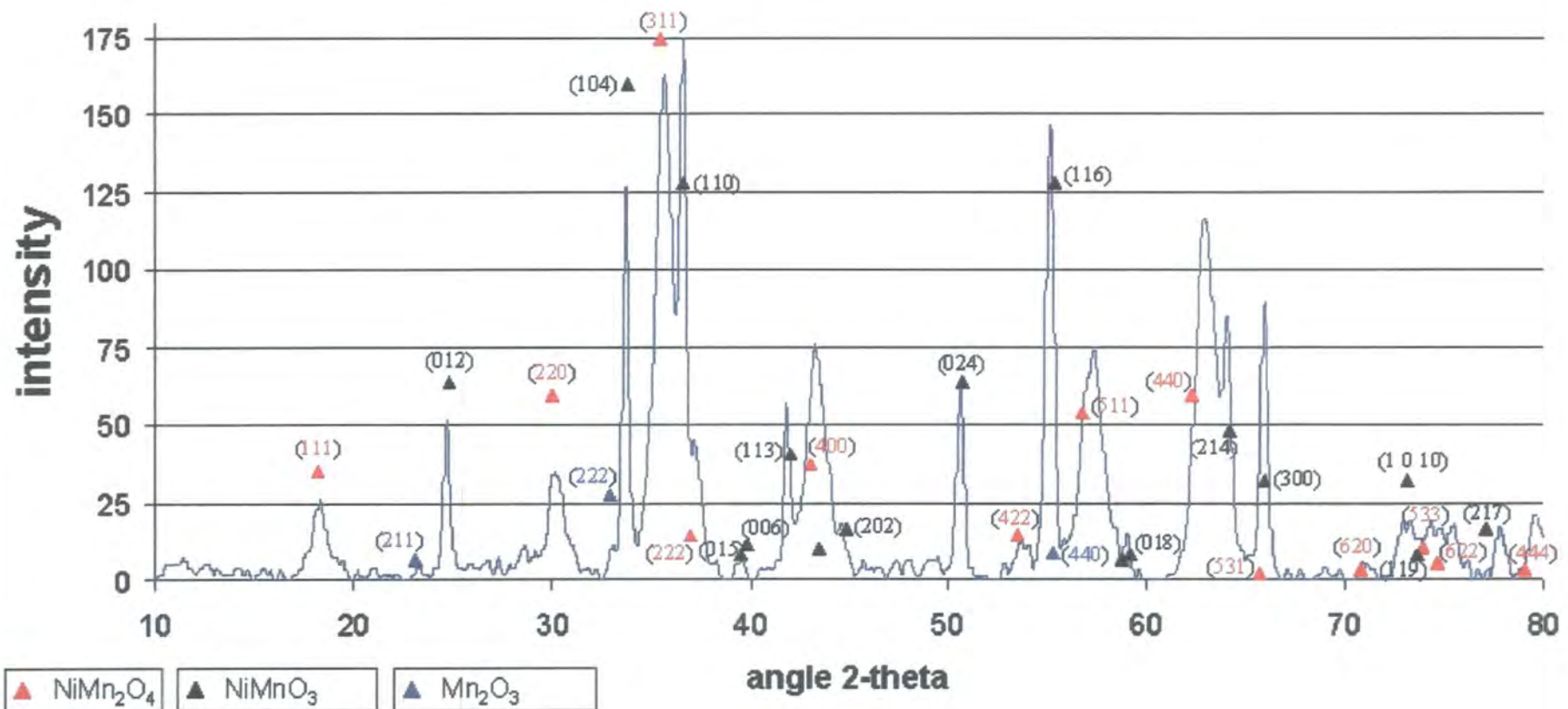
X-ray spectra of decomposed oxalates

- C1 $T_D = 350^\circ\text{C}$; 6 hours
Phases detected : NiMn_2O_4
- C2 $T_D = 450^\circ\text{C}$; 6 hours
Phases detected : NiMn_2O_4 , NiMnO_3 , Mn_2O_3 (only hints)
- C3 $T_D = 600^\circ\text{C}$; 6 hours
Phases detected : NiMnO_3 , Mn_2O_3 , Mn_3O_4 (only hints)
- C4 $T_D = 750^\circ\text{C}$; 6 hours
Phases detected : NiMn_2O_4 , NiMnO_3 , Mn_2O_3
- C5 $T_D = 850^\circ\text{C}$; 30 min, optimised process
Phases detected : NiMn_2O_4

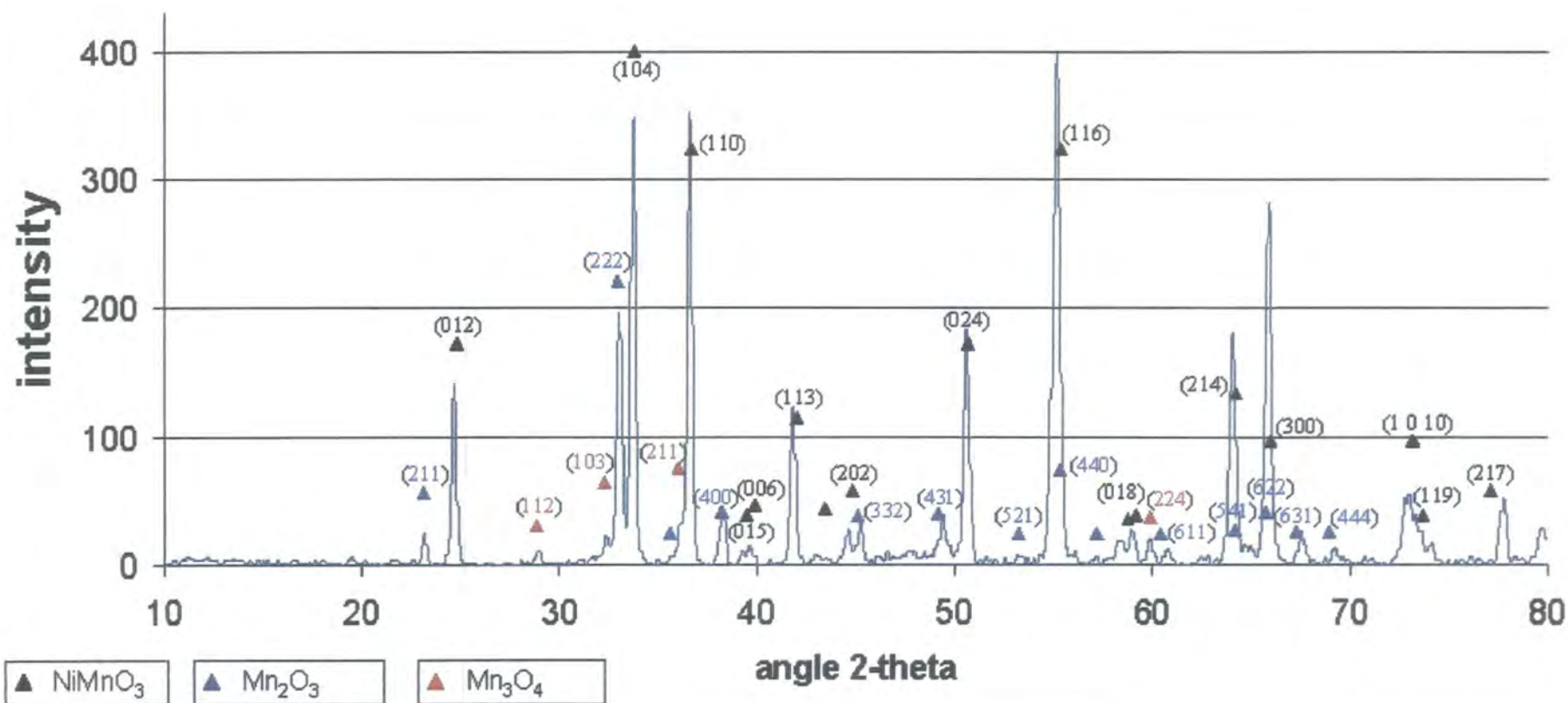
Oxalates decomposed at 350°C



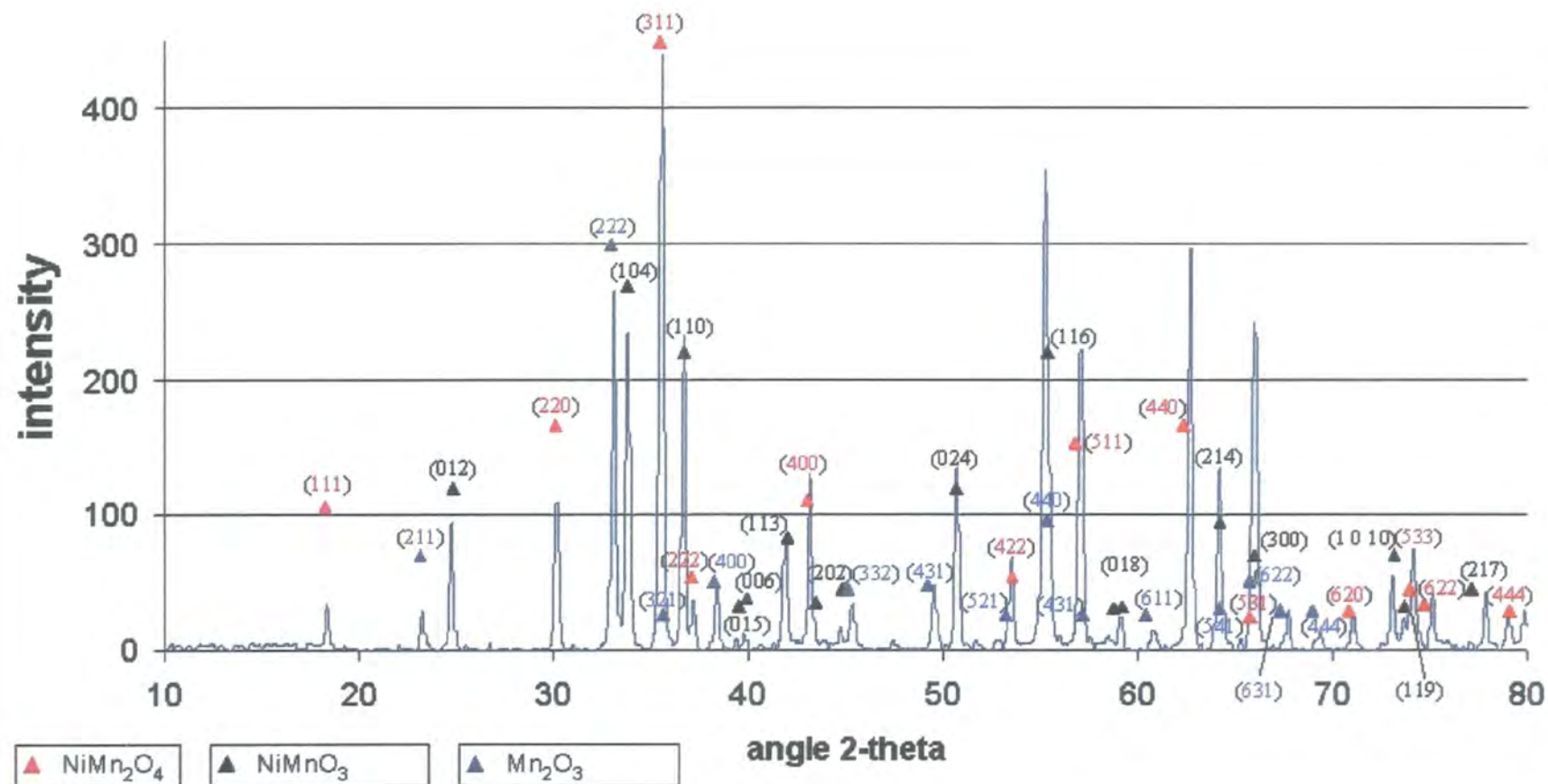
Oxalates decomposed at 450°C



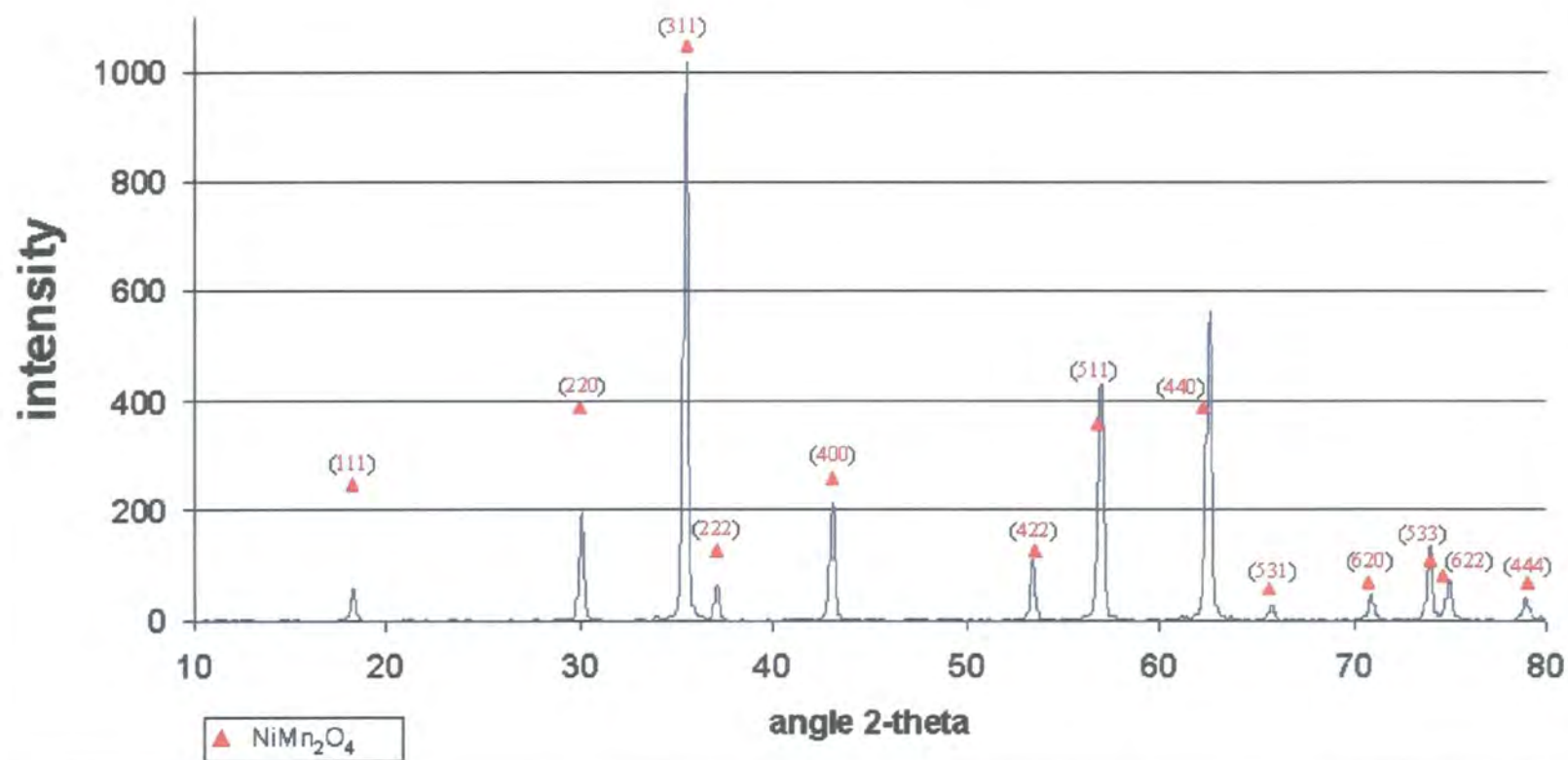
Oxalates decomposed at 600°C



Oxalates decomposed at 750°C



Oxalates decomposed at 850°C optimised process

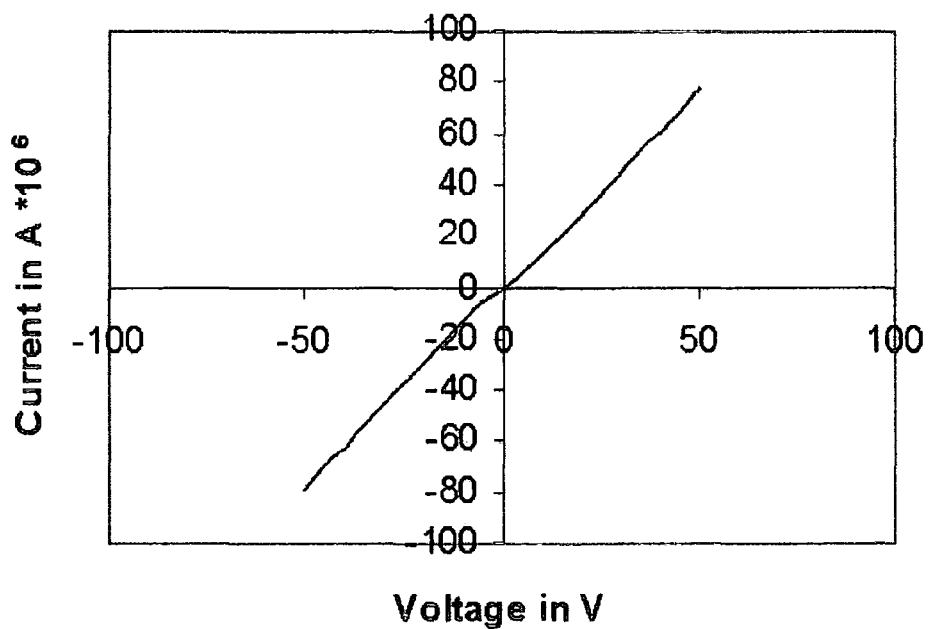


Appendix D

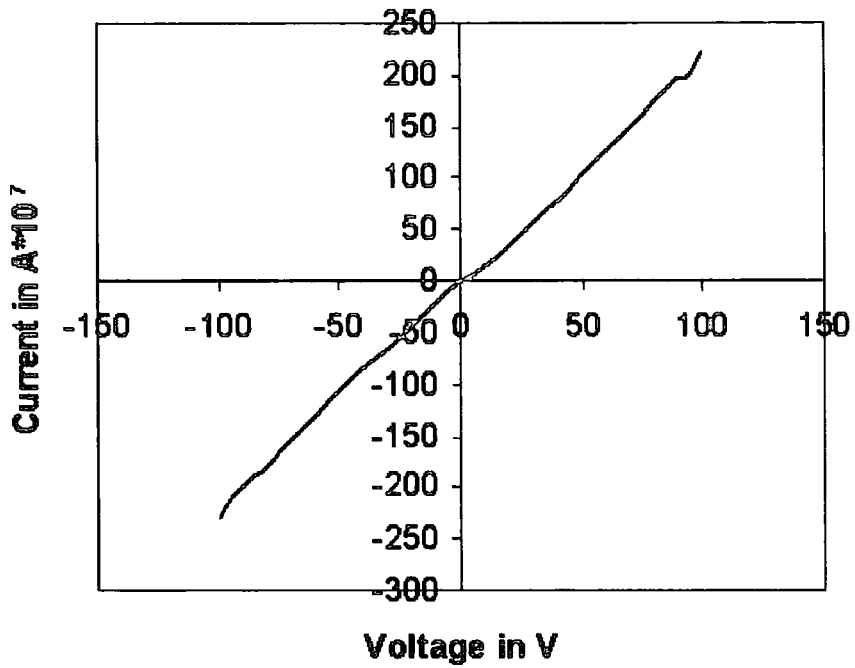
I-V behaviour of Al contacts

- D1 *I-V* characteristics at 350 K
- D2 *I-V* characteristics at 293 K
- D3 *I-V* characteristics at 150 K

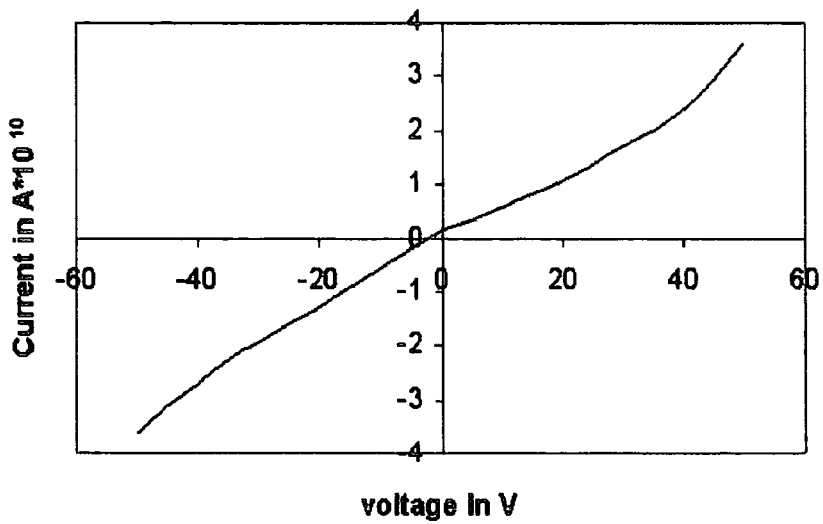
Current vs. Voltage characteristic at 350 K



Current vs. Voltage characteristic at 293.2K



Current vs. voltage characteristic at 150 K

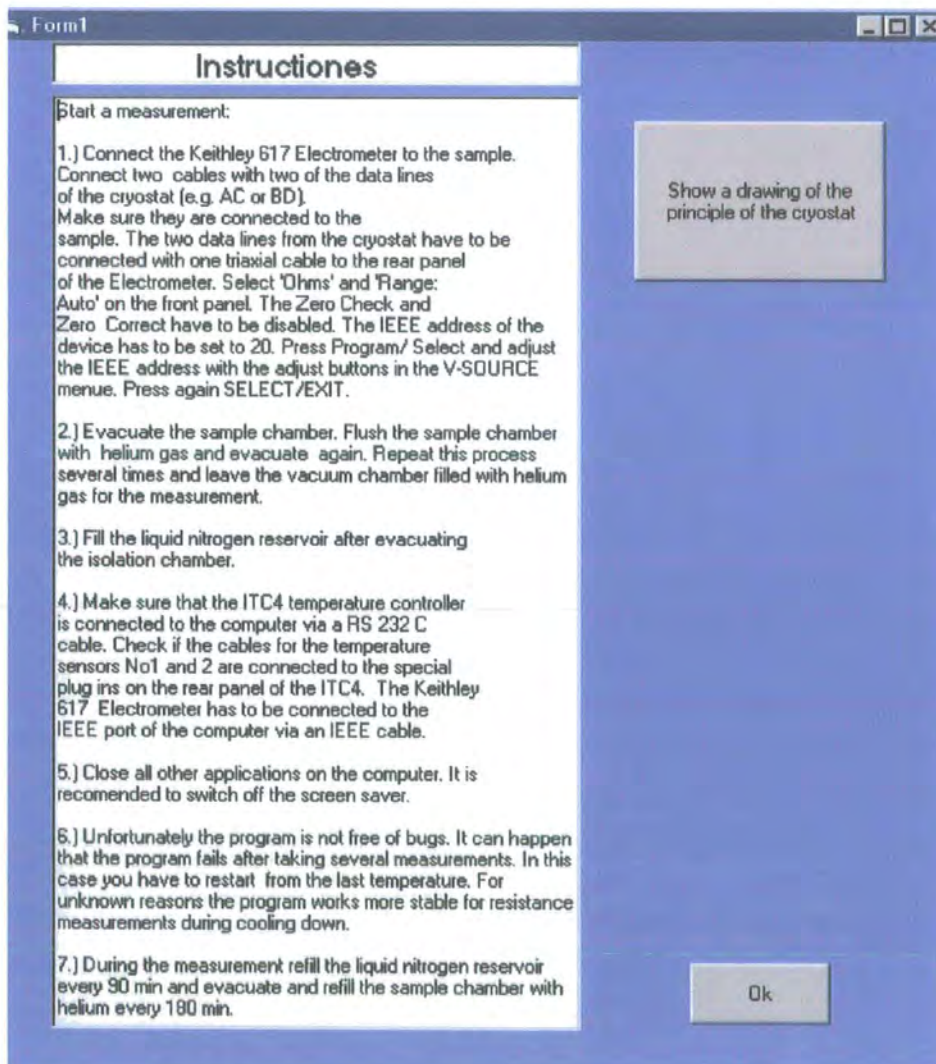


Appendix E

Control Software for automated *R-T* data acquisition

The principle underlying the program was given in the schematic diagram in Fig. 5.3, chapter 5.3.3.

Introduction window



The code behind this window is not shown here.

Data Input window

Form1

Resistance vs. Temperature Measurement

<p>Please enter the lowest temperature!</p> <p>80 K ◀ ▶ Confirmation</p> <p>The lowest temperature is 80 K!</p>	<p>Please choose a measurement program:</p> <p>1.) Measure the resistance during heating up 2.) Measure during cooling down 3.) Go in a cycle up and down 4.) Go in a cycle down and up</p> <p>1.) up 2.) down 3.) up and down 4.) down and up</p> <p>Heating up & cooling down Confirmation</p>
<p>Please enter the highest temperature!</p> <p>100 K ◀ ▶ Confirmation</p> <p>The highest temperature is 100 K!</p>	<p>Please enter a filename for the file your data will be stored in! Please use no dots or commas in the filename!</p> <p>Your data will be stored in C:\Program Files\Microsoft Visual Studio\VB98\Data\test</p> <p>Confirmation</p>
<p>Please choose the temperature increment!</p> <p>1 K ◀ ▶ Confirmation</p> <p>The temp. increment is 1 K!</p>	<p><input type="checkbox"/> Input completed successfully</p> <p>The measurement will contain 41 measurement steps! The data will be stored in C:\Program Files\Microsoft Visual Studio\VB98\Data\test You will run the measurement program No. 3</p> <p>Change Start</p>
<p>Please specify the conduction mechanism you expect for the sample under investigation. Give the values for the parameter A and B.</p> $\rho = \rho_0 T^A \exp\left(\frac{T_0}{T}\right)^{\frac{1}{B}}$ <p>A: 0.5 Confirmation A= 0.5</p> <p>B: 4 Confirmation B= 4</p>	

The code behind this window is not shown here.

Measurement window

Form1

Experiment Monitoring

Parameter

low temperature: 80 Kelvin
high temperature: 100 Kelvin
Temperature increment: 1
Number of measurements: 41
Measurement Program :3
Heating up and cooling down

Interrupt the experiment after the next measurement step

Interrupt the experiment immediately

Set temperature

80 K

Temperature sensor1

0 K

Temperature sensor2

Resistance

Operation

Wait until the set temperature is reached.

Settling down

Code :

Global Variables

Option Explicit

Global a As Single ' parameter for the conduction mechanism

Global B As Single ' parameter for the conduction mechanism

Global buff As Integer

Global Buffer As String

Global Check As Integer

Global Checkbox As String

Global CheckInterrupt As Integer ' number to be changed for interrupting the

Global Command As String 'experiment after the next measurement

Global DwellingTime As Integer ' time for the temp. to settle down; set to 1 min

Global Filename As String 'Name of the file where the data is stored in

Global i As Integer 'general counter

Global Label As Integer

Global Inresmax As Single ' maximum resistance measured so far

Global MeasurementSteps As Single 'number of measurements

Global MeasProg As Integer

Global MeasProgT As String
 Global N As Integer 'Counter for all temperature measurements
 Global NL
 Global o As Integer
 Global Path As String
 Global Pathname As String 'pathname
 Global Pathnamecheck As Integer
 Global program As Integer
 Global Resistance(1 To 210) As Single ' resistance in Ohm
 Global resmax As Single 'maximum of the resistance measured so far in one cycle
 Global Sing As Single
 Global Settemp As Integer 'settemperature in Kelvin * 10 for the ITC4 device
 Global Settempdisplay As Single
 Global t As Integer 'Counter for all valid temperature measurements
 Global Temp(1 To 2000) As Single 'Buffer for temperatures
 Global TempEnd As Integer
 Global Temperature(1 To 210) As Single
 Global TempIncrement As Integer 'temperature increment
 Global TempStart As Integer 'starting temperature in K
 Global Text As String
 Global value As Single
 Global W As Integer
 Global xt As Long

Main program

```

Private Sub Form_Load() 'Opens the data file and writes the parameter in it
    Dim MeasProgText As String
    If program = 1 Then
        MeasProgText = "Heating up"
    End If
    If program = 2 Then
        MeasProgText = "Cooling down"
    End If
    If program = 3 Then
        MeasProgText = "Heating up and cooling down"
    End If
    If program = 4 Then
        MeasProgText = "Cooling down and heating up"
    End If
    DataInput.Hide
    Monitoring.Move 200, 1200
    t = 0
    cycle = 1
    Label = 1
    graph.Show 'show the blank graph
    Ingraph.Show
    Pathname = "C:\Program Files\Microsoft Visual Studio\vb98\Data\" & Filename
    Open Pathname For Output As #1 'open the data file as #1 and print start parameter in this file
    Print #1, " Start Temperature: " & TempStart & " Kelvin"
  
```

```

Print #1, " End Temperature: " & TempEnd & " Kelvin"
Print #1, " Temperature increment: " & TempIncrement & " Kelvin"
Print #1, " Measurement program = " & program & " : " & MeasProgText
Print #1, " Measurement steps: " & MeasurementSteps
Print #1, " "
Print #1, " Temperature in Kelvin   Resistance in Ohm   1/(Temperature^" & B & ")
ln(Resistance*Temperature^-" & a & ")   "
Print #1, " _____"
Call Timer(1000)
Text9.Text = "low temperature: " & TempStart & " Kelvin" & NL & "high temperature: " &
TempEnd & " Kelvin" & NL & "Temperature increment: " & TempIncrement & NL & "Number of
measurements: " & MeasurementSteps & NL & "Measurement Program : " & program & NL &
MeasProgText
NL = Chr(13) + Chr(10) 'define NL(new line)
End Sub

```

```

-----
Private Sub Command3_Click() 'Main part of the program
    Dim Temp1 As Integer
    Dim Temp2 As Integer
    Dim v As Integer

    Dim z As Integer
    Command3.Visible = False
    Command2.Visible = True
    Command4.Visible = True
    CheckInterrupt = 0
    'Call TempSim(3)
    'Text3.Text = "Simulating 3"
    Call Initc ' Initialise the temperatur controller and set start temperature
    t = 0 ' counter for all valid temperature and resistance measurements
    N = 0 ' counter for all measurements
    If program = 1 Or program = 3 Then
        v = TempEnd
        z = TempStart - (2 * TempIncrement)
    End If
    If program = 2 Or program = 4 Then
        v = TempEnd + (2 * TempIncrement)
        z = TempStart
    End If
    If program = 3 Or program = 4 Then
        cycle = 1
    End If
    Do
        Call tempcontroller("$F1") 'Display sensor1
        Call Timer(1000)
        Text1.Text = "Set the temperature"
    
```

```

Call Settemperature(Settemp)
Settempdisplay = Settemp / 10
Text4.Text = Settempdisplay & " K"
N = 1
Call Dwell(10) 'Wait until the temperature has settled down
Call resdwelling 'Wait until the resistance is stable
t = t + 1 'count the measurement step
N = N + 1
'Call TempSim(2)
Call tempmeasurement2(N) 'Measure the temperature in the sample chamber
Temperature(t) = Temp(N) 'Temp(N)= returned value
Call resmeasurement(t) 'Measure the resistance
Print #1, Temperature(t) / 10 'returned value & "      " & Resistance(t) & "      " & (1 /
(Temperature(t) / 10)) ^ (1 / B) & "      " & Log((Resistance(t) * ((Temperature(t) ^ (-a)))
      'Write the data to the chosen file
Call Timer(1000)
Unload graph 'plots the results in a normal and a logarithmic scale
graph.Show 'remove the old graph and show the new one
Unload lngraph
lngraph.Show
If program = 1 Then

    Settemp = Settemp + (TempIncrement * 10) 'set the next temperature
End If
If program = 2 Then
    Settemp = Settemp - (TempIncrement * 10)
End If
If program = 3 Then
    If cycle = 1 Then
        Settemp = Settemp + (TempIncrement * 10)
    End If
    If Settemp > (TempEnd * 10) Then
        cycle = 2
        Label = t - 1
        v = TempEnd + (2 * TempInc)
        z = TempStart
    End If
    If cycle = 2 Then
        Settemp = Settemp - (TempIncrement * 10)
    End If
End If
If program = 4 Then
    If cycle = 1 Then
        Settemp = Settemp - (10 * TempIncrement)
    End If
    If Settemp < (TempStart * 10) Then
        cycle = 2

```

```

        Label = t - 1
        v = TempEnd
        z = TempStart - (2 * TempIncrement)
    End If
    If cycle = 2 Then
        Settemp = Settemp + (10 * TempIncrement)
    End If
End If
End If
Loop Until Settemp > (v * 10) Or Settemp < (z * 10) Or CheckInterrupt = 1 'loop until the end
Close #1          'temperature is reached or until the
Call Settemperature(2930)
Unload Monitoring 'experiment is interrupted by the user
Finish.Show 'remove the monitoring window and show the finish window
End Sub

```

```

-----
Private Sub Command1_Click() ' confirmation to continue the experiment
    Check = 1
End Sub

```

```

-----
Private Sub Command2_Click() ' interrupt the experiment

    CheckInterrupt = 1          'after carrying out the next measurement
End Sub

```

```

-----
Private Sub Command4_Click()
    Text1.Text = "Experiment interrupted"
    Text3.Text = "The data obtained so far" & NL & "is saved to the specified folder." & NL & "Please
wait until the program has shut down."
    Call Settemperature(2930)
    Call Timer(2500) ' time until the monitoring sheet disappears
    Monitoring.Hide
    Ingraph.Hide
    graph.Hide
    Finish.Show
End Sub

```

```

-----
Public Sub Timer(xt) 'Produces a time delay of X milliseconds
    Timer1.Interval = xt
    Timer1.Enabled = True 'enable Private Sub Timer1_Timer()
    Do
    DoEvents
    Loop Until Check = 3
    Check = 0
    Timer1.Enabled = False
End Sub

```

```
-----
Private Sub Timer1_Timer() ' carries out the command Check = 3 after the
    Check = 3                ' time delay set in Timer1.Interval
End Sub
-----
```

```
Private Sub MSCComm1_OnComm() 'serial port control
End Sub
-----
```

```
Public Sub InitTC() 'Initialises the temperature controller and sets the start temperature
    Text1.Text = "Initialise the ITC4 temperature controller"
    Check = 0
    Static Buffer$
    'Choose the settings for the output port
    MSCComm1.CommPort = 2
    MSCComm1.Settings = "9600,N,8,2"
    MSCComm1.InputLen = 0
    Call tempcontroller("$C3") 'Send remote enable command
    Text1.Text = "Remote enable command sent"
    Call Timer(1000) 'Waiting for sending the next command
    Call tempcontroller("$H1") 'Send command to enable sensor no. 1
```

```
Text1.Text = "Sensor 1 enabled"
```

```
Call Timer(1000)
```

```
Call tempcontroller("$F1") ' Display sensor1
```

```
Call Timer(1000)
```

```
If program = 1 Or program = 3 Then
```

```
    Settemp = TempStart * 10 'The temperature controller needs the temperature
```

```
End If                ' in K times 10
```

```
If program = 2 Or program = 4 Then
```

```
    Settemp = TempEnd * 10
```

```
End If
```

```
Call tempcontroller("$I1.0") 'set integral constant to 3
```

```
Text1.Text = "Set the integral constant to 3"
```

```
Call Timer(1000)
```

```
Call tempcontroller("$D0.5") 'set differential term to 1
```

```
Text1.Text = "Set the differential term to 1"
```

```
Call Timer(1000)
```

```
Call tempcontroller("$P3.0") 'setproportional band to 3.0
```

```
Text1.Text = "Set the proportional band to 3.0"
```

```
Call Timer(1000)
```

```
Call tempcontroller("$A1") 'Send command to Auto Heater
```

```
Text1.Text = "Heater set to Auto"
```

```
Call Timer(1000)
```

```
Text3.Text = "If your start temperature is lower than 90 Kelvin please open the valve for the liquid
nitrogen outlet completely, so that the sample chamber can cool down as fast as possible! If your start
```

temperature is higher, open the valve only half a turn (so that the little hole is on top). When the measurement has started open the valve half a turn!"

```
Command1.Visible = True
Check = 0
Do
DoEvents
Loop Until Check = 1
Command1.Visible = False
Check = 0
Text3.Text = " "
Text1.Text = " "
End Sub
```

Public Sub Dwell(W) 'Wait until the temperature has settled down and is close
'to the set temperature: difference is not more than W/10 K

```
Dim d As Integer
Dim c As Integer
Check = 0
Do
Text3.Text = "Settling down"
Text1.Text = "Wait until the set temperature is reached."

d = DwellingTime
c = 0
If Check > 0 Then
Do 'loop for a time delay of d seconds
c = c + 1
Call Timer(60000)
Loop Until c = d
End If
'Call TempSim(1)
Text3.Text = "Simulating1"
Text3.Text = "Measure the temperature from sensor No.1"
Call tempmeasurement1(N)
N = N + 1
Check = Check + 1
Text3.Text = " "
Loop Until Temp(N - 1) - Settemp < W And Temp(N - 1) - Settemp > -W
Text1.Text = " "
Do
N = N + 1 ' Counter for all temperature measurements
Text1.Text = "Checking if the temperature reading is stable."
d = DwellingTime
c = 0
Text3.Text = "Settling down"
If Check > 0 Then
```

```

Do 'loop for a time delay of d minutes
    c = c + 1
    Call Timer(60000)
Loop Until c = d
End If
'Call TempSim(1)
'Text3.Text = "Simulating1"
Text3.Text = "Measure the temperature from sensor No.1"
Call tempmeasurement1(N)
N = N + 1
Call Timer(3000)
Call tempmeasurement1(N)
N = N + 1
Call Timer(3000)
Call tempmeasurement1(N)
N = N + 1
Text3.Text = " "
Check = Check + 1
Loop Until Temp(N - 1) - Temp(N - 2) < 5 And Temp(N - 1) - Temp(N - 2) > -5 And Temp(N - 2) -
Temp(N - 3) < 5 And Temp(N - 2) - Temp(N - 3) > -5 'Loop Until the sensor reading is stable
Text1.Text = " "
Check = 0

```

```

Call Sensorcomparison(30) 'Wait until sensor1 and sensor2 differ not more
End Sub 'than 3 Kelvin

```

```

Public Sub Sensorcomparison(W) 'waits until sensor1 and sensor2 display a
Text1.Text = "Sensor comparison" 'similar temperature: difference not more
Dim sensor1 As Single 'than W/10 Kelvin
Dim sensor2a As Single
Dim sensor2b As Single
Dim sensor2c As Single
Dim sensor2 As Single
Dim P As Integer
P = 0 'counter for the comparisons
Do
If P > 0 Then ' no time delay until the first comparison
Text3.Text = "Wait until sensor1 and sensor2 have a similar temperature"
Call Timer(60000)
End If
Text3.Text = " "
P = P + 1
N = N + 1
Text3.Text = "Measure the temperature from sensor1"
Call tempmeasurement1(N)
Text3.Text = " "

```

```

sensor1 = Temp(N)
Call Timer(500)
N = N + 1
Text3.Text = "Measure the temperature from sensor2"
Call tempmeasurement2(N)
sensor2a = Temp(N)
N = N + 1
Call Timer(3000)
Call tempmeasurement2(N)
sensor2b = Temp(N)
N = N + 1
Call Timer(3000)
Call tempmeasurement2(N)
sensor2c = Temp(N)
sensor2 = (sensor2a + sensor2b + sensor2c) / 3
N = N + 1
Text3.Text = " "
Call Timer(200)
Call tempcontroller("$F1") 'display sensor1 again
Loop Until Abs(sensor2 - sensor1) < W And Abs(sensor2a - sensor2b) < 5 And Abs(sensor2b -
sensor2c) < 5 'wait until the sensors show a similar temperature
Text1.Text = " "

Call tempcontroller("$F1") 'display sensor1 again
Call Timer(1000)
End Sub

```

```

-----
Public Sub resdwelling() 'wait until the resistance is stable
Static Buffer As String
Dim ressum As Single
Dim tg As String
Dim Str As String
Dim i As Integer
Dim z As String
Dim count As Integer
Dim DevMess As Double
Dim dev As Double
Dim mev As Integer
Dim status As Integer
Dim length As Integer
Dim RetVal As String
ReDim re(1 To 30) As Single
ReDim resist(1 To 2) As Single
Text1.Text = "Wait until the resistance is stable"
mev = 0
initialize 7, 0

```

```

Send 20, "REN", status
Send 20, "F2XR0X", status
Call Timer(3000)
Do
For count = 1 To 2
    Do
        'send 20, "C1XZ1X", status
        'Call Timer(300)
        'send 20, "Z0XC0X", status
        'Call Timer(100)
        If status > 0 Then
            Text1.Text = "The Electrometer is not working!" & NL & "Check that the IEEE address is 20
and the connections!"
            Command1.Visible = True
            Do
                Loop Until Check = 1
            End If
            Check = 0
            Loop Until status = 0
            For i = 1 To 30
                Enter RetVal, 200, length, 20, status
                Call Timer(150)

                z = Right(RetVal, 11)
                re(i) = CSng(z)
                z = " "
            Next i
            'RetVal = Shell("C:\Resmeas2.exe", 2) ' Call a VisualBasic3 program which measures
                'the resistance and writes it to Resistan.txt
            'Call Timer(8000) 'time which is needed for measuring the resistance
            'AppActivate RetVal
            'SendKeys "{END}"
            'DevMess = Val(RetVal)
            Command1.Visible = False
            'Loop Until status = 0
            'Path = "C:\Resistan.txt"
            'Open Path For Input As #20 'open Resistan.txt
            'For i = 1 To 30 'read the 30 measured resistances and average them
                'Input #20, z
                'z = Right(z, 11)
                're(i) = CSng(z)
                'z = " "
            'Next i
            ressum = 0
            For i = 1 To 30
                ressum = ressum + re(i)
            Next i

```

```

resist(count) = ressum / 30 'average resistance
Text13.Text = resist(count) & " Ohm"
'Close #20
If count = 1 Then
    'send 20, "R11X", status
    Call Timer(9000)
    'send 20, "R0X", status
    Call Timer(1000)
End If
Next count
'send 20, "R11X", status
dev = Abs(resist(1) - resist(2))
If dev > (resist(1) / 100) Then
    Call Timer(60000)
End If
Loop Until Abs(resist(1) - resist(2)) < (resist(1) / 100)
Send 20, "C1XZ1X", status
    Call Timer(200)
    Send 20, "Z0XC0X", status
    Call Timer(15000)
Text1.Text = "Resistance stable!"
Call Timer(500)

```

End Sub

```

Public Sub tempmeasurement1(N) ' Measures the temperature of sensor1
    Static Buffer As String          'Choose the settings for the output port
    Dim Tempstr As String
    MSComm1.CommPort = 2
    MSComm1.Settings = "9600,N,8,2"
    MSComm1.InputLen = 0
    MSComm1.PortOpen = True
    MSComm1.Output = "$F1" & Chr$(13) 'display sensor1
    Call Timer(1000)
    MSComm1.Output = "R1" & Chr$(13) 'command for reading the temperature
    Call Timer(2000)                'from sensor1
    Buffer = MSComm1.Input 'Writes the input from the tempcontroller into a buffer
    Tempstr = Right$(Buffer, 6) 'extract the temperature from the device response
    Temp(N) = Val(Tempstr)
    Text2.Text = Temp(N) / 10 & " K"
    MSComm1.PortOpen = False 'close the output port

```

End Sub

```

Public Sub tempmeasurement2(N) 'Measures the temperature from sensor2
    Static Buffer As String          'Choose the settings for the output port
    Dim Tempstr As String

```

```

MSComm1.CommPort = 2
MSComm1.Settings = "9600,N,8,2"
MSComm1.InputLen = 0
MSComm1.PortOpen = True
MSComm1.Output = "$F2" & Chr$(13) 'display sensor2
Call Timer(500)
MSComm1.Output = "R2" & Chr$(13) 'read the temperature from sensor2
Call Timer(500)
Buffer = MSComm1.Input
Tempstr = Right$(Buffer, 6) 'extract the temperature from the device response
Temp(N) = Val(Tempstr)
Text12.Text = Temp(N) / 10 & " K"
MSComm1.PortOpen = False 'close output port
End Sub

```

```

-----
Public Sub Settemperature(Settemp) 'sets the temperature to the current set temperature
    Command = "T" & Settemp
    Call tempcontroller(Command) 'Send the command to set the temperature
    Call Timer(2000)
End Sub

```

```

-----
Public Sub tempcontroller(Command) 'Sends a command to the
    MSComm1.PortOpen = True 'temperature controller
    MSComm1.Output = Command & Chr$(13)
    Call Timer(1000)
    Buffer = Buffer & MSComm1.Input
    MSComm1.PortOpen = False
End Sub

```

```

-----
Public Sub resmeasurement(t) 'measures the resistance
    Text1.Text = "Measure the resistance"
    Static Buffer As String
    Dim ressum As Single
    Dim i As Integer
    Dim z As String
    Dim RetVal As String
    Dim length As Integer
    Dim status As Integer
    ReDim re(1 To 20) As Single
    'Shell "C:\Resmeas2.exe" ' Call a VisualBasic3 program which measures
        'the resistance and writes it to Resistan.txt
    'Call Timer(8000) 'time which is needed for measuring the resistance
    'Path = "C:\Resistan.txt"
    'Open Path For Input As #20 'open Resistan.txt
    'For i = 1 To 30 'read the 30 measured resistances and average them

```

```

'Input #20, z
'z = Right(z, 11)
're(i) = CSng(z)
'z = " "
'Next i
initialize 7, 0
Do
Send 20, "REN", status
Call Timer(200)
Send 20, "F2XR0X", status
Call Timer(200)
If status > 0 Then
Text1.Text = "The Electrometer is not working!" & NL & "Check that the IEEE address is 20
and the connections!"
Command1.Visible = True
Do
Loop Until Check = 1
End If
Check = 0
Command1.Visible = False
Loop Until status = 0

For i = 1 To 20
Enter RetVal, 200, length, 20, status
Call Timer(100)
z = Right(RetVal, 11)
re(i) = CSng(z)
z = " "
Next i
ressum = 0
For i = 1 To 20
ressum = ressum + re(i)
Next i
Resistance(t) = ressum / 20 'average resistance
'Close #20
Text13.Text = Resistance(t) & " Ohm"
'send 20, "R11X", status
End Sub

```

```

Public Sub TempSim(o) 'Simulate a temperature
If o = 1 Then 'simulate a temperature for sensor No.1
Temp(N) = Settemp
Text2.Text = Settemp / 10 & " K"
End If
If o = 2 Then 'temp for sensor No.2
Temp(N) = Settemp

```

```
Text12.Text = Settemp / 10 & " K"  
End If  
If o = 3 Then 'set the start temperature  
Settemp = TempStart * 10  
End If  
End Sub
```

